University of California
Santa Barbara

Magnetic frustration and quantum disorder in lanthanide-based $ALnX_2$ materials

A dissertation submitted in partial satisfaction
of the requirements for the degree

Doctor of Philosophy
in
Materials

by

Mitchell M. Bordelon

Committee in charge:

Professor Stephen D. Wilson, Chair
Professor Leon Balents
Professor Ram Seshadri
Professor John Harter

June 2021

The Dissertation of Mitchell M. Bordelon is approved.

Professor Leon Balents

Professor Ram Seshadri

Professor John Harter

Professor Stephen D. Wilson, Committee Chair

May 2021

Magnetic frustration and quantum disorder in lanthanide-based $ALnX_2$ materials

by

Mitchell M. Bordelon

To all of my fellow students and mentors who explore this frustrating field.

Acknowledgements

I would like to thank everybody who has helped me along my career in magnetic materials research. First, it was Prof. James Neilson and Prof. Kate Ross who introduced me to the field during my undergraduate studies at Colorado State University. They took me along on my first neutron experiments where I became enthralled by the massive amount of manpower and equipment used to look at the couple of grams of $Fe_3PO_4O_3$ sample we brought with us. These experiments and experiences I had working in Prof. James Neilson's laboratory inspired me to continue in this field and apply to the University of California Santa Barbara Materials department for a PhD.

Here at UCSB, I have worked with my advisor, Prof. Stephen Wilson, who has helped hone my interests and expertise in frustrated magnetism. Without his guidance, I would not be where I am today. He helped me refine the way I research magnetic materials, guiding me along detailed and targeted experiments to understand their properties. As every graduate student and advisor has, we had a number of failed experiments, but the ones that were fruitful truly tested my ability to learn more about materials synthesis and condensed matter physics. We delved into the mysteries of the magnetic properties of f electron $ALnX_2$ materials that became the basis for this thesis. I also thank the other members of my committee, Prof. Ram Seshadri, Prof. Leon Balents, and Prof. John Harter, who have guided me along my graduate student studies throughout the years.

I owe my heartfelt thanks to Prof. Leon Balents and Chunxiao Liu. They were both instrumental in my work as a PhD student working on these $ALnX_2$ materials. They developed the theoretical analysis for the materials in this thesis, and without their aide, our understanding of the magnetic properties of these materials would have been significantly hindered and more speculative than concrete. Together we were able

to piece together the signatures of quantum disorder in $NaYbO_2$ and develop a model that captures nearly all of the features of spiral magnetic order in $LiYbO_2$. They are a cornerstone in my successful research publications and the work of this thesis, and I hope we have the chance to continue to work together and research more about these unique materials systems.

To all of my collaborators and mentors I have had during my graduate studies. Prof. Michael Graf and his student Eric Kenney have aided my work numerous times. They collected key low temperature magnetic susceptibility data on some of our frustrated f electron materials. This allowed us to determine phase boundaries, magnetic ordering transition temperatures, and other phenomenon of these f electron materials that display most of their magnetic behavior only at low temperature. Furthermore, Dr. Tom Hogan from Quantum Design, who is a former Wilson group member, helped us secure more key magnetic data and has been a wonderful help in helping me and my fellow group members fully understand the Quantum Design instruments and their capabilities. Prof. Mark Sherwin and his group members Dr. Marzieh Kavand, Yuanqi Lyu, and Dr. Xiaoling Wang have additionally helped us obtain and understand magnetic moment anisotropies of these materials.

Of course, I also would like to thank the instrument scientists and staff at the national laboratory facilities where I spent a large portion of my degree collecting neutron scattering data, which includes staff from Oak Ridge National Laboratory and the NIST Center for Neutron Research: Prof. Nicholas Butch, Prof. Craig Brown, Dr. Daniel Pajerowski, Prof. Arnab Banerjee, Dr. Qiang Zhang, and Dr. Stuart Calder. Every time I visited a national laboratory, they were quick to help with data analysis and sample preparation, and they were always available when an instrument problem arose.

Furthermore, to all of the laboratory members of the Wilson group. I am grateful for your friendship that made the group welcoming and aid in making my research suc-

cessful. Specifically, I want to thank Lorenzo Posthuma, an undergraduate Chemistry student, who worked with me for a number of years and helped me prepare the untold number of samples we needed for all of our measurements. Additionally, to Dr. Paul Sarte, who helped me develop an understanding of f electron crystalline electric field analysis and dilution refrigerator specific heat measurements, and Dr. Brenden Ortiz, who collaborated with me on our cerium projects and showed me new flux based crystal growth methods.

I owe my thanks to my friends and family who have supported me during my PhD. My parents, sisters, and grandparents have always been supportive of my interests in magnetism and are always looking forward my next publication and a breakdown of what we discovered without the scientific jargon. You all motivate me to continue the hard work on investigating the fundamental properties of magnetic materials.

Finally, to my fiancé and best friend, Connie Dong, thank you for always being here. Your immense support, perseverance in your own PhD studies, and smile has made the hard days feel better and the great days feel even brighter. I look forward to what the future holds for us.

Curriculum Vitæ

Mitchell M. Bordelon

Education

2016−2021	Ph.D. in Materials (Expected) University of California, Santa Barbara, CA Advisor: Professor Stephen D. Wilson
2012−2016	B.S., Chemistry Colorado State University, Fort Collins, CO Advisor: Professor James R. Neilson

Publications

12 P. M. Sarte, K. Cruz-Kan, B. R. Ortiz, K. H. Hong, **M. M. Bordelon**, D. Reig-i-Plessis, M. Lee, E. S. Choi, M. B. Stone, S. Calder, D. M. Pajerowski, L. Mangin-Thro, Y. Qui, J. P. Attfield, S. D. Wilson, C. Stock, H. D. Zhou, A. M. Hallas, J. A. M. Paddison, A. A. Aczel, C. R. Weibe. *Dynamical ground state in the XY pyrochlore Yb2GaSbO7. Accepted to npj Quantum Materials.*

11 S. D. Wilson & **M. M. Bordelon**. *Quantum disorder and unconventional magnetism in ALnX2 (A = alkali; Ln = lanthanide; X = chalcogen) materials. Neutron News* **32(1)**, 19-21 (2021). [DOI: 10.1080/10448632.2021.1875780]

10 **M. M. Bordelon**, J. D. Bocarsly, L. Posthuma, A. Banerjee, Q. Zhang, S. D. Wilson. *Antiferromagnetism and crystalline electric field excitations in tetragonal NaCeO2. Phys. Rev. B* **103**, 024430 (2021). [DOI: 10.1103/PhysRevB.103.024430]

9 **M. M. Bordelon**, C. Liu, L. Posthuma, E. Kenney, M. J. Graf, N. P. Butch, A. Banerjee, S. Calder, L. Balents, S. D. Wilson. *Frustrated Heisenberg J1-J2 model within the stretched diamond lattice of LiYbO2. Phys. Rev. B* **103**, 014420 (2021). [DOI: 10.1103/PhysRevB.103.014420]

8 **M. M. Bordelon**, C. Liu, L. Posthuma, P. M. Sarte, N. P. Butch, D. M. Pajerowski, A. Banerjee, L. Balents, S. D. Wilson. *Spin excitations in the frustrated triangular lattice antiferromagnet NaYbO2. Phys. Rev. B* **101**, 224427 (2020). [DOI: 10.1103/PhysRevB.101.224427]

7 R. L. Dally, A. J. R. Heng, A. Keselman, **M. M. Bordelon**, M. B. Stone, L. Balents, S. D. Wilson. *Three-Magnon Bound State in the Quasi-One-Dimensional Antiferromagnet α-NaMnO2. Phys. Rev. Lett.* **124**, 197203 (2020). [DOI: 10.1103/PhysRevLett.124.197203]

6 **M. M. Bordelon**, E. Kenney, C. Liu, T. Hogan, L. Posthuma, M. Kavand, Y. Lyu, M. Sherwin, N. P. Butch, C. Brown, M. J. Graf, L. Balents, S. D. Wilson. *Field-tunable quantum disordered ground state in the triangular-lattice antiferromagnet NaYbO2. Nat. Phys.* **15**, 1058-1064 (2019). [DOI: 10.1038/s41567-019-0594-5]

5 B. R. Ortiz, L. C. Gomes, J. R. Morey, M. Winiarski, **M. M. Bordelon**, J. S. Mangum, I. W. H. Oswald, J. A. Rodriguez-Rivera, J. R. Neilson, S. D. Wilson, E. Ertekin, T. M. McQueen, E. S. Toberer. *New kagome prototype materials: discovery of KV3Sb5 RbV3Sb5, and CsV3Sb5. Phys. Rev. Materials* **3(9)**, 094407 (2019). [DOI: 10.1103/PhysRevMaterials.3.094407]

4 S. W. Song, J. Mao, **M. M. Bordelon**, R. He, Y. M. Wang, J. Shuai, J. Y. Sun, X. B. Lei, Z. S. Ren, S. Chen, S. D. Wilson, K. Nielsch, Q. Y. Zhang, Z. F. Ren. *Joint effect of magnetism and yttrium on enhancing thermoelectric properties of n-type Zintl Mg3+δY0.02Sb1.5Bi0.5. Mater. Today Phys.* **8**, 25-33 (2019). [DOI: 10.1016/j.mtphys.2018.12.004]

3 M. J. Tarne, **M. M. Bordelon**, S. Calder, J. R. Neilson, K. A. Ross. *Tuning the antiferromagnetic helical pitch length and nanoscale domain size in Fe3PO4O3 by magnetic dilution. Phys. Rev. B* **96**, 214431 (2017). [DOI: 10.1103/PhysRevB.96.214431]

2 A. E. Maughan, A. M. Ganose, **M. M. Bordelon**, D. O. Scanlon, J. R. Neilson. *Defect tolerance to intolerance in the vacancy-ordered double perovskite semiconductors Cs2SnI6 and Cs2TeI6. J. Am. Chem. Soc.* **138(27)**, 8453-8464 (2016). [DOI: 10.1021/jacs.6b03207]

1 K. A. Ross, **M. M. Bordelon**, G. S. Terho, J. R. Neilson. *Nanosized helical magnetic domains in strongly frustrated Fe3PO4O3. Phys. Rev. B* **92**, 134419 (2015). [DOI: 10.1103/PhysRevB.92.134419]

Abstract

Magnetic frustration and quantum disorder in lanthanide-based $ALnX_2$ materials

by

Mitchell M. Bordelon

Within the field of magnetism, magnetic frustration is a generous source of new phases of matter with unusual and exciting physical properties. Magnetic order is dictated by the interdependence of local electronic states and their real-space interactions decorating materials lattices. These local states can compete or work together to drive differing magnetic states of matter, ranging from the typical collinear (anti)ferromagnets to more exotic, highly-entangled ground states with emergent phenomena in small spin systems ($S = 1/2$). These correlated phases are predicted to arise in materials lattices that incite multiple equivalent interactions without a readily apparent magnetic ground state configuration in so called magnetic frustration. In turn, this frustration can lead to massively degenerate classical ground states hinting that instead a novel entangled phase could arise from the competition. Even with decades of research in this field, frustrated magnets remain an exciting and growing field of research as new magnetic phases are discovered.

Herein, the physical properties of insulating lanthanide-based frustrated magnets are explored from select members of the $ALnX_2$ (A = alkali, Ln = lanthanide, X = chalcogenide) family of materials. This materials family crystallizes in various structures dictated by the ratio of the lanthanide radius to the alkali and chalcogenide radii, and this thesis focuses on two frustrated crystal lattices in this family, the equilateral triangular lattice and the elongated diamond lattice. We find that triangular lattice $NaYbO_2$ does not conventionally order to 50 mK and instead contains an unconventional quan-

tum disordered ground state that is tunable in an external magnetic field. However, structurally-similar triangular lattice $KCeO_2$ magnetically orders below 300 mK with a small magnetic moment. Additionally, we show how the Heisenberg $J_1 - J_2$ model can be applied to the elongated magnetic diamond lattice in $LiYbO_2$ and $NaCeO_2$ where collinear or spiral magnetic order arises depending on the ratio of J_2/J_1. In $LiYbO_2$, spiral magnetic order undergoes an incommensurate-to-commensurate structure under an external field below 1 K while $NaCeO_2$ exhibits long range collinear antiferromagnetic order below 3.2 K. Overall, these materials studies advance the dependence of frustrated magnetic phases on external parameters, lanthanide character, and lattice geometry.

Contents

List of Figures

Chapter 1

Introduction

Electronic magnetism in solid state materials arises due to electronic moments from unpaired electrons. Although magnetism can arise from nuclear moments, the nuclear moment interaction is short-range, weak, and usually inconsequential for collective, long range magnetic behavior of a material before extremely low temperatures. In comparison, unpaired electrons can interact with each other to give a variety of electronic and magnetic phases of matter from zero Kelvin to hundreds of Kelvin. In the simplest limit, the electrons can be localized or delocalized in an insulating or metallic state. For instance, with strong onsite repulsion, a Mott insulating state forms where localized electronic moments can interact with one another via exchange mechanisms between atoms in a lattice. When onsite repulsion is weak, the electrons readily hop to form a metallic state. More exotic states such as the cuprate superconductors [17–19] or a variety of spin liquid phases [20–25] can also appear in this regime of strongly correlated electron physics and are a significant focus of the condensed matter community to understand their many body interactions. In this thesis, the focus is on materials with the goal of understanding the materials characteristics that can produce exotic magnetic phases in insulators.

1.1 Frustrated magnetism

Collective electronic phases in insulators originate when magnetic moments interact to give rise to complex magnetic behaviors. The nature of their ground state depends on the type and strength of magnetic exchange through direct and indirect exchange interactions. The ground state phases change under external perturbations such as a magnetic field or temperature, lattice geometry, moment size and dimensionality, and inherent anisotropies [20–27]. Lattice geometry is dictated by the crystal structure and moment characteristics and anisotropies are determined by the magnetic atom.

Typically, at sufficiently low temperatures below the magnetic interaction strength, these moments develop long range magnetic order, such as a ferromagnet or a Néel antiferromagnet. In these long range ordered states, nearest neighbor moments align or anti align, respectively, due to the sign of magnetic exchange J between magnetic moments. In effect, the static structure of these magnetic lattices can be deduced starting from any one magnetic moment orientation. Their correlated dynamics can form bosonic magnetic excitations called magnons with gapless modes, and in general, the ferromagnet and antiferromagnet are well understood and commonplace magnetic ground states of materials [20–27].

However, this view of (anti)ferromagnets is too simplistic for some materials systems. Other interactions can perturb these ground states and instead favor more exotic types of magnetic order. One of the most active areas of research in this topic is frustrated magnetism [20–27]. In a frustrated magnetic material, multiple magnetic interactions compete to preclude conventional (anti)ferromagnetic order. These interactions can arise in a number of different ways and act to hinder each others' favorable magnetic interactions, making the material "frustrated" that it cannot reach a low energy, favorable ground state. In theory, all a material needs to become frustrated is multiple magnetic in-

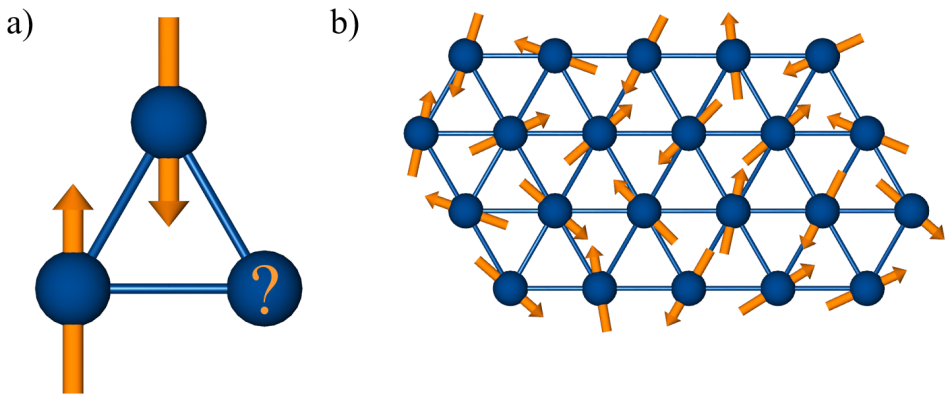

Figure 1.1: a) Geometric frustration of antiferromagnetically coupled moments on a triangle allows two moments to anti align but not all three in the Ising limit. This simplistic view of geometry and magnetism hints that antiferromagnetically coupled triangular lattice materials may exhibit unusual magnetic ordering to alleviate geometric frustration. b) One result of geometric frustration on a triangular lattice is moments may continuously fluctuate between a macroscopic set of degenerate states. In the small spin $S = 1/2$ limit, the ground state can form a quantum spin liquid.

teractions attempting to dictate the orientation of a magnetic moment. One can envision multiple ways of introducing frustration into a magnetic system. For instance, a magnetic moment can contain multiple nearest neighbor moments with differing exchange signs. In turn, the collective ground state of the magnetic system cannot be deduced from the single moment limit. This effect is distinct from other factors such as quenched chemical disorder that can inhibit conventional magnetic order and is inherent to the materials system.

These frustrated magnetic materials are highly sought after as a focal point for new magnetic phases of matter. Where conventional magnetism breaks down, new magnetic phases such as a spin liquid [20–25] can arise where moments continuously fluctuate in a cohesive manner or a spiral phase [28–30] where moments rotate along an axis in the crystal. A commonplace starting point for frustration originates in the geometry of the materials magnetic lattice. This "geometrical" frustration relies on the intrinsic magnetic interaction pathways of a material. The prototypical geometrically frustrated lattice is

the triangular lattice antiferromagnet of Ising spins [20–27]. If one attempts to anti align all magnetic moments on a triangle, at most only two moments can simultaneously be satisfied (Figure 1.1). On an infinite periodic triangular lattice, this effect is amplified and leads to an infinite degeneracy of classical ground states, all of which are unsatisfactory to the local magnetic moment. Various other lattice types exhibit geometric frustration, such as the pyrochlore lattice [27, 31, 32], honeycomb lattice [33–35], (hyper)kagome lattice [36–38], face centered cubic lattice [28–30], and square lattice [39–44], but the basic concepts driving geometrical frustration remain constant.

If one assumes that no other interactions or symmetry breaking occurs, an ideally frustrated Ising triangular lattice should never conventionally antiferromagnetically order to zero Kelvin. Instead, at low temperatures, the magnetic moments thermodynamically freeze into one of the states as a spin glass, continue to fluctuate between the degenerate states, or form a macroscopically entangled ground state [20–25]. Magnetic materials with large magnetic moments will freeze and materials with small magnetic moments (i.e. $S = 1/2$) may continue to fluctuate as a quantum spin liquid [20–25] with a ground state wavefunction related to a superposition of the degenerate states like the resonating valence bond state [45–50]. In particular, the various quantum spin liquid ground states are of interest as they are characterized by persistent fluctuations to zero temperature, fractional quantum number excitations, and emergent gauge fields [20–25] as will be detailed in the section below.

However, this view of a frustrated triangular lattice is again too simplistic for understanding real materials systems. For example, adding more degrees of freedom beyond Ising to the Heiseinberg limit instead indicates the magnetic ground state of the triangular lattice antiferromagnet is the 120 degree antiferromagnet [51–53]. Additionally, including all of the anisotropies or symmetry breaking effects of a material will pull the material from the ideally frustrated regime. Overall, a frustrated magnet always attempts to

relieve the frustration through another degree of freedom. This appears in many trinangular lattice systems such as $NaMnO_2$ [54, 55], and $NaVO_2$ [56, 57], and $LiVO_2$ [56, 58] where spin chains and orbital ordering occur, breaking the frustrated lattice geometry. Additionally, this happens in other frustrated lattices like the diamond lattice in AB_2X_4 spinel compounds. The materials $NiRh_2O_4$ [59], $MnSc_2S_4$ [60–62], $CdCr_2O_4$ [63, 64], and $ZnCr_2O_4$ [64–66] magnetically order as a result of tetragonal distortions or strong single ion anisotropies that pull away from the ideal frustrated regime.

Therefore, an overarching goal of geometrical frustrated magnetism is identifying materials where these unfavorable interactions are minimal or aid in the formation of an exotic magnetic ground state. Key to this goal is synthesizing materials devoid of chemical imperfections that randomly alter the environment surrounding the magnetic lattice, as even non magnetic species can drastically alter the magnetic ground state. However, not all materials can be made without incorporating a degree of inherent anisotropy. Instead of attempting to find materials without anisotropies, one route to finding new magnetic phases in frustrated magnets is to include these anisotropies into a relevant theoretical model and searching for new magnetic phases. Although it may naively appear that all anisotropies and symmetry breaking effects negatively impact the chance of realizing an exotic phase, certain systems rely on these perturbations.

For example, two of the most prominent triangular lattice antiferromagnetic materials proposed to be a quantum spin liquid candidate in the past decade are $YbMgGaO_4$ [48–50, 67–78] and $NaYbO_2$ [14, 79–82], which is covered in this thesis. These material are comprised of trivalent Yb ions with strongly anisotropic interactions arising from strong spin orbit coupling. The interplay of spin orbit coupling and strong electronic correlations on a frustrated antiferromagnetic lattice has introduced new routes to realizing novel quantum disordered phases of matter. As will be discussed in a later chapter, models of this material and other $4f$ triangular lattice materials indicate a quantum spin liquid may

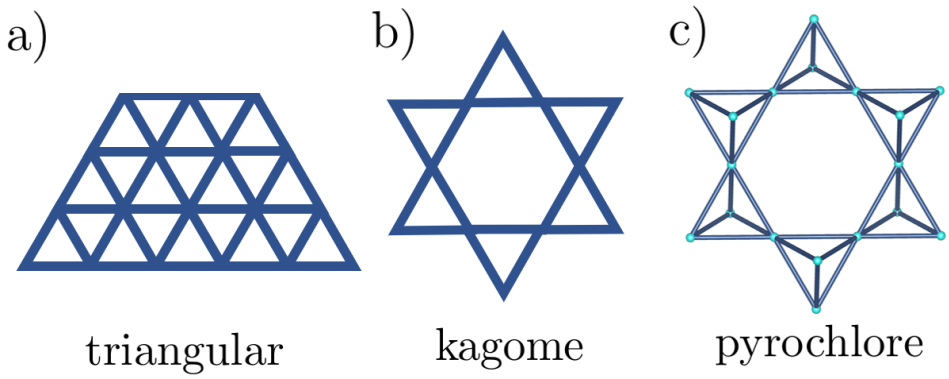

Figure 1.2: A common structural motif in materials is an equilateral triangle as the most compact way to pack spheres of atoms on a two dimensional sheet creates an equilateral triangular lattice. Luckily, this structural motif also generates geometrical frustration when the atoms are magnetic, and many frustrated materials systems are based off of frustration of triangles. a) In two dimensions, the simple triangular lattice is the triangular lattice. b) However, other geometries such as the kagome lattice can be generated, which is the 1/3 lattice point diluted variant of the triangular lattice. c) In three dimensions, one can view the frustrated pyrochlore lattice originating from the triangles in the frustrated tetrahedra, where each corner sharing tetrahedron alternates pointing into and out of the page.

arise when magnetic order yields to strong quantum fluctuations and a delicate balance of anisotropic magnetic exchange interactions residing at the phase boundary between multiple magnetic phases [12, 14, 79–87].

Overall, frustrated magnetism has a prominent focus in the condensed matter community for identifying new electronic phases of matter. Theorists and experimentalists must work together to identify promising materials systems, and the exploration of these new phases and the many body physics controlling them is a difficult and exciting challenge.

1.1.1 General frustrated materials search principles

In general, there are a few practical principles to keep in mind when searching for geometrically frustrated materials with the goal of finding unconventional magnetic phases like quantum disorder.

- *Frustrated lattice type*: Numerous types of frustrated lattices exist, most of which have been cataloged. Some examples are the triangular lattice [20–25], pyrochlore lattice [27, 31, 32], honeycomb lattice [33–35, 88], (hyper)kagome lattice [36–38], face centered cubic lattice [28–30], and square lattice [39–44]. All one needs to generate geometrical magnetic frustration is competitive magnetic interactions along geometric pathways within a lattice, and any lattice geometry with two or more neighboring interactions can be conceptualized to contain frustration. As a starting point, triangles are the prototype of geometrical frustration and any antiferromagnetic material with them, even if without equilateral triangles, may exhibit frustration phenomena. Some common examples of materials based off of triangle frustration are shown in Figure 1.2

- *Robust chemical lattice*: Almost all frustrated materials magnetism is based off of solely understanding the magnetic lattice of a material. Non magnetic species are usually disregarded when analyzing and predicting magnetic phases in materials. However, a real material does not consist of just magnetic metal ions. The single ion properties of the magnetic ions are governed by the environment surrounding them, both from determining the charge of the ion, and therefore the number of unpaired electrons, and the local site symmetry determining the energy levels of the unpaired electron states. Therefore, an ideal material with a frustrated magnetic lattice would have a robust chemical lattice, including both magnetic and non magnetic species in order to generate a globally consistent environment surrounding each magnetic ion. Chemical randomness in magnetically frustrated systems dissolves equivalent interactions along each geometric pathway needed for frustration by randomly altering the local electronic environment. This often is linked to spin glass formation rather than any coherent magnetic phase. Recent reports, however,

suggest a notable exception to this by stating non magnetic site mixing could help induce a quantum disordered ground state in $YbMgGaO_4$ [49, 68, 69], but this is not yet confirmed as a generic property of frustrated systems.

- *Simple chemical lattice*: This point coincides with the previous statement on robust chemical lattices. More complex chemical systems can become too complex to accurately model and understand. Ideally, one would search for a chemical system with as few chemical and structural motifs as possible with a straightforward single crystal synthesis method. Multiple chemical environments surrounding magnetic moments and exchange unevenness are a likely result of a complex chemical lattice as in $Ba_2Sn_2Ga_3ZnCr_7O_22$ [89]. Conversely, many of the simple materials systems have been thoroughly investigated, and understanding what breaks geometric frustration can guide identifying materials that could be ideal candidates.

  Though, at first glance, many of the simple materials systems have been explored. For instance, the frustrated lanthanide pyrochlore family $Ln_2M_2O_7$ (Ln = lanthanide, M = metal or metalloid) [90–99] contains a rich phase space of magnetic phases, from quantum spin ices and U(1) spin liquids to all in all out ferromagnets. Althought not all of these pyrochlore materials have been thoroughly investigated since the family of materials is large, the number of new and notable materials within this family is steadily decreasing.

  Another possible system to look at is the $ALnX_2$ family of layered delafossite like materials with frustrated triangular lattices [3–5, 12, 14, 79–87] with some examples presented in this thesis. However, as will be detailed in Appendix B, even though many members of this family are not fully investigated, the single crystal growth of the oxides of this family are exceedingly challenging. More work is required to figure out the single crystal growth, as understanding all of the facets of the

magnetic ground states in these materials requires high quality single crystals.

Overall, the idea is to find a relatively underexplored materials platform that has as few chemical species present as possible, a simple chemical lattice, minimal chemical disorder, and readily available crystal growth method.

- *Small moments*: Small magnetic moments with spin quantum number $S = 1/2$ or effective angular momentum $J_{eff} = 1/2$ are key to generating unconventional magnetic phases. A $S = 1/2$ system contains one unpaired electron with weak to moderate spin orbit coupling while a $J_{eff} = 1/2$ system forms from strong crystalline electric field splitting of a strongly spin orbit coupled manifold, as will be explained in the subsequent section. Strong quantum fluctuations preclude moment freezing to zero Kelvin, as the size of the moment is in the same order as its zero point motion. In some cases, it should be noted that some reports claim $S = 1$ in $NiRh_2O_4$ is small enough to be included within the regime of small moments [30, 59].

- *f vs. d electrons*: The type of magnetic atom in the material dictates the anisotropies and exchange interactions allowed. There is a trade off when searching for materials with either f or d electron magnetic moments. In d electron systems, magentic exchange is usually stronger and more extended than f electron exchange due to the limited orbital extent of f electrons. This can make modeling d electron systems more complex, as they can require many exchange interactions beyond the nearest neighbor such as in $MnSc_2S_4$ [60–62]. On the other hand, the more localized exchange of f electron insulators means that magnetic ordering phenomena do not appear until low temperatures, such as the formation of magnetic order in $KCeO_2$ at 300 mK presented in this thesis. In both cases, one must understand the role of the local anisotropies of the atom in order to accurately understand the system.

In f electron materials, this involves fitting crystalline electric field excitations to determine the ground state wave function and in d electron materials it includes understanding the interplay of weak ($3d$) to moderate ($5d$) spin orbit coupling and its effect on local magnetic moment characteristics and their exchange.

1.1.2 Quantum spin liquids

One of the goals at the forefront of frustrated magnetism is searching for magnetic quantum spin liquid phases. This name is somewhat of a misnomer as it belies the true nature of the quantum phase that is distinct from a normal definition of a liquid. These quantum disordered phases exemplify strong quantum fluctuations that prevent conventional magnetic ordering with massively entangled ground states that can support non-local, fractionalized excitations [20–25]. Their ground state wave functions directly tie to massive superposition of local degrees of freedom that combine into a highly entangled phase. Correspondingly, the entangled phase contains degrees of freedom that are an entangled collection of local states. For example, they can often be depicted using the parton approach [22] that recombines local parts of degrees of freedom for the new set of degrees of freedom. In other words, the excitations and observables of a highly entangled quantum spin liquid phase generically contains phenomena that cannot be described by any one set of local variables, and the depiction of these many body states cannot be deformed into a simple set of product states like a conventional (anti)ferromagnet [20–25].

Where conventional magnets form bosonic spin waves, a quantum spin liquid may form fractionalized variants of a spin wave from the fractionalized degrees of freedom of an entangled lattice. One of the most common examples is the spinon that carries a fractional magnon spin like $S = 1/2$ through the lattice when spin is an adequate quantum number [20–25]. These spinons are created in pairs and maintain long range

correlations as they move throughout a magnetic lattice and can form a spinon Fermi surface [20–25, 77] with a set of gapped low energy excitations. Such a state has been proposed recently for the candidate $YbMgGaO_4$ as a U(1) quantum spin liquid [50, 77].

However, this is just one example of an elementary excitation in a quantum spin liquid. Other variants such as linear phonon modes from in a U(1) Coulomb phase arise [99], and the exact type of excitations highly depend on the specific quantum spin liquid theoretical model employed and its symmetries. The differing models contain gapped, gappless, fermionic, and bosonic excitations that can arise in two and three dimensional entangled frustrated systems. For instance, a Z_2 triangular lattice spin liquid is derived from competing J_1 and J_2 interactions on a Heisenberg triangular lattice[22, 100]. Originally, Anderson suggested that instead of forming three sublattice 120 degree order, the ground state in this system may favor an entangled "resonating valence bond" state hosting gapped excitations [45–50]. In some cases, the quantum spin liquid ground state is exactly solvable, such as in the Kitaev honeycomb model [22, 33–35, 88]. Other models rely on numerical methods to search for entangled phases residing near multiple phase boundaries in a frustrated system [36, 72, 101, 102].

There are numerous detailed reviews on the theory of differing quantum spin liquid phases [20–25], and the goal of this section of the thesis was to introduce the generic basic properties of these entangled states. The following subsection will show that from a materials scientist point of view what are the experimental principles needed to search for these proposed entagled states.

Experiments for quantum spin liquids

The most vexing problem about quantum spin liquids is identifying if the material one is looking at *is* actually a quantum spin liquid. Despite all of the non-local characteristics and massive entanglement of these phases, they are exceedingly difficult to directly

probe. In part, this is due to predicting which material fits with which theoretical model. Additionally, the observables in these theoretical phases can only exist within them as they are an emergent result of entangled degrees of freedom that exist only within that state and material, and, as of this thesis, experimental measurements cannot directly measure entanglement. Instead, the general route to searching for a quantum spin liquid material involves measuring all available magnetic properties of a material inside and outside of the quantum spin liquid temperature-field regime. These measurements are then used to *exclude* all other possible explanations that would originate from a typical (anti)ferromagnet, which results in proving one has a quantum spin liquid by proving it cannot be anything else.

Since determining the presence of a quantum spin liquid is difficult, certain experimental phenomena are used in conjunction to search for these exotic phases. A brief introduction to the methodology of experiments used in this thesis are as follows. Full details of the experiments used in this thesis are in chapter 2 on Methods.

- *Magnetic susceptibility*: A material's magnetic susceptibility is usually the first measurement collected on a magnetic material. The temperature dependent susceptibility χ can be fit to the Curie-Weiss relationship to extract an effective correlation between magnetic moments called the Curie-Weiss temperature θ_{CW}. If this temperature is relatively large and no features of long range magnetic ordering exist to the lowest temperatures in the susceptibility data (e.g. splitting in zero-field cooled and field cooled data), then this suggests the material is magnetically frustrated. Ideally, a quantum spin liquid material would not exhibit magnetic order to zero Kelvin, but real experiments typically cannot reach below $\sim$ 50 mK. Additionally, a.c. magnetic susceptibility gives light to differentiations between quantum spin liquids, spin glasses, and paramagnets. In general, the a.c. susceptibility should be

frequency independent and level off in a quantum spin liquid, as all of the moments are continuously fluctuating in an entangled state with a maximal susceptibility with decreasing temperature. A spin glass should contain strong frequency dependence and a paramagnet should exhibit continuously increasing susceptibility with decreasing temperature.

- *Isothermal magnetization*: Similar to magnetic susceptibility, the isothermal magnetization of a material provides basic knowledge on the magnetic moments comprising a material. The measurements typically are used to find the maximal saturated magnetic moment or signs of hysteresis arising from an ordered magnetic phase but can sometimes provide other insightful information. For example, studies on $NaYbO_2$ [14, 79–81] and $Ba_3CoSb_2O_9$ [103–105] have shown a plateau near 1/3 of their saturated magnetizations, suggesting they behave similarly to the XXZ model of a two dimensional triangular lattice.

- *Specific heat*: Second, specific heat data is at least of two fold use for quantum spin liquid searches. As a magnetic material is cooled, it must release its magnetic entropy before $T = 0$ K. If the entropy is released in one sharp peak, this usually indicates the formation of a conventional long range ordered state. If the entropy is released slowly with temperature, this can indicate the formation of a spin glass or possibly a quantum disordered phase. The shape or number of features in the specific heat may relate directly to spin liquid models, such as the two peaks predicted for Heisenberg spins on a kagome lattice [106–108]. Additionally, the integrated magnetic specific heat C_p/T indicates the number of microstates involved and will approach $Rln(2)$ for a spin 1/2 system. The low temperature tail of specific heat can also be fit to a power law, and differing quantum spin liquid models follow different power laws. This, however, must be carefully analyzed as it is easily con-

fused with power laws for spin glasses or can be perturbed by nuclear magnetism at ultra cold temperatures.

- *Neutron scattering*: Perhaps one of the most useful techniques for studying quantum disorder is neutron scattering. This includes elastic, low energy inelastic, and high energy inelastic scattering processes. An introduction to neutron scattering will be presented in the Methods chapter. In essence, scattering neutrons contain a magnetic spin that probe static and dynamic spin-spin correlations. The static correlations are used to identify long range magnetic ordering in elastic diffraction data. The dynamical correlations at low energy are used to study spin waves or continua excitations that could arise from fractionalized excitations. These measurements are a direct analysis of the magnetic structure of a material, and are key to searching for fractionalized excitations. The information contained in low energy inelastic neutron scattering is extremely rich, providing information about the energy scale of interactions in the magnetic material and how the excitations are structured in reciprocal space. At high energy, inelastic neutron scattering directly measures the crystalline electric field of local ions and is used for determining the governing ground state wave function.

1.2 $4f$ electron magnetic moments

All magnetism in the solid state stems from the properties of single ion magnetic moment while electronic phases of matter are the result of their cooperative interactions. Magnetic moments in insulators come from unpaired electrons of the metal ions, and this section overviews the principles of $4f$ electron magnetic moments as they are the focus of the magnetic materials in this thesis.

1.2.1 Free ion electronic structure

The energy levels of an unperturbed free ion Hamiltonian, $\hat{H}_0$, is given by:

$$\hat{H}_0\psi = E\psi \tag{1.1}$$

Ignoring spin orbit coupling, its eigenvalues are based on quantum numbers n, l, m_l, s, m_s correpsonding to components of orbital and spin angular momenta. The operators are $\hat{L}^2$, $\hat{L}_z$, $\hat{S}^2$, and $\hat{S}_z$ where

$$\hat{L}^2|n, l, m_l >= l(l+1)\hbar^2|n, l, m_l >, \tag{1.2}$$

$$\hat{L}_z|n, l, m_l >= m_l\hbar|n, l, m_l >, \tag{1.3}$$

$$\hat{S}^2|s, m_s >= s(s+s)\hbar^2|s, m_s >, \tag{1.4}$$

and

$$\hat{S}_z|s, m_s >= m_s\hbar|s, m_s > . \tag{1.5}$$

The momentum along an orbital axis or spin axis is given by $m_l\hbar$ or $m_s\hbar$, respectively. Similarly, the total magnitude of the momentum is $\sqrt{l(l+1)\hbar^2}$ or $\sqrt{s(s+1)\hbar^2}$. A lone electron in an orbital has unique quantum numbers $|n, l, m_l, s, m_s >$. The magnetic moment arising from orbital or spin angular momentum along an axis is given by

$$\mu_{[l,s]} = -g_{[l,s]}\mu_B m_{[l,s]} \tag{1.6}$$

where $g = 1$ or 2 for orbital momentum and electron spin, respectively, and $\mu_B =$

$(e\hbar)/(2m_e)$ is the Bohr magneton.

Spin orbit coupling

However, the $4f$ electrons of a free lanthanide ion contain strong spin orbit coupling (SOC). Since spin orbit coupling increases approximately as atomic number Z^4, total spin angular momentum S and total orbital angular momentum L are not adequate independent quantum numbers to describe the $4f$ ions. A new Hamiltonian becomes

$$\hat{H}_1 = \hat{H}_0 + \hat{H}_{SOC} \tag{1.7}$$

This $\hat{H}_1$ requires a new set of quantum numbers and operators derived from coupling spin and orbital angular momenta into total angular momentum J. Following Hund's rules and $L-S$ coupling, the ground state multiplet is determined by $J = |L \pm S|$, with the largest value of J corresponding to the ground state multiplet of an ion with a $4f$ shell more than half filled and the lowest value of J for an ion under half filled. The free ion ground state multiplet term is ${}^{2S+1}L_J$ with multiplet degeneracy $2J+1$. It is convenient to rewrite the above operators for total angular momentum with $\hat{J}^2$ and $\hat{J}_z$ as follows with quantum numbers $|j, m_j>$ given that $\hat{J} = \hat{L} + \hat{S}$.

$$\hat{J}^2|j, m_j >= j(j+1)\hbar^2|j, m_j > \tag{1.8}$$

and

$$\hat{J}_z|j, m_j >= m_j\hbar|j, m_j > . \tag{1.9}$$

Moving between individual m_j states can be written with the raising and lower operator $\hat{J}_\pm$ as

$$\hat{J}_\pm = \hat{J}_x \pm i\hat{J}_y \tag{1.10}$$

or equivalently

$$\hat{J}_{\pm}|j, m_j >= \sqrt{j(j+1) - m_j(m_j \pm 1)}|j, m_j > \tag{1.11}$$

The magnitude of the total magnetic moment becomes $g_J\sqrt{J(J+1)}$ and the moment along an axis is $g_J\mu_B m_j$, where g_J is the Landé g factor

$$g_J = 3/2 + \frac{S(S+1) - L(L+1)}{2J(J+1)} \tag{1.12}$$

For example, a trivalent Yb^{3+} ion has 13 electrons in the 7 f orbitals. All of the electrons except one pair, giving $S = 1/2$ and maximal $L = 3$. The total angular momentum is $J = L + S = 7/2$, with a $2 * 7/2 + 1 = 8$-fold degenerate free ion multiplet. The Landé g_J is $8/7$.

These operators for the spin orbit coupled Hamiltonian $\hat{H}_1$ will be utilized in the crystalline electric field section to depict how the split J spin orbit coupled manifolds of ions are calculated.

1.2.2 Multiplet splitting

Numerous energetic effects can alter the ground state J manifold energy of a $4f$ ion in an unisolated environment. This includes interelectronic interactions from neighboring ions, crystalline electric fields, and external magnetic fields. A moderate external magnetic field is the weakest perturbation and creates Zeeman splitting of time reversal symmetric states with the energy of an electronic state in a magnetic field B being

$$E = g_J\mu_B m_j B \tag{1.13}$$

where μ_B is the Bohr magneton. For the other interactions, in $4f$ systems, the exchange interaction between ions is typically the weakest, on the order of 0 to 10 K, as shown in

the materials in this thesis, followed by the crystalline electric field and then spin orbit coupling. In some specific cases, the crystalline electric field interaction can be strong enough to be on the same order of magnitude as spin orbit coupling [15], but spin orbit coupling primarily acts to split differing total angular momentum J multiplet states. The main perturbing factor on individual J multiplet states and local magnetic moment characteristics, from ground state g tensor components to effective moment size, is the crystalline electric field interaction detailed in the following section.

1.2.3 Crystalline electric field interaction

The energy levels of a crystalline electric field (CEF) potential surrounding a free ion is based off of perturbing the free ion Hamiltonian and its matrix elements. The original spin orbit coupled Hamiltonian, $\hat{H}_1$, is perturbed to give the corresponding crystalline electric field split J manifold. As a first approximation, the crystalline electric field perturbation can be interpreted as Coulomb repulsion from q_j point charges at given locations R_j creating an electrostatic potential at a point (r, θ, ϕ) as

$$v(r, \theta, \phi) = \sum_j \frac{q_j}{|R_j - r|} \tag{1.14}$$

and including the magnetic ion's charge Q_i becomes

$$V_{CEF} = \sum_i Q_i v_i = \sum_i \sum_j \frac{Q_i q_j}{|R_j - r_i|} \tag{1.15}$$

This point charge method is simplistic and neglects any effects of orbital overlap or charge screening, but is a convenient way to calculate the energy levels of a perturbed system.

Details of calculating the electrostatic potentials for common crystalline electric fields such as cubic, tetragonal, and eight fold coordinations have been thoroughly documented

in Cartesian, polar coordinates, and in terms of the spherical harmonics Y_n^m and tesseral harmonics $Z_{n\alpha}^m$ [109]. Introducing spherical and tesseral harmonics simplifies the relation of electrostatic interactions to known wave functions describing angular momenta in ions. Rewriting v in terms of Legendre polynomials P_n^m becomes

$$v(r,\theta,\phi) = \sum_J \frac{q_j}{R_J} \sum_{n=0}^{\infty} (\frac{r}{R_j})^n P_n^m(cos(\theta)) \tag{1.16}$$

which can be related to the spherical harmonics Y_n^m by [109]

$$P_n^m(cos(\theta)) = \frac{4\pi}{(2n+1)} \sum_{m=-n}^{n} (-1)^m Y_n^{-m}(\theta_j,\phi_j) Y_n^m(\theta_i,\phi_i). \tag{1.17}$$

or to the tesseral harmonics $Z_{n\alpha}^m$ by [109]

$$P_n^m(cos(\theta)) = \frac{4\pi}{(2n+1)} \sum_{\alpha} Z_{n\alpha}^m(r) Z_{n\alpha}^m(R). \tag{1.18}$$

where it is implied α = sine and cosine tesseral harmonic terms are summed over. Therefore, the total potential v becomes

$$v(r,\theta,\phi) = q_j \sum_{n=0}^{\infty} \frac{r^n}{R_j^{n+1}} [\sum_{\alpha} \frac{4\pi}{(2n+1)} Z_{n\alpha}^m(r) Z_{n\alpha}^m(R)] \tag{1.19}$$

which is often rewritten as

$$v(r,\theta,\phi) = \sum_{n=0}^{\infty} \sum_{\alpha} r^n \gamma_n^m Z_{n\alpha}^m(\theta,\phi) \tag{1.20}$$

with

$$\gamma_n^m = \sum_{j=1}^{k} q_j \frac{4\pi}{(2n+1)} \frac{Z_{n\alpha}^m(\theta_j,\phi_j)}{R_j^{n+1}} \tag{1.21}$$

Now, the electrostatic potential can be understood directly in terms of polar or Carte-

sian (x, y, z) coordinates. The symmetry surrounding the magnetic ion must then match the symmetry of the potential function v. In other words, any symmetry operations allowed by the local ionic point group must also be followed by the potential function. This narrows down which tesseral harmonic terms can be included when calculating the potential function. The following list helps determine which terms are kept:

- Determine the point group symmetry of the magnetic ion. Align the $\hat{z}$ direction with the highest symmetry axis.
- If the point group contains a center of inversion, no odd n terms will arise. If the $\hat{z}$ axis is a-fold, then the potential function will have up to $Z_{n\alpha}^{a}$ terms.
- Consult documented tables [109] to determine the minimum allowed terms for a given magnetic ion.

Stevens operator equivalents

With the known terms, the perturbed Hamiltonian can be diagonalized to determine the new energies and wave vectors of the crystalline electric field split free ion terms. The most conventional method for fitting the new Hamiltonian is with the Stevens operator equivalent method [110] for L and J states. Here it is utilized with the new $|j, m_j>$ basis for coupling total angular momentum J with the electrostatic potential. The operator equivalent method removes the need to repeatedly calculate point charge models for every system by introducing angular momentum Stevens operators for the perturbed Hamiltonian. Simply, if a Hamiltonian is given in terms of Cartesian (x, y, z) coordinates, all position operators are replaced with $\hat{J}_x$, $\hat{J}_y$, and $\hat{J}_z$. These angular momentum operators preserve all commutation relationships of the original coordinates.

Collecting terms in the electrostatic potential in equation 1.20 into one Cartesian

dependent function becomes

$$v(r,\theta,\phi) = \sum_{n=0}^{\infty}\sum_{\alpha} r^n \gamma_n^m Z_{n\alpha}^m(\theta,\phi) = \sum_i f_{n\alpha}^m(x_i,y_i,z_i) = \theta_n < r^n > O_n^m \tag{1.22}$$

where O_n^m are the Stevens operator equivalents and θ_n and $< r^n >$ are tabulated multiplicative factors [109]. This can be further reduced to the common form

$$V_{CEF} = \sum_{nm} B_n^m O_n^m \tag{1.23}$$

with B_n^m acting as the Stevens coefficients weighting each Stevens operator and includes the proportionality constants from the conversion from tesseral harmonics. The original Stevens operators have been tabulated according to angular momentum states J by Hutchings [109].

Typically, the value of B_n^m end up being determined via experiments, but they can be predicted for a material by going back to the point charge model. In the formalism of Stevens operator equivalents, the point charge model becomes

$$B_n^m = \frac{4\pi}{2n+1}\frac{|e|^2}{4\pi\epsilon_0}\sum_j \frac{q_j}{r_j^{n+1}} a_0^n < r^n > Z_{n\alpha}^m(\theta_j,\phi_j) \tag{1.24}$$

This model takes the polar location (r_j,θ_j,ϕ_j) of the j^{th} charge q_j where $< r^n >$ is the n^{th} order expectation value of the central magnetic ion wave function, ϵ_0 is the permitivity of free space, $|e|$ is the elemental charge, and a_0 is the Bohr radius. As will be detailed in the Methods section for crystalline electric field fitting, the point charge representation of B_n^m parameters only acts as a vague starting point to refine to observable experimental values.

Although it is possible to further analyze crystalline electric field interactions on

excited J multiplets (e.g. mixing of $J = 5/2$ and $J = 7/2$ ground state and excited state multiplets), the simplest perturbation on the spin orbit coupled Hamiltonian is to neglect any multiplets beyond the ground state multiplet. In the regime where this is not possible, the intermediate coupling scheme can be utilized, which, for instance, is shown in Ref. [15]. However, the $4f$ electron materials of this thesis did not exhibit significant crossing between J multiplets, so this coupling scheme was not necessary.

Consequences of crystalline electric fields

In general, there are a number of important reasons to understand crystalline electric field splitting of the $4f$ materials. First, any odd number spin ion must follow Kramers theorem and contain at least doubly degenerate states to obey time reversal symmetry. This dictates the maximal allowed splitting of any given J manifold. For example, a $J = 5/2$ manifold that is six fold degenerate may maximally split into a set of three doublets. The only way to split the doublets further is to apply an external magnetic field to generate Zeeman splitting. However, an integer J state does not have time reversal restrictions and can form singlet states such as in UPt_2Si_2 and URu_2Si_2 with $J = 3$ [111].

Second, the crystalline electric field wave functions are utilized to understand the ground state anisotropies and moment size of the magnetic ion. Diagonalizing the Hamiltonian returns relative crystalline electric levels E_0 to E_i and corresponding eigenvectors $\phi_0^{\pm}$ to $\phi_i^{\pm}$. The g tensor components of the ground state are calculated with the ground state wave functions and Landé g factor g_J with

$$g_{//} = 2g_J| < \phi_0^{\pm}|J_z|\phi_0^{\pm} > | \tag{1.25}$$

$$g_{\perp} = g_J| < \phi_0^{\pm}|J_{\pm}|\phi_0^{\mp} > | \tag{1.26}$$

with

$$g_{avg} = \sqrt{(1/3(g_{//}^2 + 2g_{\perp}^2))} \tag{1.27}$$

Understanding the g factor anisotropy and its magnitude then dictates the moment size through $\mu = g_{avg}\mu_B m_j$. The excited state intensities of the i^{th} level from the ground state is also related to the wave functions and $\hat{J}$ operators:

$$\sum_{\hat{J}_x,\hat{J}_y,\hat{J}_z,\pm,\mp} < \phi_i^{\pm,\mp}|\{\hat{J}_x, \hat{J}_y, \hat{J}_z\}|\phi_0^{\pm} >^2 \tag{1.28}$$

Third, the magnitude of splitting of free ion spin orbit coupled J manifolds determines thermal occupation of states that may alter the magnetic moment of a given system. For instance, if the crystalline electric field is weak with the J multiplet split with a ground state only a few meV below its first excited state E_1, both of these states will be thermally occupied until $k_bT << E_1$. As a general rule of thumb, 1 meV $\tilde{1}0$ K. Systems such as $CeAl_2$ [112, 113] and $CeCuAl_3$ [114, 115] contain crystalline electric field excitations of only tens of meV, meaning that their local magnetic moments change character as they cool from room temperature. The effect of thermal population of the split states of a J multiplet is captured in magnetic susceptibility, where large curvature appears as the moment character changes. Magnetic susceptibility in terms of emu mol^{-1} is given by [13]

$$\chi = \frac{N_A}{10Z}\sum_i e^{-\beta E_i}[\beta \sum_{j,E_i=E_j} | < i|\mu|j > |^2 + 2\sum_{j,E_i\neq E_j} \frac{| < i|\mu|j > |}{E_i - E_j}] \tag{1.29}$$

where $\beta = 1/k_bT$, N_A is Avagadro's number, and E_i and E_j are neighboring energy levels in the split multiplet. The susceptibility can be calculated parallel, χ_z, and perpendicular,

$(\chi_x + \chi_y)/2$, to the maximal $\hat{z}$ axis of the crystalline electric field.

If a crystalline electric field state is well separated from its first excited state at a given temperature, one can assume that the population of states is primarily the lowest energy state. The number of degrees of freedom of the ion is reduced from its free ion state, and can instead be viewed from the state it solely occupies. A simplified example of this is a well separated ground state doublet in $NaYbO_2$ [14, 79], where the first excited state is around 35 meV. This means that when the material is well below room temperature, only the ground state doublet will be occupied. One expects then that the magnetic entropy that can then be released when forming a magnetically ordered ground state primarily derives from the entropy that can be released from the ground state doublet. The entropy it will release is $Rln(W)$ where W is the number of microstates, and since it is a doublet the entropy is $Rln(2)$.

This is sometimes further related to $J_{eff} = 1/2$ formalism, where an "effective" spin 1/2 moment equivalent is utilized to study the material rather than its full total angular momentum moment J. A consistency check to see if a material ground state doublet is purely $J_{eff} = 1/2$, the angular momentum operators can be projected back onto the ground state crystal field manifold and contain small off diagonal terms. For reference, see Ref. [116]. The basic principle of this method for $J_{eff} = 1/2$ materials is as follows:

1. Diagonalize the crystalline electric field Hamiltonian V_{CEF} with Stevens operator equivalents and coefficients.

2. Create a transformation matrix C from the eigenvectors $\phi_i^{\pm}$ where the columns are the eigenvectors sorted according to increasing eigenergy left-to-right.

3. Project all of the angular momentum operators $\hat{J}_x, \hat{J}_y, \hat{J}_z$ with the transformation matrix by $C^{-1}\hat{J}C$. The upper $2x2$ section of this projected matrix corresponds to

the ground state doublet, and if the off diagonal terms are negligible, the $J_{eff} = 1/2$ approximation is acceptable.

This method heavily relies on fully understanding the crystalline electric field wave functions and is a helpful mathematical tool for f electron materials. Overall, the $J_{eff} = 1/2$ ground state is highly favorable, as it allows access to small quantum moments with strong quantum fluctuations even with originally large total angular momentum J that would otherwise be considered classical rather than quantum without the effects of crystalline electric field splitting.

1.3 Scattering methods

X-ray and neutron scattering techniques are powerful tools for analyzing the crystallographic and magnetic structures of solid state materials. The experiments are non-destructive and ideal for analyzing the relevant length scales of materials lattices and correlations. A probe must be on the same length scale as the experiment it is trying to measure. For instance, atoms in a crystal lattice are spaced by a few Angstroms (1 Å$= 10^{-10}$m) and analysis of the unit cell structure of the lattice requires a suitably small probe.

The wavelength of x-rays with $E \sim 12$ keV are on the order of Angstroms ($\lambda = 1$ Å; $E = 12.4$ keV) and scatter from atoms in a lattice via the electromagnetic interaction with electron clouds surrounding nuclei. The energy relationship with photon wavelength is given by:

$$E = hc/\lambda \tag{1.30}$$

These chargless, massless x-ray photons can penetrate a few millimeters into a material to collect diffraction scattering information. Since this scattering process relies on the

interaction with electron clouds, the intensity of scattering scales with increasing atomic number Z. Elastic scattering of x-rays provides information about the structure of a chemical lattice by following Bragg's law:

$$n\lambda = 2dsin(\theta) \tag{1.31}$$

Neutrons carry a nuclear spin 1/2 and are massive particles. Considering the mass of the neutron, m_n, and its momentum, p_n, or velocity, v_n, the wavelength of the neutron can be calculated via

$$\lambda = \frac{h}{p_n} = \frac{h}{m_n v_n} \tag{1.32}$$

which is related to the energy E of the neutron with

$$E = 1/2\ m_n v_n^2 = \frac{h^2}{2m_n\lambda^2}. \tag{1.33}$$

For example, a neutron with wavelength $\lambda = 1$ Å, its energy is $E \sim 82$ meV and wavelength $\lambda \sim 1.8$ Å. This energy can be further related to the temperature of the neutron in Kelvin with the Boltzmann constant, k_B:

$$E = k_B T \tag{1.34}$$

A room temperature neutron at $T = 300$ K therefore has $E \sim 26$ meV. Thermal neutrons near room temperature are often used to analyze interatomic length scales in solid state materials. Decreasing T of a neutron increases its wavelength, and cold low energy neutrons with $E =$ sub 1 meV to tens of meV probe longer correlations in a lattice like spin-spin dynamics in a spin wave of an ordered antiferromagnet on nanometer length scales.

Neutrons can scatter in two different ways in a solid state material. First, a neutron scatters from the nucleus of an atom over very short nuclear distances. This scattering is relatively weak since it relies on collisions of neutrons and nuclei, meaning that the neutral neutrons can penetrate through significant distances a magnitude greater than x-rays through materials and generally requires large sample volumes. This process relies on nuclear interactions and does not scale directly with Z as in x-ray scattering. Instead, the scattering intensity depends on the coherent and incoherent scattering cross section of a nucleus and varies widely with Z and isotope. Second, neutrons also can scatter with magnetic species in materials. The natural spin of a neutron allows it to interact with a spin dipole−dipole interaction. Since both types of neutron scattering were heavily utilized in this thesis, the following section will go into further details on this method.

1.3.1 Neutron scattering specifics

In comparison to x-ray sources, neutrons sources are relatively scarce. Almost every university with researchers focused on solid state materials will contain one or more x-ray scattering instruments. They generate x-rays by imparting high energy electrons across a voltage drop onto a metal target, such as tungsten or copper, that then radiate off x-rays.

Neutrons, on the other hand, are far more complex and costly to generate. There are two common techniques for scientific solid state materials research that are used, nuclear reactors and spallation sources. They differ in the methodology in which neutrons are generated. In a nuclear reactor, neutrons are produced from nuclear fission of ^{235}U and give off a constant flux of neutrons as long as the fuel persists. Spallation sources generate neutrons by smashing a heavy metal target made of Hg with high-energy protons. Negatively charged protons are sped up in a particle ring to around 1 GeV and period-

ically smashed into the target which spalls off neutrons. Both of these types of sources are costly to create and maintain, and are usually located at national laboratory facilities such as Oak Ridge National Laboratory or the NIST Center for Neutron Research. Even the rare case university that has a nuclear reactor, the flux of neutrons required for a solid state materials measurement cannot be generated there and require high flux setups from these national facilities.

Controlling the energy, and therefore wavelength, of neutrons from these research sources is necessary for any solid state materials measurement. This enables the precise determination of energy and momentum transfer of the incident particle on the sample. As a first step, neutrons from hot reactors can be thermalized with a bath held at a specified temp outside of the reactor to create a distribution of energies around that temperature. The neutrons are passed through a series of collimators to align the beam and filters that further reduce noise to generate one wavelength of neutrons before imparting on a sample. Then, large coaligned single crystal monochromators are used to diffract specified wavelengths of neutrons off of crystal planes into the desired direction with Bragg's law 1.31, such as the Ge(113) filter used for 2.41 Åneutrons at the HB-2A powder diffractometer at Oak Ridge National Laboratory. Other monochromators such as highly oriented pyrolytic graphite, Be, and BeO are commonplace at national facilities.

Spallation source neutrons are generally moderated with a time-of-flight technique [117, 118] that relies on the pulses of neutrons spalling from the source. As shown in equation 1.33, the energy, wavelength, and velocity of a neutron are all interrelated. Therefore, neutron wavelengths can be split by the time it takes the neutrons to travel a given distance in a given time. This is often achieved with chopper disks with narrow slits that rotate at a given frequency at different interval lengths in a tube. Much of the neutron flux is thrown away as only neutrons of a given wavelength $n\lambda$ can pass through both slits. A third chopper is often used to filter out the n harmonics of the incident neu-

trons. This type of setup is used at the Angle Resolved Chopper Spectrometer (ARCS) at Oak Ridge National Laboratory. The wavelength of neutrons can be determined via :

$$\lambda = \frac{h(t + t_0)}{m_n(L + L_0)}. \tag{1.35}$$

where the initial flight path length, L_0, and flight time, t_0, are calibrated from the spallation pulses and initial moderator. Neutron wavelength and corresponding energy is then controlled with their offset time t and travel distance L. This method can also be reformulated to determine the time t an neutron will take from the incident flight path, L_i, to a sample and outgoing flight path to the detector, L_f, with corresponding initial and final wavelengths by

$$t = \frac{m_n}{h}(L_i\lambda_i + L_f\lambda_f). \tag{1.36}$$

Neutrons can scatter from nuclei and magnetic moments in elastic and inelastic scattering processes. Elastic scattering is characterized when the energy transfer to the sample or probe (neutron in this case) is assumed to be zero. The general formula for momentum transfer is:

$$Q = k_i - k_f \tag{1.37}$$

where k_i is the incident momentum of the scattering particle and k_f is the final momentum, and $k = 2\pi/\lambda$ is the traditional definition of wavevector modulus. There is also a corresponding energy conservation relationship:

$$E = E_i - E_f \tag{1.38}$$

The convention is incident$-$final for these relationships. In an elastic process, $E_i = E_f$, and in an inelastic process, the two are not equal.

The general way of viewing a scattering process is with the scattering triangle in Fig-

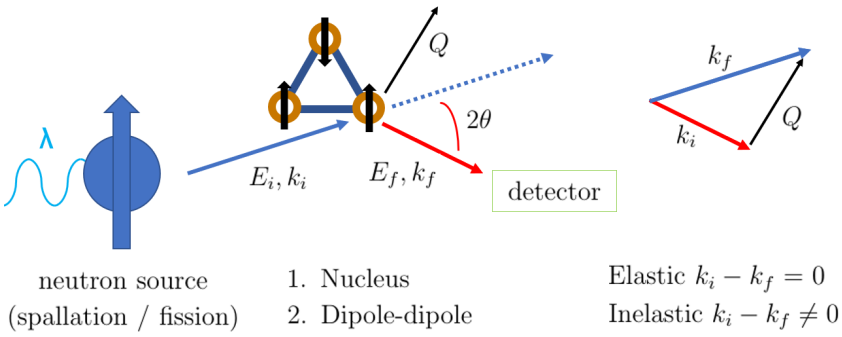

Figure 1.3: An incident neutron is neutrally charged and carries nuclear spin 1/2. They are produced from spallation or fission sources and pass through a series of moderators and monochromators to generate a tight distribution centered around a given incident energy E_i and momentum k_i. They can interact directly with the nucleus to scatter and give structural information about a material or dipole-dipole scatter with magnetic moments for magnetic information before scattering into a detector. The scattering triangle on the far right is a vector representation of the process, where elastic scattering occurs when the magnitude of the incoming and outgoing momenta are equal and inelastic when they are not.

ure 1.3 depicting the incoming and outgoing vectors of neutrons imparting on a sample. The incident neutrons carry $[E_i, k_i]$ and scatter through an angle 2θ to $[E_f, k_f]$. One can readily calculate

$$|Q| = k_i - k_f = \frac{4\pi\ sin(\theta)}{\lambda} \tag{1.39}$$

with

$$Q = \sqrt{k_i^2 + k_f^2 - 2k_i k_f cos(2\theta)}, \tag{1.40}$$

which leads back to Bragg's law in equation 1.31. Differing spectrometer setups can be either direct or indirect geometry to measure Q and its relation to energy transfer. The two setups differ by how they measure energy transfer to and from a material, or in other words, if changes in incident or outgoing changes in energy are determined.

Cross sections

A neutron scattering experiment measures the total number of particles scattered in a specific direction from an incident flux of neutrons, Φ, to determine $S(Q, w)$, the dynamic structure factor. In general, any process beyond scattering such as neutron absorption is initially ignored. The flux of neutrons are scattered into 2θ and ϕ in the solid angle $\Delta\Omega$ steradians. The number of neutrons through the differential solid angle $d\Omega$ is called the differential cross section, $d\sigma/d\Omega$. This cross section can be further split by energy into the double differential cross section, $\frac{d^2\sigma}{d\Omega dE}$. The double differential cross section relates the number of neutrons scattered through a given solid angle with final energy between dE and E_f. Typically, elastic scattering measurements are not fully energy resolved and approximate zero energy transfer with total scattering such that they measure the differential cross section. An inelastic scattering measurement will integrate over a small energy window to determine this double differential cross section.

The double differential cross section is related to the dynamic structure factor $S(Q, w)$ as $\frac{d^2\sigma}{d\Omega dE}$ by:

$$\frac{d^2\sigma}{d\Omega dE} = \frac{\sigma}{4\pi\hbar}\frac{k_f}{k_i}S(Q,\omega) \tag{1.41}$$

The dynamic structure factor contains information about the sample and how it influences the total scattering event contained in the double differential cross section.

Neutron scattering depends on the nucleus or magnetic moment it scatters from. For nuclear scattering, the scattering length is specified as b and is approximately constant and isotropic over the short range nuclear interaction that generates it as a point source. The values of b are experimentally determined and tabulated [119]. The scattering length is defined by the average value and standard deviation for atomic isotopes

$$b = \langle b \rangle \pm \ \Delta b \tag{1.42}$$

with corresponding variance

$$\langle b^2 \rangle = \langle b \rangle^2 + (\Delta b)^2. \tag{1.43}$$

The scattering cross section is defined as

$$\sigma_{total} = \frac{d\sigma}{d\Omega} = 4\pi b^2 \tag{1.44}$$

and can be split into two components: coherent and incoherent.

$$\sigma_{coherent} = 4\pi \langle b \rangle^2 ; \sigma_{incoherent} = 4\pi (\Delta b)^2. \tag{1.45}$$

Simply, coherent scattering arises from repeating patterns of correlated motions of atoms (the mean b) and incoherent scattering arises from deviations in the pattern or self correlations of atoms (distribution of b). The coherent scattering depends on Q while incoherent scattering is uniform in Q, and the double differential cross section can be split into two components

$$\frac{d^2\sigma}{d\Omega dE} = [\frac{d^2\sigma}{d\Omega dE}]_{coh} + [\frac{d^2\sigma}{d\Omega dE}]_{inc} \tag{1.46}$$

In general, the coherent cross section for elements is the main component contributing to the scattering cross section σ_{total}. However, a major deviation from this is hydrogen where the incoherent cross section is significant. A neutron scattering experiment with hydrogen either must embrace the incoherent scattering to, for instance, track the location of hydrogen, or eliminate it from the sample. Hydrogen contamination in samples generates a large incoherent background, a mushy noise of intensity with minimal structure in Q. Most experimentalists replace hydrogen with deuterium for this reason.

Magnetic moment scattering depends on the inherent magnetic dipole moment, μ_n,

of a neutron. A neutron has a moment of

$$\mu_n = -1.913\mu_N \tag{1.47}$$

where μ_N is the nuclear magneton. A spin 1/2 neutron can be spin up or spin down, and its orientation is sometime specified for experiments. In most situations, a mix of spin up and spin down impart onto the sample. The neutron moment interacts with a magetic sample moment in a dipole-dipole fashion and is therefore dependent on the charge of the magnetic ion and falls off with a different form factor than nuclear scattering. In fact, the form factor for magnetic scattering is closer to x-ray scattering than nuclear neutron scattering, as they both involve electron cloud processes. Overall, the scattering from magnetic processes in materials is on the same order of magnitude as nuclear scattering, but depends on the magnetic moment size μ of the material under investigation.

The double differential cross section similarly becomes:

$$[\frac{d^2\sigma}{d\Omega dE}]_{mag} = (\gamma r_0)^2 \frac{k_f}{k_i} S_{mag}(Q,\omega) \tag{1.48}$$

where γ appears from the gyromagnetic ratio of the neutron and r_0 is the electron radius. A peculiar effect of magnetic scattering is the neutron is only sensitive to magnetization perpendicular to Q. Nuclear and atomic moments have an orientation and their dipole-dipole interactions depend on their relative orientations.

1.4 $ALnX_2$ crystal structures

Materials studied in this thesis live in the $ALnX_2$ (A = alkali, Ln = lanthanide, X = chalcogenide) materials that crystallize in a number of different space groups depending on the radii of the constituent ions. The differing space groups have been previously

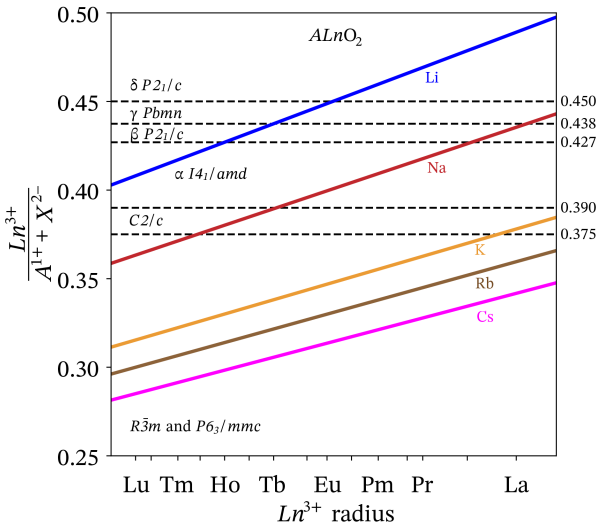

Figure 1.4: The $ALnX_2$ (A = alkali, Ln = lanthanide, X = chalcogenide) materials contain seven different crystal structures that are adopted based off of the radii of the ions in the material. This empirical plot was derived from Shannon-Prewitt effective atomic radii and tabulated crystal structures [1, 2]. The dashed lines represent crossover between the neighboring crystal structures. Some of the reported compounds reside proximate to this dashed line and can crystallize in both neighboring structures (e.g. $NaErO_2$ has a $C2/c$ and $R\bar{3}m$ synthesis route [3]). In general, the larger cations favor the triangular lattice $R\bar{3}m$ and $P6_3/mmc$ structures.

observed [3–12] with seven distinct space groups $R\bar{3}m$ and $P6_3/mmc$, $C2/c$, α-$I4_1/amd$, β-$P2_1/c$ γ-$Pbmn$, δ-$P2_1/c$. The nomenclature of Hashimoto et al. [4] is used for the depiction of $\alpha, \beta, \gamma, \delta$. A comparison of the tabulated Shannon-Prewitt [1, 2] ionic radii shows an empirical relationship between the ions and crystal structures in this system with $Ln^{3+}/(A^{1+}+X^{2-})$. The oxide compounds, shown in Figure 1.4 cross all of the seven major space groups. Increasing the radius of the chalcogenide ion pushes the radius ratio rule down, and by the time all of the materials contain Te^{2-}, all of the crystal structures are triangular lattice $R\bar{3}m$ or $P6_3/mmc$ in Figure 1.5.

Materials that reside proximate to the dashed lines in Figure 1.4 and Figure 1.5 can adopt both of the neighboring crystal structures. This has been observed, for example, in $NaErO_2$ that can be synthesized with both $R\bar{3}m$ and $C2/c$ room temperature structures

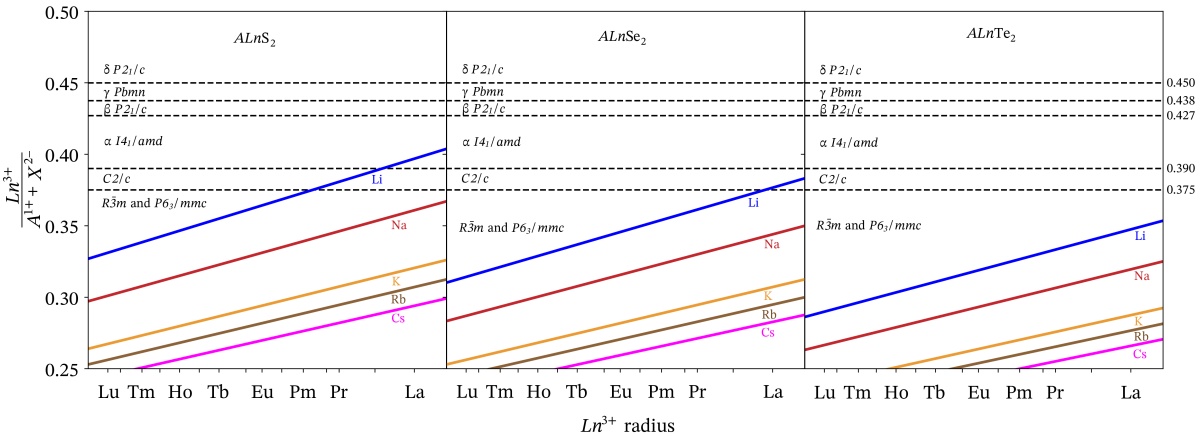

Figure 1.5: Increased anionic species radius pushes the crystal structures toward the triangular lattice space groups at the bottom of the empirical relationship plot. The number of reported crystal structures for these materials is fewer than for the oxides [3–12].

[3] based off of the maximum heating temperature. Also, the material $LiErO_2$ undergoes a $\alpha - I4_1/amd$ (high temperature phase) to $\beta - P2_1/c$ (low temperature phase) structural phase transition at 15 K [4].

The triangular lattice crystal structure is comprised of two space groups: $R\bar{3}m$ and $P6_3/mmc$. These two crystal structures are highly similar and only differ in stacking sequences of triangular lattice planes. In the $R\bar{3}m$ structure, the equilateral triangular planes stack in a ABC sequence, with each neighboring triangular plane vertices residing at the projected center of a triangular sheet. In comparison, the $P6_3/mmc$ structure type crystallizes with an AAA stacking sequence with all triangular lattice planes coaligned. Surprisingly, this distinction does not directly relate to the current understanding of the empirical radius ratio rule presented here, but it has been suggested that the large cations such as Cs^{1+} favor the AAA stacking in the $P6_3/mmc$ structure [12].

It should also be noted that this radius ratio rule does not capture one distinct phase of the $ALnX_2$ family of materials, the disordered $Fm\bar{3}m$ structure. This structure type is related to the familiar NaCl structure, but with disorder of the A and Ln cations

on the Na site. Reports of this structure type have indicated that it forms at a high temperature phase boundary and when the alkali ion A is close in size to the Ln ion [10]. For instance, the material $NaNdS_2$ shows the disordered $Fm\bar{3}m$ structure above 880 °C and $R\bar{3}m$ structure below [10]. It was suggested that this phenomenon could be an order-disorder chemical transition.

Furthermore, although there are many d electron materials that crystallize with the same chemical formula AMX_2 where $M = d$ electron metal, they do not all obey this radius ratio rule. There are a few factors to consider why this occurs. First, the d metal ions contain slightly smaller atomic radii than lanthanide ions, even with the lanthanide contraction. This introduces the possibility of an even smaller radius ratio of $M^{3+}/(A^{1+} + X^{2-})$ that goes below the bottom of the plots in Figure 1.4 and Figure 1.5 and includes other space groups such as $C2/m$ observed in $NaMnO_2$ [54, 55]. Second, the d electron systems can have strong electronic character at room temperature with orbital overlaps and magnetic exchange, where, in contrast, the f electron systems readily adapt to the assumption that they can be treated from their lone ionic state. For example, materials such as $NaTiO_2$ which should be $R\bar{3}m$ undergoes a $C2/m$ phase transition around 280 K likely resulting from orbital ordering [56, 58, 120] as will be further explored in Appendix A. In effect, these electronic interactions heavily influence the crystal structure of the d electron systems and they do not always abide by the radius ratio rule for $ALnX_2$ materials.

This thesis focuses on two space groups, $R\bar{3}m$ and $I4_1/amd$, based on Yb and Ce magnetic cations. The depiction of their crystal structures is shown in Figure 1.6.

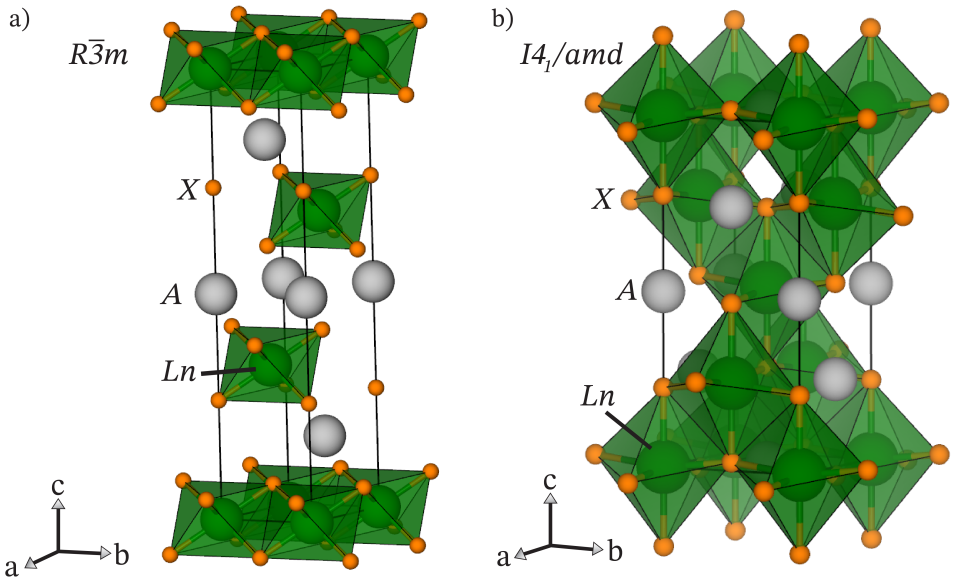

Figure 1.6: Two of the crystal structures of the $ALnX_2$ materials are focused on in this thesis as they contain geometrically frustrated magnetic lattices. a) The $R\bar{3}m$ space group of the $ALnX_2$ materials contains equilateral planes of Ln^{3+} ions in trigonally compressed D_{3d} LnX_6 chalcogenide octahedra. The triangular planes stack in an ABC sequence and are separated by monolayers of A alkali cations. $NaYbO_2$, $KCeO_2$, and high temperature $NaTiO_2$ adopt this crystal structure. b) The $I4_1/amd$ space group has an elongated diamond lattice of Ln^{3+} ions three dimensional connected along the c axis. The LnX_6 octahedra are distorted in a local D_{2d} environment. Both $NaCeO_2$ and $LiYbO_2$ crystallize in this space group.

1.5 Chapter overview

The purpose of this thesis was to primarily explore the unusual magnetic phases of frustrated $4f$ electron based materials in the $ALnX_2$ family. In the introduction, the basis of geometric frustration, quantum spin liquids, $4f$ magnetism, and the structures of $ALnX_2$ materials were covered. The number of compounds in this family is large and relatively underexplored in comparison to other frustrated f electron systems such as the pyrochlores. We chose to investigate four preliminary compounds from this series of materials with frustrated magnetic lattices: $NaYbO_2$ [79, 80], $KCeO_2$, $LiYbO_2$ [121], and $NaCeO_2$ [122]. These citations are the published papers on these materials, and a

manuscrip on $KCeO_2$ is underway. After the following chapter on experimental methods used in the study of these compounds, the chapters are split by material and space group. The two $R\bar{3}m$ triangular lattice materials, $NaYbO_2$ and $KCeO_2$, are presented in chapters 3 and 4 and the $I4_1/amd$ tetragonal materials, $LiYbO_2$ and $NaCeO_2$, follow in chapters 5 and 6.

Chapter 2 initiates with the experimental methods used from creation to full exploration of the materials properties of these systems. The methods for synthesis for the polycrystalline materials will be presented first and the rational behind the method used for each material. Second, the basics of bulk magnetic property measurements will be introduced, detailing the methods used for analyzing the $4f$ electron magnetism in these materials, which are primarily focused on magnetic susceptibility, magnetization, and specific heat measurements. Third, an overview of the scattering techniques utilized in these studies will be presented. Differences in laboratory x-ray diffraction and neutron diffraction are discussed. More detail on inelastic and elastic neutron scattering are reviewed, as they become key to understanding many of the collective magnetic phenomena. Key neutron scattering measurements include elastic diffraction, low energy inelastic scattering, and high energy inelastic scattering, all of which probe differing energy scales of the magnetic structures of these compounds.

The third chapter introduces the material $NaYbO_2$. Our investigations on this material have revealed that it contains a quantum disordered ground state arising from strongly antiferromagnetically coupled, highly anisotropic, $J_{eff} = 1/2$ Yb^{3+} moments. We resolve a continuum of scattering with low energy inelastic neutron scattering that evolves into spin waves with an applied external field. This change coincides with the appearance of elastic neutron scattering Bragg reflections that is fit to an $up-up-down$ three sublattice magnetic structure at $\mu_0 H = 5$ T. The total entropy of this system coincides with a $J_{eff} = 1/2$ ground state, and our high energy inelastic neutron scattering

data reveal a well separated ground state Kramers doublet in D_{3d} symmetry. Our theoretical collaborators Professor Leon Balents and Chunxiao Lui analyze the magnetic XXZ Hamiltonian of this system and resolve moderate easy plane anisotropy of $J_z = 0.45$ and $J_{xy} = 0.51$ meV. This two dimensional triangular lattice Hamiltonian is connected to the fully three dimensionally frustrated $R\bar{3}m$ lattice, and the optimal ground state for this model is a U(1) Dirac spin liquid with gapless fermionic spinons.

In the fourth chapter, our studies of $KCeO_2$ are presented. Depsite sharing a similarly geometrically frustrated triangular lattice of antiferromagnetically coupled trivalent lanthanide ions as $NaYbO_2$, the Ce^{3+} magnetic moments order below 300 mK in this material. We find that the magnetic ordering in this system is apparent in specific heat measurements where magnetic entropy approaches $Rln(2)$ and show that low energy inelastic neutron scattering data contains dynamic excitations reminiscent of spin waves. However, elastic neutron diffraction is unable to resolve any magnetic peaks at 300 mK, likely due to a small Ce magnetic moment less than 0.6 μ_B in an antiferromagnetic structure. High energy inelastic neutron scattering shows the ground state Kramers doublet is separated by a large 120 meV, but surprisingly a single extra crystalline electric field mode arises at 170.5 meV. This extra mode is sharp, well above the phonon cutoff, and is not related to rampant chemical impurities. Currently, we are unsure of the origin of this extra mode, and this chapter will depict how the normal explanations of extra crystalline electric field modes do not fit $KCeO_2$.

Chapter 4 presents the frustrated $J_1 - J_2$ model on an elongated diamond lattice and its relation to magnetic order in $LiYbO_2$. This material magnetically orders in two successive steps at 1.13 K and 0.45 K with new magnetic Bragg peaks in elastic neutron scattering data. The peaks are fit to a spiral magnetic structure that is incommensurate under zero field and 'locks-in' to a commensurate spiral structure under $\mu_0 H = 3$ T. The two magnetic transitions in temperature are shown to be linked to the bipartite

nature of the diamond lattice, as the only degree of freedom left to order at 0.45 K is the relative phasing between the two magnetic sublattices. Our theoretical collaborators Professor Leon Balents and Chunxiao Lui reformalize the $J_1 - J_2$ Heisenberg model of the diamond lattice to the stretched lattice in $LiYbO_2$, showing that the propagation wave vector value is inherently linked to the ratio of $|J_2|/J_1$. The model captures most of the experimental details except the subtle phasing transition at 0.45 K where the symmetry between the magnetic sublattices is broken. Weak splitting in the crystalline electric field excitations in high energy inelastic neutron scattering measurements suggest that the Yb environment may not be uniform or a minor lattice deformation occurs which could account for the sublattice symmetry breaking. However, our high resolution synchrotron x-ray diffraction does not show any deviations from the ideal chemical structure. What incites the symmetry breaking remains a mystery.

Chapter 5 builds upon the frustrated Heisenberg $J_1 - J_2$ model from $LiYbO_2$ by analyzing another structurally similar material $NaCeO_2$. This material also magnetically orders below 3.4 K into a collinear antiferromagnetic structure that is commensurate with the underlying lattice. The structure is fit with elastic neutron powder diffraction data, revealing Ce moments of 0.57 μ_B align with the crystallographic c axis. Within the framework of the Heisenberg $J_1 - J_2$ model, this material is less frustrated than $LiYbO_2$ but helps parameterize the phase space of the model. Additionally, even though $NaCeO_2$ shares chemical similarities to $KCeO_2$, no extra crystalline electric field excitation are present in this material.

Appendix A covers studies of a similar material to $NaYbO_2$ and $KCeO_2$. Triangular lattice $NaTiO_2$ crystallizes in the $R\bar{3}m$ space group at room temperature and undergoes a phase transition to monoclinic $C2/m$ at 280 K. Nominally, the trivalent Ti metal ions should contain $S = 1/2$ magnetic moments that should magnetically order. However, despite numerous attempts with elastic neutron diffraction and inelastic neutron diffrac-

tion, no resolvable magnetic intensity at low temperatures is observed. This appendix will speculate on the origin of this discrepancy, as it may be related to orbital ordering or metal-metal bonding. Additionally, handling this material is notoriously difficult as has been reported by Clarke et al. [120] who conducted extensive studies on the material. The material is shown to contain some site mixing of Na and Ti ions, and this chemical disorder may influence the magnetic properties.

Despite numerous attempts, we were unable to move away from polycrystalline material to single crystals in any of the oxide based $ALnX_2$ materials. The efforts in these attempts are detailed in Appendix B. The types of crystal growth techniques implemented were flux growths, sealed silver tubing hydroxide growths, hydrothermal growths, and optical and laser floating zone growths. In general, the $ALnO_2$ materials are frustrated even in synthesis due to the differing chemical natures and reactivities of alkali ions and lanthanide oxides. Alkali chemistry is typically low temperature or solution and flux based because at high temperatures they readily volatilize. Lanthanide oxides are generally unreactive chemically and require high temperatures to react because the oxides are extremely stable. These competing factors are discussed in each of the single crystal growth techniques and the mitigation attempts and rationale employed in each technique.

Chapter 2

Experimental methods

This chapter covers the generic aspects of the experimental methods used in the studies on $NaYbO_2$, $KCeO_2$, $NaCeO_2$, $LiYbO_2$, and $NaTiO_2$. Sample-specific methods beyond these methods are explained in their respective chapters.

2.1 Polycrystalline synthesis of $ALnX_2$ materials

All of the experimets conduted on $NaYbO_2$, $KCeO_2$, $NaCeO_2$, $LiYbO_2$, and $NaTiO_2$ are on polycrystalline samples. The details of the single crystal growth attempts are shown in Appendix B.

2.1.1 Air stable compounds

The trivalent Yb cation is relatively stable to its other divalent and tetravalent oxidation states. In $NaYbO_2$ and $LiYbO_2$, the Yb ions are trivalent. For the most part, this indicates that these compounds should be relatively stable under normal atmospheric conditions. Therefore, the synthesis of these materials was conducted in open alumina crucibles and the handling of the materials were not strictly limited to controlled atmo-

spheric environments.

However, it is known that materials of the form AMO_2 absorb water. For instance, the material $NaCoO_2$ absorbs water, which, surprisingly makes it superconducting with the right concentration of water incorporation [123, 124]. But, for the purposes of these experiments on $LiYbO_2$ and $NaYbO_2$, water exposure was limited as much as feasibly possible. After synthesis, the materials were held at 200 °C until they were stored in an inert Ar filled glove box. Exposure to the humid atmosphere of Santa Barbara was limited to at most 30 minutes prior to experiments. Any time these materials were sent to collaborators or to neutron scattering sources, they were vacuum sealed in quartz ampules.

The basics of synthesizing $NaYbO_2$ and $LiYbO_2$ start from the same point. The corresponding carbonate Li_2CO_3 (99.997%, Alfa Aesar) or Na_2CO_3 (99.997%, Alfa Aesar) dried at 600 °C were mixed with Yb_2O_3 (99.99%, Alfa Aesar) dried at 900 °C. The powders were then placed in a 1200 °C box furance at 1000 °C for three days. The powders were ground and reheated for 12-24 hrs at 1000 °C until phase purity was reached. Both powders were white and chalky.

In this synthesis, the volatility of the carbonate species is highly important to understand and mitigate. Although the boiling point of Li_2CO_3 is above 1300 °C and Na_2CO_3 is above 1500 °C, they do have substantial vapor pressures at 1000 °C and will slowly evaporate over the course of the synthesis. Therefore, designing the syntheses of these materials had to balance reaction time, crucible size, and excess amount of carbonate species to produce phase pure $NaYbO_2$ and $LiYbO_2$. For example, reacting a 1:1 ratio of the carbonate to Yb_2O_3 in an open crucible would result in an impurity of Yb_2O_3 in the product as some of the carbonate evaporates. The longer the reactants were held at 1000 °C, the more Yb_2O_3 was left over. We qualitatively found that the size of the crucible along with if the crucible was capped altered how much carbonate was lost. For

consistency, capped one inch diameter alumina crucibles were used once the effect was figured out.

For pure $NaYbO_2$, the ratio of Na_2CO_3 to $NaYbO_2$ to create a pure product was 1.25:1.0 and the ratio of Li_2CO_3 to $LiYbO_2$ to create a pure product was 1.10:1.0. It should be noted that the carbonates readily absorb water and become amorphous, so determining the amount of leftover carbonate was not possible with x-ray diffraction. Therefore, the ratios chosen here were determined when no extra peaks of Yb_2O_3 were present by x-ray diffraction after 3 days heating and two regrinds and reheatings. If the materials are prepared with this stoichiometry ratio and heated longer or in differing sized crucibles, the products will contain Yb_2O_3.

There is one specific peak of Yb_2O_3 near 22 $^\circ$ 2θ with Cu-Kα radiation that is well separated from any $NaYbO_2$ and $LiYbO_2$ structural peaks that was used to verify if any leftover Yb_2O_3 was present. When this peak was within noise of the measurement, the samples were deemed pure but likely contained small excesses of the carbonate reactants. In terms of understanding the magnetism of $LiYbO_2$ and $NaYbO_2$, it was imperative that Yb_2O_3 was not present as it also contains magnetic trivalent Yb moments that would interfere with sensitive bulk magnetic properties measurements like magnetic susceptibility. Therefore, the excess of carbonate reactants was tolerated. It should be noted that some reports [14, 84] indicate that the carbonate can be removed with washing with water or ethanol, but this directly contaminates the samples with compounds that could intercede into the lattices of $LiYbO_2$ and $NaYbO_2$, which is detrimental to magnetic properties analysis.

2.1.2 Air sensitive compounds

In comparison to trivalent Yb cations, trivalent Ce cations and Ti cations are not the typically stable valence. In both trivalent Ce and trivalent Ti, they are one electron loss away from being isovalent with the noble gases Ar and Xe. Therefore, typically the oxides of these materials are found as tetravalent CeO_2 and TiO_2 at standard conditions. In order to make these cations trivalent, they must be reduced to gain an electron and then handled extremely carefully to prevent oxidation.

This means that after synthesis of $NaCeO_2$, $KCeO_2$, and $NaTiO_2$, all products were strictly handled in an inert Ar filled glove box. However, it was found that even under these conditions the minute amount of water and oxygen introduced into a glove box with use could interfere with the quality of the powders as indicated by discoloration of the powders. Pure $NaCeO_2$ is a yellow-green powder, $KCeO_2$ is red-brown, and $NaTiO_2$ is dark black. When oxidized to their tetravalent state, they begin to turn yellow-white and then white. Over the course of a month, a typical capped powder would show discoloration near the top and sides of a tube. In order to prevent this, we adopted sealing the powders in quartz ampules or double and triple sealing vials in mylar bags.

Perhaps the most notoriously difficult material of the three to handle was $NaTiO_2$. When left in air for roughly 30 seconds, one can visibly see water droplets coalescing on the surface of the powder. After 5 minutes, the powder turns into a wet mush. This means that practically instantaneous exposure to air begins to decompose $NaTiO_2$ as has been previously noted by Clarke et al. [120]. The other two materials, $NaCeO_2$ and $KCeO_2$, similarly degraded with air exposure but took roughly twice as long to absorb the same quantity of water from the air. Measurements involving air exposure were either mitigated or rapidly conducted to maintain the integrity of these materials.

To synthesize these materials, we adopted the techniques from previous $NaTiO_2$ re-

ports [16, 120] that reduced TiO_2 in the presence of liquid Na metal. Originally, the reports placed the reactants in Ni or Fe tubes sealed with an arc. This was at first used for the synthesis of $NaTiO_2$ with steel tubes sealed in an arc melter. However, we came across a few issues with this method. The volume available in the arc melter was roughly half of a liter, which limited the size of the tubes we could use. At first, we stuck with tubes no larger than a quarter inch diameter and two inch length. Before loading the tubes, one side was crimped together with a vise and sealed in the arc melter by carefully positioning the tube vertically in the chamber. After loading the tubes with Na and TiO_2, the other end was crimped with a vise in the glove box and transferred to the chamber. The end of the tube was bent into a "L" shape so that the crimped end stuck upwards while the tube rested on the side of the chamber. The arc was then quickly swept across the end of the tube to seal it. However, this failed about half of the time. Any minor excess Na metal near the seal would rapidly evaporate and create a bubble in the tubing, and if the arc was too hot or left on the tube too long, a hole easily formed. When a hole formed and the tubing got too hot, the rest of the Na in the tubing liquefied and expelled from the tubing. Preparing enough single phase material for measurements such as neutron scattering became difficult.

To get around this issue of small tubing and easily failed preparations, a different method was used. Large half inch diameter stainless steel 316 tubing was cut and capped with Yor-lok fittings from McMaster-Carr. The fittings were tightened fully to create a metal bond with the tubing that at the elevated temperatures of the reactions fused together. The tubing with one cap was loaded with Na and TiO_2 and reacted at 1000 °C for 3 days in an active vacuum tube furnace. The outside of the steel tubing evaporates slowly at this temperature, giving the vacuum sealed quartz tubing a green hue after reacting, likely from oxides of Cr and Mn. The vessels were kept in active vacuum to mitigate oxidation of the steel tubing at 1000 °C for 3 days with the likelihood that the

vessel was under a large amount of pressure. Normally, the amount of Na metal used per reaction was around 1 g, meaning that following $PV = nRT$ ideal gas law in a cylinder of roughly three inch length and half inch diameter, the pressure could reach around 50 atm. Of course, the liquid metal likely reacted with the TiO_2 prior to fully vaporizing, but an experiment where the tubing was left in air resulted in the top cap getting lodged in the roof of a furnace.

This method of stainless steel capped tubing was utilized to refine the syntheses of $NaTiO_2$, $NaCeO_2$, and $KCeO_2$ to create pure products. An excess of Na or K metal was necessary to push the reactions to completion, an the excess likely coated the walls of the tubing. For $Na_{0.99}TiO_2$, Na (99.95% Alfa Aesar) was reacted with TiO_2 (99.995% Alfa Aesar) dried at 1000 °C in a 1.2:1.0 molar ratio. Reducing the amount of Na excess resulted in less Na content in this compound, and this effect can be tracked with the lattice parameters as previously reported by Clarke et al. [120]. For $NaCeO_2$, Na (99.95% Alfa Aesar) was reacted with CeO_2 (99.99% Alfa Aesar) dried at 900 °C in a 1.1:1.0 molar ratio. In $KCeO_2$, K (99.95% Alfa Aesar) was reacted with CeO_2 (99.99% Alfa Aesar) dried at 900 °C in a 1.1:1.0 molar ratio.

In all three materials, the sealed tubing were placed in the vacuum furance at at 1000 °C for 3 days. The tubes were then opened in the glove box with a tube cutter and the powder was thoroughly mixed. Some discoloration from the steel tubing was present on the surfaces of the powders, meaning that a small amount of steel impurities did incorporate into the products. However, we found that the larger diameter tubing with its smaller surface area to powder volume ratio than the original arc melted quarter inch diameter tubing made more consistent products. For sensitive magnetic susceptibility measurements, the samples were carefully sifted through to find sections that did not get exposed to the surface of the steel tubing, as even a hundredth of a milligram of ferromagnetic impurity like Fe_3O_4 from steel would appear in magnetic susceptibility

data. This was more of an issue with small spin magnetic moment $NaTiO_2$ where the magnetic susceptibility was small as will be shown in Appendix A.

2.2 Magnetization

2.2.1 Magnetic susceptibility

The bulk magnetic properties of the materials were measured on multiple instruments. Low-field d.c. magnetization data from 2 to 300 K were collected on a Quantum Design Magnetic Properties Measurement System (MPMS3) with a 7 T magnet. Isothermal d.c. magnetization data between 2 to 300 K were collected on the same instrument and on a Quantum Design Physical Properties Measurement System (PPMS) equipped with a vibrating sample magnetometer insert and a 14 T magnet.

The sample environment for these measurements typically consisted of a brass rod holder and a polypropylene sample holder. The large magnetic moments of the lanthanide materials overwhelmed the background from the sample holders, and sample masses had to be kept below 10 mg for high field measurements. The low magnetic moment of the Ti^{3+} ion in $NaTiO_2$ required more sample mass or a lower background holder like a drinking straw to house a gelatin capsule sample holder.

Careful attention to air sensitive $NaCeO_2$, $KCeO_2$, and $NaTiO_2$ was taken to obtain magnetic data. These materials, as stated above, rapidly degrade in contact with air. The gelatin capsules and polypropylene sample holders were prepared in a glove box and quickly transferred to the instruments to obtain data. In order to maintain an air free environment, the sample holders were wrapped with a few layers of Kapton tape where the two sides of the gelatin capsule or polypropylene holder joined.

This allowed the transfer of samples to the instruments for measurement, but on

occasion, the $NaTiO_2$ sample degraded even with this air free precaution. This generally showed up during the experiment as multiple apparent transitions in susceptibility data and after the experiment as white, degraded powder. This will be covered in further detail in Appendix A. Therefore, the optimal method for obtaining magnetic data for $NaTiO_2$ involved sealing a nuclear magnetic resonance (NMR) tube of approximately two inch length with sample pressed into the bottom by the top of a gelatin capsule. The NMR tube was secured inside of a drinking straw before measurement and no sample quality degradation visibly occurred.

Additionally, the synthesis method of these materials required sealed stainless steel tubes. Small insidious amounts of ferromagnetic impurities often seeped into the samples in quantities not detectable by x-ray diffraction. In the large magnetic moment lanthanides, this was not a great issue, but in the small moment $NaTiO_2$, a small ferromagnetic impurity on the order of a hundredth of a milligram dwarfed the magnetic signal as will be shown in Appendix A. The ferromagnetic impurity, likely Fe based, creates hysteretic splitting of M-T data all the way up to room temperature and is easily identified. To avoid this issue, samples were taken from the center of the large stainless steel tube reactions where the ferromagnetic impurities had a lower chance of diffusing to.

In the following subsections, details on the analysis of magnetic susceptibility and magnetization curves are presented.

M vs. T

Magnetic susceptibility relates the induced magnetization of a material M to an applied external field H by

$$\chi = \frac{M}{H} \tag{2.1}$$

In general, the calculation of χ depends on the relationship between M and H being linear. Typically, this is approximated by using a weak H on the order of tens of Oersted (1 T = 10000 Oe) if the M-H relationship is not linear at all fields. The common units of χ are emu mol^{-1} or μ_B mol^{-1} which are calculated by

$$\chi[\frac{\text{emu}}{\text{mols magnetic ion Oe}}] = \frac{M[\text{emu}]}{H[\text{Oe}]}(\frac{\text{F.W. [g/mol]}}{\text{sample mass [g]}})(\frac{1\,\text{mol sample}}{\#\text{ ions per F.U.}}) \tag{2.2}$$

$$\begin{aligned}\chi[\frac{\mu_B}{\text{magnetic ion Oe}}] \\ = \frac{M[\text{emu}]}{H[\text{Oe}]}(\frac{\text{F.W. [g/mol]}}{\text{sample mass [g]}})(\frac{1\,\text{mol sample}}{\#\text{ ions per F.U.}})(\frac{1\,\text{mol}}{N_A})(\frac{1\,\mu_B}{9.2741*10^{-21}\,\text{emu}}) \\ = \frac{\chi[\frac{\text{emu}}{\text{mols ion Oe}}]}{5584.9[\frac{\text{emu ions}}{\text{mol}}]}\end{aligned}$$

The sign of magnetic susceptibility determines the dominant magnetic effect in a material. Positive susceptibility can indicate paramagnetism and negative susceptibility indicates diamagnetism. Diamagnetic behavior is related to negative χ, or repulsion from a magnetic field, and typically arises from paired electrons in a material. This value is generally small and temperature independent, as the number of paired electrons does not vary with temperature. An exception is diamagnetic superconductivity, but as none of the materials in this thesis are superconductors this is not considered herein.

Paramagnetism is one of the simplest forms of magnetic behavior with temperature with reversible magnetization and linear M-H curves and arises from unpaired electrons in a material. A perfect Curie law paramagnet has non interacting magnetic moments

with a hyperbolic linear dependence

$$\chi = C/T \tag{2.3}$$

The Curie constant C captures the total angular momentum J (or total spin) of the magnetic moment in the system. It is defined as

$$C = \frac{N_A g_J^2 \mu_B^2 J(J+1)}{3k_b T} \tag{2.4}$$

or

$$C = \frac{N_A \mu_{eff}^2}{3k_b} \tag{2.5}$$

where μ_{eff} is the effective magnetic moment. Typically, the effective magnetic moment is the more desirable quantity and can be calculated from

$$\begin{aligned} \mu_{eff}[\mu_B] &= \sqrt{\frac{3k_B C}{N_A}} \\ &\sim \sqrt{8C} \rightarrow C[\frac{\text{emu K}}{\text{mol Oe}}] \\ &= g\sqrt{J(J+1)} \end{aligned} \tag{2.6}$$

Additionally, the hyperbolic susceptibility can be made linear by taking the inverse

$$\chi^{-1} = T/C \tag{2.7}$$

where $1/C$ is the slope. A perfect Curie paramagnet will intercept the origin in this inverted relationship.

However, most magnetic materials are not Curie paramagnets. They contain magnetic moments that interact with each other even at elevated temperature above their ordering transition. The internal magnetic interaction competes with the external magnetic

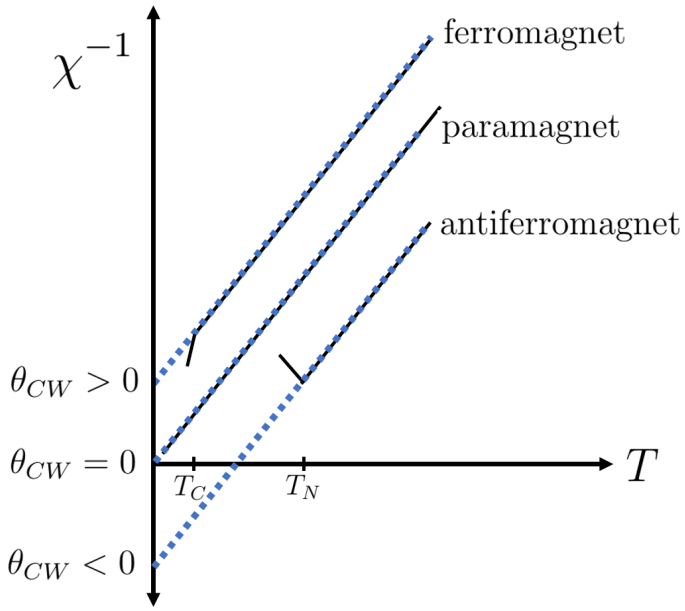

Figure 2.1: The Curie-Weiss law relates the magnetic correlations θ_{CW} of the magnetic susceptibility χ of a material in its paramagnetic temperature regime. Example data is shown as solid black lines overplotted with dashed blue lines fits to the Curie-Weiss law. A perfect Curie paramagnet will intercept zero inverse susceptibility at zero temperature. Extrapolating the high temperature Curie-Weiss relationship of a correlated magnet to zero temperature reveals a positive intercept (positive θ_{CW}) for a ferromagnet and negative intercept (negative θ_{CW}) for an antiferromagnet. Most correlated materials magnetically order below T_C or T_N and deviate from the Curie-Weiss law as indicated by rapid changes in slope in this depiction.

field attempting to align moments and temperature. At high temperatures, magnetic moments will have enough thermal energy to overcome a moderate magnetic field at internal magnetic interactions.

The general interpretation of interacting paramagnetic moments is captured within the Curie-Weiss law, which is a modification of the Curie law. The interactions of magnetic moments is simply placed in one new parameter, the Curie-Weiss temperature θ_{CW}, and the new equation is given by

$$\chi = \frac{C}{T - \theta_{CW}} + \chi_0 \tag{2.8}$$

where χ_0 is a temperature independent background term from the sample and sample environment (e.g. diamagnetic contributions). The Curie-Weiss temperature is a relative measure of overall interaction strength between magnetic moments in the paramagnetic regime of a material. If the value is positive, the interactions are deemed ferromagnetic, and if the value is negative, antiferromagnetic. This alters the intercept location of the inverse susceptibility given by

$$\frac{1}{\chi - \chi_0} = \frac{(T - \theta_{CW})}{C} \tag{2.9}$$

A ferromagnetic Curie-Weiss relationship will have a positive intercept extrapolated to $T = 0$ and an antiferromagnetic one will have a negative value. The magnitude of the intercept indicates the interaction strength and the intercept value is θ_{CW}. A Curie-Weiss fit extracts θ_{CW}, C, and χ_0 from susceptibility data (Figure 2.1).

Ideally, if the Curie-Weiss relationship is valid and the fit of χ^{-1} is conducted properly, the absolute value of θ_{CW} should align with the magnetic ordering transition of a material. In a ferromagnet, this is called the Curie temperature T_C and in an antiferromagnet it is called the Néel temperature T_N. To get a feel for where the Curie-Weiss law should be properly used, the following steps can help:

- Fit only the temperature range where the material should be in the paramagnetic regime. The spins must have enough thermal energy to overcome neighboring interactions to reorient relative to an applied field (thermal fluctuations >> interaction strength).

- Plotting χ^{-1} vs T can suggest where the paramagnetic regime is. This regime should appear somewhat linear and above any magnetic transition temperatures.

  - If the plot is perfectly linear, a χ_0 term is unnecessary.

  - If the data is not linear (often the case), then keep the temperature independent χ_0 term. Attempt a fit in an estimated paramagnetic temperature regime. Replot as $1/(\chi - \chi_0)$ vs T after an initial fit, and the fit region should now be linear with the subtracted off χ_0 term. If it is not, try a different temperature range for the initial fit.

- Additionally, in f electron materials, one must be wary of thermal population of elevated crystalline electric field states. If the population of doublets changes with temperature, then curvature in χ^{-1} arises that is not a result of a temperature independent χ_0 term. The Curie-Weiss law can only be used properly in the ground state doublet temperature regime below the curvature. Otherwise, an anomalously large θ_{CW} value is likely to be extracted from a fit. Both $LiYbO_2$ and $NaYbO_2$ exhibit this phenomena and will be discussed in their chapters.

Deviations from the Curie-Weiss relationship also occurs as a result of magnetic frustration. A geometrically frustrated magnetic material will contain strong magnetic interactions, captured in θ_{CW}, but are prohibited from magnetically ordering at $|\theta_{CW}|$ due to competing interactions. If a geometrically frustrated material orders, one can qualitatively inspect the frustration with the frustration parameter $f = \frac{|\theta_{CW}|}{T_N}$. The stronger the degree of magnetic frustration, the lower in temperature the material needs to go in order to magnetically order.

M vs. H

Magnetization versus field data was utilized to determine the saturated moment and Van Vleck susceptibility of materials. The Van Vleck susceptibility relates the population of neighboring crystalline electric field levels from the ground state with increasing external magnetic field [73]. The slope of the M-H curves above saturation is linearly related

to Van Vleck susceptibility, as seen by dividing out one H in the Van Vleck susceptibility equation:

$$\chi^{vv} = \frac{2\mu_0\mu_B^2}{V}\sum_n \frac{|<0|(\hat{L}+g\hat{S})\cdot H|n>|^2}{E_n - E_0} \tag{2.10}$$

$$\chi = \frac{M}{H} \text{ and } \chi^{vv} \propto H^2 \tag{2.11}$$

$$\implies M^{vv} \propto H \tag{2.12}$$

Population of electronic transitions occur as a result of the increasing magnetic field, H, rotating the ground state into excited states. In the zero field limit of χ^{vv}, only the ground state is populated and the g factor can be extracted from the intercept of χ^{vv}:

$$\hat{\mu}\,|0\rangle = g_J\mu_B J\,|0\rangle \tag{2.13}$$

$$\implies M(H=0) = g\mu_B J = g\mu_B J_{eff} = \frac{g\mu_B}{2} \tag{2.14}$$

For the polycrystalline samples that saturated in the regime of 0 to 14 T, the powder averaged g_{avg} was calculated with this method.

2.3 Specific heat

Specific heat measurements were carried out between 2 to 300 K on Quantum Design Physical Properties Measurement System (PPMS) with a 9 T or 14 T magnet for $NaYbO_2$, $LiYbO_2$, $KCeO_2$, and $NaCeO_2$. Dilution refrigerator measurements bewteen 50 mK to 4 K were collected with a Quantum Design dilution refrigerator insert. Data with

external magnetic fields between $\mu_0 H = 0$ to 14 T were obtained. A sample was attached to a heat capacity puck that had been previously calibrated with a set amount of thermal grease (usually N grease for low temperature measurements), and the PPMS measured the specific heat starting from low temperature and ending at high temperature. Flat, pressed pellet samples were used to ensure that the sample had sufficient contact with the sample platform with a minimal amount of grease. Additionally, the grease was used as an air free barrier for $KCeO_2$ and $NaCeO_2$ measurements.

Specific heat is measured at constant pressure and is defined as

$$C_p = (\frac{dQ}{dT})_p \tag{2.15}$$

where dQ is the differential amount of heat required to raise the material temperature by dT. The general units for specific heat are J K^{-2} mol^{-1}.

Overall, the measurement probes the chemical and magnetic lattice specific heat of a material. At low temperatures, the magnetic specific heat dominates in the lanthanide materials over the chemical specific heat. In these measurements, the desired quantity was the magnetic specific heat and it was obtained by subtracting out lattice contributions. As an estimate, the lattice contributions can be calculated with the Debye law:

$$C_p = 9R\frac{T}{\theta_D}^3 \int_0^{\theta_D/T} \frac{x^4 e^x}{(e^x - 1)^2} \tag{2.16}$$

where θ_D is the characteristic Debye temperature of the lattice and $C_p \sim C_v$ since the crystal volume does not rapidly change. The Debye model works well for simple lattices, but it does not generally capture all of the features of the chemical lattice specific heat. For these experiments, double Debye law fits were utilized with two characteristic Debye temperatures $\theta_{D,1}$ and $\theta_{D,2}$.

A more accurate representation of chemical lattice contributions to specific heat can be obtained with nonmagnetic analogue materials. For $NaYbO_2$, the material $NaLuO_2$ was synthesized and measured to directly subtract out the chemical lattice specific heat contributions.

Magnetic entropy was determined by integrating the specific heat with respect to temperature:

$$\Delta S_{mag} = \int \frac{C_p}{T} dT \tag{2.17}$$

Where $\Delta S_{mag} = Rln(W)$. Since the ground states of $NaYbO_2$, $LiYbO_2$, $KCeO_2$, and $NaCeO_2$ are Kramers doublets, the magnetic specific heat approached $Rln(2)$.

2.4 Crystalline electric field analysis

This methods section builds upon the $4f$ magnetism introduction section. The cystalline electric fields (CEF) of $NaYbO_2$, $KCeO_2$, $NaCeO_2$, and $LiYbO_2$ were determined with data from the high energy inelastic neutron scattering data on the Angle Resolved Chopper Spectrometer (ARCS) at Oak Ridge National Laboratory, TN combined with electron spin resonance (ESR) data for g factor anisotropy determination. Overall, calculating the crystalline electric field of these materials follows a simple flow but involves carefully crafting the correct J multiplet matrices and operators for each material.

First, the total angular momentum of the materials is calculated. For $NaYbO_2$ and $LiYbO_2$, the trivalent $4f^{13}$ Yb ions have total angular momentum $J = 7/2$ ($L = 3, S = 1/2$) and for $KCeO_2$ and $NaCeO_2$, the trivalent $4f^1$ Ce ions have total angular momentum $J = 5/2$ ($L = 3, S = 1/2$).

Second, the local CEF symmetry is determined. Triangular lattice $NaYbO_2$ and $KCeO_2$ contain YbO_6 and CeO_6 in D_{3d} environments. Tetragonal lattice $LiYbO_2$ and

$NaCeO_2$ YbO_6 and CeO_6 reside in D_{2d} environments. Following Kramers' theorem, the J manifolds of Ce and Yb maay be maximally split into a series of doublets based on the degeneracy of the manifold. The Yb $J = 7/2$ can split into four doublets and the Ce $J = 5/2$ can split into three doublets.

Third, the CEF Hamiltonian is determined. The number and symmetry of terms depends on the total angular momentum and CEF symmetry and only the minimal number of terms are kept. Each material has a different CEF Hamiltonian, and the forms will be presented in their respective sections. The local $\hat{z}$ direction is chosen to align with the highest fold symmetry axis. The general equation for the CEF Hamiltonian with Stevens parameters B_n^m and operators $\hat{O}_n^m$ is in equation 1.23. The form of Stevens operators $\hat{O}_n^m$ are tabulated in Hutchings [109].

The CEF Hamiltonian is a representation of the Coulomb potential of surrounding charges around the central magnetic lanthanide ion. Diagonalization of the CEF Hamiltonian with a set of Stevens parameters will return the eigenenergies E_i and eigenvectors $\phi_i^{\pm}$ of each of the i doublets. The g factors and intensities are calculated with equations 1.25, 1.26, and 1.28.

Fourth, to approximate the doublet splitting, the point charge model in equation 1.24 is used to get a first estimate of Stevens parameters. This model is dominated by the shell of charges closest to the central magnetic lanthanide ion and falls off with increasing distance. For the materials, point charges involving differing sized shells were used as initial guesses for Stevens parameters. These point charge models are almost never accurate, but they give a physically-grounded initial starting point for B_n^m and show which ionic shells maximally effect the CEF environment.

Fifth, the initial CEF Hamiltonian eigenenergies, eigenvectors, g factors, and intensities are compared with Q integrated E cuts of high energy inelastic neutron scattering data from ARCS. The values are minimized with χ^2 error following a random-walker

approach in the following loop:

1. The CEF Hamiltonian is approximated with a point charge model, reports of Stevens parameters on a similar magnetic material, or a randomly generated set of Stevens parameters.

2. The CEF Hamiltonian is diagonalized to determine energy eigenvalues, ground state wave functions, g-factors, and intensity ratios.

3. A χ^2 error is calculated with: $\chi^2_{tot} = \chi^2_{energies} + \chi^2_{g_{avg},g_{//},g\perp} + \chi^2_{intensities}$, where: $\chi^2 = \sum \frac{|obs-calc|^2}{obs}$. The individual χ^2 values represent deviations of the model from the observed values.

4. Between one to all of the Stevens parameters B^m_n are randomly modified (random walker) to increase or decrease by a multiplicative factor and have a small 5% chance to change sign.

5. Accept the new Stevens parameters if $\chi^2_{tot,new} < \chi^2_{tot,old}$.

6. Iterate until a minimum is reached.

7. Repeat the process with new initial starting parameters until a global minimum is determined.

This sequence was built upon the numerical error minimization techniques previously implemented in Mantid Plot [13].

In order for the calculations above to work, the correct matrix forms of the $\hat{J}$ operators are needed. Each calculation minimally relies on $\hat{J}_z$, $\hat{J}_+$, and $\hat{J}_-$ when utilizing the built-in CEF operations in Mantid Plot [13]. The $\hat{J}$ matrix is a diagonal matrix of m_j values arranged from lowest to highest pairwise (i.e. $\pm m_j$ paired along the diagonal), from the

top left to bottom right corner. Then, the $\hat{J}_+$ matrix elements raise the value of each m_j value in the corresponding row and column and the $\hat{J}_-$ lowers the m_j value. Matrix rows where the m_j value cannot be raised to or lowered to are left empty so that there are a total of $m_j - 1$ matrix elements. The matrix elements for raising are determined from

$$r_i = \sqrt{J(J+1) - (m_{j_{start}} + (i-1))(m_{j_{start}} + 1)} \tag{2.18}$$

and lowering from

$$l_i = \sqrt{J(J+1) - (m_{j_{start}} + (i-1))(m_{j_{start}} - 1)}, \tag{2.19}$$

where i is the i^{th} raise or decrease starting with $i = 1$ for the *lowest* m_j value.

An example for $J = 5/2$ is as follows. The lowest m_j is $m_j = -5/2$ and the matrices are $6x6$. The raising and lowering matrix elements are calculated with $r_i = \sqrt{J(J+1) - (-5/2 + (i-1))(-5/2 + 1)}$ and $l_i = \sqrt{J(J+1) - (-5/2 + (i-1))(-5/2 - 1)}$ for $i = [1, 6]$.

$$\hat{J}_z = \begin{pmatrix} -1/2 & 0 & 0 & 0 & 0 & 0 \\ 0 & 1/2 & 0 & 0 & 0 & 0 \\ 0 & 0 & -3/2 & 0 & 0 & 0 \\ 0 & 0 & 0 & 3/2 & 0 & 0 \\ 0 & 0 & 0 & 0 & -5/2 & 0 \\ 0 & 0 & 0 & 0 & 0 & 5/2 \end{pmatrix}$$

$$\hat{J}_+ = \begin{pmatrix} 0 & 0 & r_2 & 0 & 0 & 0 \\ r_3 & 0 & 0 & 0 & 0 & 0 \\ 0 & 0 & 0 & 0 & r_1 & 0 \\ 0 & r_4 & 0 & 0 & 0 & 0 \\ 0 & 0 & 0 & 0 & 0 & 0 \\ 0 & 0 & 0 & r_5 & 0 & 0 \end{pmatrix}$$

$$\hat{J}_- = \begin{pmatrix} 0 & l_4 & 0 & 0 & 0 & 0 \\ 0 & 0 & 0 & l_5 & 0 & 0 \\ l_3 & 0 & 0 & 0 & 0 & 0 \\ 0 & 0 & 0 & 0 & 0 & l_6 \\ 0 & 0 & l_2 & 0 & 0 & 0 \\ 0 & 0 & 0 & 0 & 0 & 0 \end{pmatrix}$$

These elements are read as raising/lowering *column* onto *row* from $\hat{J}_z$. For example, the raising element r_2 can be read as raising $m_j = -3/2$ (column 3) onto $m_j = -1/2$ (row 1) or l_6 as lowering $m_j = 5/2$ (column 6) onto $m_j = 3/2$ (row 4). Notice how the fifth row of $\hat{J}_+$ and sixth row of $\hat{J}_-$ are empty and the elements r_6 and l_1 are not used. This corresponds to the m_j value cannot be raised to in $\hat{J}_+$ ($m_j = -5/2$ in row 5) or lowered to in $\hat{J}_-$ ($m_j = +5/2$ in row 6). In other words, $m_j = -5/2$ in row 5 of $\hat{J}_z$ cannot be raised to from a lower $m_j = -7/2$ in $\hat{J}_+$ since that state does not exist in $J = 5/2$ and vice versa in $\hat{J}_-$ for $m_j = +5/2$.

These three matrices are used to calculate the g factors and intensities with equations 1.25, 1.26, and 1.28, where $\hat{J}_x = 1/2(\hat{J}_- + \hat{J}_+)$ and $\hat{J}_y = 1/2(\hat{J}_- - \hat{J}_+)$ provided the eigenvectors have been calculated. In Mantid Plot, the CEF Hamiltonian can be diagonalized with a given symmetry setting and Stevens parameters B_n^m. The CrystalField function

returns a matrix of eigenvectors that can be arranged according to $\hat{J}$ to then calculate g factors and relative intensities. Initially, Mantid Plot returns the eigenvectors as columns arranged corresponding to $-m_j$ to $+m_j$. In the above example, they can be reordered as $[4, 3, 5, 2, 6, 1]$ to work with the given matrices.

2.5 Magnetic structure determination

Magnetic structures are generally determined from elastic neutron scattering data. The dipole-dipole neutron to magnetic moment interaction gives Bragg scattering. A magnetic material well above its ordering temperature (paramagnetic phase) will not show Bragg reflections as no long range structure is present. As it approaches its ordering temperature, diffuse scattering, or broad features in diffraction data, arise from short range correlations. Below its ordering temperature, magnetic Bragg reflections appear that can be used to determine the magnetic structure. The intensity of these reflections fall off with the magnetic form factor $F(Q)$ of the given magnetic species in the material.

The simplest magnetic structures are collinear ferromagnets and antiferromagnets, where all moments reside in a plane and can only take two orientations: spin up or spin down. These structures can exhibit magnetic unit cells on the same size or larger underlying structural lattice. Magnetic structures that repeat the chemical lattice unit cell like a simple ferromagnet will produce increased intensity at the original peak locations when the system is magnetically ordered. Larger magnetic unit cells produce new Bragg reflections separate from the underlying lattice, making their magnetic structural determination slightly easier.

Other more complex types of magnetic ordering exist. In the introduction chapter, the concept of quantum spin liquids were introduced. These materials do not exhibit long range magnetic ordering and therefore do not have magnetic Bragg reflections. Another

type of magnetic ordering is spiral/helical or conical magnetic ordering. In this case, the magnetic moments rotate from one site to the next along a given propagation axis. The difference between helices and cones is the amount of magnetic moment contained within the propagation axis. A helix has magnetic moments perpendicular to the propagation direction while a cone can tilt its moments by an angle ϕ into the propagation direction.

Magnetic structures have their own set of symmetries that are inherently linked to the underlying chemical lattice. Determination of the magnetic structure is detailed in the following subsection.

Magnetic structure from elastic neutron scattering

The determination of a magnetic structure can be split into four components. First, one must obtain neutron scattering data with suitable resolution for the experiment below the ordering temperature of a material. Essentially, a suitably resolved experiment is able to see intensity from magnetic peaks. Sometimes, small spin materials like a $S = 1/2$ Ti^{3+} based one will have a difficult time sifting through experimental noise to find magnetic Bragg reflections. In some cases, subtracted data sets of high temperature paramagnetic data minus low temperature magnetic data can be instructive to determine magnetic peaks.

Second, the chemical structure must be well known and fit. This is typically done with a Rietveld refinement of the material just above its magnetic ordering temperature as to not include any added intensity to reflections from magnetic components. It shoudl be noted that data collected too close to the ordering transition may contain diffuse scattering from short range correlations, and data collected too far to the ordering transition may have lattice parameters too distinct from the ordered phase from thermal expansion.

Third, the new magnetic reflections are indexed to a wave vector with a program such as $k - search$ implemented in the Fullprof software suite [125]. The wave vector

and chemical lattice information are programmed into a symmetry analysis program like SARAh representational analysis and SARAh refine [126] to determine allowed basis function irreducible representations of a magnetic structure within that chemical lattice.

Finally, the differing representations are refined and compared to determine the magnetic structure which can be visualized by the product of coefficients and basis vectors of an irreducible representation. Only one wave vector and set of irreducible representations should be necessary to fit a structure, but on occasion multi-k structures arise such as in the ordered phase in $NaYbO_2$ under a magnetic field [79].

If the irreducible representation analysis does not seem to work, one can instead try the differing magnetic structure representations implemented in Fullprof [125]. For instance, the program suite contains a specific helical and conical mode where the only input information needed is the magnetic moment size, propagation direction of the cone/helix, wave vector, and angle of the cone/helix. However, with due diligence, the irreducible representation should also produce the same result as this method and is more commonly accepted.

Chapter 3

Quantum disorder and field-induced up-up-down order in triangular lattice $NaYbO_2$

3.1 Introduction

[1]

The triangular lattice antiferromagnet is the prototypical geometrically frustrated lattice where unconventional magnetic phases, such as the aforementioned quantum spin liquid phases [20–25], have been predicted to appear. Theoretical and experimental studies attempt to control the formation of these unconventional phases by targeting

[1] This chapter is based on two of our publications on $NaYbO_2$:[79] Mitchell M. Bordelon, Eric Kenney, Chunxiao Liu, Tom Hogan, Lorenzo Posthuma, Marzieh Kavand, Yuanqi Lyu, Mark Sherwin, N.P. Butch, Craig Brown, M.J. Graf, Leon Balents, and Stephen D. Wilson. Field-tunable quantum disordered ground state in the triangular-lattice antiferromagnet $NaYbO_2$, *Nature Physics*, **15** 1058-1064 (2019). Copyright 2019, The Author(s), under exclusive license to Springer Nature Limited. [80] Mitchell M. Bordelon, Chunxiao Liu, Lorenzo Posthuma, P. M. Sarte, N. P. Butch, Daniel M. Pajerowski, Arnab Banerjee, Leon Balents, and Stephen D. Wilson. Spin excitations in the frustrated triangular lattice antiferromagnet $NaYbO_2$, *Physical Review B*, **101**, 224427 (2020). Copyright 2020 American Physical Society.

materials with strong antiferromagnetic frustration while simultaneously incorporating inherent anisotropies and quantum fluctuations with spin 1/2 moments. There are relatively few materials with small spin moments on an equilateral triangular lattice and even fewer with ideal anisotropies and strong frustration. When the material's magnetic moment anisotropy is isotropic, Heisenberg moments form three sublattice 120 ° magnetic order in the classical and quantum limits [51–53]. Exotic magnetic phases can be formed by perturbing away from the Heisenberg limit, such as resonating valence bond [45–50], quantum dimer [127–129], and other quantum spin liquid phases [53, 72, 100, 102, 130–134]. These unique phases are of particular interest to the condensed matter physics community, as some of the phases incite long range quantum entanglement and fractionalized excitations.

However, real materials with ideal chemical compositions, structural lattices, and anisotropies are rare. These often unwelcome perturbations detrimentally alter the frustrated system and promote conventional magnetic order or spin glass formation. For example, materials can exhibit additional interlayer exchange interactions [135–137], chemical site disorder or vacancies [48–50, 67–78, 138–141], and intralayer exchange such as Dyzaloshinsky-Moriya (DM) antisymmetric exchange [142–146]. These additional contributions to the overall magnetism in a material heavily influences the resultant magnetic ground state of the frustrated lattice. Often, including all of the perturbing factors of an ideal lattice is computationally and theoretically unfeasible, so experimentalists first search for materials that exhibit properties predicted by the models. If a system is found in which some of the predicted properties arise, then subsequent theoretical investigations can further introduce the key additional contributions to the low energy Hamiltonian to fully understand a frustrated material.

Over the past few years, one of the most prominent research areas for frustrated triangular lattices has been based in rare earth oxide materials. The equilateral triangular

magnetic planes form from $4f$ magnetic moments with strong spin orbit coupling and inherent anisotropies. The strong crystalline electric field interaction from the oxygen environment produces magnetic moment ground state Kramers doublets that are well separated from their first excited state. They can be considered as $J_{eff} = 1/2$ magnetic moments in their ground state Kramers doublet with strong quantum fluctuations.

In particular, the first evidence for these frustrated $4f$ systems arose within the $YbFe_2O_4$ structure type materials, such as $YbMgGaO_4$ [48–50, 67–78] and $TmMgGaO_4$ [147–149]. The proposed low energy Hamiltonian for these materials incorporates the spin orbit entangled trivalent $4f$ moments with strong anisotropic magnetic exchange. Their strong quantum fluctuations predict some quantum spin liquid states [72, 101]. Experimental studies of these systems have indicated that they do not conventionally order into a long range magnetic state to sub 100 mK temperatures, and they instead may promote the formation of an entangled phase. Specifically, $YbMgGaO_4$ has shown a continuum of magnetic excitations with a bandwidth of ~ 1 meV [76].

One key issue with these two $YbFe_2O_4$ structure type materials is they contain 50/50 site mixing of nonmagnetic Mg^{2+} and Ga^{3+} that surround the equilateral triangular lattice Ln^{3+} planes. The Mg^{2+} and Ga^{3+} ions share the Fe site of the $YbFe_2O_4$ structure type with a random distribution in $YbMgGaO_4$ and $TmMgGaO_4$. Some reports have claimed that the nonmagnetic site mixing induces local randomness in the electric field surrounding the Ln^{3+} planes, which perturbs the magnetic exchange interactions randomly throughout the lattice [70, 147–149]. This bond exchange randomness may promote a weakly bound spin glass state that eventually freezes at low temperature with a set of low lying excitations that would mimic a quantum spin liquid continuum [70]. However, conflicting experimental reports claim the spins do not freeze to 30 mK [48, 68]. Additionally, recent theoretical work indicates that the randomness of exchange helps produce a quantum spin liquid by further frustrating and prohibiting conventional

magnetic order [69].

However, whether or not the chemical disorder in $YbMgGaO_4$ or $TmMgGaO_4$ is beneficial or a hindrance for quantum spin liquid phase formation sidesteps the main relevant question: can a quantum spin liquid phase form in a chemically ideal version of the $4f$ trivalent lanthanide equilateral triangular lattice? To answer this, an alternative $4f$ materials system with $4f$ equilateral triangular planes was found within the $ALnX_2$ (A = alkali, Ln = lanthanide, X = chalcogenide) family of materials. With the correct radius ratio of the constituent ions, either $P6_3/mmc$ or $R\bar{3}m$ space group triangular lattice materials crystallize (Figure 1.4). Many of the triangular lattice materials have shown promise to host unusual magnetic ground states [12, 14, 79–87]. These materials crystallize without native 50/50 chemical disorder on nonmagnetic cation sites as is found in the $YbFe_2O_4$ structure type materials. Most of these systems have been previously studied with bulk magnetic probes between 2 to 300 K [3–5, 84], and more detailed studies of low temperature magnetic properties with neutron scattering, μSR, nuclear magnetic resonance (NMR), and a.c. susceptibility are rapidly appearing in recent literature.

In this chapter, one promising candidate, $NaYbO_2$, will be covered. $NaYbO_2$ crystallizes in the $R\bar{3}m$ space group, contains equilateral triangle Yb^{3+} magnetic planes, and does not show chemical disorder within experimental resolution. The local D_{3d} YbO_6 crystalline electric field generates $J_{eff} = 1/2$ magnetic moments with mixed m_j ground state character, and the anisotropic moments ($\mu_{eff} = 2.63(19)\mu_B$) are antiferromagnetically coupled with $\theta_{CW} = -10.3$ K. Between the two dimensional magnetic layers resides a monolayer of Na^+ cations. All chemical sites are fully occupied within resolution and the equilateral triangular lattice remains robust without a structural transition.

The data collected on $NaYbO_2$ suggest it hosts a quantum disordered ground state that can be tuned with an external magnetic field. The zero field data indicate the material does not conventionally order. Susceptibility data to 50 mK at varying frequencies

shows no glassy behavior or signs of long range magnetic ordering. Specific heat data reveals two broad features that evolve with increasing magnetic field and is consistent with a number of low temperature theoretical spin liquid models following short-range correlations. In zero field, no new magnetic Bragg reflections arise in inelastic neutron scattering data to 330 mK, below the lowest feature in specific heat data.

However, the appearance of a sharp specific heat transition at $\mu_0 H = 5$ T coincides with new magnetic Bragg reflections in elastic neutron scattering data, a phase transition in a.c. susceptibility data, and the development of spin waves in low energy inelastic neutron scattering data. New magnetic Bragg reflections arise at $Q = (1/3, 1/3, z)$ where $z = 0, 1, 3, 4$ with two ordering wave vectors $k_1 = (1/3, 1/3, 0)$ and $k_2 = (0, 0, 0)$. The field-induced magnetic structure is fit to a collinear "up-up-down" magnetic state, which is a hallmark of the two dimensional XXZ Hamiltonian under an external field [150]. This phase occurs at 1/3 of the saturated magnetization of $NaYbO_2$ between $\mu_0 H = [3, 5]$ T that approaches a high field phase boundary into a polarized state by $\mu_0 H = 10$ T. Low energy dynamics from inelastic neutron scattering show a zero field continuum of excitations develops a flat band of spin waves in the ordered regime.

Field cycling above the critical phase boundary back into the up-up-down state alters the crystallographic directional dependence of the up-up-down ordered phase. Originally, the field-induced up-up-down state starting from $\mu_0 H = 0$ T lacks any intensity at $Q = (1/3, 1/3, 2)$, locking the up-up-down orientation close to $< 1, -1, -1 >$. From the high field state at $\mu_0 H = 10$ T, the $Q = (1/3, 1/3, 2)$ reflection contains intensity. The exact reason for this hysteresis phenomenon is not fully understood and likely requires single crystal diffraction measurements, but its implications are explored in terms of a second ordered noncollinear high field phase.

Theoretical analysis in collaboration with Chunxiao Liu and Prof. Leon Balents of the full $NaYbO_2$ spin Hamiltonian suggests the ordered phase is a canted up-up-down

state. We follow the evolution from the three-sublattice order ground state of the XXZ Hamiltonian into the canted up-up-down state with powder averaged linear spin wave models. The models show slight easy plane exchange anisotropy of $J_{xy} = 0.51$ meV and $J_z = 0.45$ meV and tracks the experimentally observed flat band pushing up in energy with increasing external field to $\mu_0 H = 5$ T. Prior to crossing the high field phase boundary, a second ordered V-state is predicted at $\mu_0 H = 9.5$ T , as has been suggested by NMR measurements [81] and the hysteresis of the $Q = (1/3, 1/3, 2)$ reflection in the up-up-down phase.

The linear spin wave model captures the majority of the observed low energy dynamics of $NaYbO_2$ in its ordered phases except for an extra broad mode observed at 1.5 meV. This mode arises at $\sim 3J$ and and $\mu_0 H = 5$ T, indicating strong multimagnon interactions. Other materials with up-up-down phases like $Ba_3CoSb_2O_9$ do not show this extra mode [103–105]. In conjunction with a reduced ordered moment and strong quantum fluctuations of $J_{eff} = 1/2$ Yb moments in $NaYbO_2$, this suggests the scattering weight of the low energy inelastic neutron data relocates to longitudinal spin fluctuations at 1.5 meV.

$NaYbO_2$ crystal structure

The general crystal structure for $R\bar{3}m$ $ALnX_2$ materials is shown in Figure 1.6. $NaYbO_2$ adopts the $R\bar{3}m$ structure, and its geometrically frustrated triangular lattice dictates the allowed magnetic interactions in the material. At 1.6 K, the Yb-Yb distance is ~ 3.35 Å(Figure 3.2). The trivalent Yb cations reside in trigonally compressed D_{3d} YbO_6 octahedra. The octahedra sides along the c axis are shorter relative to those in the ab plane. Between each Yb-Yb bond is a point of inversion, and no Dyzaloshinsky-Moriya (DM) exchange is allowed.

The crystal structure of $NaYbO_2$ contains similar structural motifs as the previously

studied spin liquid candidate $YbMgGaO_4$ [48–50, 67–78]. They both contain equilateral triangular planes of YbO_6 $D3d$ octahedra stacked in an ABC sequence along the c axis. However, the overall interlayer spacing of triangular Yb planes in $NaYbO_2$ is significantly closer, making three dimensional magnetic exchange an important factor in the magnetic ground state of the system. The ABC stacking sequence of Yb planes in the $R\bar{3}m$ space group further promotes geometric frustration. The projection of one Yb plane onto another along the c axis places projected Yb moments at the center of Yb triangles. Three equivalent bonds can be drawn from the center of a triangle to its vertices, generating geometric frustration (Figure 3.1). In the $P6_3/mmc$ $ALnX_2$ materials, the stacking sequence is unfrustrated AAA. Interlayer interactions in these systems may promote magnetic ordering along the c axis. It will be shown that the frustrated ABC stacking in $NaYbO_2$ likely aids in the formation of a quantum spin liquid ground state and that $NaYbO_2$ is not a purely two dimensionally frustrated triangular lattice antiferromagnet.

3.2 Experimental methods

The synthesis and basic analysis methods for $NaYbO_2$ are presented in Chapter 2. This section overviews the specific instrumental setups and measurement conditions for the material.

3.2.1 Magnetic measurements

The general bulk magnetic properties specific heat measurements, magnetic susceptibility, and isothermal magnetization were collected on $NaYbO_2$ with a Quantum Design PPMS and MPMS3. Magnetic susceptibility from 2 to 300 K was collected under $\mu_0 H = 20$ Oe and was analyzed with the Curie-Weiss law. Isothermal magnetization was collected up to $\mu_0 H = 9$ T at temperatures from 2 to 300 K. Specific heat measurements

were obtained with the traditional PPMS heat capacity setup and with the dilution refrigerator insert for the PPMS. Data on sintered $NaYbO_2$ pellets between 80 mK and 300 K were stitched together under $\mu_0 H = 0, 2.5, 5$, and 9 T. The high temperature lattice contributions to the specific heat were approximated by scaling specific heat data collected on $NaLuO_2$ from 2 to 300 K. Below 2 K, $NaLuO_2$ displayed no additional lattice specific heat. The magnetic portion of specific heat of $NaYbO_2$ was obtained by integrating C_p/T after subtracting out the lattice contributions from $NaLuO_2$ with equation 2.17.

Additional a.c. magnetic susceptibility from $\mu_0 H = 0$ to 7 T in quarter and half T steps was obtained on a susceptometer at 711.4Hz with a 0.1Oe (7.96 A m^{-1}) drive field. It was equipped with a ^{3}He insert capable of reaching 330 mK. Both temperature dependent a.c. maganetic susceptibility and isothermal a.c. susceptibility was measured on this setup. The contribution from the sample holder is approximately linear in this temperature and field range and was subtracted out for final data analysis. These measurements were analyzed in conjunction with a.c. susceptibility data from 10 Hz to 10 kHz obtained on a PPMS equipped with a dilution refrigerator from 50 mK to 4 K with a 1 Oe drive field. An empty sample holder measurement was utilized to subtract out measurement background and trim coils were used to null the background frequency dependence.

Electron paramagnetic resonance (EPR) data at 4.2 K from an EMXplus Bruker spectrometer in the perpendicular mode was used to measure the anisotropic g tensor of $NaYbO_2$. The shape and features of the spectrum was modeled with the MATLAB EasySpin package [151]. Signifiacnt broadening of the $g_{//}$ component of full width half maximum (FWHM) 0.40(7) was necessary to reproduce the observed spectrum, but no $g_{\perp}$ broadening was required.

3.2.2 Elastic neutron scattering

Powder elastic neutron diffraction data was obtained on the high-resolution powder diffractometer BT-1 at the National Institute of Standards and Technology (NIST) Center for Neutron Research (NCNR). Initially, the spectrometer was equipped with a cryostat capable of reaching 1.6 K for crystal structure refinement measurements. The $NaYbO_2$ polycrystalline sample was loaded in a vanadium canister and measured at $T = 1.6, 300$ K with incident neutrons of wavelength 1.5399 Å(Cu(311) monochromator) and 2.0774 Å(Ge(311) monochromator). Then, the instrument was equipped with a 7 T vertical field cryostat and a ^{3}He insert capable of reaching 330 mK to 1.5 K. Fields of $\mu_0 H = 0$, 5, and 7 T were employed with 2.0774 Å(Ge(311) monochromator) neutrons. These low temperature measurements required a copper canister.

Refinement of the structural data was performed in the FullProf software suite [125] and GSAS/EXPGUI program [152, 153]. Rietveld refinements to the 1.6 K and 300 K data are shown in Figure 3.3 and Table 3.1. No phase changes were observed between 300 K to 1.6 K.

Refinement of the magnetic structure followed the general procedure outlined in the Methods chapter. The SARAh refine and representational analysis programs [126] were used to determine the symmetry allowed magnetic structure of $NaYbO_2$ at $\mu_0 H = 5$ T. The magnetic structure was refined with subtracted data sets of 330 mK 5 T minus 1.5 K 0 T. There was extra intensity in the elastic line originating from the sample environment and small Na_2CO_3 impurities that subtracted out to leave behind pure magnetic Bragg reflections. Additionally, magnetic intensity appeared directly on the lowest angle (003) structural peak and required the subtraction to quantify properly.

3.2.3 High energy inelastic neutron scattering

High energy inelastic neutron scattering (INS) data $S(Q, \hbar\omega)$ was collected on the Angle Resolved Chopper Spectrometer (ARCS) at Oak Ridge National Laboratory (ORNL). Approximately 5 g of polycrystalline $NaYbO_2$ powder was loaded into an aluminum canister and placed in a cryostat capable of reaching 5 K. Incident neutron energies were chosen to observe the $J = 7/2$ ground state multiplet splitting of the $4f^{13}$ Yb3+ ions by the local D_{3d} crystalline electric field (CEF) with $E_i = 150$ meV (Fermi 2, Fermi frequency 600 Hz). Furthermore, to resolve broadening of the lowest energy excitation, incident neutrons with energies $E_i = 60$ meV were used. Background contributions from the aluminum sample can were subtracted out by measuring an empty canister under the same conditions. These data are presented in Figures 3.4 and 3.5.

The eight fold degenerate multiplet can maximally split into four doublets and is perturbed by surrounding ions approximated by the point charge model in equation 1.24.

Details of the general CEF setup is explained above in the Introduction and Methods chapters. The specific changes for $NaYbO_2$ are as follows: The minimal CEF Hamiltonian describing $NaYbO_2$ with Stevens parameters and operators is:

$$H_{CEF} = B_2^0\hat{O}_2^0 + B_4^0\hat{O}_4^0 + B_4^3\hat{O}_4^3 + B_6^0\hat{O}_6^0 + B_6^3\hat{O}_6^3 + B_6^6\hat{O}_6^6 \tag{3.1}$$

Diagonalizing the CEF Hamiltonian returns the eigenenergies and eigevectors. The eigenvectors were used to determine g factor components and relative intensity ratios of the excited states with equations 1.25, 1.26, and 1.28. The refinement of CEF Stevens parameters was conducted with the process outlined in the Methods chapter.

3.2.4 Low energy inelastic neutron scattering

Two instruments were used to measure the low energy dynamics of $NaYbO_2$. First, low energy INS data $S(Q, \hbar\omega)$ were obtained on 8g of powder at the Disc Chopper Spectrometer (DCS) at NCNR loaded in a copper canister. The spectrometer was equipped with a 10 T vertical magnet and a dilution refrigerator insert. Neutrons with incident wavelengths of $E_i = 3.27$ meV under the medium-resolution chopper setting provided an optimal flux to resolution setting for this experiment. The background was determined by subtracting out the negative scattering from the spectra. Second, additional data was obtained on the Cold Neutron Chopper Spectrometer (CNCS) at ORNL on 10g of $NaYbO_2$ powder loaded in a copper canister. This instrument was equipped with a 7 T vertical magnet and dilution refrigerator insert. HIgh flux neutrons with incident wavelengths of $E_i = 3.32$ meV were used. An empty can measurement was collected at 1.8 K as a background to subtract out.

Additional analysis of the elastic line of DCS data was employed by integrating over the elastic line from $E = [-0.1, 0.1]$ meV in Figure 3.12a). This instrument had sufficient $|Q|$ resolution to resolve the field induced magnetic peaks observed on BT-1 at $\mu_0 H = 5$ T and tracked their evolution from 0 T to 10 T and 10 T to 0 T. This data was relatively unperturbed by sample environment issues observed in BT-1 data, allowing for a more precise determination of integrated intensity of the magnetic peaks as a function of external magnetic field. Particularly, the $Q = (1/3, 1/3, 0)$ and $Q = (1/3, 1/3, 2)$ peaks were tracked in Figure 3.12b)-c). The area of these peaks was determined by fitting the peak shape to a Gaussian and integrating the area under the curve. The location of the peaks were restricted to $|Q| = [1.2, 1.29]$ Å^{-1} and $|Q| = [1.38, 1.52]$ Å^{-1}, respectively.

3.3 Results

3.3.1 Crystalline electric field

The high energy inelastic neutron scattering data for $NaYbO_2$ are shown in Figures 3.4 and 3.5. With incident neutrons of $E_i = 150$ meV, three crystalline electric field (CEF) excitations are revealed. They are centered at $E_1 = 33.9$ meV, $E_2 = 58.2$ meV, and $E_3 = 82.6$ meV. The ground state Kramers doublet is well separated from E_1, meaning that at low temperatures the system should primarily occupy this state. Extracted data from cuts to the scattering spectra are shown in Table 3.2 along with point charge calculations with equation 1.24.

Two strong candidate fits were found for this material, labeled Fit 1 and Fit 2. The main difference between the two fits is that Fit 2 is motivated by a point charge model incorporating atoms surround a central Yb ion to 3.5 Å. This includes the D_{3d} YbO_6 octahedra, six Na^+ cations, and nearest-neighbor Yb^{3+} cations as shown in Figure 3.6. This point charge model contains the same signs of Stevens parameters B_n^m as Fit 2. In comparison to Fit 1, Fit 2 has a larger χ^2 value. However, Fit 1 does not resemble a point charge model of any size. These results overall indicate that the local Yb CEF environment is strongly perturbed by ions further away than just the closest O^{2-} anions.

Further comparison of the two models is shown with inverse susceptibility data in Figure 3.4. In Mantid Plot [13], the susceptibility was calculated from the Stevens parameters of Fit 1 and Fit 2. However, both fits did not reproduce the observed d.c. susceptibility from 2 to 300 K. In most $4f$ systems, the mean field exchange is relatively weak and on the order of a few Kelvin at most. In $NaYbO_2$, the strong $\theta_{CW} = -10.3$ K heavily influences the overall shape of the magnetic susceptibility. To model the susceptibility with the CEF fits, the antiferromagnetic exchange had to be included. In Mantid

Plot, the effective susceptibility is calculated via:

$$\chi_{eff}(T) = \frac{\chi_{calc}(T)}{1 - \theta_{CW}\chi_{calc}(T)} \tag{3.2}$$

With the incorporated θ_{CW}, both Fit 1 and Fit 2 resemble the observed magnetic susceptibility of $NaYbO_2$.

A closer look at the lowest energy excitation E_1 was conduced with incident neutrons of $E_i = 60$ meV in Figure 3.5. The inelastic neutron scattering data here revealed that E_1 is broader than the instrumental resolution. This is represented as dashed lines in Figure 3.6. The broadening of E_1 was modeled with two Gaussian peaks centered at 35.3(1.3) meV and 33.4(1.4) meV split by $\Delta E_1 = 2.1$ meV. A narrow splitting of 2.1 meV was not resolvable in the higher $E_i = 150$ meV data.

The origin of the broadening of E_1 sparks a couple of ideas. The $J = 7/2$ Kramers doublets cannot inherently broaden or split without breaking time reversal symmetry. First, if there were multiple Yb environments, one would expect multiple sets of CEF excitations. This was ruled out with a combination of point charge calculations and analysis of elastic neutron powder diffraction data. As mentioned above, there is no site mixing or strong chemical vacancies in $NaYbO_2$ from Rietveld refinement analyses. To generate peak splitting where two peaks are nearly equivalent in integrated intensity, one would expect two Yb environments of nearly equal occupation. Such a large systematic chemical impurity would readily appear in Rietveld analysis. Also, point charge models where chemical impurities were strategically introduced in Table 3.3 show that randomly introducing chemical impurities would result in multiple new CEF modes. Some of these modes would be well separated from the original CEF set and would be resolvable at $E_i = 150$ meV.

Therefore, the most likely explanation of the split E_1 is due to the strong mean field

exchange in $NaYbO_2$. This occurs when nearest neighbor antiferromagnetic exchange introduces CEF dispersions as a perturbing effect on the ideal CEF structure [154]. While we were unable to map out this dispersion, single crystal measurements could simultaneously look for this and further explore chemical imperfections.

3.3.2 Bulk magnetic properties

The high temperature magnetic susceptibility of $NaYbO_2$ fit to the Curie-Weiss law is shown in Figures 3.7 and 3.10. The high temperature paramagnetic regime above 100 K contains magnetic contributions from multiple Kramers doublets and fits to the Curie-Weiss law here do not accurately represent the antiferromagnetic correlations in the ground state Kramers doublet. However, below 100 K, only the ground state Kramers doublet is primarily occupied. Curie-Weiss fits to the susceptibility data between 20 to 100 K reveal a local moment of $\mu_{eff} = 2.63(8)\mu_B$ that are antiferromagnetically coupled with $\theta_{CW} = -10.3(8)$ K. A small temperature independent background χ_0 is used to make the inverse susceptibility linear in this temperature regime. When compared with structurally similar $YbMgGaO_4$ [48–50, 67–78] with $\theta_{CW} = -4$ K, the antiferromagnetic correlations are heightened in $NaYbO_2$, likely due to slightly closer spacing of Yb-Yb distances in $NaYbO_2$.

Electron paramagnetic resonance (EPR) data in Figure 3.7 reveal an anisotropic g factor. The average $g_{avg} = 3.03$, calculated with equation 1.27, and the individual tensor components are $g_{//} = 1.726(9)$ and $g_{\perp} = 3.294(8)$. The high symmetry three fold axis of the local Yb environment coincides with the crystallographic c axis, meaning that $g_{//} = g_c$ and $g_{\perp} = g_{ab}$.

Isothermal magnetization is presented in Figure 3.7 up to $\mu_0 H = 9$ T. The system does not saturate in this field range at any temperature recorded, and the expected

maximal moment of the Yb ions is $\sim 1.5\ \mu_B$. The Yb moments reach 1 μ_B per ion at $\mu_0 H = 9$ T. Other reports have shown that $NaYbO_2$ saturates around $mu_0 H = 14$ T [14].

A.c. susceptibility data under varying frequencies from 10 Hz to 10 kHz are shown in Figure 3.7 down to 50 mK. The material does not exhibit any frequency dependence or flattening of susceptibility, which is consistent with Yb moments not freezing or magnetically ordering. However, this is not native behavior of a quantum spin liquid either, as the susceptibility should reach a maximum and flatten off as the spins form a cohesive phase. Further a.c. susceptibility measurements under increasing field show the $\chi'(T)$ signal begins to turn over with increasing field and flattens by $\mu_0 H = 2$ T (Figures 3.7 and 3.8). The interpretation of the zero field data is that a fraction of Yb moments are left free and do not enter the quantum disordered phase. These free moments are then quenched under an external magnetic field, which is tracked by following the inflection in $\chi'(T)$ with increasing external magnetic field. The inflection linearly increases in temperature with increasing field before flattening at $\mu_0 H = 2$ T, following Zeeman splitting of free Yb moments. The Zeeman splitting is defined as

$$\Delta E = 2\mu_b g_{avg} J_{eff} H \tag{3.3}$$

where H is the external magnetic field. The relationship between the Zeeman splitting and field is represented by the orange stars in Figures 3.7 and 3.20.

Quantifying the free Yb spins was determined by fitting a Curie-Weiss model of the field saturated $\mu_0 H = 2$ T minus the zero field data. The moment size was limited by the original Curie-Weiss analysis of d.c. susceptibility between 20 to 100 K, but the mean field exchange was allowed to vary. The free moments were slightly coupled with a small $\theta_{CW} = -0.45(4)$ K and accounted for roughly 14.4(6)% of the Yb moments.

Additionally, the 2 K isothermal magnetization was fit to a Brillouin function comprised of free Yb moments and antiferromagnetically coupled Yb moments of the main phase. This is shown in Figure 3.10. This separate analysis revealed that approximately 7% of the Yb moments were free at 2 K up to $\mu_0 H = 9$ T.

Although the two different models differ, they roughly parameterize the free spin fraction in $NaYbO_2$. Since a quantum disordered phase does not go through a traditional phase transition that requires symmetry breaking, the entire lattice does not have to enter the quantum disordered phase. Also, these free spins are not a result of any chemical impurities or site mixing as determined by elastic neutron powder diffraction. No quantifiable chemical imperfections were observed in this material, and the free spin concentration is inherent to the quantum disordered phase.

Further high field a.c. susceptibility data was obtained and is displayed in Figure 3.8. Isothermal $\chi'(H)$ at 330 mK reveals three distinct features of the quantum disordered phase of $NaYbO_2$. First, the $\chi'(H)$ signal begins at a non zero value from the free Yb spins that are quenched by $\mu_0 H = 2$ T. Between $\mu_0 H = 2$ to 3 T, the susceptibility increases as a field induced phase boundary is approached. Strong quantum fluctuations at a critical point increase the susceptibility. Subsequently, the susceptibility bottoms out and approaches zero between $\mu_0 H = 4$ to 5 T, consistent with a conventionally ordered magnetic phase. As will be discussed later in the elastic neutron powder diffraction section, this phase was determined to be an up-up-down equal moment magnetic phase. The ordered phase persists to higher fields, but again the susceptibility increases up to the highest field measured of $\mu_0 H = 7$ T, where another possible ordered phase boundary is approached. This second phase boundary is not fully mapped out here, but as discussed later on, it is likely close to a canted V phase.

The $\chi'(T)$ susceptibility at varying fields in Figure 3.8 further explores the ordered phases of $NaYbO_2$. Between $\mu_0 H = 3$ to 7 T, a sharp inflection in susceptibility is

present near 1 K. This suggests the ordering temperature in external field of the up-up-down phase is at 1 K.

In fact, the ordered phase transition can be readily seen in specific heat measurements of $NaYbO_2$ in varying external magnetic fields in Figure 3.8. Four different magnetic fields were collected, $\mu_0 H$ = 0, 2.5, 5, and 9 T. The zero field data displays only two convolved broad features centered at 1 K and 2.5 K. A nonmagnetic analogue $NaLuO_2$ was also measured, and subtracting off its lattice heat capacity from the overall signal in $NaYbO_2$ reveals the magnetic specific heat of $NaYbO_2$. The integrated C_p/T of $NaYbO_2$ approaches 95% of $Rln(2)$, which is what is expected for a $J_{eff} = 1/2$ system. With increasing external field, the lower feature begins to sharpen and the upper feature pushes up in temperature. At $\mu_0 H = 5$ T, the lower sharp feature indicates the transition of $NaYbO_2$ into the long range ordered up-up-down magnetic phase. The transition temperature of 1 K coincides directly with $\chi'(T)$ measurements. At $\mu_0 H$ = 9 T, the sharp anomaly softens again as the material approaches the canted V phase boundary and moment polarization.

The low temperature tail of specific heat is fit to a power law relationship $T^{2.04(2)}$ in Figures 3.8 and 3.10. The bottom of the tail is influenced by a nuclear Schottky anomaly that initially made the specific heat appear as if it never approached zero at zero Kelvin. Contribution from the nuclear feature was determined by subtracting $\mu_0 H = 5$ T minus $\mu_0 H = 0$ T specific heat data, as the nuclear moments are polarized in an external field. The subtracted data was then fit to the power law relationship.

3.3.3 Long range magnetic order

Low temperature elastic neutron powder diffraction analysis was conducted by combining temperature subtracted data from BT-1 in Figure 3.9 and elastic cuts from DCS

in Figure 3.12. First, the crystal structure of $NaYbO_2$ was fit with data from BT-1 and is shown in Figure 3.3 and Table 3.1. Temperature subtracted data sets of 330 mK minus 1.5 K BT-1 data at $\mu_0 H = 0$, 5, and 7 T were then utilized to determine long range order in the material. In zero field, no new magnetic Bragg reflections arose, but at $\mu_0 H = 5$ and 7 T, new superlattice reflections arose at $Q = (1/3, 1/3, z)$, where $z = 0$, 1, 3, and 4. Intensity also appeared directly on the structural (003) reflection, indicating some ferromagnetic contribution to the ordered state. In the $R\bar{3}m$ space group, these new reflections were fit to double ordering wave vectors $k_1 = (1/3, 1/3, 0)$ and $k_2 = (0, 0, 0)$. The reflections were limited by the instrumental resolution with a minimum correlation length of 450 Å.

The refined magnetic structure at $\mu_0 H = 5$ T is shown in Figure 3.9 and corresponds to the equal moment up-up-down magnetic state with 1.36(1) μ_B Yb moments. The expected saturated Yb moment is 1.5 μ_B, and the missing moment fraction arises from the free Yb moments not in the ordered phase and strong remnant quantum fluctuations. The same magnetic structure arises at $\mu_0 H = 7$ T, but the overall intensity of the reflections is reduced as $NaYbO_2$ approaches the canted V phase (Figure 3.10).

In the BT-1 data, the $Q = (1/3, 1/3, 2)$ magnetic reflection contains no intensity. Absence of intensity at this momentum transfer limited the number of allowed magnetic structures for the system. For instance, the three sublattice 120° antiferromagnet cannot reproduce the observed data, as it always contains intensity at $Q = (1/3, 1/3, 2)$. Furthermore, the number orientations the up-up-down magnetic structure could adopt was also limited by absence of intensity at this reflection. The allowed orientations with symmetry related ordering wave vectors is shown in Figure 3.11. In the case of $k_1 = (1/3, 1/3, 0)$ and $k_2 = (0, 0, 0)$, the moments are locked into an orientation near the $< 1, -1, -1 >$ direction.

The elastic cuts of DCS data in Figure 3.12 further explored the $Q = (1/3, 1/3, 2)$ reflection. From the low field phase boundary of $\mu_0 H = 3$ T into the ordered state at $\mu_0 H = 5$ T, the DCS data reconfirmed that no intensity arose at this reflection. However, after field cycling to $\mu_0 H = 10$ T and approaching the ordered phase from high field, the reflection contained intensity. As seen in a.c. susceptibility measurements, the high field phase boundary of the up-up-down state is close to $\mu_0 H = 7$ T. The overall up-up-down order was tracked by following the integrated intensity of the $Q = (1/3, 1/3, 0)$ reflection, which contained near identical intensity from the low or high field phase boundaries. In comparison, tracking the $Q = (1/3, 1/3, 2)$ reflection saw that it contained intensity only on field ramp down from $\mu_0 H = 10$ T. The shape of the $z = 2$ integrated intensity curve followed that of the $z = 0$ curve from the high field phase boundary, meaning that the reflections all correspond to one ordered magnetic phase. This hysteretic dependence of the $z = 2$ reflection indicates that the high field phase boundary is strongly first order as the up-up-down phase goes into a noncollinear state like the V phase [155]. The exact reason why the up-up-down phase is orientationally locked originally and why it loses this dependence is unknown and prompts further investigations with single crystals.

3.3.4 Low energy spin dynamics

Studying the low energy spin dynamics of a frustrated magnet is the key way to understanding its magnetic ground state. For $NaYbO_2$, the low energy dynamics were probed with inelastic neutron scattering measurements on DCS at NCNR and CNCS at ORNL. The field dependence of scattering measurements are shown for DCS and CNCS in Figures 3.14 and 3.15, respectively. The DCS data reached up to $\mu_0 H = 10$ T and the CNCS data collected high flux spectra up to $\mu_0 H =$7 T. The data obtained in these figures were collected below the lowest temperature specific heat anomaly in $NaYbO_2$.

For DCS, the temperatures ranged from 67 mK to 100 mK, with some field induced sample heating. The CNCS measurement held steady at 125 mK with increasing field. Additionally, the temperature dependence of the low energy dynamics in $NaYbO_2$ were obtained on CNCS and shown in Figure 3.16.

In $\mu_0 H = 0$ T, the low energy inelastic neutron scattering spectra from DCS and CNCS show a continuum of excitations. The excitations originate from the two dimensional magnetic zone center of $Q = (1/3, 1/3, 0)$ and extend up to $E = 1$ meV. The spectral weight peaks near 0.25 meV, but the modes are gapless from $E = 0$ meV. This result is consistent with gapless excitations from deconfined spinons. The DCS and CNCS figures plot the evolution of the gapless modes into the ordered up-up-down phase and then into the high field regime. The spectral weight originally splits into two components with increasing magnetic field. The first falls into the elastic line with intensity near the magnetic zone center. The second is a flat band that slowly pushes up to 1 meV with increasing field. The band is energetically maximal and flattest at $\mu_0 H = 5$ meV. Further increasing the field beyond the up-up-down phase again pulls the flat 1 meV mode back into the elastic line. Some spectral weight is visible that originates from the magnetic zone center that steeply diverges toward $Q = 0$ Å^{-1} at $\mu_0 H = 10$ T.

Taking E cuts through the data at varying fields centered at the magnetic zone center track the evolution of the continuum as it develops these two features. This data is presented in Figure 3.19. The maximum of spectral weight near 0.25 meV at $\mu_0 H = 0$ T broadens and eventually develops the 1 meV flat band at $\mu_0 H = 5$ T and a second lower band centered at 0.5 meV. These bands indicate the softening of the up-up-down magnetic modes as the field increases.

Additionally, in the high resolution CNCS data in Figure 3.15, a third mode at the convolved energy of 1 meV plus 0.5 meV arises. The linear spin wave theory (LSWT) models presented later will show that all the modes are accounted for below 1 meV. The

presence of this third mode at $E^* = 1.5$ meV is at $3J$ and cannot originate from the single magnon bands of the material. Instead, the presence of E^* suggests that strong multi magnon interactions occur [156]. This could be checked in future single crystal experiments by analyzing the longitudinal spin channel, where two magnon scattering would arise. Furthermore, the presence of E^* could originate in an unconventional spin wave that would lower the ordered magnetic moment. The refined moment value of 1.36 μ_B is lower than the expected 1.5 μ_B moment, but again single crystals will be needed to verify this claim.

3.3.5 XXZ Hamiltonian and spin wave analysis

This section overviews the Hamiltonian and linear spin wave theory (LSWT) used to model the inelastic neutron scattering data and interactions in $NaYbO_2$. This section was developed by Leon Balents and Chunxiao Liu. It is shown here to fully illustrate the properties in $NaYbO_2$. Without this, we would not have been able to fully investigate the material. The full analysis is shown in Ref. [79]. In particular, the model we investigated incorporates an external magnetic field along an arbitrary direction, which allowed us to generate powder averaged dynamic spin structure factor $S(Q, \hbar\omega)$ plots to compare with the DCS and CNCS data.

First, the symmetry allowed exchange interactions in $NaYbO_2$ were analyzed. In the $R\bar{3}m$ space group and Yb atoms at (0,0,0), the nearest neighbor in plane Yb-Yb bonds coincide with the a and b crystallographic axes. There is no symmetric difference between a or b. These bonds contain an inversion center and no Dyzaloshinsky-Moriya (DM) antisymmetric exchange is allowed. The two dimensional Hamiltonian incorporates an XXZ interaction and directionally dependent bond interactions. The bond dependent

interactions are shown here in the compass format

$$H_{2d} = \sum_{\langle ij \rangle} \Big\{ J_{xy} \left(S_i^x S_j^x + S_i^y S_j^y \right) + J_z S_i^z S_j^z + J_c \left(\hat{e}_{ij} \cdot S_i \right) \left(\hat{e}_{ij} \cdot S_j \right) + J_{cz} \left[\left(\hat{z} \cdot \hat{e}_{ij} \times S_i \right) S_j^z + \left(\hat{z} \cdot \hat{e}_{ij} \times S_j \right) S_i^z \right] \Big\} \quad (3.4)$$

The operators $\hat{e}_{ij}$ indicate the three different bond directions in the ab crystallographic plane. They are incorporated in the compass J_c term and the J_{cz} term that couples the compass direction and out of plane spin component. The J_{xy} and J_z terms are XXZ components.

Similarly, the interplane Yb-Yb bonds follow compass like terms. This arises since the neighboring Yb planes stack in an ABC sequence with Yb ions centered in the projected triangles (Figure 3.1). These bonds also preclude any DM exchange. The interplane Hamiltonian becomes:

$$H' = \sum_{\langle\langle ij \rangle\rangle} \Big\{ J'_{xy} \left(S_i^x S_j^x + S_i^y S_j^y \right) + J'_z S_i^z S_j^z + J_c \left(\hat{f}_{ij} \cdot S_i \right) \left(\hat{f}_{ij} \cdot S_j \right) + J'_{cz} \left[\left(\hat{f}_{ij} \cdot S_i \right) S_j^z + \left(\hat{f}_{ij} \cdot S_j \right) S_i^z \right] \Big\} \quad (3.5)$$

In this case, the suffixes i and j indicate Yb ions on neighboring planes and the vector $\hat{f}_{ij}$ points along the projected bonds that run perpendicular to the blue triangular bonds in Figure 3.1.

The two dimensional Hamiltonian H_{2d} supports a variety of classical long range ordered phases. The ground state can be three sublattice 120° order, collinear stripe phases, and up-up-down phases. The ground state of $NaYbO_2$ derives from the 120° three sublattice order as no magnetic order is observed and the interplane H' further frustrates the system. The interplane J' works to further frustrate 120° order but does not frustrate

the other two dimensional phases and instead promotes full three dimensional magnetic ordering. Therefore, H_{2d} works with H' to form degenerate classical states that promote the formation of a quantum disordered ground state in $NaYbO_2$.

Assuming the ground state order in $NaYbO_2$ is based off of three sublattice 120° order, the governing two dimensional Hamiltonian reduces as accidental degeneracy of the compass model makes the J_{cz} terms vanish. The Hamiltonian can be rewritten as:

$$H = \sum_{\langle i,j \rangle} J_z S_i^z S_j^z + J_{xy}(S_i^x S_j^x + S_i^y S_j^y) - \sum_i \mu_B g_{\mu\nu} B^\mu S_i^\nu, \tag{3.6}$$

where $\mu, \nu = x, y, z$, $g_{\mu\nu} = \text{diag}(g_{xy}, g_{xy}, g_z)$. The onsite single ion term for this material is considered to be $D = 0$, and this Hamiltonian above will be used going forward. For full details of the theoretical background and study of this Hamiltonian, please see references [79] and [80].

This Hamiltonian supports different magnetic phases depending on the plane of anisotropy and external magnetic field. The phase diagram of anisotropy and field direction is shown in Figure 3.13. In the easy plane anisotropy regime where $A = (0, 1)$, a paramagnetic and canted-I ground state can arise.

$$\begin{cases} \frac{h_{xy}^2}{9} + \frac{h_z^2}{(1/A+2)^2} \geq 1: & \text{paramagnetic phase} \\ \frac{h_{xy}^2}{9} + \frac{h_z^2}{(1/A+2)^2} < 1: & \text{canted-I phase} \end{cases} \tag{3.7}$$

The paramagnetic phase has a singular ground state while the canted-I has degenerate ground states in a one dimensional manifold. In the easy axis anisotropy regime where $A > 1$, a paramagnetic, a Y phase, and a V phase can appear. The Y and V phases indicate the orientation of the three base spins generating the phases. The Y phase has all three spin orientations unique from each other while the V phase has two spins with the same orientation and one that is unique. The phase boundaries between these phases

with magnetic field is given by:

$$\begin{cases} \frac{h_{xy}^2}{(A+2)^2} + \frac{h_z^2}{(1/A+2)^2} \geq 1: & \text{paramagnetic phase} \\ \frac{h_{xy}^2}{(A+2)^2} + \frac{h_z^2}{(1/A+2)^2} < 1: & \text{V phase} \\ \text{and } h_z \geq h_{z,0}(A, h_{xy}) & \\ h_z \leq h_{z,0}(A, h_{xy}): & \text{Y phase} \end{cases} \tag{3.8}$$

The critical field $h_{z,0}$ is determined by the smallest positive nonzero solution to the following group of equations:

$$\begin{aligned} A(a+c-h_z)\sqrt{1-a^2} &= a(\sqrt{1-a^2}+\sqrt{1-c^2}-h_{xy}), \\ A(2a-h_z)\sqrt{1-c^2} &= c(2\sqrt{1-a^2}-h_{xy}), \\ c &= h_z - a^3(A^{-1}-1) - 2a. \end{aligned} \tag{3.9}$$

The parameters a and c indicate the three spin z components in the V phase.

As is detailed below, $NaYbO_2$ exhibits easy plane anisotropy of $J_{xy} = 0.51$ meV and $J_z = 0.45$ meV. The ground state therefore is the canted-I phase with critical fields

$$B_{z,\mathrm{c}} = 21.15\,\mathrm{T}, \qquad B_{xy,\mathrm{c}} = 12.03\,\mathrm{T} \tag{3.10}$$

between the canted-I and paramagnetic phases along the anisotropic crystallographic directions in the lattice. In comparison to the fit up-up-down magnetic structure in Figure 3.9, the canted-I ground state is not exactly the same. The canted-I does create states that are canted variants of the up-up-down structure. Either the strong remnant quantum fluctuations in $NaYbO_2$ promotes the collinear up-up-down refined phase or

the resolution of the experiment cannot resolve minor canting that would align with the canted-I phase.

Even though the refined up-up-down structure is not the exact ground state predicted in the classical phase diagram, the dynamics of the canted-I up-up-down and collinear up-up-down phase are similar. The spin wave spectra are only weakly influenced by minor canting from the collinear state. Reproducing the powder averaged spectra of Figures 3.15 and 3.14 required slight easy plane anisotropy of $J_{xy} = 0.51$ meV and $J_z = 0.45$ meV. These values were kept fixed and the variation of the calculated two step averaged dynamic spin structure factor in increasing external magnetic field is shown in Figures 3.17 and 3.18. The strong quantum fluctuations of $NaYbO_2$ likely heavily influences the spectral intensity outside of the field induced up-up-down ordered regime. Therefore, the spin wave calculations only validly resemble the spin waves of the up-up-down state between approximately $\mu_0 H = 3$ to 7 T.

There are three key features of the spin wave spectra that can be determined. First, gapless zero energy itensity originates from the magnetic zone center at all external magnetic fields. This is strongest at $\mu_0 H = 0$ T and originates from a Goldstone mode. The spectral weight pushes up to a small finite energy with increasing magnetic field and eventually dissipates by high fields of $\mu_0 H = 22$ T. This coincides with the canted-I ground state. The canted-I state has a Goldstone mode for a given set of external field orientation and magnitude within its one dimensional degenerate manifold. Once the critical in plane field $B_{xy,c}$ is reached near $\mu_0 H = 12.03$ T, the in plane modes become gapped. The out of plane modes do not become gapped until $B_{z,c} = 21.15$ T is reached. Once all of the Goldstone modes are gapped, the gapless modes disappear.

Second, the spectral intensity at zero momentum can be tracked with external field. There is minimal $Q = 0$ intensity at zero field that originates near 0.4 meV and follows and upward slope to a flat band near 0.8 meV. The $Q = 0$ intensity slowly rises and

flattens off with increasing external field and becomes part of the 1 meV flat mode at $\mu_0 H = 5$ T. As field further increases, the $Q = 0$ intensity follows its trend and continues to rise. Eventually, the $Q = 0$ intensity becomes a sharply falling dispersion after the Goldstone modes have been gapped out.

Finally, the model shows the field evolution of the flat mode observed on DCS and CNCS in the up-up-down ordered phase. The flat mode begins close to 0.8 meV at $\mu_0 H = 0$ T that diverges into two flat modes by $\mu_0 H = 3$ T at the up-up-down phase boundary. The upper mode resides close to 1.0 meV and coincides with the strong spectral intensity observed on DCS and CNCS. The lower mode becomes the top of the modes dispersing from the magnetic zone center and resides below 0.8 meV. As the external field is pushed higher, the spectral weight of the flat modes get renormalized into other modes and disappear. By $\mu_0 H = 9$ T, the flat modes cannot be seen in the calculated spin wave spectra.

3.4 Discussion

3.4.1 Crystalline electric field

The crystalline electric field (CEF) calculations of $NaYbO_2$ are shown in Figures 3.4, 3.5, 3.6 and Table 3.2. The CEF approximates the local single ion limit of Yb^{3+} ions in a D_{3d} environment. Two different fits were obtained for $NaYbO_2$, labeled fit 1 and fit 2. The two do not differ strongly in relative quality of their fits. The first fit, fit 1, however, has a slightly lower χ^2 value and the second fit, fit 2, is motivated by a point charge calculation for $NaYbO_2$. Another recent report on $NaYbO_2$ also calculated the CEF manifold of $NaYbO_2$ [14]. Their results also indicated a mixed m_j ground state doublet. However, their fit differs in that they used the magnetic susceptibility to calculate the

CEF instead of inelastic neutron scattering data. The analysis of magnetic susceptibility works well when free ion magnetic moments are not strongly perturbed by a mean field interaction. In other words, their fit differs since they fit the magnetic susceptibility without a θ_{CW} term. Overall, though, both fit 1 and the fit from [14] qualitatively share similar features, such as the mixed m_j ground state Kramers doublet.

Additionally, this work resolved splitting of the lowest CEF excitation in Figure 3.5. The splitting was modeled with two Gaussian peaks separated by about 2.1 meV. Effects from site mixing were estimated by incorporating chemical impurities into the point charge model in Table 3.3. Chemical distributions of Na^+ and Yb^{3+} show that disorder induces CEF shifts of at least 4 meV and multiple Kramers doublets shift with each impurity. This suggests that splitting of the lowest excitation by 2.1 meV would manifest in other peaks and at a larger magnitude. The resultion of the $E_i = 150$ and $E_i = 60$ meV ARCS measurements would have resolved this splitting. We cannot completely exclude chemical impurities on a small local scale producing this effect, but since the split peaks are nearly equivalent in integrated intensity, it would naively require a significant chemical impurity fraction in $NaYbO_2$. Our Rietveld refinement of the structure in Figure 3.3 did not indicate that such rampant chemical impurities existed.

Another explanation for the splitting of the E_1 excitation arises from strong antiferromagnetic exchange between Yb ions. The Yb ions are only 3.35 Åapart with $\theta_{CW} = -10.3$ K. There should be significant f orbital overlap that would create CEF dispersions of the single ion manifolds. This has been reported in other closely spaced Ln materials [157, 158]. At $E_i = 150$ meV, the splitting is not resolvable due to the resolution at this energy transfer. If all of the other excited states exhibit splitting on the order of 2.1 meV, this would also be outside of the resolution of the $E_i = 150$ meV experiment. The strong antiferromagnetic Curie-Weiss θ_{CW} suggests the origin of the dispersion is from exchange splitting. In comparison to other Yb materials like $YbMgGaO_4$ [48–50, 67–78],

the θ_{CW} is roughly twice as large. In $YbMgGaO_4$, exchange splitting is not resolved but other CEF environments from the mixing of Mg and Ga cations does arise.

3.4.2 Quantum disorder and magnetic order

Low energy zero field inelastic neutron scattering data reveals a continuum of excitations centered near the $Q = (1/3, 1/3, 0)$ magnetic zone center. The origin of this continuum derives from the highly frustrated quantum disordered ground state of $NaYbO_2$. The continuum has bandwidth of approximately 1 meV and is not consistent with a long range ordered state. For instance, the liner spin wave theory (LSWT) calculations show that at zero field there should not be a pile up of continuous spectral weight in Figure 3.17. Cuts of the data in Figure 3.19 also show that the excitions at zero field are gapless. The resolution of the experiment is 0.1 meV. However, the spectral weight is peaked at zero field near 0.25 meV and falls off until 1 meV. Together, these facts suggest that the continuum is partially gapped and partially gapless. This could happen, for example, through damped magnons that coexist with the continuum [159] or may just be an inherent feature of the continuum.

The most likely explanation for this continuum derives from the two dimensional triangular lattice quantum disordered models. Assuming $NaYbO_2$ contains ground state properties based off of 120° correlations, as explained in the results section, then it is likely connected to the spin liquid at a phase boundary of the classically ordered 120° phase space [160] with moderate J_{cz}. This indicates that the quantum disordered ground state of $NaYbO_2$ is related to the two dimensional triangular lattice model. The common spin liquid ground state in this instance is a U(1) Dirac state calculated with variation partions [161]. It contains gapless fermionic spinons and coincides with 2+1 dimensional quantum electrodynamics (QED) conformal field theory QED_3.

Additionally, a Dirac state predicts a quadratic relationship of C_p/T. This is shown in Figures 3.8 and 3.10 where the magnetic specific heat tail falls off as $T^2.04(2)$. There are two features in the specific heat above the tail, however, that could arise from other quantum disordered models. For instance, degenerate lines of spiral states in the zero field rhombohedral XXZ model [162] which contains two dimensional spin fluctuations in a three dimensionally coupled lattice. This state is referred to as the Rastelli-Tassi spiral state, but we do not observe spiral order in any other measurements. The field induced phase at $\mu_0 H = 5$ T suggests that the correlations in $NaYbO_2$ derive from 120° zero field correlations. Additionally, two specific heat peaks have been predicted in triangular [106] and kagome [107, 108]. The exact nature of the peaks heavily depends on the model employed and magnetic moments creating the quantum disordered phase. For example, the high temperature peak could indicate the formation of short range trimers and doublet states with subsequent low temperature quantum spin liquid state [106]. The peaks could also indicate the onset of gapped chiral fluctuations in the short range upper peak [163], where the ratio of the specific heat locations in the spin 1/2 version of this model predict $T_l/T_h \sim 0.36$, and this is consistent with what is observed for $NaYbO_2$. However, this model predicts $J \sim 5$ K, which is half of the observed θ_{CW} for $NaYbO_2$.

Under an external magnetic field, the classical degeneracy of the 120° Hamiltonian is lifted. Correlations in the 120° phase are primarily inside of the *ab* crystallographic plane that are strongly influenced by an external field. In fact, the quantum XXZ model predicts a plateau at 1/3 the saturated magnetization [150, 164] as the magnetic field helps stabilize a long range ordered ground state. In $NaYbO_2$, reports indicate the saturated powder averaged magnetization is near $\mu_0 H = 14$ T [14], meaning that the 1/3 plateau is at $\mu_0 H = 5$ T which is the ordered up-up-down regime. This also corresponds to the plateau in a.c. susceptibility measurements versus field in Figure 3.8 where χ' is quenched and the field regime where elastic neutron scattering resolved the collinear

up-up-down structure nearly parallel to the $< 1, -1, -1 >$ direction. The up-up-down phase begins to appear near $\mu_0 H = 2.75$ T in low energy inelastic neutron scattering data. A low energy flat band appears in Figure 3.15 that then increases up to the $\mu_0 H =$ 5 T 1.0 meV band. This follows the LSWT model for the canted-I state. At higher field, the mode softens as second ordered phase begins to appear. Nuclear magnetic resonance (NMR) measurements [81] have shown that a second phase near 70% of the saturated magnetization appears at $\mu_0 H = 9.5$ T. This is likely the V phase induced by a magnetic field from the ground state canted-I.

Furthermore, upon entering the high field phase and then approaching the up-up-down phase, hysteresis in the $Q = (1/3, 1/3, 2)$ peak appears. This is a highly first order phase transition as there is irreversibility in the orientation of the up-up-down phase. The exact form of this phase boundary will require single crystal analysis, but the orientational dependence indicates that the interplane coupling could be influencing the up-up-down phase, which is consistent with numerical mean field models [155]. Appearance of the $Q = (1/3, 1/3, 2)$ peak that unlocks the orientational dependence of the up-up-down phase further suggests that the high field phase is noncollinear. Together with the NMR reports, it is likely the V phase, but single crystal measurements of this hysteretic regime would be able to confirm this model.

The final low energy inelastic neutron scattering feature is the 1.5 meV E$*$ mode in Figures 3.15 and 3.19. This mode appears above the single magnon cuttoff for $NaYbO_2$ in the canted-I state and is well resolved at $\mu_0 H = 5$ T. Two other modes at $\mu_0 H = 5$ T are present at 0.5 meV and 1.0 meV, suggesting E* is a convolution of the two and results from multi magnon interactions. This idea aligns with $NaYbO_2$ exhibiting strong quantum fluctuations in the ordered phase that transfer scattering weight to longitudinal spin fluctuations in multi magnon modes.

Other materials like $Ba_3CoSb_2O_9$ [103–105] and Cs_2CuBr_4/Cs_2CuCl_4 [136, 145, 146]

also show a magnetization plateau near 1/3 saturated magnetization. The stacking of their triangular lattices, however, is unfrustrated AAA three dimensionally. In fact, the layer separation in the $Ba_3CoSb_2O_9$ and related materials is also significantly further than in $NaYbO_2$, meaning that interlayer interactions are less significant. The fact that these materials do not have interlayer interactions but still exhibit the magnetization plateau from a two dimensional XXZ model offer insight into how $NaYbO_2$ behaves. In other words, $NaYbO_2$ primarily is influenced by its two dimensional XXZ Hamiltonian and is somewhat influenced by three dimensional frustration. This leads to the etra E^* mode in $NaYbO_2$ that is not present in the other magnetization plateau materials. We expect that the additional three dimensional frustration has a twofold purpose of inhibiting long range order and pulling $NaYbO_2$ out of th purely two dimensional regime where long order is naturally precluded by low dimensionality.

3.4.3 Other $ALnX_2$ materials

$NaYbO_2$ is just one triangular lattice antiferromagnet in the $ALnX_2$ family of materials. A number of other systems have been reported to exhibit similar quantum disordered phenomena. Two other prominent members are $NaYbS_2$ [83, 86, 87] and $NaYbSe_2$ [85] that have Yb^{3+} ions in the same type of D_{3d} local environment as $NaYbO_2$. Their CEF interactions are weaker, however, due to the more dispersed S^{2-} and Se^{2-} anions relative to O^{2-} anions. In turn, this alters their Kramers doublet ground states, but at low temperatures they still form $J_{eff} = 1/2$ isolated doublets. Other Ln cations also can exhibit this property on this triangular lattice. For example, the following section will cover $KCeO_2$, but other Ce materials [12] and Er materials [165] have been reported. There is a vast potential for modifying the XXZ Hamiltonian presented here for $NaYbO_2$ and its inherent anisotropies simply by swapping the Ln ion responsible for the magnetic

correlations. The entire $ALnX_2$ family is also large and many of these compounds are known to exist.

3.5 Conclusions

$NaYbO_2$ is a promising quantum spin liquid candidate material. It contains strongly geometrically frustrated antiferromagnetically coupled Yb moments on an equilateral triangular lattice and does not magnetically order under zero field to 50 mK. The local Yb environment produces a well separated $J_{eff} = 1/2$ Kramers doublet ground state with a heightened g factor and heavily mixed m_j character. Strong correlations further split the crystalline electric field environment, producing a split first excited state on the order of 2 meV. These correlated Yb moments exhibit a continuum of excitations extending up to 1 meV that originate from the $Q = (1/3, 1/3, 0)$ magnetic zone center. Under an external field, $NaYbO_2$ evolves into an ordered up-up-down long range magnet as seen in elastic neutron scattering. The interplay of external field and XXZ anisotropy indicates that the ground state of $NaYbO_2$ is primarily generated by 120° correlations. Our linear spin wave theory models capture the ordered state with slight easy plane anisotropy. A feature above the single magnon cutoff appears suggestive of strong multimagnon interactions. At high external magnetic fields, the ordered phase begins to disappear as a second ordered phase is approached that creates a hysteretic orientational dependence on the up-up-down state.

The strong interplay of magnetic field and quantum disorder in $NaYbO_2$ make it a prime material for exploring correlated systems with accessible critical phase boundaries. However, not everything about $NaYbO_2$ is known. First and foremost, single crystal growth of this material has proven quite difficult, as will be discussed in Appendix B. Furthermore, the origin of the hysteresis behavior, reduced ordered moment size, and free

Yb spins are not fully understood. Single crystals would be imperative to exploring these features of $NaYbO_2$. While single crystal synthesis attempts of $NaYbO_2$ are underway, other $R\bar{3}m$ materials with ABC three dimensionally frustrated triangular lattices could additionally be studied. The chemical tunability across all three elements in the $ALnX_2$ system allows for a deeper delve into the behavior of frustrated triangular lattice materials and their local magnetic ion dependence.

T		300 K					1.6 K				
λ		1.5399 Å					2.0774 Å				
$a = b$		3.35185(3) Å					3.34556(3) Å				
c		16.5319(3) Å					16.4559(3) Å				
Atom	Wyckoff	x	y	z	U_{iso} (Å^2)	Occupancy	x	y	z	U_{iso} (Å^2)	Occupancy
Yb	3a	0	0	0	0.54(2)	1.000(2)	0	0	0	0.53(1)	1.000(2)
Na	3b	0	0	0.5	1.59(7)	0.996(6)	0	0	0.5	0.85(5)	1.000(6)
O	6c	0	0	0.26355(6)	0.83(3)	0.999(3)	0	0	0.26423(6)	0.53(2)	1.000(2)

Table 3.1: Parameters extracted from Rietveld refinements of $NaYbO_2$ elastic neutron powder diffraction data collected on BT-1 at 1.6 K and 300 K. No structural changes or significant refinable chemical impurities are observed.

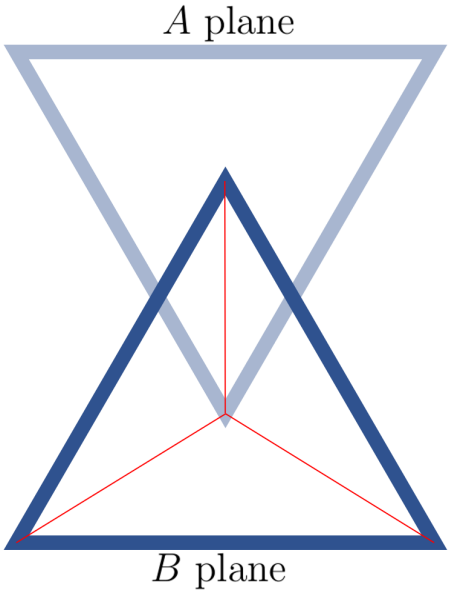

Figure 3.1: In the $ALnX_2$ materials family, the $R\bar{3}m$ space group contains ABC stacking of triangular lattice planes. Projecting one plane A onto the next B along the c axis places the projected vertices of A at the center of the triangles of B (similarly for B to C or C to A). This is pictorially represented here, where the blue triangles contain the original two dimensional geometric frustration and the projected triangle generates three new equivalent red bonds for further geometric frustration.

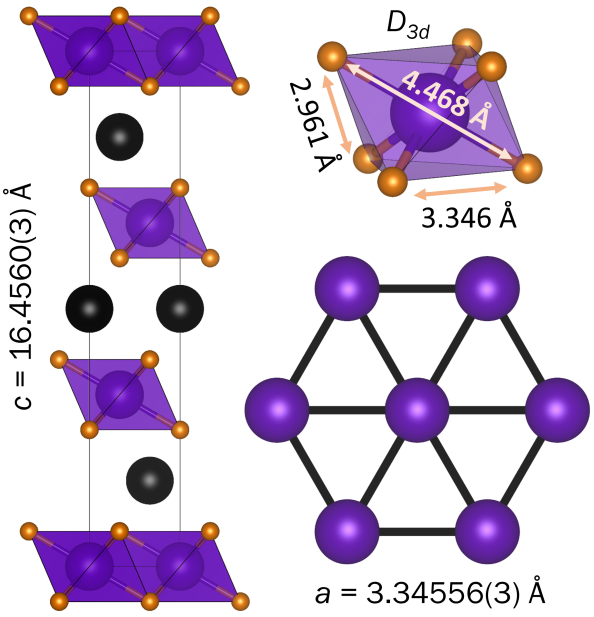

Figure 3.2: $NaYbO_2$ (Yb: purple, O: orange, Na: black) at 1.6 K contains equilateral triangular planes of D_{3d} trigonally compressed YbO_6 octahedra. Three Yb layers are stacked between Na monolayers. Within experimental resolution, all sites are fully occupied without site mixing.

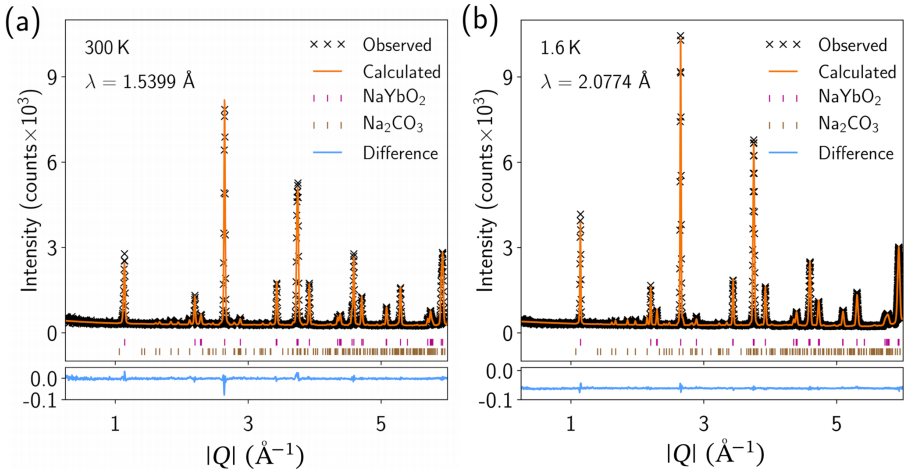

Figure 3.3: Elastic neutron powder diffraction of $NaYbO_2$ collected on BT-1 at NCNR at a) 300 K and b) 1.6 K. The orange line is the overall Rietveld fit to the data and blue line is the difference between the observed data and the fit. Pink dashes correspond to the main $NaYbO_2$ phase and brown are from a small amount of Na_2CO_3 in the sample of 4.1% by mass. As described in the synthesis, the Na_2CO_3 impurity is nonmagnetic and cannot be removed without washing the sample which introduces impurities into the main $NaYbO_2$ phase.

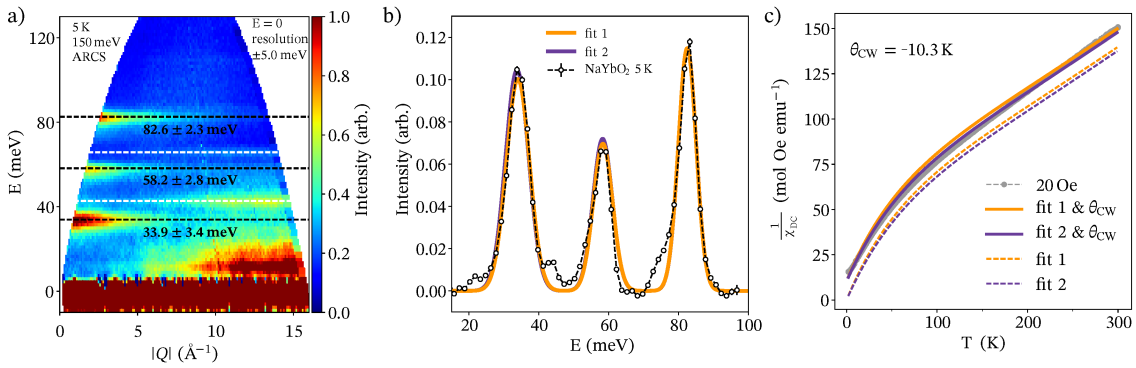

Figure 3.4: a) Color plot of the inelastic neutron scattering spectrum $S(Q, \hbar\omega)$ collected on $NaYbO_2$ with incident neutrons of $E_i = 150$ meV at $T = 5$ K on the ARCS spectrometer. The dashed black lines represent the centers of the crystalline electric field excitations from the ground state Kramers doublet. Error bars represent the full width half maximum (FWHM) of the instrumental resolution at the specified energy transfer. Strong phonons observed in E cuts are highlighted with dashed white lines. b) An E cut of the data in panel a) integrated from $|Q| = [3.0, 3.5]$ Å^{-1} overplotted with two crystalline electric field model fits to the data. Fit 1 has the lowest overall χ^2 value but fit 2 also captures the data quite well. Fit 2 contains Stevens parameters with values closer to a point charge model with a physical basis in Table 3.3. c) With Mantid Plot [13], the inverse magnetic susceptibilities of the two fits were calculated and overplotted with the data collected on $NaYbO_2$ at $\mu_0 H = 20$ Oe. The dashed lines are the data without incorporating an effective magnetic exchange in θ_{CW} while the solid lines include $\theta_{CW} = -10.3$ K.

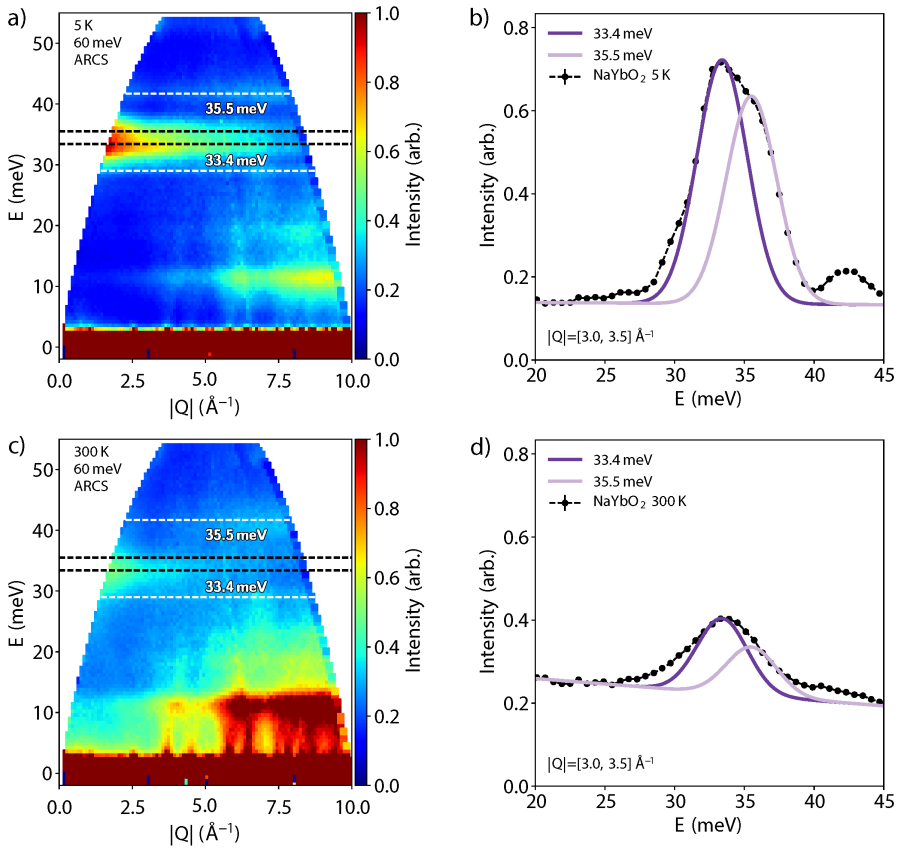

Figure 3.5: a) Color plot of the inelastic neutron scattering spectrum collected on $NaYbO_2$ with incident neutrons of $E_i = 60$ meV at $T = 5$ K on the ARCS spectrometer. The dashed black lines correspond to the two centers of the two peaks used to model the broadening of the lowest energy CEF mode in $NaYbO_2$ in panel b). The dashed white lines correspond to strong phonons that are nearby the CEF mode. b) An E cut of the data integrated from $|Q| = [3.0, 3.5]$ Å^{-1} is plotted with two Gaussian peaks centered at 33.4 and 35.5 meV. These two peaks capture the broadening of the lowest CEF mode, likely cased by exchange splitting from the strongly antiferromagnetically coupled Yb moments. The two peaks are separated by 2.1 meV. c-d) At 300 K, the splitting in the lowest energy CEF mode is still apparent. The same Gaussian peaks with the same energies are used to model the splitting. The model in panel d) reduces the scale factor of the model in panel b).

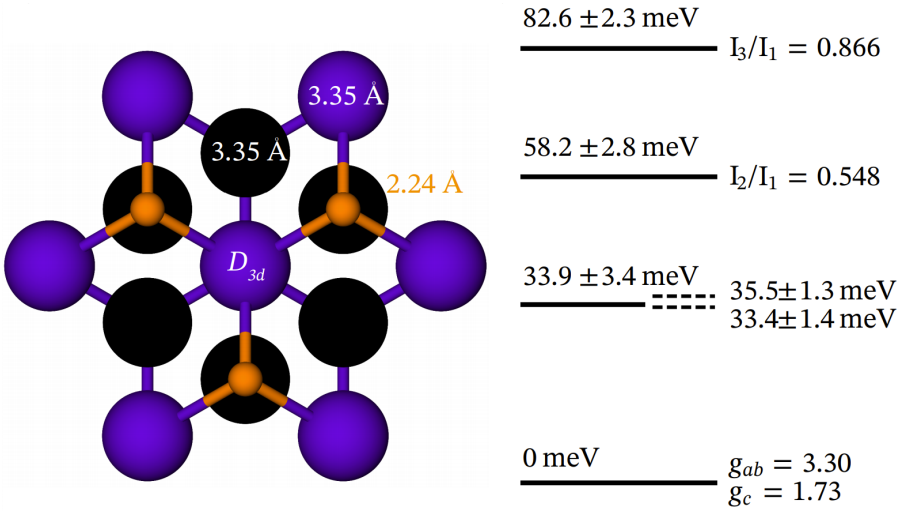

Figure 3.6: Looking down the c axis of $NaYbO_2$, the differing point charge model environments generating the ground state multiplet splitting can be observed. The first local environment is the D_{3d} YbO_6 octahedral environment where the closest shell of O^{2-} anions reside 2.24 Åaway from the central Yb^{3+} ion. The second shell expands to the nearest Na^{+} cations that reside three in a plane above and three in a plane below the central Yb. A third shell incorporates the nearest neighbor Yb^{3+} cations at a distance 3.35 Å, which is equal to the a lattice parameter. These differing ionic shells are the primary influence of the ground state multiplet splitting of the $J = 7/2$ Yb ions. The observed multiplet structure, instrumental resolutions, intensity ratios, and ground state g factor components are shown on the right. The two dashed lines of the first multiplet represent the splitting observed in Figure 3.5.

Table 3.2: The crystalline electric field fits for $NaYbO_2$ and point charge model calculations simulating the local Yb environment. Data is extracted from E cuts to a high energy inelastic neutron scattering spectrum from ARCS at ORNL with $E_i = 150$ meV. The g factor components were determined with EPR in Figure 3.7. The two point charge models increase the number of neighboring ions surrounding a central Yb ion, where PC 3.0 Åincludes six O^{2-} anions and PC 3.5 Åadditionally includes nearest-neighbor Yb^{3+} and Na^{+} cations. The two fits differ in that fit 1 has a better χ^2 value but fit 2 resembles PC 3.5 Å.

	E_1	E_2	E_3	$\frac{I_2}{I_1}$	$\frac{I_3}{I_1}$	g_c	g_{ab}	χ^2	B_2^0	B_4^0	B_6^0	B_4^3	B_6^3	B_6^6
PC (3.0 Å)	70.5	146.4	191.5	0.037	0.033	7.86	0.36	342.0	-5.0675	0.016956	0.00015465	-0.64149	-0.00034913	0.0014353
PC (3.5 Å)	19.2	35.8	87.5	0.588	0.061	0.83	3.44	16.5	1.6302	0.020578	0.00017436	-0.66203	-0.00022040	0.0017501
Fit 1	34.0	58.4	82.5	0.579	0.880	1.70	3.38	0.005	-0.79877	0.00085658	0.0028000	0.51143	0.011036	0.015580
Fit 2	33.8	58.3	82.5	0.574	0.845	1.68	3.48	0.012	0.28257	0.0058508	-0.00055392	-0.76448	-0.010493	0.025079
Observed	33.9	58.2	82.6	0.548	0.866	1.72	3.30							

Fit 1:

$$|\omega_{0,\pm}\rangle = -0.029|\mp 1/2\rangle \mp 0.496|\pm 1/2\rangle - 0.578|\mp 5/2\rangle \pm 0.034|\pm 5/2\rangle \mp 0.038|\mp 7/2\rangle + 0.646|\pm 7/2\rangle$$
$$|\omega_{1,\pm}\rangle = -0.001|\mp 1/2\rangle \mp 0.473|\pm 1/2\rangle + 0.805|\mp 5/2\rangle \mp 0.002|\pm 5/2\rangle \mp 0.001|\mp 7/2\rangle + 0.358|\pm 7/2\rangle$$
$$|\omega_{2,\pm}\rangle = \pm 0.025|\mp 1/2\rangle + 0.727|\pm 1/2\rangle \pm 0.128|\mp 5/2\rangle - 0.004|\pm 5/2\rangle - 0.023|\mp 7/2\rangle \pm 0.673|\pm 7/2\rangle$$
$$|\omega_{3,\pm}\rangle = \pm 0.614|\mp 3/2\rangle + 0.789|\pm 3/2\rangle$$

Fit 2:

$$|\omega_{0,\pm}\rangle = 0.075|\mp 1/2\rangle \pm 0.582|\pm 1/2\rangle - 0.528|\mp 5/2\rangle \pm 0.068|\pm 5/2\rangle \mp 0.078|\mp 7/2\rangle + 0.604|\pm 7/2\rangle$$
$$|\omega_{1,\pm}\rangle = 1|\pm 3/2\rangle$$
$$|\omega_{2,\pm}\rangle = \mp 0.574|\mp 1/2\rangle - 0.034|\pm 1/2\rangle \mp 0.047|\mp 5/2\rangle + 0.803|\pm 5/2\rangle + 0.149|\mp 7/2\rangle \mp 0.009|\pm 7/2\rangle$$
$$|\omega_{3,\pm}\rangle = -0.004|\mp 1/2\rangle \mp 0.570|\pm 1/2\rangle + 0.263|\mp 5/2\rangle \mp 0.002|\pm 5/2\rangle \mp 0.005|\mp 7/2\rangle + 0.779|\pm 7/2\rangle$$

Table 3.3: The point charge model in equation 1.24 was used to approximate the effect of chemical disorder on the crystalline electric field energies in $NaYbO_2$. The ideal point charge model of two shells is 3.5 Åand is close to fit 2 presented in Figure 3.4. Altering the local environment was produced by swapping one or more Na^{+} cations with Yb^{3+} cations, as this is a common chemical impurity as is found in $NaTiO_2$ in Appendix A. These local swaps heavily influence the crystalline electric field states of the central Yb ion, and help show that the splitting of the lowest mode in $NaYbO_2$ of 2.1 meV is not likely caused by these drastic local alterations. Significant chemical disorder would generate numerous new excitations.

	E_1	E_2	E_3
PC (3.5 Å)	19.2	35.8	87.5
PC one Na on Yb site	34.2	62.6	97.8
PC one Yb on Na site	23.8	62.5	94.2
PC one Na and Yb site swap	24.9	76.0	130.2
PC two Na on Yb site	47.3	91.1	159.4
PC two Yb on Na site	36.4	50.7	102.1
PC two Na and Yb site swaps	24.3	96.0	200.9

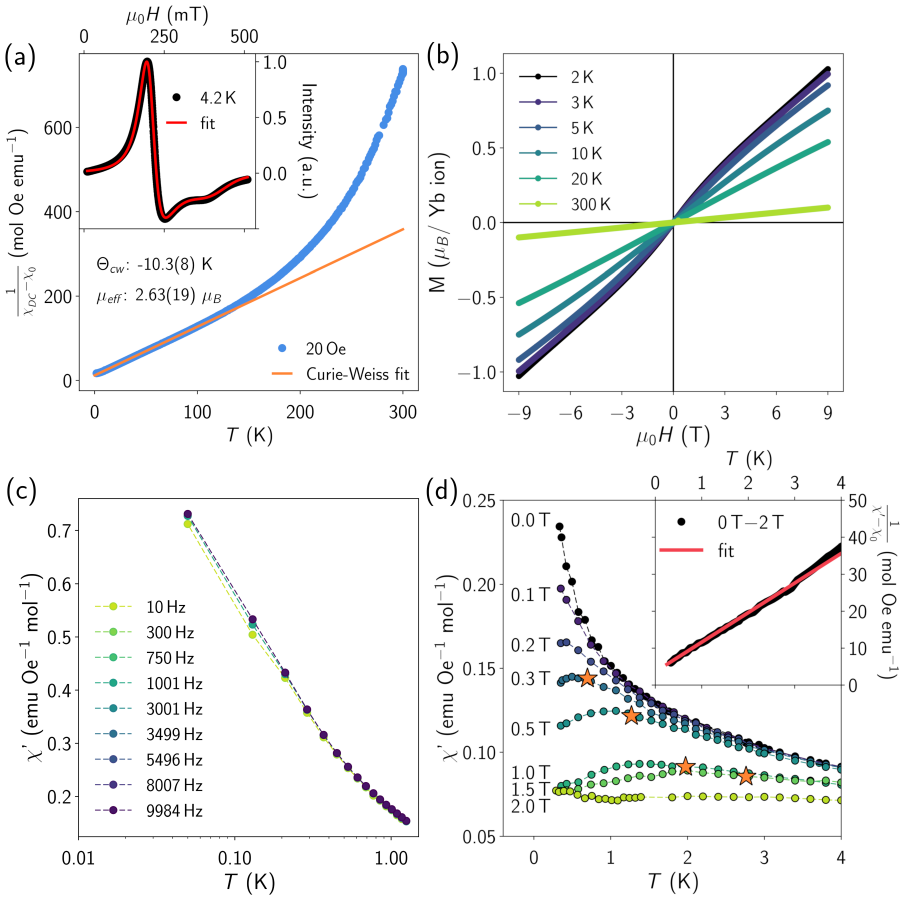

Figure 3.7: a) The magnetic susceptibility of the ground state Kramers doublet of $NaYbO_2$ can be approximated with a Curie-Weiss fit to $mu_0H = 20$ Oe magnetic susceptibility data between 20 to 100 K. The Curie-Weiss $\theta_{CW} = -10.3$ K is relatively strong for $4f$ magnetic systems due to the close Yb-Yb spacing of ~ 3.35 Å. The effective moment in the ground state Kramers doublet is $2.63(19)\mu_B$, corresponding to a $J_{eff} = 1/2$ moment with a heightened g factor. Inset: The g factor components were determined by modeling EPR data collected at 4.2 K. The values are $g_{//} = 1.726(9)$ and $g_{\perp} = 3.294(8)$. b) Isothermal magnetization from $\mu_0 H = [-9, 9]$ T at $T = 2, 5, 10, 20, 300$ K show that the Yb moments begin to polarize at high fields. Other reports [14] show that fields near $\mu_0 H = 14$ T are required to saturate the moments. c) A.c. susceptibility data from 50 mK to 4 K under varying frequencies shows no frequency dependence that would indicate glassy behavior or long range magnetic order of Yb moments. d) A.c. susceptibility data with increasing external magnetic field shows how the initially increasing $\chi'(T)$ signal turns over and flattens off by $\mu_0 H = 2$ T. The inflection of the turnover in orange stars is where excess free moments are Zeeman split and quenched in an external field. Inset: Subtracting the flat $\mu_0 H = 2$ T data from the $\mu_0 H = 0$ T data reveals a Curie-Weiss dependence of the free moments akin to the high temperature Curie-Weiss fit.

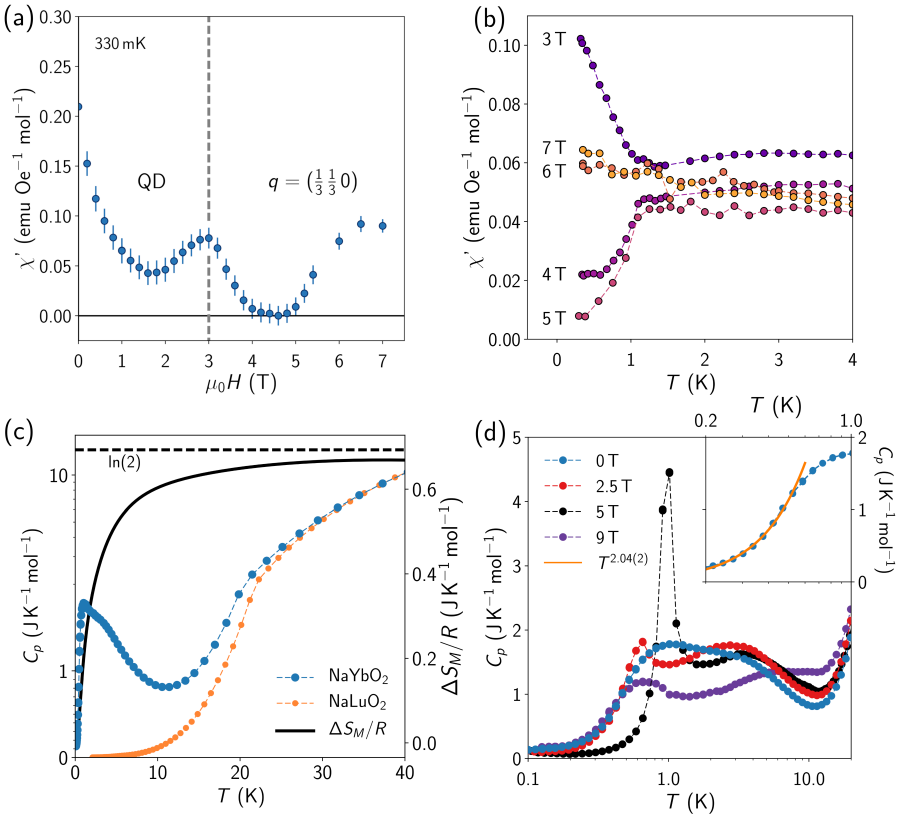

Figure 3.8: a) A.c. susceptibility data versus field at 330 mK initially decreases with increasing field to 2 T. The susceptibility then increases to a phase boundary at $\mu_0 H = 3$ T and approaches $\chi'(H) = 0$ between $\mu_0 H = [4, 5]$ T. This coincides with the onset of long range magnetic order with wave vectors $k_1 = (1/3, 1/3, 0)$ $k_2 = (0, 0, 0)$ observed in elastic neutron scattering refinements at $\mu_0 H = 5$ T. The value of $\chi'(H)$ increases out of the ordered phase and approaches another phase boundary near $\mu_0 H = 7$ T that is not fully resolved in this experiment. As mentioned in the text, the second phase may be a canted V phase. b) A continuation of Figure 3.7d) shows the evolution of $\chi'(T)$ with increasing external magnetic field. Strong inflections near $T = 1$ K coincide with the onset of magnetic order under an external field. c) Specific heat of $NaYbO_2$ (blue) overplotted with nonmagnetic analogue $NaLuO_2$ (orange). The integrated C_p/T difference in the two curves represents the magnetic entropy of $NaYbO_2$ plotted on the right hand axis. The entropy ΔS_M approaches 95% $Rln(2)$. d) Specific heat of $NaYbO_2$ under varying external magnetic fields. Two broad features in the specific heat at $\mu_0 H = 0$ T centered near 1 K and 3 K evolve in an external field. The lower feature sharpens into a peak at $\mu_0 H = 5$ T that corresponds to long range up-up-down magnetic order. The upper feature remains broad and is a result of short range correlations. Inset: The tail of $\mu_0 H = 0$ T data can be fit to a power law $T^{2.04(2)}$ after removing the heat capacity of nuclear moments below 100 mK shown in Figure 3.10c).

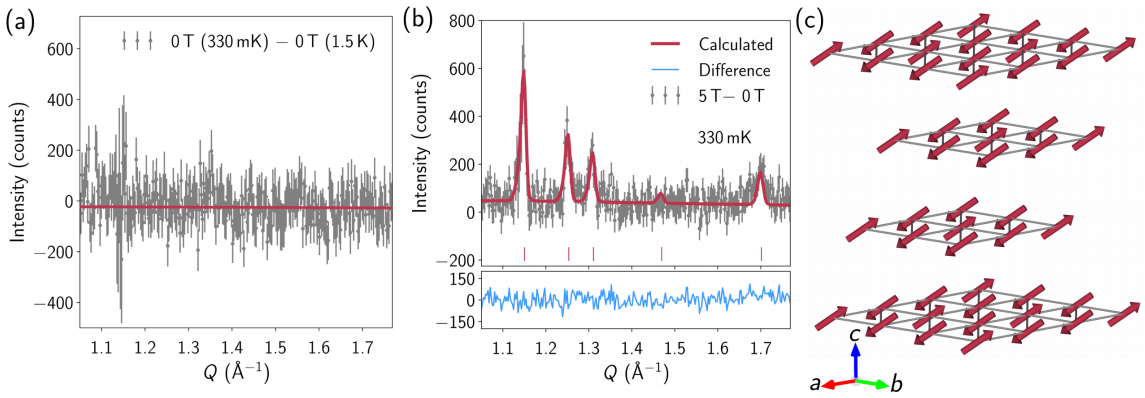

Figure 3.9: a) Subtracted 330 mK minus 1.5 K elastic neutron scattering data from BT-1 at NCNR at $\mu_0 H = 0$ T. The red line is a constant background term fit to the subtracted data. Within resolution, no new magnetic Bragg reflections are resolvable. b) However, under $\mu_0 H = 5$ T at 330 mK, the subtracted data reveal four new magnetic Bragg reflections. They can be indexed to double ordering wave vectors $k_1 = (1/3, 1/3, 0)$ $k_2 = (0, 0, 0)$. The red line corresponds to the best fit of the data, which is highly restricted by the absence of resolvable intensity at $Q = (1/3, 1/3, 2)$. The size of the Yb moment is refined to 1.36(10) μ_B. c) A model representation of the best fit is the equal moment up-up-down magnetic structure pinned nearly parallel to the $< 1, -1, -1 >$ direction. It has symmetrically equivalent variants generated by a three fold rotation along the c axis, and they are shown in Figure 3.11.

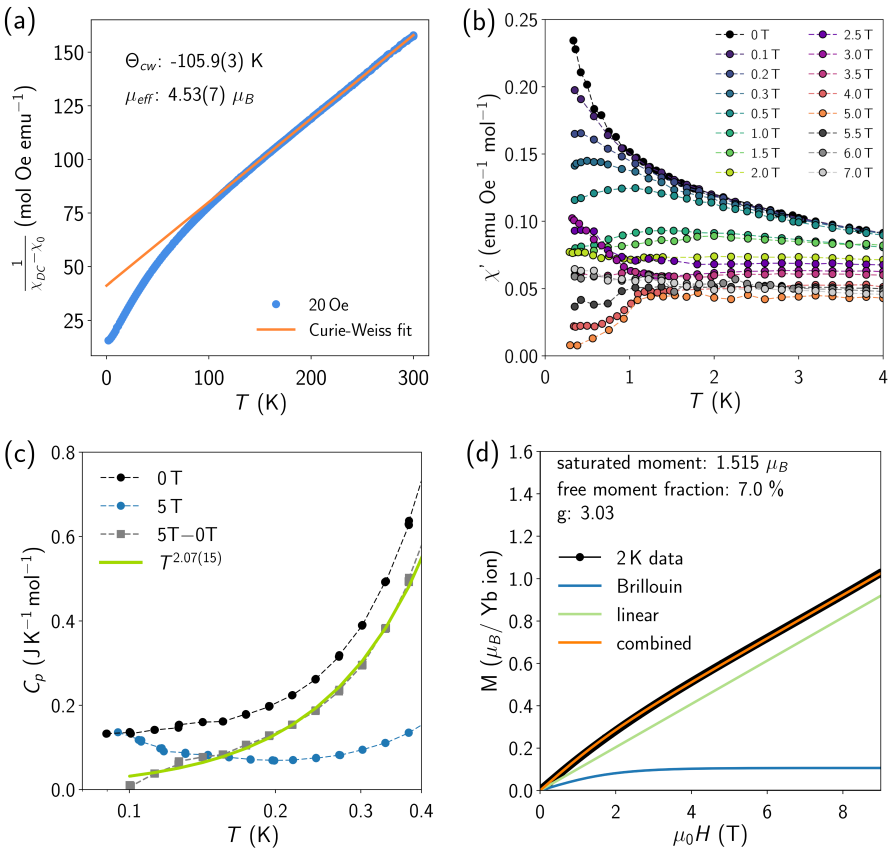

Figure 3.10: a) In comparison to Figure 3.7a), the magnetic susceptibility of $NaYbO_2$ is fit to the Curie-Weiss law in the high temperature regime from 200 K to 300 K generates a θ_{CW} an order of magnitude larger and μ_{eff} close to the free ion $J = 7/2$ value of 4.54 μ_B. However, this large linear regime is not representative of the correlations of the ground state Kramers doublet of $NaYbO_2$. The shift upwards in Curie-Weiss temperature θ_{CW} and curvature in the blue data just below the orange line Curie-Weiss fit results from change in population of Kramers doublets in the crystalline electric field. This figure is included to illustrate that linear regimes do not always mean the Curie-Weiss law is valid. b) A.c. susceptibility continued from Figure 3.7b) with all external magnetic field data collected overplotted. c) The specific heat data in Figure 3.8d) for $NaYbO_2$ contain influences from nuclear moments below 400 mK. The nuclear anomaly is centered around 100 mK, as both the $\mu_0 H = 0$ T (black) and 5 T (blue) approach the same value at 100 mK. To determine the power law relationship for the specific heat tail of Yb magnetism in $NaYbO_2$, the green power law line was fit to subtracted 0 T minus 5 T data. d) Elastic neutron powder diffraction data collected on BT-1 at $\mu_0 H = 7$ T subtracting out the $\mu_0 H = 0$ T 1.5 K data. The up-up-down magnetic reflections still appear, but are significantly weaker as the phase approaches the high field phase boundary.

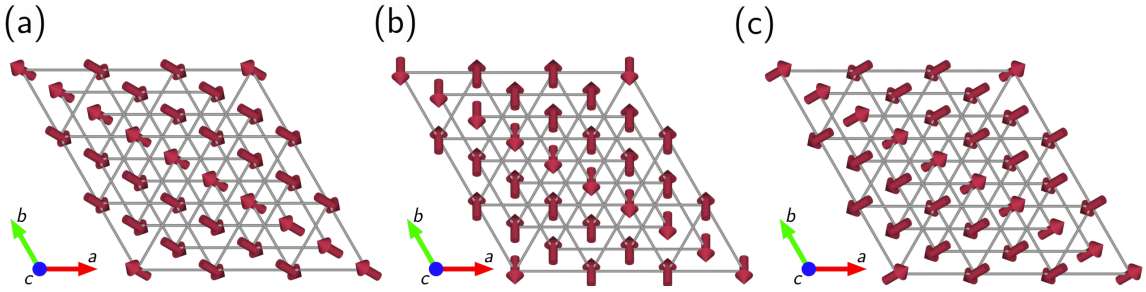

Figure 3.11: The refined up-up-down magnetic structure at $\mu_0 H = 5$ T (when approached from $\mu_0 H = 0$ T) has three equivalent representations. These three structures in a) to c) are all symmetry related equal moment up-up-down structures with 1.34(20) μ_B Yb moments. a) The top-down view of the $< 1, -1, -1 >$ direction structure with $k_1 = (1/3, 1/3, 0)$ and $k_2 = (0, 0, 0)$ from Figure 3.9c). b) The version where Yb moments align to $< 1, 2, -1 >$ direction with $k_1 = (2/3, -1/3, 0)$ and $k_2 = (0, 0, 0)$. c) The final version with Yb moments near $< -2, -1, -1 >$ direction with $k_1 = (1/3, -2/3, 0)$ and $k_2 = (0, 0, 0)$.

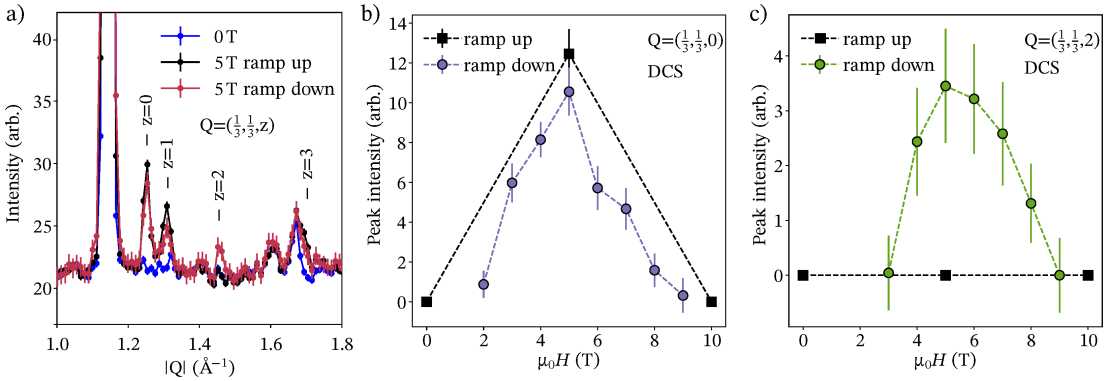

Figure 3.12: a) Inelastic neutron powder diffraction data collected on DCS at NCNR integrated over the elastic line from $E = [-0.1, 0.1]$ meV at 67 mK reveals the magnetic Bragg reflections that appear at $\mu_0 H = 5$ T. However, there is a hysteretic dependence of these reflections. As shown in Figure 3.9b), the $Q = (1/3, 1/3, 2)$ reflection is not resolvable which locks the up-up-down magnetic structure to the $< 1, -1, -1 >$ direction. If the up-up-down phase is approached from $\mu_0 H = 10$ T (red) instead of $\mu_0 H = 0$ T (black), the $Q = (1/3, 1/3, 2)$ reflection contains intensity. b) The integrated intensity of the change in the $Q = (1/3, 1/3, 0)$ is tracked by fitting the peak to a Gaussian at each external magnetic field collected. Overall, the intensity is maximal in the ordered up-up-down state no matter whether the phase is approached from high field or zero field. c) Tracking the intensity of the $Q = (1/3, 1/3, 2)$ reflection shows that no intensity appears until the up-up-down phase is approached from the high field side of the ordered phase. Intensity here is maximal at the same central maximum of the $Q = (1/3, 1/3, 0)$ reflection near $\mu_0 H = 5$ T.

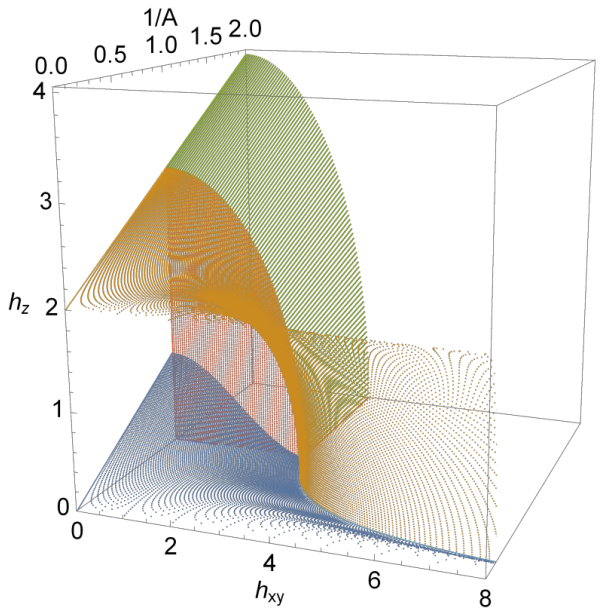

Figure 3.13: One octant of the classical phase diagram of the two dimensional XXZ Hamiltonian of the triangular lattice in 3.6. The ground state of this system evolves into multiple phases depending on the XXZ anisotropy A and external field components $h_{xy} = \sqrt{h_x^2 + h_y^2}$ and h_z. The dotted surfaces separate the classical phases and easy plane / easy axis regions, and the conditions for the phases are described in the main text. Blue: Y to V phase; red: $A <$ to $A > 1$; green: canted-I to paramagnetic with $A < 1$; orange: V to paramagnetic with $A > 1$.

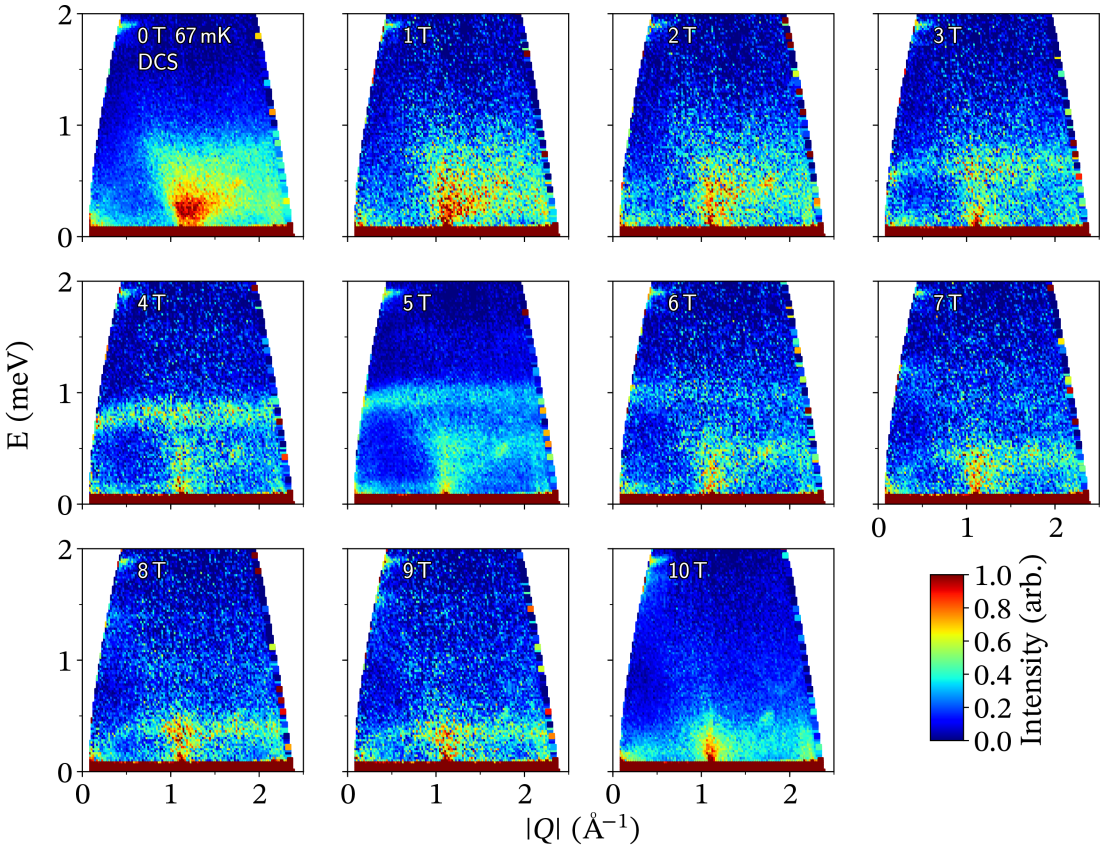

Figure 3.14: Low energy inelastic neutron scattering data $S(Q, \hbar\omega)$ from DCS at NCNR collected for $NaYbO_2$ at 67 mK. Integer steps in external field show the broad continuum of excitations at $\mu_0 H = 0$ T develop a flat band near 1 meV at $\mu_0 H = 5$ T that falls back into the elastic line at $\mu_0 H = 10$ T. The ordered regime corresponds to the up-up-down phase in $NaYbO_2$. Data at $\mu_0 H = 0$, 5, and 10 T were measured with scans six time the length of the others to maximize statistical resolution. The DCS spectrometer contains spurious signals at $[Q, E] = [0.5, 1.8]$ and $[1.75, 0.4]$ that do not originate from the sample.

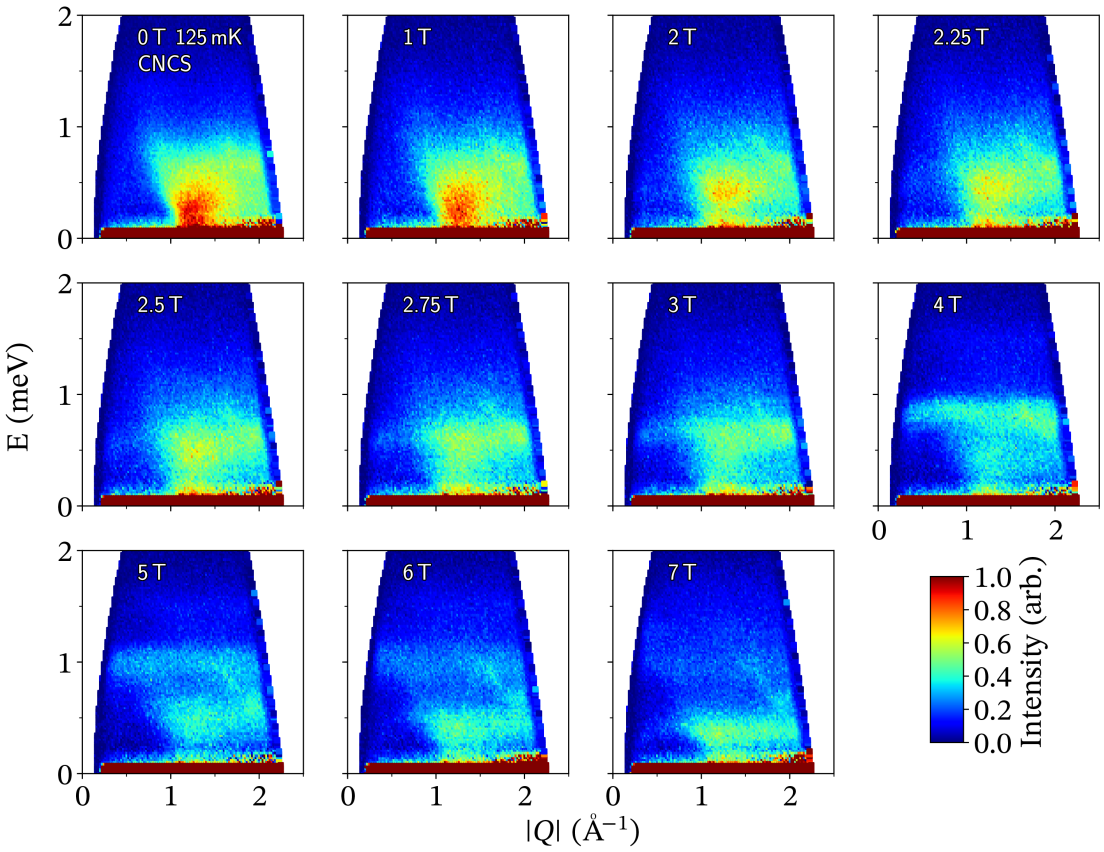

Figure 3.15: Low energy inelastic neutron scattering data $S(Q, \hbar\omega)$ from CNCS at ORNL collected for $NaYbO_2$ at 125 mK and $E_i = 3.32$ meV. The high flux instrument duplicates the observed results in Figure 3.14. A new feature is observed near 1.5 meV at $\mu_0 H = 4$ to 7 T called E*. This mode arises from multimagnon scattering of the two lower modes near 0.5 meV and 1.0 meV. Cuts of this data set is presented in Figure 3.19.

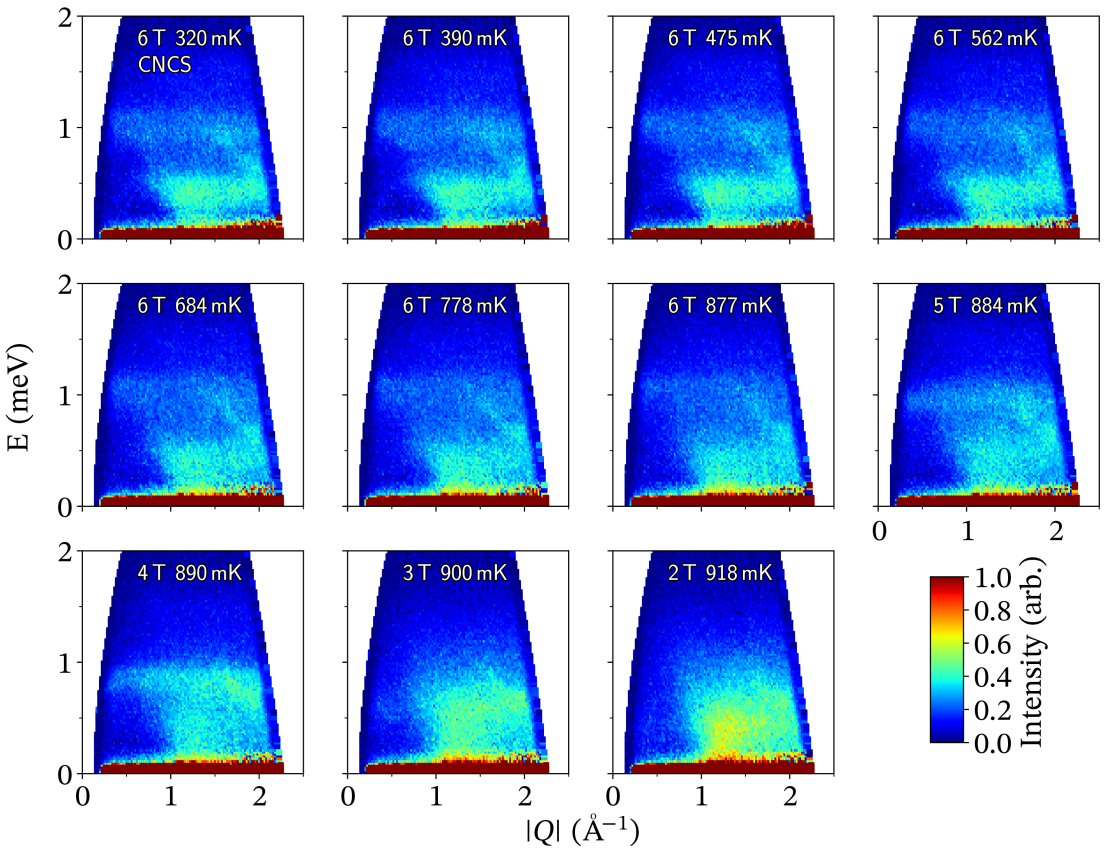

Figure 3.16: Low energy inelastic neutron scattering data $S(Q, \hbar\omega)$ versus temperature from CNCS at ORNL collected for $NaYbO_2$ at 125 mK and $E_i = 3.32$ meV. The boundaries of the up-up-down phase are tracked with temperature and field dependence of the flat 1.0 meV mode. Constant field $\mu_0 H = 6$ T versus increasing temperature show the flat 1.0 meV mode remains stable while the spectral weight below 0.5 meV falls into the elastic line. From $\mu_0 H = 6$ to 3 T, the flat 1.0 meV mode collapses with $T = 900$ mK at the boundary of the up-up-down phase.

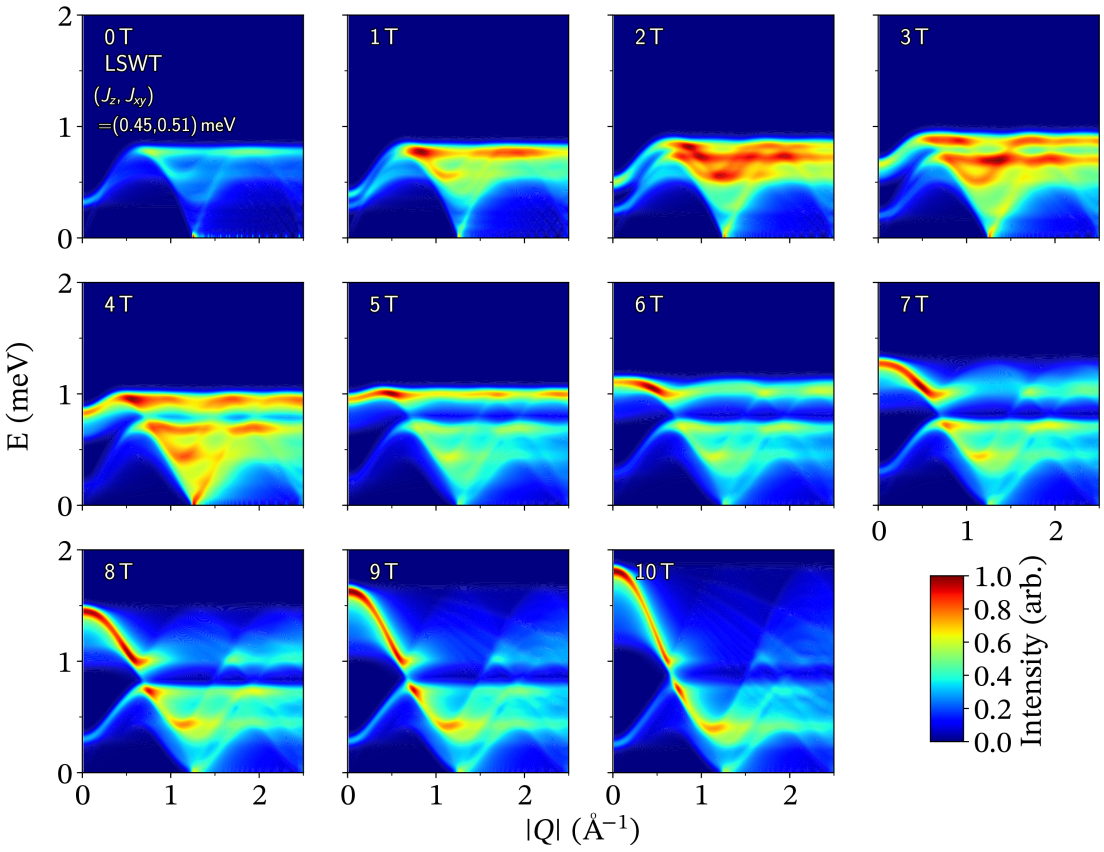

Figure 3.17: Linear spin wave theory (LSWT) calculations of $S(Q, \hbar\omega)$ at external powder averaged magnetic fields from $\mu_0 H = 0$ to 10 T. The model incorporates slight easy plane anisotropy with $J_z = 0.45$ meV and $J_{xy} = 0.51$ meV. In zero field, the model does not predict the continuum of excitations observed in the quantum disordered regime of $NaYbO_2$. However, with increasing external field, $NaYbO_2$ develops conventional long range magnetic order that is reproduced with the model. At $\mu_0 H = 5$ T, the 1.0 meV flat mode well resolved in Figures 3.15 and 3.14 appears.

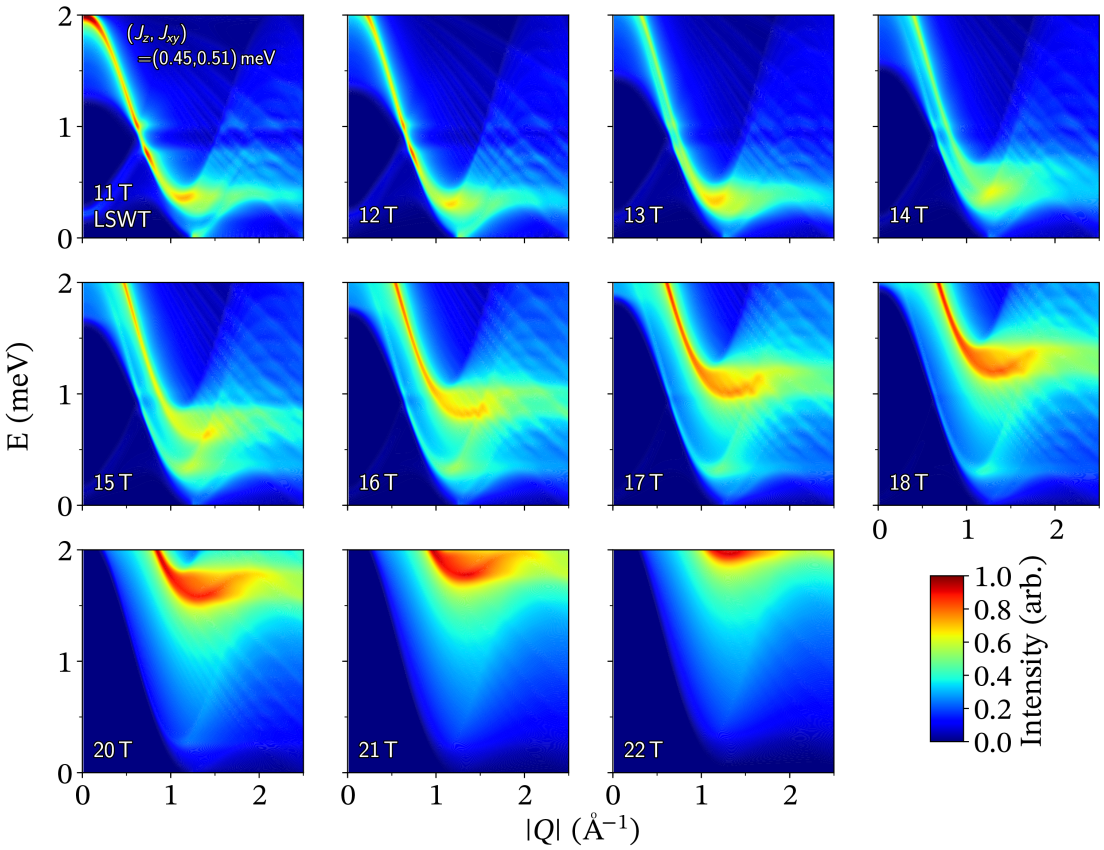

Figure 3.18: Linear spin wave theory (LSWT) calculations of $S(Q, \hbar\omega)$ at external powder averaged magnetic fields from $\mu_0 H = 11$ to 22 T. The model predicts the critical field for moment polarization depends on the orientation of the field relative to the unit cell. The values are $B_c = 21.15$ T and $B_{ab} = 12.03$ T. The powder averaged model here shows the development of steep dispersions as the polarized state is entered.

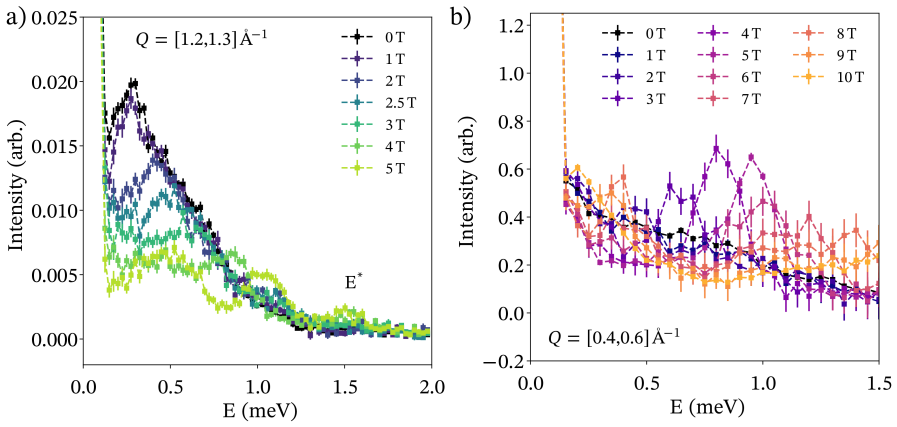

Figure 3.19: High flux low energy inelastic neutron scattering data from CNCS at ORNL reveals the field evolution of scattering weight in $NaYbO_2$ between 0 to 2 meV. a) $Q = [1.2, 1.3]$ Å^{-1} integrated cuts show a new feature, labeled E* arises at $\mu_0 H = 5$ T in the up-up-down ordered regime. This magnetic mode is likely caused by multimagnon interactions that convolves the two lower energy features near 0.5 meV and 1.0 meV captured in the linear spin wave model of $NaYbO_2$ and is maximally separated from the lower bands at $\mu_0 H = 5$ T. b) $Q = [0.4, 0.6]$ Å^{-1} integrated cuts track the flat up-up-down band with increasing field. The mode reaches 1 meV at $\mu_0 H = 5$ T.

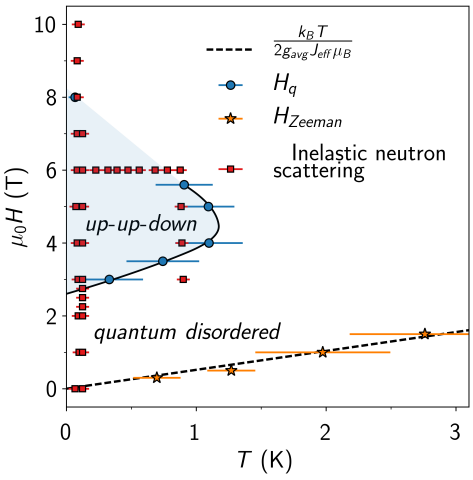

Figure 3.20: Overall proposed phase diagram for $NaYbO_2$ based on magnetic susceptibility and neutron scattering measurements. The orange stars represent the Zeeman splitting of free spins observed in a.c. susceptibility measurements that follow $\frac{k_B T}{2 g_{avg} J_{eff} \mu_B}$. Red squares are points where neutron scattering data was collected and blue circles are inflections from a.c. susceptibility measurements. The high field phase boundary may enter a second ordered V phase, but our neutron scattering experiments did not directly resolve this phase. Instead, a hysteretic dependence of the up-up-down phase was found after approaching it from the high field regime.

Chapter 4

Spiral magnetic order and the frustrated elongated diamond lattice in $LiYbO_2$

4.1 Introduction

[1]

Three dimensionally frustrated lattices such as the diamond lattice and pyrochlore lattices have been widely studied over the past couple of decades. The frustrated diamond lattice is based off of bipartite frustration in cubic symmetry and the frustrated pyrochlore lattice contains corner sharing tetrahedra frustrated three dimensionally. For example, these frustrated lattices form within the transition metal spinels AB_2X_4 (A and B = transition metal or metalloid; X = chalcogenide) and the pyrochlore materials $Ln_2M_2O_7$

[1]This chapter is based on our publication on $LiYbO_2$:[121] Mitchell M. Bordelon, Chunxiao Liu, Lorenzo Posthuma, Eric Kenney, M.J. Graf, N. P. Butch, Arnab Banerjee, Stuart Calder, Leon Balents, and Stephen D. Wilson. Frustrated Heisenberg $J_1 - J_2$ model within the stretched diamond lattice of $LiYbO_2$, *Phys. Rev. B*, **103** 014420 (2021). Copyright 2021 American Physical Society.

(Ln = lanthanide; M = metal or metalloid). The spinels contain both a diamond and pyrochlore sublattice. The A site corresponds to a diamond lattice and the B site is a pyrochlore lattice. In the pyrochlore materials, the Ln and M sublattices form a pyrochlore lattice. Magnetic frustration in these lattices can preclude long range magnetic order and instead incite unconventional magnetic states. This includes classical spin liquids [95, 96], quantum and classical spin ices [92, 97–99], and quantum and classical spiral spin liquids [28–30]. When magnetic moments forming these phases are small, their strong quantum fluctuations can favor the highly correlated quantum disordered states [20–25].

Comparatively, the diamond lattice is less studied than the pyrochlore lattice. This is in part due to the large number of materials in the $Ln_2M_2O_7$ exhibiting frustrated characteristics. The chemical tunability across the Ln elements allows for a controlled method of studying unconventional magnetism. On the other hand, even though there are a large number of AB_2X_4 materials, not all of them crystallize in the ideal cubic limit with varying metal magnetic ions, disrupting both the ideal frustration on both of its magnetic sublattices. The magnetic moments comprising the spinels are also usually transition metal ions versus the Ln ions in the pyrochlore materials. The Ln ions can readily form $J_{eff} = 1/2$ ground states in half integer total angular momentum systems with strong spin orbit coupling and crystalline electric fields. Their magnetic correlations are also short range due to limited f orbital extent. For example, the pyrochlore material $Yb_2Ti_2O_7$ [99, 157] is a well studied quantum spin ice material deriving from Yb moments in a strong YbO_8 crystalline electric field. Transition metal spinels contain magnetic moments that can occasionally form $S = 1/2$ ground states when there is exactly one unpaired electron or $J_{eff} = 1/2$ ground states with moderate spin orbit coupling (e.g. Co^{2+} [116]). Their magnetic exchange is usually further and can include multiple neighboring magnetic ions since d orbitals extend further from the nucleus. This can make understanding the base

reason of their magnetic ground states more difficult, as many magnetic interactions will be necessary to model them.

In this chapter, the elongated frustrated diamond lattice will be introduced, where its exchange interactions will be based on combining the frustrated diamond lattice with Ln magnetic moments. Despite a large number of the $ALnX_2$ materials crystallizing in the triangular lattice $R\bar{3}m$ or $P6_3/mmc$ space groups, another frustrated lattice forms in this materials family. The $I4_1/amd$ crystal structure in Figure 4.2 contains a bipartite lattice of Ln ions that is related to the bipartite diamond lattice. Frustration of the diamond lattice originates from two interpenetrating face centered cubic sublattice decorated with an inter-sublattice exchange J_1 and intra-sublattice exchange J_2. In the Heisenberg limit, this becomes:

$$H = J_1 \sum_{<i,j>} \mathbf{S_i} \cdot \mathbf{S_j} + J_2 \sum_{<<i,j>>} \mathbf{S_i} \cdot \mathbf{S_j} \tag{4.1}$$

A number of magnetic phases appear depending on the relative ratio of J_2 to J_1. When either J_1 or J_2 is zero, the Heisenberg diamond lattice is unfrustrated and forms a conventional long range Néel state. In the limit when $J_2 > 0$ and $|J_1| > 0$, the model becomes frustrated. In particular, a highly degenerate manifold of coplanar spirals forms when $J_2/|J_1| \geq 1/8$ [28–30]. The spirals form a continuous momentum surface in reciprocal space where each spiral has its own momentum wave vector at finite temperature[28–30]. Differing points on the spiral surface contain more degeneracy than others, and the degeneracy can be lifted by reducing the temperature to the model with an order by disorder mechanism [28–30]. Therefore, eventually at low temperature, this model contains long range magnetic order. However, when the system is comprised of small spin moments (i.e. $S \leq 1$), then quantum fluctuations can prevent the long range order where a quantum spiral spin liquid forms that persistently fluctuates between the degenerate spirals [30]. Even though this is an exciting prospect, relatively few materials systems

have been proposed that could form a quantum spiral spin liquid as it necessitates ideal Heisenberg interactions of small moment ions on transition metal spinels. The main material that has been studied is $NiRh_2O_4$ [30, 59] where $S = 1$ Ni moments form the diamond lattice.

Therefore, a large materials push to identify systems that could generate this spin liquid phase in the Heisenberg limit is needed. The transition metal spinels are heavily perturbed by further neighbor interactions and even cubic $Fm\bar{3}m$ to tetragonal $I4_1/amd$ or $I\bar{4}2d$ phase transitions. These unfavorable interactions lift the spiral state degeneracy even without necessitating order by disorder mechanisms and few spinel model materials exist. Some of the most prominent examples in the literature are $MgCr_2O_4$ [166, 167], $MnSc_2S_4$ [60–62], $CoRh_2O_4$ [168], and the aforementioned $NiRh_2O_4$ [30, 59]. Each of these materials has at one point been proposed to contain an unusual ground state that originates from $J_1 - J_2$ frustration in the Heisenberg diamond lattice, but they all require expanding upon the model Hamiltonian significantly. For example, $MnSc_2S_4$ requires at least three neighboring interactions to fully understand its ordered state. In $NiRh_2O_4$, single ion anisotropies are necessary to understand the full extent of neutron scattering results. The material does not magnetically order but does tetragonally distort. One explanation for the lack of ordering is strong single ion anisotropy from the Ni magnetic ions that pushes the material into a paramagnetic state[30, 59]. Other materials like $CoRh_2O_4$ [168] also tetragonally distort and then exhibit long range magnetic ordering.

However, the tetragonal distortion in these spinels is usually small. It is a compression or elongation along one of the cubic axes and creates nonequivalent magnetic exchange interactions in the tetragonal limit. In other words, the tetragonal distortion breaks the cubic symmetry and magnetic exchange symmetry, but none of the distorted magnetic exchange interactions can be ignored. In particular, the J_2 interaction originally has twelve equivalent bond pathways, but under a tetragonal elongation, four short and eight

long bonds are created. This is pictorially shown in Figure 4.1 In the non cubic limit, the spiral surface formed in reciprocal space is destroyed. Still, the materials $MnSc_2S_4$ [60–62], $CoAl_2O_4$ [169–171], and $NiRh_2O_4$ [30, 59] are possibly close enough to the cubic limit to produce spiral spin liquid or related phases.

Another method to examining the Heisenberg limit of the $J_1 - J_2$ model is by exploring an alternative frustrated diamond lattice. This chapter covers the extreme limit of tetragonal elongation of the $J_1 - J_2$ model in $LiYbO_2$ and how the highly localized $J_{eff} = 1/2$ Yb moments approximate the Heisenberg limit. Of course, the material does not strictly fall within the Heisenberg limit, but it is not perturbed by further neighbor interactions and the split J_2 bonds will be shown unnecessary to understand the magnetic ground state in this system. The material does not exhibit a spiral spin liquid surface, but instead the tetragonal elongation favors a doubly degenerate spiral ordering wave vector at low temperature. $LiYbO_2$ will be shown to magentically order by 1 K in an incommensurate spiral that then evolves in an external magnetic field. An intermediate phase with disorder between the bipartite sublattices suggests that the $J_{eff} = 1/2$ Yb moments with strong quantum flucutations may perturb the classical Heisenberg model. In total, these studies suggest that realizing an ideal quantum spiral spin liquid phase could follow an alternative route than the transition metal spinels. If a material with Yb^{3+} moments was in an ideal cubic $Fm\bar{3}m$ setting, it has potential to adopt the properties of the $J_1 - J_2$ Heisenberg model.

4.2 Experimental Methods

The synthesis and basic analysis methods for $LiYbO_2$ are shown in Chapter 2. This section overviews the specific instrumental setups and measurement conditions for this material.

4.2.1 Magnetic measurements

The general bulk magnetic properties specific heat measurements, magnetic susceptibility, and isothermal magnetization were collected on $LiYbO_2$ with a Quantum Design PPMS with a 14 T magnet and a MPMS3 with a 7 T magnet. Magnetic susceptibility from 2 to 300 K was collected under $\mu_0 H = 50$ Oe and was analyzed with the Curie-Weiss law at high and low temperature, and isothermal magnetization was collected up to $\mu_0 H = 14$ T at temperatures from 2 to 300 K. Low temperature a.c. magnetic susceptibility in zero field from 330 mK to 2 K was obtained on a susceptometer at 711.4Hz with a 0.1 Oe (7.96 A m^{-1}) drive field with a ^{3}He insert. The contribution from the sample holder was approximately linear in this temperature range and was subtracted out in the data presented here.

Specific heat measurements were obtained with the PPMS heat capacity option from 2 K to 300 K and with the Quantum Design dilution refrigerator insert from 100 mK to 4 K. Data on pressed and sintered $LiYbO_2$ pellets between 100 mK and 300 K were combined from the high temperature heat capacity measurements and dilution measurements. Several magnetic fields of $\mu_0 H = 0, 3, 5$, and 9 T were collected. The high temperature lattice contributions to the specific heat were approximated with a double Debye fit explained in Chapter 2 with $\Theta_{D1} = 230.5$ K and $\Theta_{D2} = 615.3$ K. No nonmagnetic analogue was able to be synthesized to more accurately model the chemical lattice contributions to specific heat. Therefore, the magnetic specific heat was determined by subtracting out the Debye model and then integrating C_p/T in equation 2.17 for $\mu_0 H = 0, 3, 5$, and 9 T data.

4.2.2 Elastic neutron scattering

Powder elastic neutron diffraction data was obtained on the high-resolution powder diffractometer HB-2A at the High Flux Isotope Reactor (HFIR) at Oak Ridge National Laboratory (ORNL). A 8 g sintered polycrystalline sample was placed in a cryostat with a ^{3}He insert capable of reaching $\mu_0 H = 5$ T vertical field. Data was collected at temperatures between 270 mK to 1.5 K. The sample was contained in a Cu canister filled with a small amount of ^{3}He exchange gas. Incident neutrons of 2.41 Å(Ge(311) monochromator) were used.

Refinement of the chemical structural data was performed in the FullProf software suite [125] with data collected at 1.5 K. These values were then kept constant for analyzing the magnetic structure of $LiYbO_2$. Rietveld refinements to the 1.5 K and 300 K data are in Figure 4.8 and Table 4.1. Refinement of the magnetic structure followed the general procedure outlined in the Methods chapter where the SARAh refine and representational analysis programs [126] were utilized for determining the symmetry allowed magnetic structures of $LiYbO_2$. To remove remnant signals from the sample environment, the magnetic structure of $LiYbO_2$ was refined by subtracting out the 1.5 K $\mu_0 H = 0$ T data set.

Determining the magnetic structure of $LiYbO_2$ required simultaneous use of FullProf and SARAh. As will be explained in the Results chapter, the ordered phase of $LiYbO_2$ is an incommensurate spiral at $\mu_0 H = 0$ T that becomes commensurate under an external magnetic field of $\mu_0 H = 3$ T. Initial propagation wave vector analysis with k-search could not determine the propagation wave vector for $LiYbO_2$. The program repeatedly indicated that the propagation wave vector was most likely (0,0,0), but this would not generate the incommensurate peaks observed. Instead, the only way to determine the propagation wave vector was to first look at the $\mu_0 H = 3$ T commensurate peaks and

use a bit of intuition about the diamond lattice Heisenberg model where it is known that spiral phases with $k = (q, q, 0)$ like wave vectors form. The peaks at $\mu_0 H = 3$ T were then indexed to $k = (1/3, \pm 1/3, 0)$. Following this logic, the $\mu_0 H = 0$ T should be related and was found that an incommensurate $k = (q, \pm q, 0)$ accounted for all of the peaks. Then, the helical/spiral magnetic refinement mode in FullProf gave an initial starting point for understanding the structure of the $LiYbO_2$ ordered phase at both fields, but it was not strictly limited by symmetry allowed magnetic structures of the lattice. This refinement mode, described in Chapter 2, takes as input a propagation wave vector, magnetic moment size, helical/cone angle, and a relative magnetic phase factor. This mode allows for the most fluid analysis of the magnetic structure, where one can easily control the real space visualization of the magnetic structure in comparison to the more traditional basis vector notation. However, the final magnetic structures of $LiYbO_2$ were presented in the basis vector notation. To generate the basis vectors, the FullProf Studio program was used as it gave components of (001) (100) and (010) basis vectors determined by SARAh. The final structure was refined with the SARAh determined basis vector notation.

4.2.3 11-BM x-ray scattering

Additional high-resolution powder diffraction data was collected for $LiYbO_2$. A nested capillary with $LiYbO_2$ was mailed in for high-resolution chemical structure data shown in Figure 4.3. Data was collected at 100 K and with x-rays of $\lambda = 0.4579$ Å. The data was refined with the FullProf software suite [125]. Loading the capillary required diluting $LiYbO_2$ with finely ground SiO_2 to reduce signal attenuation. The quartz capillary was loaded with $LiYbO_2$ mixed with SiO_2 in a glove box and was flame sealed with a hydrogen-oxygen torch. The seal was checked over two days to ensure no air leakage

occurred. Even though $LiYbO_2$ is air stable, water absorption is unfavorable and could have resulted in some subtle lattice changes that 11-BM would have detected.

4.2.4 High energy inelastic neutron scattering

High energy inelastic neutron scattering (INS) data $S(Q, \hbar\omega)$ was collected on the Angle Resolved Chopper Spectrometer (ARCS) at Oak Ridge National Laboratory (ORNL). Polycrystalline $LiYbO_2$ powder (5 g) was placed in an aluminum canister and placed in a cryostat with a 5 K to 300 K temperature range. Incident neutron energies were chosen to analyze the $J = 7/2$ ground state multiplet splitting of the $4f^{13}$ Yb3+ ions by the local D_{2d} crystalline electric field (CEF) with $E_i = 300$ meV (Fermi 1, Fermi frequency 600 Hz). A lower $E_i = 150$ meV (Fermi 2, Fermi frequency 600 Hz) was also collected at 5 K to determine broadening of the lower two crystalline electric field excitations. These data are presented in Figures 4.6 and 4.7. Background contributions from the aluminum sample can were subtracted out by measuring an empty canister under the same conditions.

The eight fold degenerate $J = 7/2$ multiplet can split into four doublets following Kramers theorem. Details of the general CEF setup is explained above in the Introduction and Methods chapters, and the specific changes for $LiYbO_2$ are as follows: The minimal CEF Hamiltonian describing $LiYbO_2$ with Stevens parameters and operators is:

$$H_{CEF} = B_2^0\hat{O}_2^0 + B_4^0\hat{O}_4^0 + B_4^4\hat{O}_4^4 + B_6^0\hat{O}_6^0 + B_6^4\hat{O}_6^4 \tag{4.2}$$

Diagonalizing the CEF Hamiltonian returns the eigenenergies and eigevectors. The eigenvectors were used to determine g factor components and relative intensity ratios of the excited states with equations 1.25, 1.26, and 1.28. The refinement of CEF Stevens parameters was conducted with the process presented in the Methods chapter. Three point

charge models with equation 1.24 were calculated and shown in Table 4.2 alongside the final crystalline electric field fits of $LiYbO_2$.

4.2.5 Low energy inelastic neutron scattering

Low energy inelastic neutron scattering spectra $S(Q, \hbar\omega)$ of $LiYbO_2$ were obtained on the Disc Chopper Spectrometer (DCS) instrument at the NIST Center for Neutron Research (NCNR). $LiYbO_2$ was loaded into a copper canister and placed in a dilution refrigerator insert capable of reaching 30 mK. The spectrometer had a 10 T vertical magnet. Neutrons with incident wavelengths of $E_i = 3.32$ meV under the medium-resolution chopper setting were used. The background was determined by subtracting out the negative scattering from the spectra. External magnetic fields of $\mu_0 H = 0$ to 10 T were collected below the 1 K magnetic transition in $LiYbO_2$.

4.3 Results

4.3.1 $I4_1/amd$ chemical structure

The chemical structure of $LiYbO_2$ was determined with elastic neutron powder diffraction collected on HB-2A at ORNL and from elastic x-ray scattering from 11-BM. The Figures 4.3, 4.2, and 4.8 and Table 4.1. The crystal structure remains in the $I4_1/amd$ space group throughout all temperatures measured. The 11-BM data was collected at 100 K and HB-2A at 1.5 K. Within resolution of both experiments, the occupancies of the Li, Yb, and O ions are full. There is also no distinctive impurity phase present that would impart on the magnetic measurements of $LiYbO_2$. Additionally, the high resolution 11-BM data provides insight into any minor reduced symmetry away from the $I4_1/amd$ space group. Originally, the splitting observed in the crystalline electric field

was thought to originate from a slight distortion from the $I4_1/amd$ setting. However, the 11-BM data rules this out down to 100 K as no peak splitting was observed in this high resolution experiment.

The crystal structure shown in Figure 4.2 contains edge sharing D_{2d} YbO_6 octahedra. These octahedra connect into a three dimensional lattice network of Yb ions that can be viewed as two interpenetrating, elongated face centered cubic sublattices. The sublattice view of only the Yb ions is shown in Figure 4.1 where one sublattice is in blue and the other is in gray. The sublattices are connected with two bonds above and two bonds below each Yb ion from a $Yb_{A(B)}-Yb_{B(A)}$ distance 3.336 Åat 1.5 K, labeled J_1 in the figure. The J_1 bonds form a stretched tetrahedron surrounding a central Yb ion. The next nearest neighbor Yb-Yb bond is within one Yb sublattice and in the ab plane. There are four equivalent $Yb_{A(B)}-Yb_{A(B)}$ bonds at a distance 4.4382 Åand this is labeled J_2. Even though the difference in the bond lengths of J_1 and J_2 is significant and over 1 Å, these two bonds can have a geometrically frustrated interaction where both bonds are of similar correlation strength. The superexchagne pathway along J_1 is close to 90° while along J_2 is close to 180°. This promotes antiferromagnetic superexchange along J_2 relative to J_1. Furthermore, the exchange pathways through the oxygen anions along each bond are nearly the same at 4.473 Åand 4.410 Åfor J_1 and J_2, respectively. One can imagine that the two antiferromagnetic superexchange interactions could be relatively similar in magnitude when the moments are relatively isotropic.

The lattice becomes geometrically frustrated when $|J_1| > 0$ and $J_2 > 0$. This can be originally viewed by imagining the $J_1 - J_2$ frustration from the diamond lattice. The magnetic diamond lattice, when elongated along one of its cubic axes, becomes the Yb lattice of $LiYbO_2$ as shown in Figure 4.1. The diamond lattice is a well studied geometrically frustrated bipartite lattice [28–30, 90, 91, 172]. However, stretching the diamond lattice breaks some of the degenerate J_2 interactions. In $LiYbO_2$ specifically,

the elongation breaks J_2 into J_{2a} at 5.5090 Åalong the elongated axis and J_{2b} at 4.4380 Åin the perpendicular plane. Normally, in the cubic diamond lattice transition metal spinels, there is one O^{2-} anion for each superexchange pathway for all J_2 interactions. The elongation in $LiYbO_2$ makes J_{2a} have two O^{2-} between each Yb ion while J_{2b} remains with one. This difference between the spinels and $LiYbO_2$ means that the J_{2a} interaction has significantly weaker superexchange relative to J_{2b} in $LiYbO_2$ but not in the slightly tetragonally distorted transition metal spinels. In other words, the tetragonally elongated spinels cannot ignore the single superexchange J_{2a} but $LiYbO_2$ can neglect J_{2a} since it is a long, double superexchange pathway.

For the rest of this thes""is, the subscripts on J_2 are dropped and the J_{2a} interaction is considered weak enough to be ignored. We relabel J_{2b} as simply J_2.

4.3.2 Crystalline electric field

The crystalline electric field (CEF) analysis method is outlined in Chapter 2, and the specifics of the analysis and data collection for $LiYbO_2$ are presented here. Inelastic neutron scattering (INS) $S(Q, \hbar\omega)$ data on $LiYbO_2$ was collected at 5 K and 300 K at $E_i = 300$ meV and $E_i = 150$ meV. The $E_i = 300$ meV data shows the CEF multiplet structure of the Yb^{3+} ions while the $E_i = 150$ meV data shows some splitting of two of the Kramers doublets. Three excitations in the $E_i = 300$ meV data arise centered at 45, 63, and 128 meV as shown in Figure 4.6. The ground state Kramers doublet is separated by 45 meV from the first excitation, making it a well separated $J_{eff} = 1/2$ ground state Kramers doublet at low temperature.

Integrating a cut along E shows the excitations along with their full width half maximum (FWHM) energy resolution. At $E_i = 300$ meV, all of the CEF excitations are within the resolution of the spectrometer. The integrated intensities of these excitations

in this energy window were used for analyzing the $J = 7/2$ multiplet structure of $LiYbO_2$ and the results are shown in Table 4.2. Additionally, the CEF fit was constrained by a powder averaged g_{avg} determined from the intercept of the saturated isothermal magnetization curve in Figure 4.4. Results of the CEF fit indicate that $g_{//} = 0.58$ and $g_{\perp} = 3.71$ where g_{avg} is determined by equation 1.27.

The best model of the CEF multiplet structure does not closely match any of the point charge (PC) models in Table 4.2. It is closest to a PC model including two coordination shells at a distance of 3.1 Åin sign of the Stevens parameters B_n^m. However, the magnitude of the B_2^0 parameter is significantly different. This suggests that the primary CEF contribution is the O^{2-} anions surrounding the Yb ion and secondarily the Li^+ cations. A PC model is never perfectly accurate, but it does help give insight to the primary causes of the CEF multiplet splitting.

With an $E_i = 150$ meV, only the first two multiplet excitations centered at $E_1 = 45$ meV and $E_2 = 63$ meV are visible. They show additional splitting in Figure 4.6 that is not observable at the higher $E_i = 300$ meV incident neutron energy due to the higher FWHM energy resolution in that instrumental setting. These two peaks are asymmetrically split with $E_{1a} = 39.5$ meV, $E_{1b} = 47.0$ meV, $E_{2a} = 55.6$ meV, and $E_{2b} = 62.6$ meV. When integrating the areas under the asymmetrically split peaks, their intensities match what was observed for E_1 and E_2 at $E_i = 300$ meV. This is shown in Figure 4.6, and indicates that the split peaks at $E_i = 150$ meV do combine into doublets.

At first, the most likely explanation for this peak splitting was a slightly lower symmetry than $I4_1/amd$ that would generate subtle peak splitting in x-ray diffraction data. This would have made two or more inequivalent Yb sites with different CEF splittings and would have been an easy explanation for the observed multiple multiplet structure. However, the 11-BM data in Figure 4.3 does not show any indication of a lower space group symmetry than $I4_1/amd$. Also, even though there are two Yb sublattices, the

Yb ions in each sublattice are equivalently surrounded by the same CEF environment. Another explanation could be exchange splitting as discussed in the $NaYbO_2$ chapter, but the larger splitting closer to 10 meV in $LiYbO_2$ does not match the weaker mean field exchange of $\theta_{CW} = -3.4$ K. Another possibility is strong lattice-phonon coupling, but there is not any distinctively strong phonon branch in the INS data that would suggest this. Currently, the CEF analysis ignores the splitting of E_1 and E_2 and treats the CEF environment originating from the observed intensities in the $E_i = 300$ meV INS data.

4.3.3 Bulk magnetic properties

The magnetic property measurements of $LiYbO_2$ are shown in Figures 4.4 and 4.5. In the low temperature regime below 100 K, the ground state Kramers doublet is primarily occupied in $LiYbO_2$. This region is fit for analysis with the Curie-Weiss law. The extracted parameters from the linear regime show antiferromagnetically coupled Yb ions with a mean field $\theta_{CW} = -3.4$ K and effective magnetic moment of $\mu_{eff} = 2.74\mu_B$. This also indicates the Curie-Weiss g_{avg} is 3.13 from $J_{eff} = 1/2$ Yb ions. Above 100 K, there is a second linear regime. However, this regime is dominated by intermultiplet excitations within the CEF manifold and does not indicate the true mean field Curie-Weiss interaction. Another method for determining g_{avg} was conducted by taking a Van Vleck susceptibility fit of the isothermal magnization curve at 2 K above $\mu_0 H = 10$ T and extrapolating it to $\mu_0 H = 0$ T. The Van Vleck susceptibility slope was $\chi_{VV} = 0.0206$ cm^3 mol^{-1} Yb ion and indicates the field induced rotations into neighboring crystalline electric field (CEF) levels. The g_{avg} in this case was 2.98 calculated with $intercept = g_{avg}\mu_B/2$, and is within error of the Curie-Weiss one. Since the Curie-Weiss analysis can be perturbed easily by any sources of non linearity, the g_{avg} from the isothermal magnetization curve was used for analyzing the CEF of $LiYbO_2$.

A.c. magnetic susceptibility in Figure 4.4 shows two features in the low temperature regime. There is a broad hump near 1.5 K and a sharp upturn at 0.45 K. The broad hump is an indication of the onset of short range correlations and the sharp upturn is the onset of long range magnetic order. This was determined by comparing this data with the specific heat data in 4.5. There are two sharp features in the $\mu_0 H = 0$ T specific heat data at $T_{N1} = 1.13$ K and $T_{N2} = 0.45$ K. There is also a broad short range correlation hum in this specific heat data above T_{N1}. As will be shown in the section detailing the long range magnetic order from elastic neutron scattering experiments, these two sharp specific heat anomalies indicate the onset of spiral magnetic order in $LiYbO_2$, where the lower temperature one is the onset of full three dimensional order and the higher temperature one has disorder between the Yb magnetic sublattices. These specific heat features relatively well match the a.c. susceptibility features, where the sharp 0.45 K upturn is T_{N2}.

In Figure 4.5, $\mu_0 H = 0$, 3, 5, and 9 T data down to roughly 100 mK was collected. The two sharp anomalies and the upper broad peak shift with increasing field up in temperature. The integrated magnetic entropy at all fields collected nearly reaches 98% $Rln(2)$ after subtracting out the double Debye lattice specific heat fit, as expected for a $J_{eff} = 1/2$ Yb ground state Kramers doublet. The dashed black lines in these figures at half of $Rln(2)$ show that half of the magnetic entropy is released prior to the sharp anomalies. This corresponds with the short range broad peak above T_{N1} that shifts upward in temperature with increasing external magnetic field. In other words, the onset of short range correlations increases in temperature with increasing external magnetic field. Additionally, the location of T_{N1} shifts up in temperature with increasing external magnetic field. By $\mu_0 H = 9$ T, T_{N1} shifts to 1.40 K and there is no indication of a lower T_{N2} peak. The T_{N2} anomaly broadens with increasing magnetic field and eventually is invisible by $\mu_0 H = 5$ T. The disappearance and suppression of T_{N2} with a magnetic field

suggests that $\mu_0 H = 0$ T fluctuations and ground state degeneracy influence long range magnetic order in this system through geometrical frustration.

4.3.4 Spiral magnetic order

Understanding the long range magnetic order in $LiYbO_2$ required analysis with elastic neutron powder diffraction. The data is presented in Figures 4.8 and 4.9 and shows the temperature and field evolution of spiral magnetic order in $LiYbO_2$. These data were taken at specific points between T_{N1} and T_{N2} observed in specific heat data in Figure 4.5. New magnetic reflections appear in the powder neutron diffraction data below T_{N1} that evolve with decreasing temperature and increasing external magnetic field. There are three regions in which the data were analyzed: (1) $\mu_0 H = 0$ T below the second ordering transition T_{N2} at $T < 0.45$ K; (2) $\mu_0 H = 0$ T between T_{N1} and T_{N2} at $T = 0.83$ K in the intermediate ordered regime; and (3) $\mu_0 H = 3$ T and below T_{N2} at $T < 0.45$ K. The structural data was refined at 1.5 K and is shown in Figure 4.8. This data was used as a paramagnetic background subtraction to analyze the ordered magnetic regimes. Figure 4.9 shows the subtracted data sets and Rietveld refinement fits. It should be noted that there is a large over and under subtraction at 1.5 Å^{-1} due to a nuclear reflection that slightly shifts with temperature and external magnetic field. The following subsections overview the magnetic order in each regime.

Region 1: $\mu_0 H = 0$ T at 0.27 K Below T_{N2}, there are four new magnetic reflections that appear. They are incommensurate peaks that can be fit with a doubly degenerate wave vector $k = (0.384, \pm 0.384, 0)$. A best model of these reflections is a spiral magnetic structure that is shown in Figure 4.9. Generating this spiral structure requires the Γ_1 irreducible representation in the Kovalev scheme produced in SARAh [126]. Three basis vectors $bv_1 = (1, 0, 0)$, $bv_2 = (0, 1, 0)$, and $bv_3 = (0, 0, 1)$ are used to describe the structure

with this irreducible representation. Viewing the spiral structure can be decomposed into two components: an ordering wave vector k and the propagation direction of the spirals. The ordering wave vector is the repeat length of the magnetic structure while the spiral propagation direction describes a vector that is perpendicular to the plane of rotation of the magnetic spins. In other words, the spiral propagation direction is always perpendicular to the plane that the moments reside in for a helix. The model of the data was optimal when the propagation direction was within the ab plane, but the direction within the ab plane was not restricted. In other words, as long as the moments rotated perpendicular to the c axis, equivalent fits were obtained.

In the representation of this structure in Figure 4.9, the b axis was chosen as the helical propagation direction. The magnetic moments reside in the ac plane and rotate from one site to the next within the ac plane. In this model, the coefficients of the basis vectors bv_i are shown in Table 4.3.

Since $LiYbO_2$ is bipartite (i.e. contains two Yb sublattices), an additional degree of freedom arises when fitting this magnetic structure. This is the relative magnetic phasing between the two Yb sublattices that can vary from 0 to π. The differing phase values are shown in Figure 4.10, and the best model of the data in Region 1 is with a phase value of 0.58 π. The refined ordered magnetic moment is 1.26(10) μ_B, which is at 84% of the expected 1.5 μ_B moment from the saturated moment from isothermal magnetization.

Region 2: $\mu_0 H = 0$ T at 0.83 K Between T_{N2} and T_{N1}, the incommensurate magnetic structure changes slightly. The system still has a doubly degenerate ordering wave vector $k = (0.384, \pm 0.384, 0)$ with magnetic reflections at the same location as below T_{N2}. However, the intensity and relative intensities of the reflections is different than below T_{N2}. Order below T_{N1} appears to still be long range with the incommensurate structure as the lowest angle peak can be fit with a Lorentzian function to estimate the minimum correlation length. Below T_{N2} and in Region 2 below T_{N1}, the minimum correlation

length remains the same at $\sim$ 364 Å.

There are two ways to model this region. The first is to take the the exact same structure as Region 1 and reduce the moment size, or essentially scale it down. This is shown as the green curve in Figure 4.9. This model has too much intensity at the reflections at 1.2 $Å^{-1}$, however, suggesting that it is not the correct stucture. In fact, no structure with a single magnetic sublattice phasing value between 0 to π appeared to represent the data well. The second method for fitting this intermediate Region 2 was to allow the magnetic sublattice phasing to take any value between 0 to π and then average over them all to create the fit. The magnetic moment size is kept at 1.26(10) μ_B and only the phase value is allowed to change. This is shown as the orange curve in Figure 4.9. This essentially states that the long range magnetic order in $LiYbO_2$ is established at T_{N1} but then the sublattice phasing is not selected until T_{N2}. This corresponds to magnetic entropy being released at T_{N2} in specific heat data in Figure 4.5.

Region 3: $\mu_0 H = 3$ T at 0.27 K The application of an external magnetic field above the lowest temperature zero field magnetic ground state alters the spiral magnetic order in $LiYbO_2$. A field of $\mu_0 H = 3$ T drives the system into a different doubly degenerate ordering wave vector of $k = (1/3, \pm 1/3, 0)$. However, even though this wave vector is different, the general principles of the ordered magnetic phase remain the same. It is still a long range ordered spiral state with propagation direction within the *ab* plane. The magnetic moment size is 1.26(9) μ_B, which is consistent with the zero field state. Additionally, the magnetic sublattice phase value is 0.42 π. This field induced transition can be viewed as a 'lock in' transition to a commensurate state, and the theoretical origins of why this happens will be discussed alter on.

4.3.5 Low energy dynamics

The low energy dynamics of $LiYbO_2$ is shown in Figures 4.12 and 4.11. The dynamics were investigated in all of the differing ordered regimes talked about above in the elastic neutron diffraction section. Since this was a powder experiment, the dynamics are a bit difficult to interpret, but it does show some key aspects that are important to understanding $LiYbO_2$ and spiral magnetic order. Bwlow T_{N2}, the bandwidth of spin excitations goes to 1 meV with the majority of the spectral weight originating near the magnetic zone center of the doubly degenerate ordering wave vector $k = (0.384, \pm 0.384, 0)$ and the Γ point. With increasing external field into the 'lock in' $\mu_0 H = 3$ T regime, the dynamics of the system do not change much. The order in field and in zero field are relatively the same, with the same type of long range magnetic order, only differing by their ordering wave vector. Additionally, when in Region 2 below T_{N1} but above T_{N2}, the long range magnetic order of $LiYbO_2$ has already set in. The dynamics of this regime are also similar to the zero field ground state below T_{N2} since Region 2 also has long range spiral magnetic order. To investigate more into the low energy dynamics, a high field $\mu_0 H = 10$ T subtraction was used to approximate the background at low field. This is shown in Figure 4.12 for Regions 1, 2, and 3. However, the data here qualitatively contain the same information as in Figure 4.11, only highlighting the spin wave branches. A cut through the data in Figure 4.13 shows that the peak of the gapless excitations originating near the magnetic zone center is at 0.8 meV.

4.3.6 Theoretical analysis and the $J_1 - J_2$ Heisenberg model

This section overviews the theoretical analysis of the Heisenberg Hamiltonian constructed for $LiYbO_2$ and was first presented in Ref. [121] and was formulated by Leon Balents and Chunxiao Liu. This section and the following sections on the theoretical

analysis of $LiYbO_2$ are presented here for completeness to understand the entirety of the current understanding of $LiYbO_2$. Without the analysis by Chunxiao Liu and Leon Balents, we would not have been able to fully understand $LiYbO_2$ and $NaCeO_2$ in the subsequent chapter. The analysis here is the main synopsis of the findings, and the full analysis is in Ref. [121].

The Hamiltonian uses isotropic Yb moments with nearest neighbor and next nearest neighbor magnetic exchange interactions and is used to calculate the ordering wave vector and model the spin dynamics of $LiYbO_2$.

In $LiYbO_2$ in $I4_1/amd$, the minimal Hamiltonian for nearest neighbor (NN) interactions becomes:

$$\begin{aligned} H_1 = &\sum_{\langle i,j \rangle} J_z S_i^z S_j^z + J_{xy}(S_i^x S_j^x + S_i^y S_j^y) \\ &+ J_\delta (S_i \cdot f_{ij})(S_j \cdot f_{ij}) + J_{cz}(S_i \cdot f_{ij} S_j^z + S_i^z \cdot f_{ij}\hat{z}), \end{aligned} \tag{4.3}$$

where f_{ij} is the projection of the bond vector e_{ij} onto the base plane. For next nearest neighbor (NNN), the interactions become:

$$\begin{aligned} H_2 = &\sum_{\langle\langle i,j \rangle\rangle} J_z' S_i^z S_j^z + J_{xy}'(S_i^x S_j^x + S_i^y S_j^y) \\ &+ J_\delta' (S_i \cdot e_{ij})(S_j \cdot e_{ij}) + D_{ij} \cdot S_i \times S_j, \end{aligned} \tag{4.4}$$

where the Dzyaloshinskii-Moriya (DM) vectors for the NNN bonds $\langle ij \rangle$ along a and b are $D_{ij} = (-1)^{\mu(i)} Da \times \hat{z}$ and $D_{ij} = (-1)^{\mu(i)} Db \times \hat{z}$, respectively. The term $\mu(i) = 0, 1$ for the sublattice $i = A, B$ in Figure 4.1 determines the sign of the DM vector alternates between layers. No additional terms beyond NNN are taken into account for this model, as the $4f$ interaction is usually short range. Additionally, $4f$ systems usually behave relatively well under a Heisenberg approximatoin where $J_z = J_{xy} = J_1$, and $J_z' = J_{xy}' = J_2$. The

total Hamiltonian is therefore:

$$H = J_1 \sum_{\langle ij \rangle} S_i \cdot S_j + J_2 \sum_{\langle\langle ij \rangle\rangle} S_i \cdot S_j + D_{ij} \cdot S_i \times S_j. \tag{4.5}$$

To a first approximation, the DM term in equation 4.5 can be neglected. The classical ground state of this new Hamiltonian is exactly solvable. The Hamiltonian is rewritten in momentum space as:

$$H = \sum_{q,\mu,\nu} S_{q,\mu} J_q^{\mu\nu} S_{-q,\nu}, \tag{4.6}$$

with

$$J_q^{11} = J_q^{22} = J_2(\cos q \cdot a + \cos q \cdot b),$$
$$J_q^{12} = J_q^{21*} = J_1 \left(e^{-i\frac{q \cdot c}{4}} \cos \frac{q \cdot a}{2} + e^{i\frac{q \cdot c}{4}} \cos \frac{q \cdot b}{2} \right).$$

This leads to the band's lower branch as:

$$\lambda_q = J_q^{11} - |J_q^{12}|. \tag{4.7}$$

which can be solved for the minimum of λ_q. This corresponds to a classical ground state with incommensurate or commensurate spiral where the ordering wave vector is determined by:

$$q = \frac{2\pi}{a}(q, q, 0) \quad \text{or} \quad q = \frac{2\pi}{a}(q, -q, 0), \tag{4.8}$$

where

$$q \equiv \begin{cases} \pm\frac{1}{\pi} \arccos \frac{|J_1|}{4J_2}, \\ 0, \end{cases}$$

$$\text{respectively for} \begin{cases} |J_1| \leq 4J_2, \\ |J_1| > 4J_2. \end{cases}$$

The antiferromagnetic and ferromagnetic structures with this wave vector notation are both $k = (0, 0, 0)$.

For the rest of this analysis, the value of $J_2 > 0$ is taken as this is the only way that spiral magnetic order such as seen in $LiYbO_2$ can be generated. From the experiment, the doubly degenerate ordering wave vector is $k = \frac{2\pi}{a}(0.384, \pm 0.384, 0)$, which corresponds to:

$$J_1 = \pm 4\cos(0.384\pi)J_2 = \pm 1.426 J_2. \tag{4.9}$$

The eigenvector corresponding to λ_q is $u_q = \frac{1}{\sqrt{2}}(e^{i\phi_q}, 1)^T$, where the phase $\phi_q = \pi + \mathrm{Arg}J_q^{12}$ dictates the relative angle (i.e. sublattice phasing) between the spins of the two sublattices. The magnetic order is

$$S_{r_i} = (0, \cos q \cdot r_i, \sin q \cdot r_i) \tag{4.10}$$

or any coplanar configuration that is related to equation 4.10 by a global SO(3) rotation. This can also be viewed by presenting the model in a different fashion. The Heisenberg $J_1 - J_2$ model can be rewritten as a sum of all the elementary triangles $\triangle$ with two NN bonds and one NNN bond. Each NNN bond is only within one $\triangle$ and each NN bond is shared between two $\triangle$. The two spins connected by NNN are labeled $S_{\triangle,1}$ and $S_{\triangle,2}$, and the third spin with only NN bonds as $S_{\triangle,3}$. The new Hamiltonian becomes:

$$H = \text{Constant} + \frac{J_2}{2}\sum_{\triangle}\left(S_{\triangle,1} + S_{\triangle,2} + \frac{J_1}{2J_2}S_{\triangle,3}\right)^2. \tag{4.11}$$

This rewritten Hamiltonian gives an intuitive condition for the classical ground state that must satisfy

$$S_{\triangle,1} + S_{\triangle,2} + \frac{J_1}{2J_2}S_{\triangle,3} = 0 \tag{4.12}$$

for all $\triangle$. The angle between two vectors S_1 and S_2 can be written as $\langle S_1, S_2 \rangle$. Therefore,

$$\begin{aligned}
&\langle S_{\triangle,1}, S_{\triangle,3} \rangle = \langle S_{\triangle,2}, S_{\triangle,3} \rangle \\
&= \begin{cases} \pi - \arccos \frac{J_1}{4J_2} > \frac{\pi}{2}, & 4J_2 \geq J_1 > 0 \\ \arccos \frac{|J_1|}{4J_2} < \frac{\pi}{2}, & 4J_2 \geq -J_1 > 0 \end{cases}, \\
&\langle S_{\triangle,1}, S_{\triangle,2} \rangle = 2 \arccos \frac{|J_1|}{4J_2}.
\end{aligned} \tag{4.13}$$

This other method of analyzing the Hamiltonian is in direct agreement with the exact diagonalization result above. When $J_1 = 1.426 J_2 > 0$ with a sublattice phasing of π, the angle between the two spins in a primitive cell must be $\pi - \arccos(1.426/4) = 1.935 \sim 111°$. Other sublattice phasing values except 0 are not allowed by symmetry.

However, the sublattice phasing value of the theoretical analysis does not match the experimentally observed value. The experiment predicts the spins are staggered in alternating 34° and 172° angles with a sublattice phasing of 0.58 π. This breaks the sublattice symmetry of the model above that must have spins equally rotating at 111°. One way to explain this discrepancy is that there is some lattice symmetry breaking effect that is generated by a subtle shift away from $I4_1/amd$ that might be outside of the 11-BM or HB-2A experiments.

The way to model this scenario is to begin with a subtle lattice displacement as follows: Suppose the $\mu = 1$ sublattice, originally $\delta = a/2 + c/4$ part from the $\mu = 0$ sublattice, becomes offset by ε from its original position. The offset $\varepsilon = (\epsilon, \epsilon, 0)$. What this does is changes the NN vectors from the central Yb ion to $\frac{a}{2} + \frac{c}{4} + \varepsilon$, $-\frac{a}{2} + \frac{c}{4} + \varepsilon$, $\frac{b}{2} - \frac{c}{4} + \varepsilon$, and $-\frac{b}{2} - \frac{c}{4} + \varepsilon$. These new bonds can be relabeled as J_1', J_1'', J_1', J_1'', respectively. The values of J_1', J_1'' are kept greater than zero to produce antiferromagnetic exchange expected from the experimental data. The DM contribution to this new Hamiltonian vanishes when the different sublattices have the same magntic order. The neighboring

sublattices have opposite DM contributions that cancel out perfectly with a net zero DM energy.

The new Hamiltonian rewritten in momentum space contains a new off diagonal element and becomes:

$$\begin{aligned} J_q^{12} = J_q^{21*} &= \frac{J_1'}{2}\left(e^{iq\cdot\left(\frac{a}{2}+\frac{c}{4}+\varepsilon\right)} + e^{iq\cdot\left(\frac{b}{2}-\frac{c}{4}+\varepsilon\right)}\right) \\ &+ \frac{J_1''}{2}\left(e^{iq\cdot\left(-\frac{a}{2}+\frac{c}{4}+\varepsilon\right)} + e^{iq\cdot\left(-\frac{b}{2}-\frac{c}{4}+\varepsilon\right)}\right) \\ &= \frac{1}{2}e^{iq\cdot\varepsilon}\left(J_1' e^{iq\cdot\left(\frac{a}{2}+\frac{c}{4}\right)} + J_1' e^{iq\cdot\left(\frac{b}{2}-\frac{c}{4}\right)}\right. \\ &\left. + J_1'' e^{iq\cdot\left(-\frac{a}{2}+\frac{c}{4}\right)} + J_1'' e^{iq\cdot\left(-\frac{b}{2}-\frac{c}{4}\right)}\right), \end{aligned} \tag{4.14}$$

where the terms $q_x = q\cdot a$, $q_y = q\cdot b$, and $q_z = q\cdot c$. This can then be solved for λ_q as:

$$\begin{aligned} \lambda_q \geq J_2(\cos q_x + \cos q_y) &- \sqrt{\frac{J_1'^2}{4} + \frac{J_1''^2}{4} + \frac{1}{2}J_1'J_1''\cos q_x} \\ &- \sqrt{\frac{J_1'^2}{4} + \frac{J_1''^2}{4} + \frac{1}{2}J_1'J_1''\cos q_y}, \end{aligned} \tag{4.15}$$

The minimum energy state is reached when $q_x = q_y \equiv q_0$ and $q_z = 0$. Here $q_0 = 0.384\times 2\pi$ from experimental data is used to minimize $f(q) = J_2\cos q - \sqrt{\frac{J_1'^2}{2} + \frac{J_1''^2}{2} + J_1'J_1''\cos q}$. This produces:

$$\cos q_0 = \frac{J_1'^2 J_1''^2 - 4J_2^2(J_1'^2 + J_1''^2)}{8J_2^2 J_1' J_1''} \tag{4.16}$$

This equation restricts the value between J_1'/J_2 and J_1''/J_2. The original Hamiltonian can be regenerated by setting $J_1' = J_1'' = J_1$ with $J_1 = 4\cos\frac{q_0}{2} = 4\cos\pi q$. The eigenvector corresponding to λ_q is $u_q = \frac{1}{\sqrt{2}}(e^{i\phi_q}, 1)^T$ and the new phase is

$$\begin{aligned} \phi_{q_0} &= \pi + q_0\cdot\varepsilon + \arctan\left(\tan\left(\frac{\pi}{4}-\beta\right)\tan\frac{q_0}{2}\right) \\ &\approx \pi + \arctan\left(\tan\left(\frac{\pi}{4}-\beta\right)\tan\frac{q_0}{2}\right), \end{aligned} \tag{4.17}$$

where $\tan\beta = J_1''/J_1'$ and $q\cdot\varepsilon$ is small enough to be neglected. This equation indicates that the sublattice phasing and angle difference between neighboring NN spins is dependent on the spiral wave vector and the ratio of the NN exchange energies. Using the previously experimentally determined $\phi_{q_0} = 360° - 34° = 172°$, we obtain $\tan\beta \approx 6$. In other words, this says that the lattice distortion requires a large exchange ratio in order to reproduce the experimentally observed sublattice phasing, which is highly unlikely. This analysis suggests that another factor, such as single ion properties, could be responsible for the sublattice phasing experimentally observed and that distortions away from $I4_1/amd$ are not the origin.

4.3.7 Linear spin wave theory

With the Heisenberg J_1-J_2 model for $LiYbO_2$, we now turn to calculate the dynamical structure factor of of the material where we assume the lattice is not distorted away from $I4_1/amd$. First, Holstein-Primakoff (HP) bosons are used:

$$S_i \cdot a_i = \sqrt{s}\frac{a_i + a_i^\dagger}{\sqrt{2}},\ S_i \cdot b_i = \sqrt{s}\frac{a_i - a_i^\dagger}{\sqrt{2}i},\ S_i \cdot c_i = s - n_i \tag{4.18}$$

where $c_i = u\cos\widetilde{q}\cdot r_i + v\sin\widetilde{q}\cdot r_i$ is the spin order (u and v are orthogonal unit vectors spanning the order plane), $b_i = u \times v$, and $a_i = b_i \times c_i$. The angle between spins must remain greater than 90° from our theroetical analysis, so we define $\widetilde{q} = \frac{2\pi}{a}(1-q, 1-q, 0)$. We can now write the spin wave Hamiltonian as:

$$H = \sum_{k\in \mathrm{BZ}^+} \Phi_k^\dagger \mathcal{H}(k) \Phi_k, \tag{4.19}$$

with HP bosons $\Phi_k = \left(a_{k,0}, a_{k,1}, a^\dagger_{-k,0}, a^\dagger_{-k,1}\right)^T$ in momentum space. The term $\mathcal{H}(k)$ is

$$\mathcal{H}(k) = 2\begin{pmatrix} h_{11} & h_{12} & p_{11} & p_{12} \\ h^*_{12} & h_{11} & p^*_{12} & p_{11} \\ p_{11} & p_{12} & h_{11} & h_{12} \\ p^*_{12} & p_{11} & h^*_{12} & h_{11} \end{pmatrix}, \tag{4.20}$$

with

$$\begin{aligned} h_{11} &= J_2 \sum_{\delta=a,b} \left(2s\cos k\cdot\delta\left[\frac{1}{4}(c_\delta+1)\right] - sc_\delta\right) \\ &\quad -J_1 \sum_{\delta=\pm\frac{a}{2}-\frac{c}{4},\pm\frac{b}{2}+\frac{c}{4}} \frac{s}{2}c_\delta, \end{aligned} \tag{4.21a}$$

$$h_{12} = J_1 \sum_{\delta=\pm\frac{a}{2}-\frac{c}{4},\pm\frac{b}{2}+\frac{c}{4}} se^{ik\cdot\delta}\left[\frac{1}{4}(c_\delta+1)\right], \tag{4.21b}$$

$$p_{11} = J_2 \sum_{\delta=a,b} 2s\cos k\cdot\delta\left[\frac{1}{4}(c_\delta-1)\right], \tag{4.21c}$$

$$p_{12} = J_1 \sum_{\delta=\pm\frac{a}{2}-\frac{c}{4},\pm\frac{b}{2}+\frac{c}{4}} se^{ik\cdot\delta}\left[\frac{1}{4}(c_\delta-1)\right], \tag{4.21d}$$

and

$$c_\delta \equiv \cos\widetilde{q}\cdot\delta = \begin{cases} -J_1/4J_2, & \delta\in \text{NN}, \\ 2\left(\frac{J_1}{4J_2}\right)^2 - 1, & \delta\in \text{NNN}. \end{cases}$$

Diagonalization of $J\mathcal{H}(k)$ returns the spin wave energy spectrum $\Lambda = (\lambda_1, \lambda_2, -\lambda_1, -\lambda_2)$. The values of λ are defined as:

$$\lambda_{1,2} = \sqrt{(h_{11} \pm |h_{12}|)^2 - (p_{11} \mp |q_{12}|)^2}. \tag{4.22}$$

The calculated spin wave spectrum along the (110) direction is shown in Figures 4.15

and 4.16. There is gapless intensity at $q = (0, 0, 0)$ and related momenta by a C_4 rotation along the c axis.

$$q = (0, 0, 0), \quad \pm\frac{2\pi}{a}(q, q, 0), \quad \text{and} \quad \pm\frac{2\pi}{a}(1-q, 1-q, 0), \tag{4.23}$$

It follows that the dynamical spin structure factor is:

$$\begin{aligned}
&\mathcal{S}(k,\omega) \\
&= \sum_{i,j=1}^{3}(\delta_{ij} - (\hat{k})_i(\hat{k})_j)\sum_{\mu,\nu=0}^{1}\langle m_\mu^i(-k,-\omega)m_\nu^j(k,\omega)\rangle \\
&= 2s\mu_B^2\sum_{e=1}^{4}\delta(\omega - J\lambda_{k-\widetilde{q},e})\left[V_{k-\widetilde{q}}^\dagger K_1^\dagger g^\dagger P_k g K_1 V_{k-\widetilde{q}}\right]_{e,e} \\
&\qquad + \delta(\omega - J\lambda_{k+\widetilde{q},e})\left[V_{k+\widetilde{q}}^\dagger K_1^T g^\dagger P_k g K_1^* V_{k+\widetilde{q}}\right]_{e,e} \\
&\qquad + \delta(\omega - J\lambda_{k,e})\left[V_k^\dagger K_2^\dagger g^\dagger P_k g K_2 V_k\right]_{e,e},
\end{aligned} \tag{4.24}$$

The projector operator was defined as $P_k = 1_{3\times3} - \hat{k}\hat{k}^T$. The dynamical spin structure factor has three different contributions from k. They are at $k \pm q$ and k and the powder averaged result is shown in Figure 4.16 for the (110) direction in the lattice. Normally there should be intensity strongly at zero energy near the magnetic zone centers, but there is an exact cancellation of the destructive interference from the two sublattices at the Γ point and $|q| = 0.384$. This only occurs in the exact undistorted $I4_1/amd$ structure, and any distortion away from this would imply that zero energy intensity should arise. The real experimental data does suggest that there is intensity there, and the only way to remove it is by subtracting out the high field $\mu_0 H = 10$ T background.

4.3.8 Spiral plane free energy

The $J_1 - J_2$ Heisenberg model does not initially select a plane for the spirals to propagate within. It natively has SO(3) symmetry. Other perturbing effects like spin orbit coupling or lattice distortions could energetically lift the SO(3) symmetry and select a plane for the spirals to reside within. This section takes a look at these perturbations to determine if there are any symmetry related aspects that appear in this model.

The spiral order parameter can be defined with two orthogonal vectors u and v. Its Fourier transform of magnetic order is then:

$$d = e^{i\theta(r)}(lu + imv) \tag{4.25}$$

where $\theta(r)$ is the direction spins orient in the spiral plane and m and l determine the ellipticity of the spirals. When $m = l$, the spirals project into perfect circles in a two dimensional plane. When $m \neq l > 0$, the spirals are elliptical. When $m = 0$, we recover linear magnetic order. These cases correspond to zero, moderate, and high external magnetic fields, respectively. It should be noted that normally a spiral magnet will have a constant $\theta(r)$ without fluctuations in zero field. Near the incommensurate to commensurate (IC-C) 'lock in' transition observed in $LiYbO_2$ at $\mu_0 H = 3$ T, however, necessitates spatial fluctuations in $\theta(r)$ that eventually will polarize into a linear phase at high enough external magnetic field.

This analysis begins by following the previous analysis for the zero field $l = m$ case in the cubic diamond lattice [29]. The symmetry generators for $LiYbO_2$ in $I4_1/amd$ are $T_{1,2,3}$, S_{4z}, C_{2y} and P. The little group of the wave vector $\widetilde{q}$ from the previous section therefore has P, $T_{1,2,3}$, S_{4z}^2, and $S_{4z}^3 C_{2y}$: $(x, y, z) \rightarrow (y - 1/2, x - 1/2, 3/2 - z)$. We can

now write the magnetic order parameter down as follows:

$$P: \quad d \to e^{i\pi\widetilde{q}} d^*, \tag{4.26a}$$

$$S^2_{4z}: \quad d \to \mathrm{Diag}(-1,-1,1) d^*, \tag{4.26b}$$

$$T_{1,2}: \quad d \to d, \tag{4.26c}$$

$$T_3: \quad d \to e^{-2i\pi\widetilde{q}} d, \tag{4.26d}$$

$$S^3_{4z} C_{2y}: \quad d \to \begin{pmatrix} & 1 & \\ 1 & & \\ & & 1 \end{pmatrix} e^{i2\pi\widetilde{q}} d, \tag{4.26e}$$

We can now compose the free energy density as:

$$f(d) = c_0 |d|^2 + c_1 (d_1^* d_2 + c.c.) + c_2 d_3^* d_3. \tag{4.27}$$

where we note that $T_3 S^3_{4z} C_{2y}: d \to (d_y, d_x, d_z)$. What this ends up telling us is that by minimizing this free energy $f(d)$ we find that the spiral plane depends on the values of c_1 and c_2. The propagation direction of the spirals, which is the axis perpendicular to the plane in which the moments rotate in, is then restricted to the (001), $(1\bar{1}0)$, or (110) planes in $LiYbO_2$.

Experimentally, we know that the wave vector $\widetilde{q}$ in zero field is incommensurate but becomes commensurate under an applied magnetic field. This corresponds to the case when $l \neq m$ as the spirals become more elliptical with some net magnetization within the spiral plane. This invalidates some of the symmetry transformations we applied for $l = m$, but if we assume that these perturbations are weak then we can build upon them as they are approximately correct. The free energy of the commensurate $q = 2\pi(\frac{1}{3}, \frac{1}{3}, 0)$

requires a new term:

$$f_{\mathrm{C}} = f(d) - \widetilde{c}_6 \left((d \cdot d)^3 + c.c. \right). \tag{4.28}$$

To depict the transition of IC-C, a phenomenological sine-Gordon model is used. First, the ground state is assumed IC spiral with set J_1 and J_2 parameters. The IC spiral has wave vector q and the nearby C spiral has wave vector k. We can write:

$$q = k + \delta k + \nabla\theta \tag{4.29}$$

where $\nabla\theta$ is the spatial fluctuation of the order parameter with $l \neq m$. In this approximation, we expand the classical energy around k:

$$\lambda = \lambda_0 + 2\delta \cdot \nabla\theta + \frac{\kappa_{xy}}{2}((\partial_x\theta)^2 + (\partial_y\theta)^2) + \frac{\kappa_z}{2}(\partial_z\theta)^2, \tag{4.30}$$

where $\lambda_0 = -\frac{J_1^2}{4J_2} - 2J_2$. The rigidity for θ is therefore

$$\kappa_{xy} = -\frac{a^2}{16J_2}(J_1^2 - 16J_2^2), \qquad \kappa_z = \frac{c^2 J_1^2}{32J_2}. \tag{4.31}$$

with

$$\delta = \kappa_{xy}\delta k \tag{4.32}$$

Put together, the whole equation becomes:

$$F[\theta] = A \int d^3x \left(\frac{\kappa}{2}(\nabla\theta)^2 + 2\delta \cdot \nabla\theta - c_6 \cos 6\theta \right) \tag{4.33}$$

The equation is the sine-Gordon model [173]. The essence of this model says that there is a soliton number N that determines if the system is IC or C. When $N = 0$, it is IC and when $N = \pm 1$, it is C. The soliton number represents the lowest energy solution of

equation 4.33, so the transition from IC to C depends on the relative energies of $N = 0$ and $N = \pm 1$. We can then derive the critical relation between the two as

$$\kappa^2 c_6 / 4\kappa\delta k = \pi^2/32 \tag{4.34}$$

The IC phase occurs when $\kappa^2 c_6/4\kappa\delta k < \pi^2/32$. Knowing that $l \neq m$ when an external field H is applied, we can then see that the coefficient c_6 trends as:

$$c_6 \propto (l^2 - m^2)^3 \propto H^6 \tag{4.35}$$

Therefore, the transition from IC to C occurs with an increasing external magnetic field that eventually pushes IC q to C k. In $LiYbO_2$, this occurs near $\mu_0 H = 3$ T.

4.4 Discussion

The magnetic properties of $LiYbO_2$ can be understood from the perspective of a stretched diamond lattice. This is similar to the magnetism seen in transition metal spinels with a Heisenberg $J_1 - J_2$ model and indicates that they both have the same underlying physical principles. In both the cubic spinels and the stretched $LiYbO_2$ lattice, bipartite frustration in the $J_1 - J_2$ limit generates spiral magnetic phases. In the cubic limit, the $J_1 - J_2$ model forms spiral magnetic order when $J_2/|J_1| > 1/8$ [29]. The spirals are oriented along high symmetry directions of the lattice at $(q, q, q), (q, q, 0)$, and $(0, 0, q)$ where q is a commensurate or incommensurate value. This also similarly occurs in the extended lattice of $LiYbO_2$ when $|J_1| \leq 4J_2$, but in this case, the wave vectors take on a doubly degenerate $(q, \pm q, 0)$ form only. The tetragonal elongation along the cubic axis severely limits the number of allowed magnetic spiral orders in $LiYbO_2$ as was found in our theoretical analysis. There is not a spiral spin liquid surface in $LiYbO_2$

that can appear that does arise in the ideal cubic diamond lattice limit [28–30]. Our analysis clearly shows that there is a doubly degenerate magnetic ordering wave vector in $LiYbO_2$, but there is not an indication of degeneracy lifting into one of the states or the other.

In zero external magnetic field, the spiral ordering process occurs in two temperature steps at $T_{N1} = 1.13$ K and $T_{N2} = 0.45$ K. These two transition temperatures were determined with specific heat measurements in Figure 4.5. The first transition is an intermediate state where the best representation of the data is an incommensurate spiral state on each of the two bipartite Yb sublattices. However, there is disorder between the relative magnetic phasing of the two sublattices in this intermediate regime. The frustration in $LiYbO_2$ forms this partially ordered state and may reflect other magnetic interactions beyond the $J_1 - J_2$ limit. Additionally, the fully ordered state below T_{N2} breaks the sublattice symmetry required in the Heisenberg $J_1 - J_2$ model we analyzed. The model shows that moments must rotate along the spiral axis with an angle between neighboring spins of 111°. This angle difference maintains the symmetry between both of the Yb sublattices. The experimental data, however, indicates that the magnetic moments break this symmetry and alternate in a staggered magnetic fashion with 34° nearest neighbor rotation followed by 172° nearest neighbor rotation. The spins nearly run antiparallel between the two magnetic Yb sublattices in the experimental data. The origin of this staggered magnetization could be from further single ion properties not included in the Heisenberg limit. We do note that including Ising anisotropy at the nearest and next nearest neighbor limit does not explain this, however [121].

Additionally, the sublattice symmetry breaking could be explained by a lattice symmetry breaking inherent to the system. The crystalline electric field data also suggests that there could be multiple Yb environments by producing split excitations in the $E_i = 150$ meV data. However, our analysis of the distorted model for the Heisenberg

Hamiltonian indicates that a large lattice distortion would be required to account for the staggered magnetic spiral structure we observed. Investigations with high resolution 11-BM data do not indicate that $LiYbO_2$ contains such a lattice symmetry breaking, which leads us to conclude that the staggered magnetization and the multiple crystalline electric field peaks are not caused by a lattice distortion. The high resolution crystallographic data then suggests single crystal measurements to delve into the staggered magnetic structure will be required to investigate further single ion properties that could account for both the crystalline electric field splitting and the staggered spiral magnetic structure with magnetic phasing of 0.58 π.

Upon applying an external magnetic field, $LiYbO_2$ shows an incommensurate to commensurate lock in transition. This occurs at $\mu_0 H = 3$ T in our elastic neutron scattering data. This generic type of lock in transition has also been observed in the related transition metal spinels. For instance, the materials $MnSc_2S_4$ [29, 60–62] and $CoCr_2O_4$ [174–176] show this behavior. However, in the spinels, the incommensurate to commensurate transition happens as a function of temperature rather than external magnetic field. Both $MnSc_2S_4$ and $CoCr_2O_4$ originally have incommensurate spiral order that locks into a commensurate order with decreasing temperature. In the case of $LiYbO_2$, we can explain the lock in transition by the sine-Gordon model where the originally circular spirals become elliptical with a moderate magnetic field. Eventually, the energetics of the commensurate order becomes more favorable under slight ellipticity, which forces the system into a lock in spiral magnetic order at $\mu_0 H = 3$ T. This sine-Gordon model simply takes the $J_1 - J_2$ Heisenberg model and adds an external magnetic field and does not require any further perturbations to the Heisenberg limit.

Overall, the majority of the magnetic behavior in $LiYbO_2$ originates in the $J_1 - J_2$ Heisenberg model we adapted from the cubic diamond lattice. First, the doubly degenerate ordering wave vector of $(q, \pm q, 0)$ is recovered from this model that we observe

in elastic neutron scattering experiments. The theoretical analysis of the spiral planes shows that they should reside perpendicular to $(0, 0, 1)$, $(1, \bar{1}, 0)$, or $(1, 1, 0)$ crystallographic planes. We observe that our experimental data does not allow for the spirals in $LiYbO_2$ to be perpendicular to the ab plane, which rules out the $(0, 0, 1)$ spirals. With our powder experiments, however, we cannot determine any further information. The neutron powder diffraction data does not distinguish between spiral ordering planes as long as they reside perpendicular to the crystallographic c axis. If the lowest energy planes are perpendicular to $(1, \bar{1}, 0)$ or $(1, 1, 0)$, determining this will require a detailed single crystal experiment.

Second, the $J_1 - J_2$ Heisenberg model allows us to determine the ratio of $|J_1|/J_2$ explicitly from the value of q in $(q, \pm q, 0)$. Since $q = 0.384$ at $\mu_0 H = 0$ T, we conclude that $|J_1|/J_2 = 1.426$. This has a physical basis within the lattice too, as we expect that J_1 should be stronger than J_2, but not overwhelm it for $LiYbO_2$. Looking back at the superexchange pathways along J_1 and J_2, they are relatively the same in length even though J_1 is much shorter at 3.3 Åthan J_2 at 4.5 Å. Furthermore, the superexchange pathway of J_1 is nearly 90° while J_2 is close to 180°, which enhances the antiferromagnetic superexchange of J_2 relative to J_1.

Other materials that do not have this superexchange relationship but do have the same type of magnetic sublattice exist. The materials $KRuO_4$ [177] and $KOsO_4$ [178, 179] have the same bipartite magnetic lattices of Ru and Os, respectively, in the $I4_1/amd$ space group. However, their formula contains two extra oxygen anions. The crystallographic structure of these two materials then contains localized RuO_4 and OsO_4 units with antiferromagnetic superexchange requiring two O^{2-} anions. Since J_1 is over 1 Åcloser than J_2 as in $LiYbO_2$, the lack of a strong antiferromagnetic superexchange along J_2 makes J_2 essentially negligible relative to J_1. Both of these materials show commensurate linear order with moments parallel to the c axis where $J_2 \sim 0$ in our Heisenberg model with

unfrustrated magnetic order.

The lowe energy spin dynamics of $LiYbO_2$ reveal the approximate values of J_1 and J_2. The calculated spin structure factor and powder averaged spin wave spectrum in Figures 4.16 and 4.15 show that $J_2 \sim 1/3$ meV and $J_1 \sim 0.475$ meV. However, the experimental data and the calculated spin structure factor do differ. There is a build up of spectral intensity in the experimental data near $E = 0$ meV originating from the Γ point and the magnetic zone centers near $|q| = \frac{2\sqrt{2}\pi}{a} \times 0.384$. The simulations indicate that there is a cancellation of intensity at these points in the ideal $I4_1/amd$ space group with 111° rotating spins in the spiral magnetic phase. This is an exact cancellation produced by the three components accidentally canceling out from $k \pm q$ and k. In the simulation, the two sublattices cancel each other out near zero energy since the symmetry of the sublattices is maintained. In the experiment, this symmetry is inherently broken.

However, even though the $J_1 - J_2$ Heisenberg model cannot account for this magnetic phasing difference in the elastic and inelastic neutron powder diffraction measurements, this work shows that the $J_1 - J_2$ Heisenberg model captures the majority of the behavior of the bipartite frustrated lattice in $LiYbO_2$. This model extends what was previously known for the cubic spinel diamond lattice $J_1 - J_2$ frustration, and opens the door for other materials with a similar magnetic lattice to be explored for unusual magnetic phase behavior such as incommensurate magnetic spirals. If one was able to find a material in which the magnetic Yb ions of $LiYbO_2$ were in the ideal cubic limit, then perhaps the (quantum) spiral spin liquid theorized in the cubic diamond lattice would arise. The Yb ions are uniquely suited for this as they do not suffer from some of the issues the transition metal spinels have, such as magnetic exchange beyond nearest and next nearest neighbor limits.

4.5 Conclusions

Spiral magnetic order in $LiYbO_2$ originates from the local $4f$ electron magnetic moments in a bipartite frustrated magnetic lattice. The lattice can be derived from the cubic diamond lattice by elongating it along one of its cubic axes. In $LiYbO_2$, long range incommensurate spiral order occurs in two steps at $T_{N1} = 1.13$ K and $T_{N2} = 0.45$ K with an ordering wave vector of $k = (0.384, \pm 0.384, 0)$. Between T_{N1} and T_{N2}, an intermediate ordered regime occurs where there is magnetic phase disorder between the two Yb sublattices. In an external magnetic field, $LiYbO_2$ undergoes an incommensurate to commensurate transition where spiral magnetic order is maintained but the ordering wave vector becomes $k = (1/3, \pm 1/3, 0)$. The spiral magnetic behavior below T_{N2} and the incommensurate to commensurate transition can be captured with a $J_1 - J - 2$ Heisenberg model and the overall phase diagram of $LiYbO_2$ is presented in Figure 4.17. This model is adapted from the cubic diamond lattice and re-derived for $LiYbO_2$. There are some discrepancies between the model and the experimental data, such as the two step magnetic ordering in temperature and breaking of the sublattice symmetry upon ordering. The experimental data shows nearly staggered magnetic order between the two sublattices that breaks the sublattice symmetry that could be due to other perturbations on the Heisenberg model that we do not include. Exploring these discrepancies and synthesizing single crystals of $LiYbO_2$ could significantly enhance our understanding of this material and the $J_1 - J_2$ Heisenberg model for both the elongated lattice in $LiYbO_2$ and in the ideal cubic limit.

Table 4.1: Rietveld refinement structural parameters at 1.5 K from elastic neutron scattering measurements on $LiYbO_2$ on HB-2A in the $I4_1/amd$ space group and origin setting two. Within error of the measurement, all ions refined to full occupation and no quantifiable site mixing is present.

T		1.5 K				
χ^2		3.421				
λ		2.41 Å				
$a = b$		4.3824(2) Å				
c		10.0625(2) Å				
Atom	Wyckoff	x	y	z	B_{iso} (Å^2)	Occupancy
Yb	4a	0	0	0	0.28(9)	1.000(6)
Li	4b	0	0	0.5	2.02(30)	1.00(5)
O	8e	0	0	0.22546(7)	0.74(9)	1.00(3)

Table 4.2: Point charge (PC) models of three different coordination shells and crystalline electric field (CEF) fit for $LiYbO_2$ obtained by minimizing observed parameters from $E_i = 300$ meV inelastic neutron scattering (INS) data. Three PC models of increasing size include one (O^{2-} ions), two (O^{2-} and Li^+ ions) and three (O^{2-}, Li^+, and Yb^{3+} ions) surrounding a central Yb^{3+} ion, respectively. The fit resembles the second PC model in sign of the Stevens parameters.

	E_1	E_2	E_3	$\frac{I_2}{I_1}$	$\frac{I_3}{I_1}$	g_{avg}	χ^2	B_2^0	B_4^0	B_6^0	B_4^4	B_6^4
PC (2.5 Å)	33.3	33.8	69.0	0.98	0.08	3.6	51.0	-0.67210	-0.031153	0.000064591	-0.17420	-0.0012000
PC (3.1 Å)	30.9	86.2	87.5	0.10	0.06	3.7	27.8	2.1336	-0.029755	0.000069724	-0.19050	-0.0012660
PC (3.5 Å)	108.6	149.9	156.6	0.07	0.08	4.5	232.0	-4.2146	-0.033288	0.000081398	-0.18211	-0.0014202
Fit	45.0	62.8	127.9	1.74	0.10	3.0	0.002	0.31777	-0.072378	0.0010483	-0.27051	0.0015364
Observed	45.0	63.0	128.0	1.76	0.10	3.0						

Fit wave functions:

$|\omega_{0,\pm}\rangle = 0.901|\mp 1/2\rangle + 0.434|\pm 7/2\rangle$

$|\omega_{1,\pm}\rangle = -0.434|\mp 1/2\rangle + 0.901|\pm 7/2\rangle$

$|\omega_{2,\pm}\rangle = 0.849|\pm 3/2\rangle + 0.529|\mp 5/2\rangle$

$|\omega_{3,\pm}\rangle = -0.529|\mp 3/2\rangle + 0.849|\pm 5/2\rangle$

Table 4.3: Coefficients of the magnetic basis vectors creating the helical models of the base temperature magnetic structure of $LiYbO_2$ at 0 T and 3 T, where $bv_1 = (100)$, $bv_2 = (010)$, and $bv_3 = (001)$ determined from SARAh [126].

	270 mK, 0 T $\mathbf{k} = (0.384, \pm 0.384, 0)$			270 mK, 3 T $\mathbf{k} = (1/3, \pm 1/3, 0)$		
atom (x, y, z)	bv_1	bv_2	bv_3	bv_1	bv_2	bv_3
Yb_1 (0, 0.75, 0.125)	0	-1.26i	1.26	0	-1.26i	1.26
Yb_2 (0, 0.25, 0.875)	0	-1.26i	1.26	0	-1.26i	1.26

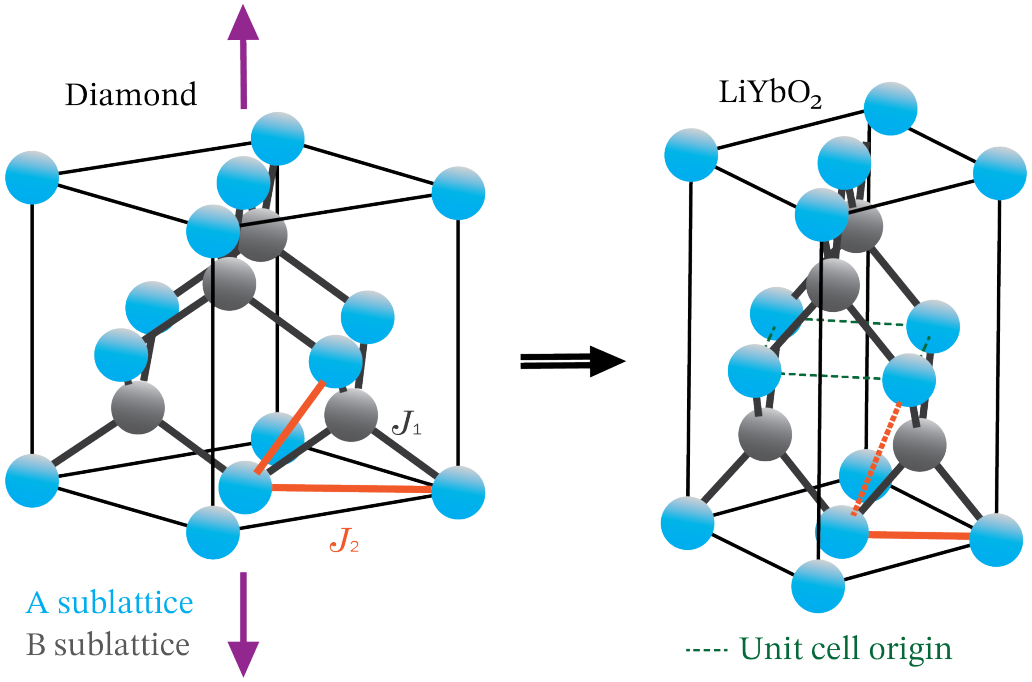

Figure 4.1: The frustrated $J_1 - J_2$ model on a diamond lattice contains two interpenetrating face centered cubic sublattices labeled A (blue) and B (grey) of one magnetic ion in $Fm\bar{3}m$. The nearest neighbor interaction is J_1 which goes between sublattices and the next nearest neighbor J_2 is within a sublattice. When stretched along one of its cubic axes (purple arrows), the equivalency of the J_2 bonds within the plane and the stretched axis is broken. This is represented by one of the original J_2 bonds as a dashed line. The new space group is $I4_1/amd$, and if the elongation is significant enough, the new stretched J_2 bond may be effectively negligible in theoretical analysis. In $LiYbO_2$, the normal unit cell origin is shown with dashed green lines and the dashed J_2 bond is negligible.

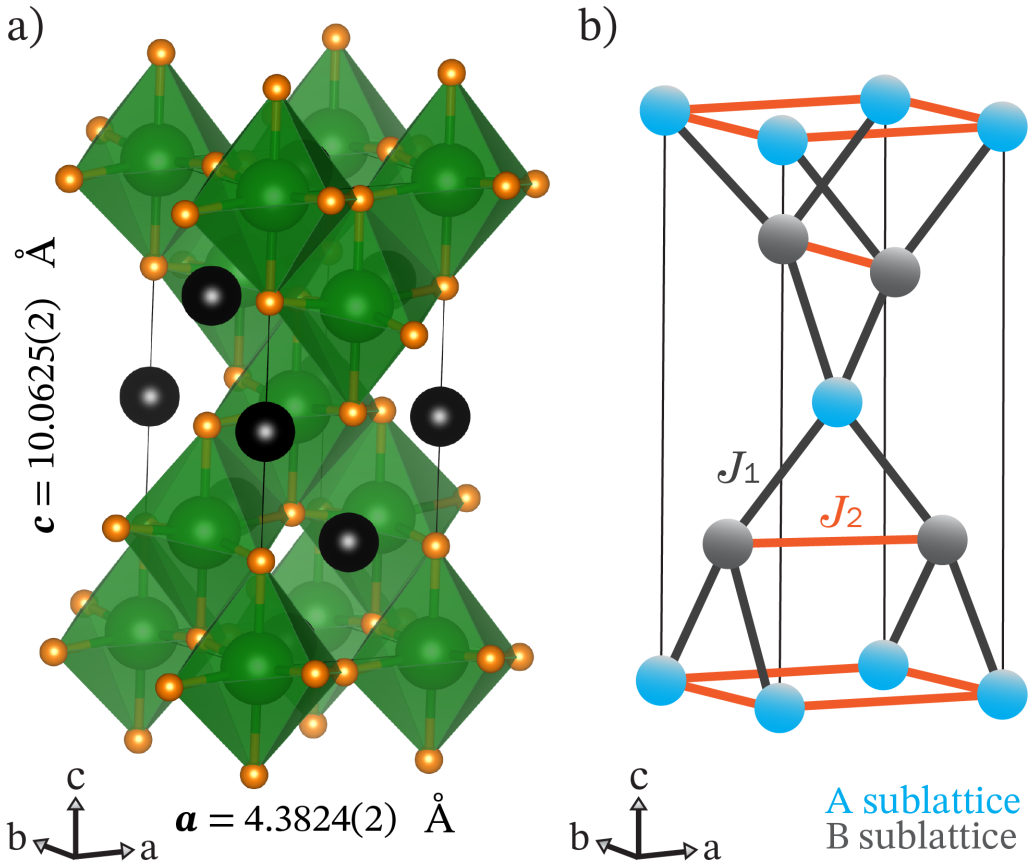

Figure 4.2: a) The crystal structure of $LiYbO_2$ with refined parameters from HB-2A elastic neutron powder diffraction data. The Yb ions (green) are encased in D_{2d} distorted YbO_6 octahedra with interspersed Na ions (black). b) When viewing only the Yb lattice, there are two separate sublattices related by a translation of (0, 1/2, 1/2). This is the elongated diamond lattice, and the bonds shown in orange are J_2 and black are J_1 for the Heisenberg model presented in the main text. All other further neighbor bonds and local anisotropies are not inherently included into the Heisenberg model.

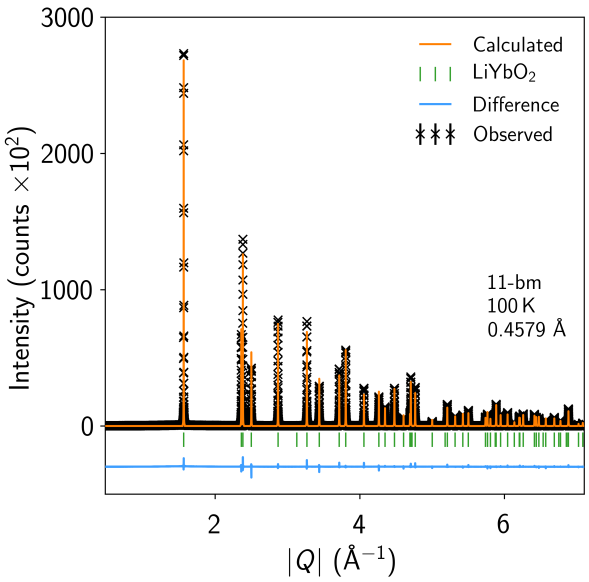

Figure 4.3: Rietvelt refinement of 11-BM data collected on $LiYbO_2$ at 100 K. Despite observing evidence of splitting in crystalline electric field excitations, no subtle peak splitting appeared in this data that would indicate $LiYbO_2$ adopts a slightly lower symmetry setting than $I4_1/amd$. The refined structural parameters are all within resolution of full occupancies and the lattice parameters closely match those of the HB-2A structural refinements from elastic neutron scattering.

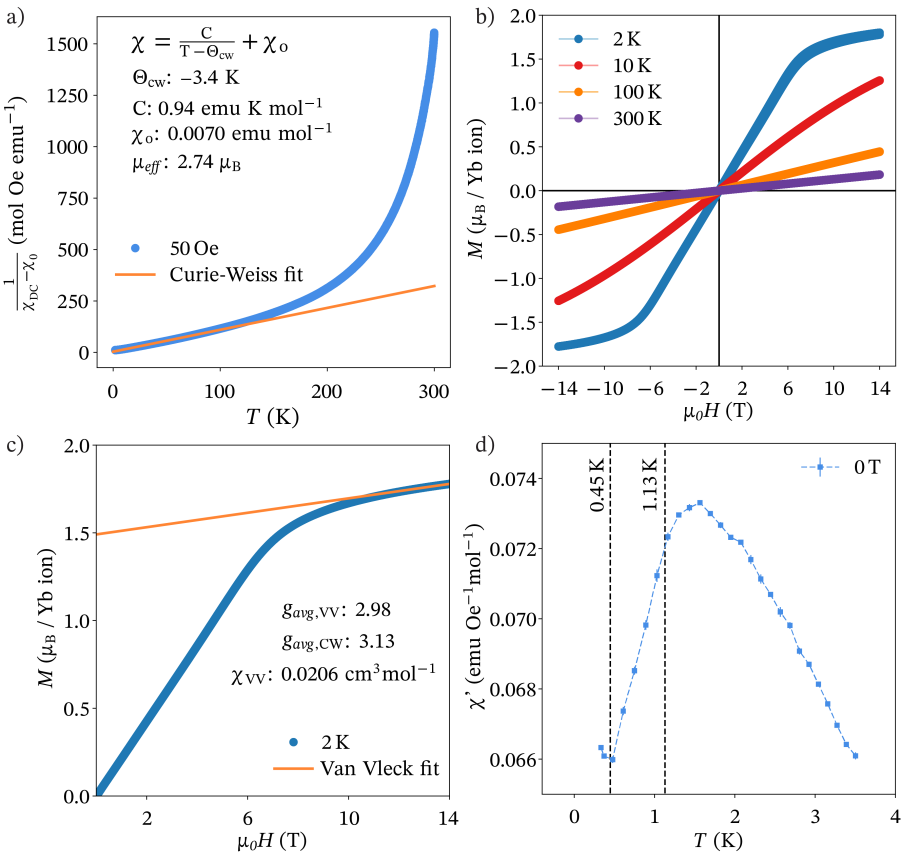

Figure 4.4: a) Inverse magnetic susceptibility of $LiYbO_2$ fit to the Curie-Weiss model from 20 K to 100 K. The high temperature regime from roughly 250 K to 300 K is linear, but this corresponds to multiple Kramers doublets being occupied above the ground state Kramers doublet. Within the ground state Kramers doublet, the Yb ions have an effective moment of 2.74 μ_B with antiferromagnetic mean field interaction strength of $\theta_{CW} = -3.4$ K. A small temperature independent χ_0 term is used. b) Isothermal magnetization of $LiYbO_2$ from 2 K to 300 K and up to $\mu_0 H = 14$ T. Above $\mu_0 H = 10$ T, the Yb moments are saturated at 2 K. c) The slope of the 2 K isothermal magnetization curve above $\mu_0 H = 10$ T can be fit to a line where the intercept at $\mu_0 H = 0$ T corresponds to the powder averaged g factor. The equation is $intercept = g_{avg}\mu_B/2$. The slope of the curve is the Van Vleck susceptibility of field induced transitions to neighboring crystalline electric field states. d) A.c. magnetic susceptibility data shows two features. The first is a broad hump near 1.5 K and the second is an upturn at 0.45 K. The broad feature is just above $T_{N1} = 1.13$ K and the second corresponds to $T_{N2} = 0.45$ K observed in specific heat and elastic neutron powder diffraction data.

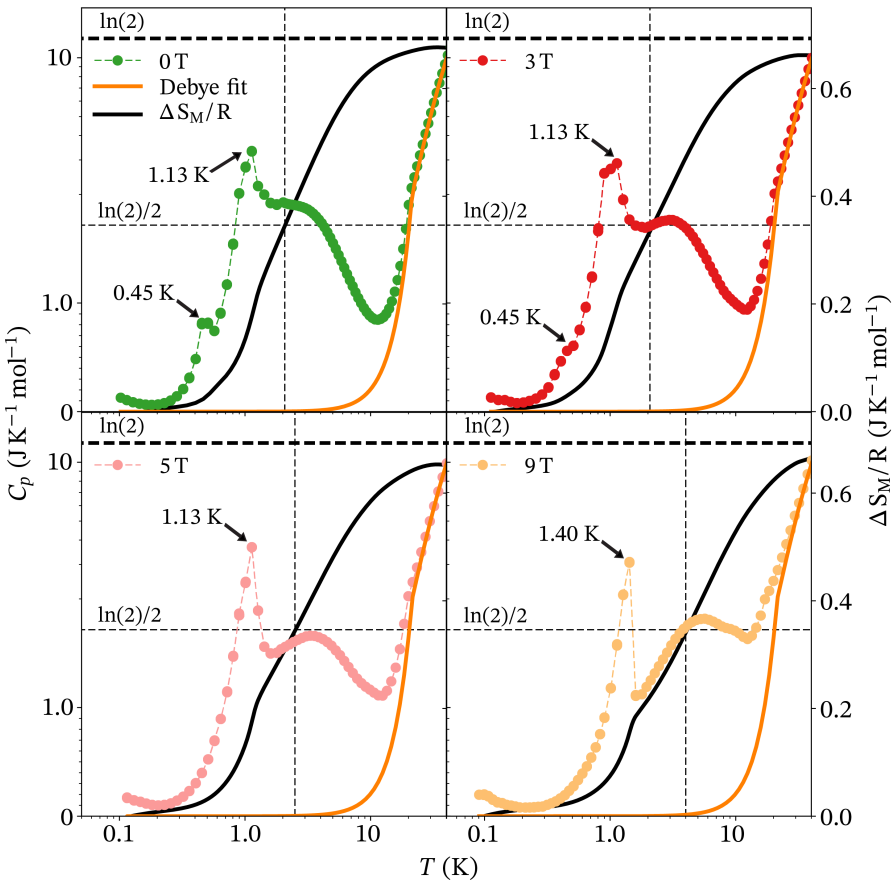

Figure 4.5: a-d) Specific heat $C_p(T)$ of $LiYbO_2$ in varying external magnetic fields overplotted with integrated entropy. The orange line is the double Debye model fit to the high temperature portion of the specific heat curve that is subtracted out to determine the magnetic portion of specific heat of $LiYbO_2$. The dashed black lines correspond to $Rln(2)$ and $Rln(2)/2$. $LiYbO_2$ approaches $Rln(2)$ by 20 K and releases $Rln(2)/2$ between the high temperature specific heat broad feature and low temperature sharp transition at $\mu_0 H = 0$ T. The location of $Rln(2)/2$ shifts up in temperature with increasing external magnetic field.

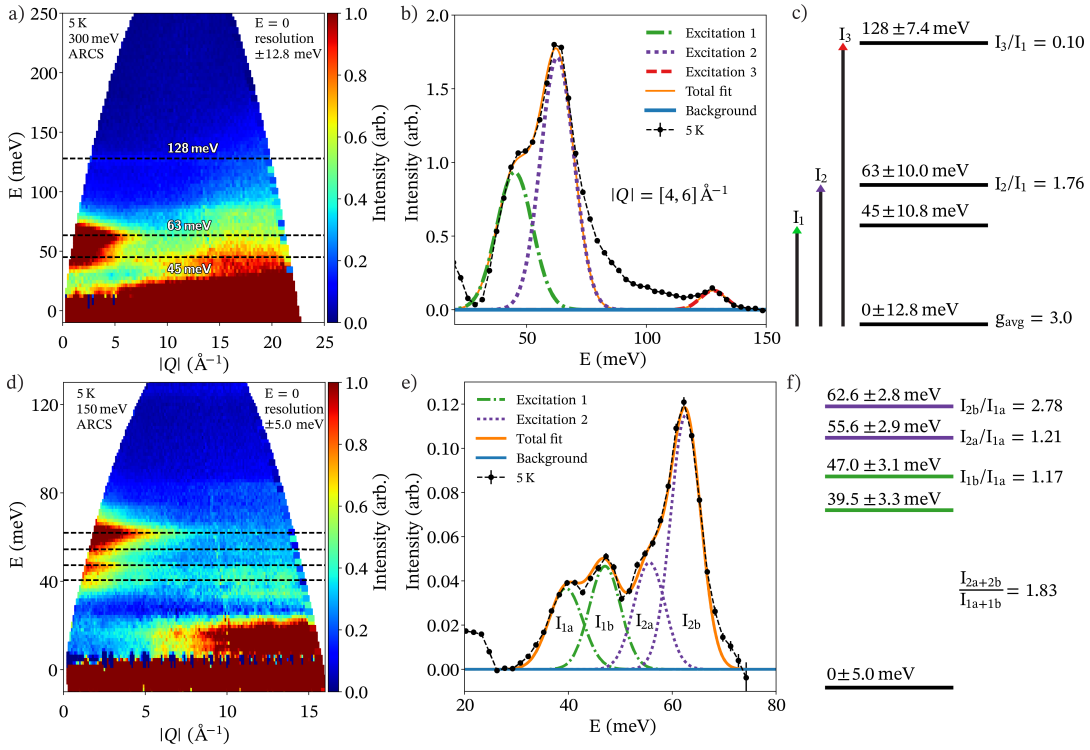

Figure 4.6: Inelastic neutron scattering (INS) data $S(Q, \hbar\omega)$ at 5 K for $LiYbO_2$ on the ARCS spectrometer at ORNL. a) At $E_i = 300$ meV, the full width half maximum (FWHM) resolution is 12.8 meV. There are three excitations from the ground state Kramers doublet centered near 45, 63, and 128 meV represented by the dashed black lines through the color plot. b) Integrating the $S(Q, \hbar\omega)$ color plot from $|Q| = [4, 6]$ Å^{-1} reveals the three crystalline electric field (CEF) modes. The peaks were fit with Gaussian functions to determine the integrated intensity of each CEF level. A linear background term (blue line) was set to zero in this figure. c) The representation of the CEF modes of $LiYbO_2$. The error bars represent the FWHM error of the ARCS instrument at the center of each CEF energy transfer. The ground state g_{avg} was taken from Figure 4.4 isothermal magnetization data. Intensity ratios of I_2/I_1 and I_3/I_1 were calculated relative to the 45 meV first excited state transition. d) At $E_i = 150$ meV, the FWHM resolution is 5 meV. The dashed black lines correspond to the split peaks of the first and second excited state from panels a)-c) in the top half of the figure. b) The splitting of the peaks can be easily seen by taking an integrated cut from $|Q| = [4, 6]$ Å^{-1}. Two separate peaks create each of the excited state Kramers doublets. They are labeled as $1a$ and $1b$ for the first excited state and $2a$ and $2b$ for the second. d) Examining the integrated intensities of these split peaks shows that the total integrated intensity in this lower E_i window matches the overall integrated intensity in the $E_i = 300$ meV window. The error bars represent the FWHM at the energy transfer for ARCS at the center of each peak. The origin of the splitting is discussed in the main text.

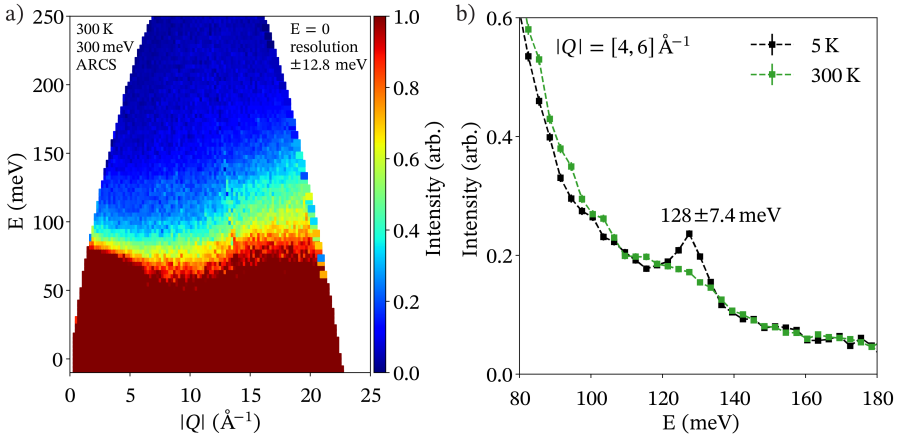

Figure 4.7: In order to verify that the weak 128 meV excitation corresponded to a crystalline electric field (CEF) mode, comparisons of 300 K and 5 K data were conducted. a) The 300 K color plot of $E_i = 300$ meV data does not readily show the CEF excitations from Figure 4.6. b) However, an integrated cut from $|Q| = [4, 6]$ Å^{-1} of the 5 K (black) and 300 K (green) overplotted shows that the 128 meV excitation is still present at 300 K. The mode is thermally broadened, but is still part of the spectrum.

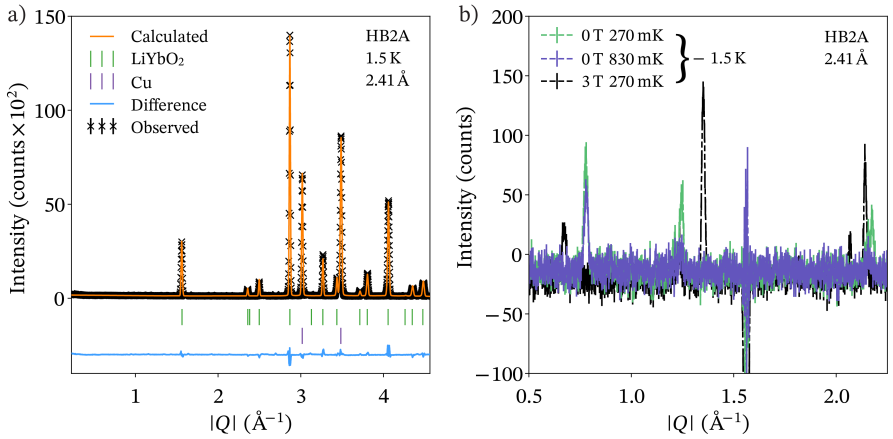

Figure 4.8: a) Neutron powder diffraction data of $LiYbO_2$ collected on HB-2A at ORNL. The Rietveld refinement fit to $LiYbO_2$ structural parameters at 1.5 K (green ticks) is plotted with the signal from the Cu sample can (purple ticks). At 1.5 K, no new magnetic Bragg reflections appear and $LiYbO_2$ is in the $I4_1/amd$ space group. b) Subtracting out the 1.5 K data in panel a) from lower temperature data sets shows new Bragg reflections corresponding to long range magnetic order in $LiYbO_2$. At $\mu_0 H = 0$ T, incommensurate peaks appear at 830 mK that grow in intensity down to 270 mK. At $\mu_0 H = 3$ T, a new set of commensurate magnetic reflections appear as the incommensurate zero field ones disappear.

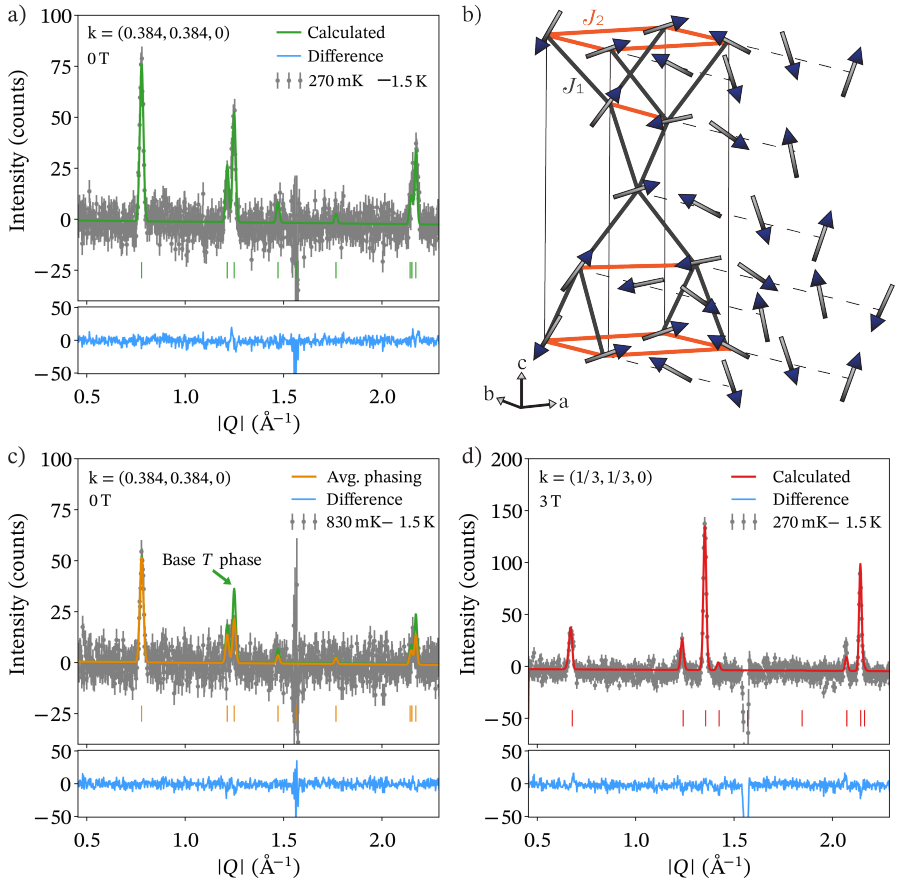

Figure 4.9: Magnetic structure refinements of the 1.5 K subtracted neutron powder diffraction data of $LiYbO_2$ collected on HB-2A at ORNL. a) At 270 mK and $\mu_0 H = 0$ T, the magnetic structure corresponds to a spiral magnetic phase with doubly degenerate ordering wave vector $k = (0.384, \pm 0.384, 0)$ with 1.26(10) μ_B magnetic moments and phasing of 0.58π. There are multiple ways of representing this spiral structure, and the details of the fit are in the main text. b) One of the representations of the spiral structure contains the magnetic moments rotating in the ac plane and propagating along the b axis below T_{N2}. c) Between T_{N1} and T_{N2}, the data still reveals new magnetic Bragg reflections. Two different models for fitting this data include taking the fit from below T_{N2} and reducing its moment size (green) or allowing the sublattice phasing to be random with the same ordered magnetic structure and magnetic moment size (orange). The averaged phasing model best represents this data, meaning that the degree of freedom lost at T_{N2} is the magnetic phase factor of sublattice A to B that takes all values between $[0, \pi]$ above T_{N2} and fixed at one value below T_{N2}. d) At 270 mK and $\mu_0 H = 3$ T, the magnetic structure shifts to lock in to a commensurate spiral phase as shown in the fit in red. This phase contains all of the same qualitative characteristics of the fit in panel a), but the doubly degenerate ordering wave vector is $k = (1/3, \pm 1/3, 0)$.

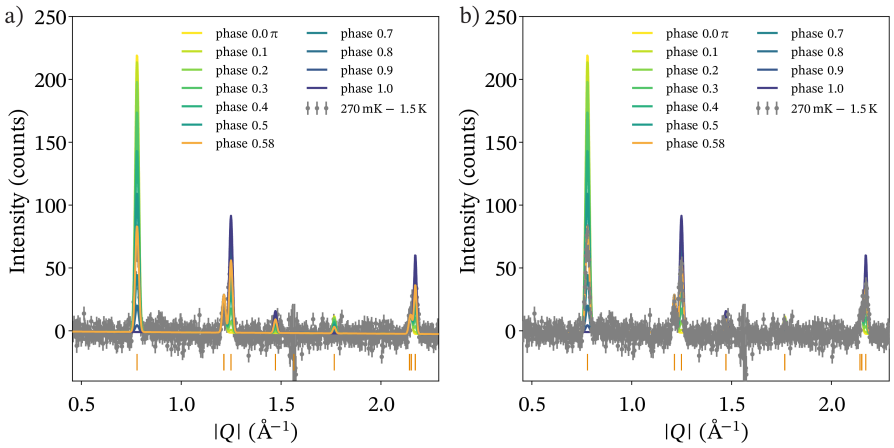

Figure 4.10: Neutron powder diffraction data collected for $LiYbO_2$ on HB-2A at the High Flux Isotope Reactor compared with plots of different relative magnetic phasing between the Yb sublattices. The data is temperature subtracted with a 1.5 K high temperature background. The incommensurate spiral structure has an ordered moment of 1.26(10) μ_B and doubly degenerate ordering wave vector $k = (0.384, \pm 0.384, 0)$. The phasing plots from $[0, \pi]$ show how the intensity of the incommensurate peaks heavily depend on the phase value. The orange fit is the best fit of 0.58π from Figure 4.9. The difference between a) and b) is if the data is plotted on top of the phasing plots or the other way around.

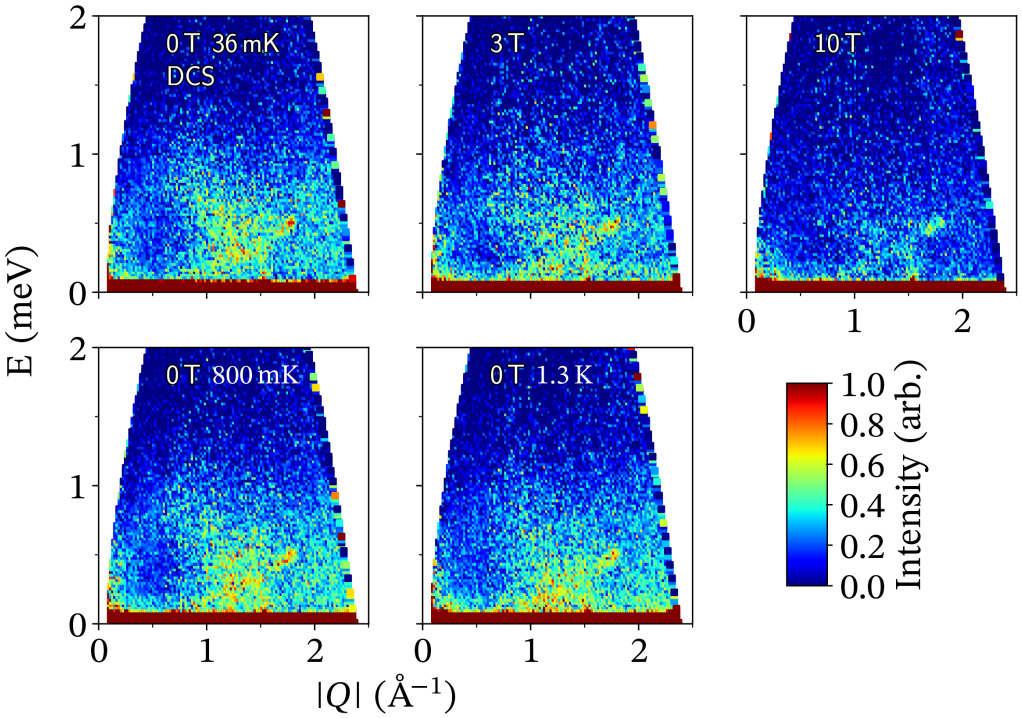

Figure 4.11: Low energy inelastic neutron scattering (INS) data $S(Q, \hbar\omega)$ collected on the DCS spectrometer at NCNR. At $\mu_0 H = 0$ T and 36 mK, $LiYbO_2$ is magnetically ordered in a helical state. Between 450 mK and 1.13 K, $LiYbO_2$ is still ordered but with a disordered relative lattice magnetic phasing value. The difference in the low energy inelastic spectra at $\mu_0 H = 0$ T and 3 T are minimal, where the main difference arises from lower intensity as some spins begin to align with the vertical external magnetic field. By $\mu_0 H = 10$ T, the material enters a spin polarized state. Detector spurions can be seen in the $\mu_0 H = 10$ T near $|Q| = 1.75$ $^{-1}$ Åand $E = 0.5$ meV.

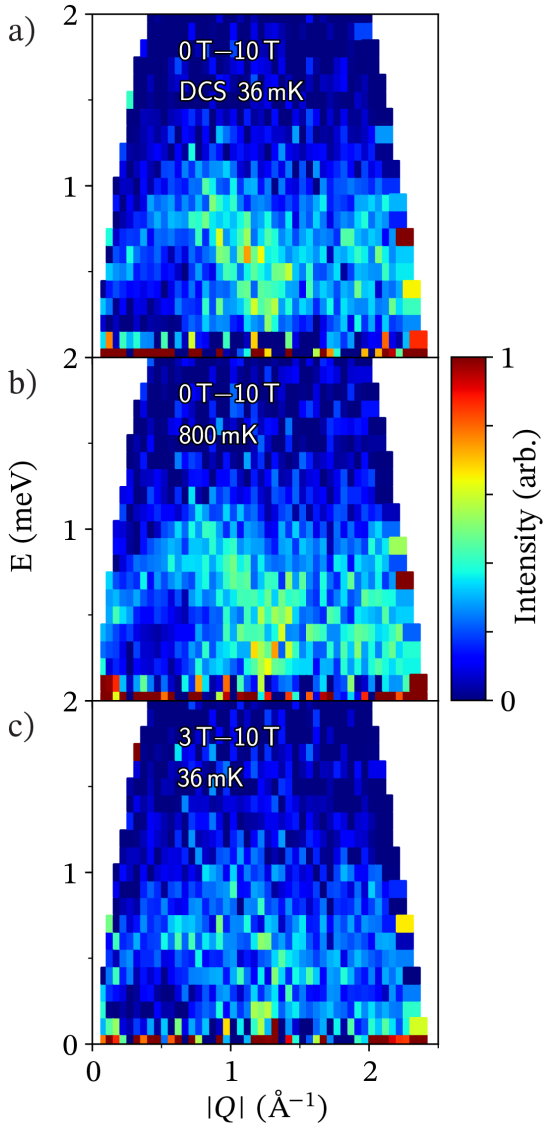

Figure 4.12: Low energy inelastic neutron scattering (INS) data $S(Q, \hbar\omega)$ collected on the DCS spectrometer at NCNR subtracting out the $\mu_0 H = 10$ T data to highlight the spin waves of the spiral phase. a) $\mu_0 H = 0$ T at 36 mK, b) $\mu_0 H = 0$ T at 800 mK, and c) $\mu_0 H = 3$ T at 36 mK. At $\mu_0 H = 3$ T and 36 mK, $LiYbO_2$ undergoes an incommensurate to commensurate transition, but the underlying dynamics of the phase still originate from spiral magnetic order. The $\mu_0 H = 10$ T state is field polarized as shown in Figure 4.11.

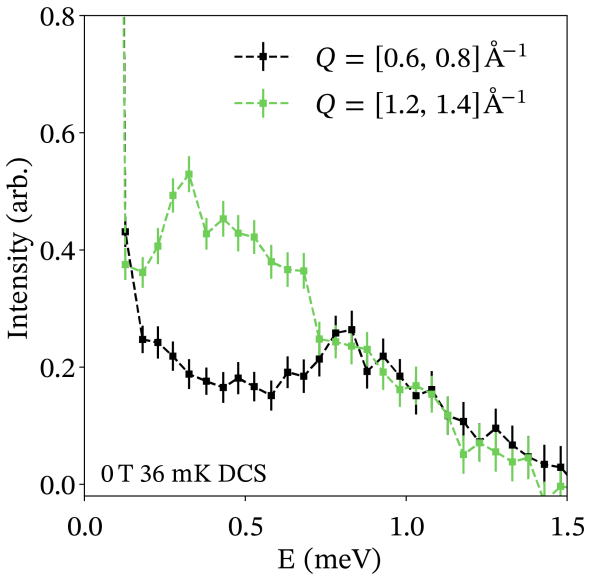

Figure 4.13: Low energy inelastic neutron scattering (INS) data $S(Q, \hbar\omega)$ integrated cuts overplotted to show the spectral weight origin of $LiYbO_2$. The spectral weight is centered near the incommensurate magnetic zone center at $\mu_0 H = 0$ T and peaks near 0.3 meV as shown in green. The upper branch of spin waves is centered near 0.8 meV as shown by the high Q cut in black.

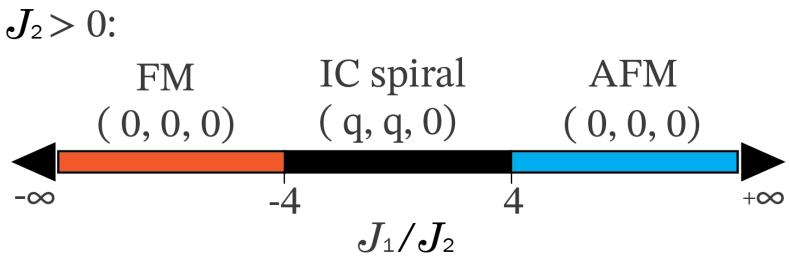

Figure 4.14: A portion of the magnetic phase diagram of the $J_1 - J_2$ Heisenberg model on the elongated diamond lattice. In this case, J_2 is always greater than 0. FM stands for ferromagnetic, AFM stands for antiferromagnetic, and IC spiral stands for incommensurate/commensurate spiral. The FM and AFM structures are commensurate with the lattice.

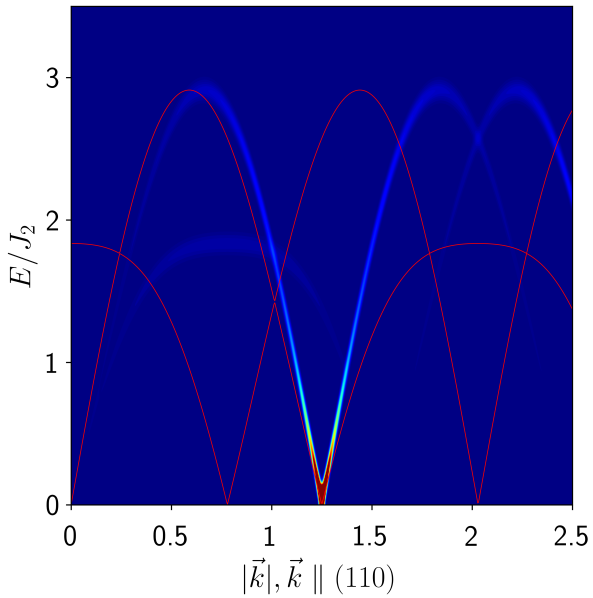

Figure 4.15: Calculated spin wave spectrum and structure factor for $LiYbO_2$ given that $J_1 = 1.42565J_2 > 0$. The strongest intensity resides near the magnetic zone center as similarly seen in the low energy inelastic neutron scattering data in Figures 4.12 and 4.13.

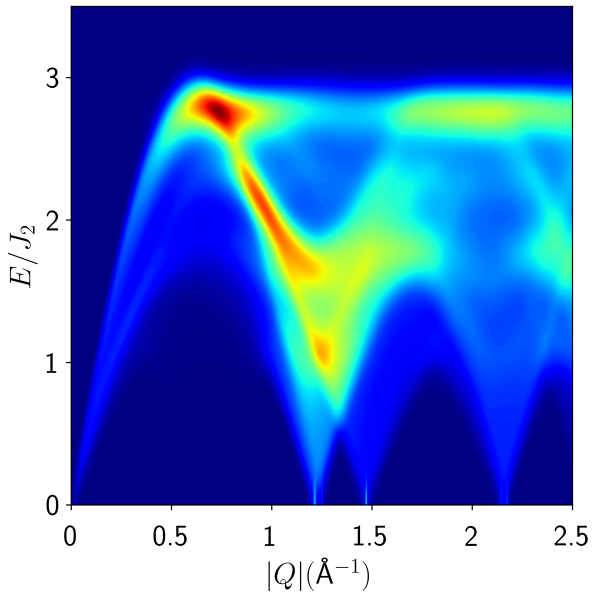

Figure 4.16: The averaged angular structure factor from Figure 4.15 with $J_1 = 1.42565J_2 > 0$. This spin wave spectrum matches the $mu_0H = 0$ T minus 10 T spectrum from Figure 4.12 qualitatively. The branches extend up to $E/J_2 = 3$, meaning that $J_2 \sim 1/3$ meV since the center of the upper band is 0.8 meV in Figure4.13.

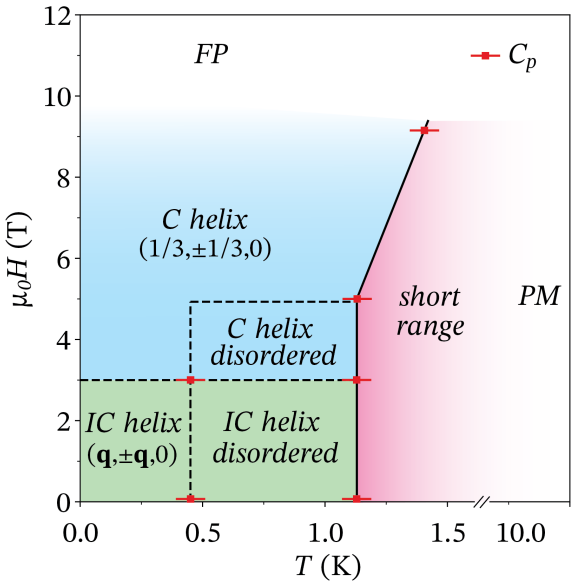

Figure 4.17: The overall phase diagram of $LiYbO_2$ as a function of temperature and external magnetic field. This diagram was created by extrapolating specific heat measurements and elastic neutron powder diffraction refined magnetic structures. The red boxes represent features in specific heat and the differing magnetic phases are from the refined structures. At high temperature, $LiYbO_2$ is in a paramagnetic state. Below approximately 100 K, only the ground state Kramers doublet is occupied, which is responsible for the majority of the single ion properties of the Yb ions in $LiYbO_2$. Below 10 K, short range correlations set in as seen by broad features in specific heat data. Then, a sharp feature appears at $T_{N1} = 1.13$ K at $\mu_0 H = 0$ T followed by another feature at $T_{N2} = 0.45$ K. The upper anomaly shifts up in temperature to 1.40 K at $\mu_0 H = 9$ T as the lower anomaly is suppressed under field. The neutron scattering data suggests that T_{N1} sets incommensurate spiral magnetic order wave vector in $LiYbO_2$ and T_{N2} dictates the relative magnetic sublattice phasing of the spirals. Upon increasing the field to $\mu_0 H = 3$ T, this incommensurate state undergoes a lock in transition to a commensurate spiral phase with similar characteristics.

Chapter 5

Antiferromagnetic order in tetragonal $NaCeO_2$

5.1 Introduction

[1]

The story of $NaCeO_2$ is related to that of $LiYbO_2$ in the previous chapter and our publication on $LiYbO_2$ [121]. Both materials crystallize in the same space group, $I4_1/amd$, with a bipartite network of trivalent magnetic Ln ions. The geometrical magnetic frustration of the $J_{eff} = 1/2$ Yb^{3+} ions in $LiYbO_2$ were shown to form spiral magnetic order in the previous chapter. The spiral order developed as a function of external magnetic field and temperature. In zero field, $LiYbO_2$ showed incommensurate spiral order with a doubly degenerate ordering wave vector that locked into a commensurate doubly degenerate ordering wave vector at $\mu_0 H = 3$ T. These features and the spin dynamics of $LiYbO_2$

[1]This chapter is based on our publication on $NaCeO_2$:[122] Mitchell M. Bordelon, Joshua D. Bocarsly, Lorenzo Posthuma, Arnab Banerjee, Qiang Zhang, and Stephen D. Wilson. Antiferromagnetism and crystalline electric field excitations in tetragonal $NaCeO_2$, *Phys. Rev. B*, **103** 024430 (2021). Copyright 2021 American Physical Society.

were primarily captured in a relatively simple Heisenberg $J_1 - J_2$ model. The propagation wave vector is directly related to the ratio of $J_2/|J_1|$ in the Heisenberg Hamiltonian:

$$H = J_1 \sum_{<i,j>} \mathbf{S_i} \cdot \mathbf{S_j} + J_2 \sum_{<<i,j>>} \mathbf{S_i} \cdot \mathbf{S_j} \tag{5.1}$$

Therefore, the ground state of $NaCeO_2$ is likely connected to the same Hamiltonian as the one describing $LiYbO_2$ as it shares the same type of Ln^{3+} magnetic lattice. We expected that the Hamiltonian describing $LiYbO_2$ would also contain the strongest relevant interactions for $NaCeO_2$. From the previous chapter, we showed that spiral magnetic order originates when J_1 and J_2 compete, but other magnetic phases can arise such as the collinear ferromagnet and antiferromagnet. Additionally, the chemical species constructing the lattice are similar, with monovalent alkali ions and oxygen anions constructing the $I4_1/amd$ setting with the Ln ions, suggesting that any differences between the value of J_1 and J_2 $LiYbO_2$ and $NaCeO_2$ should originate in the difference in Ln ion identity. We note, however, that the ground state in the Heisenberg Hamiltonian only depends on $J_2/|J_1|$, neglecting any local anisotropies brought about by the specific character of the exact Ln ion and lattice parameter shifts due to increasing alkali ion size from Li^+ to Na^+ and Ln size from Yb^{3+} to Ce^{3+}. Similar rare earth dependent phenomena have been reported for the cubic pyrochlores where quantum/classical spin ices and quantum/classical spin liquids [20–25, 29, 30, 92, 93, 95–99, 172], order by disorder phenomena [28, 90, 91, 180], and hidden multipolar order [31, 32, 181–188] have all been reported. The ground state in these pyrochlore materials heavily depends on the local properties of the specific rare earth magnetic ion. This study on $NaCeO_2$ begins to explore the rare earth dependence of magnetic properties in the $I4_1/amd$ space group of the $ALnX_2$ materials.

This chapter overviews our study on $NaCeO_2$ in order to further parameterize the $J_1 - J_2$ model developed for $LiYbO_2$ in the previous chapter. The crystal structure

of $NaCeO_2$, shown in Figure 5.1, is the $I4_1/amd$ structure from the $ALnX_2$ family of materials. As a side note, relative to $NaYbO_2$, $NaCeO_2$ adopts this space group since the Ce^{3+} ions are larger than Yb^{3+} ions, pushing it away from the $R\bar{3}m$ space group in the radius ratio rule Figure 1.4. In $NaCeO_2$, this chapter will show that the local Ce environment generates an extremely well separated ($\sim$ 120 meV) $J_{eff} = 1/2$ Kramers doublet ground state from the free ion $J = 5/2$ manifold. Low temperature bulk magnetic measurements combined with elastic neutron powder diffraction will show that $NaCeO_2$ undergoes long range antiferromagnetic ordering at $T_N = 3.18$ K. The magnetic structure is an A-type antiferromagnet with Ce moments aligned to the crystallographic c axis. In the $J_1 - J_2$ Heisenberg model, we reveal that this structure sits at the limit when $J_1 > 0$ and J_2 is weak.

5.2 Experimental Methods

The synthesis based off of previous reports [189–191] and basic analysis methods for $NaCeO_2$ are shown in Chapter 2. This section overviews the specific instrumental setups and measurement conditions for this material.

5.2.1 Magnetic measurements

Bulk magnetic properties of $NaCeO_2$ were collected with a Quantum Design MPMS3 with a 7 T magnet and a Quantum Design PPMS with a 14 T magnet and vibrating sample magnetometer. Magnetic susceptibility from 2 K to 300 K was collected under $\mu_0 H = 50$ Oe in the Quantum Design MPMS3 and analyzed with the Curie-Weiss law above 20 K. Since $NaCeO_2$ was synthesized in an encased steel tube and is highly air sensitive, the data was collected multiple times. Insidious amounts of ferromagnetic impurities and oxidation of $NaCeO_2$ often worked their way into the measurements.

They appeared as large, unexplainable offsets between the zero field cooled and field cooled data sets and random sharp transitions that were unrepeatable. The samples that oxidized returned from the instrument slightly white colored versus the original yellow-green color. This type of randomness is detailed more in the Appendix A on $NaTiO_2$, where the same features were observed. This chapter uses magnetic susceptibility data without any of these issues with clean data collected on unoxidized $NaCeO_2$.

Specific heat data was obtained with a Quantum Design PPMS from 2 K to 300 K in external magnetic fields of $\mu_0 H = 0$, 3, 5, and 9 T. The $NaCeO_2$ powder was pressed into a pellet beforehand but not sintered as sintering often lead to $NaCeO_2$ degredation by Na evaporation.

5.2.2 Elastic neutron scattering

Elastic neutron powder diffraction data were collected on the POWGEN diffractometer at the Spallation Neutron Source (SNS) at Oak Ridge National Laboratory (ORNL). The $NaCeO_2$ powder was sealed in a He filled glove box in a vanadium canister with a metal-metal seal lid. The sample was placed in a He flow cryostat capable of reaching 1.5 K. Time-of-flight diffraction data were obtained at 1.5 K and 10 K in Frame 2 (centered at $\lambda = 1.5$ Å) and Frame 3 (centered at $\lambda = 1.5$ Å). Refinement of this data was done in the Topas Academic software suite [192] and Fullprof software suite [125] to determine the crystal structure and magnetic structure. The analysis of the magnetic structure was set up with the help of ISODISTORT [193, 194] that fed into Topas. Also, the magnetic peaks observed in $NaCeO_2$ were the exact same magnetic peaks observed previously in $KRuO_4$ [177] which helped narrow down the ordered structure possibilities. The data are shown in Figure 5.6 and Table 5.2. Two small impurity phases of 2.2(1)% Ce_2O_3 and 2.1(2)% Na by weight were observed in these data.

5.2.3 High energy inelastic neutron scattering

High energy inelastic neutron scattering (INS) data $S(Q, \hbar\omega)$ was collected on the Angle Resolved Chopper Spectrometer (ARCS) at ORNL. Polycrystalline $NaCeO_2$ powder (5 g) was placed in an aluminum canister and loaded into a cryostat with a roughly 5 K to 300 K temperature range. Neutrons with incident energies of $E_i = 150$ meV (Fermi 2, Fermi frequency 600 Hz) were used to analyze the $J = 5/2$ ground state multiplet structure of $NaCeO_2$. Neutrons with incident energies of $E_i = 600$ meV (Fermi 1, Fermi frequency 600 Hz) were used to look at the intermultiple excitations to the $J = 7/2$ state. These data are presented in Figures 5.2 and 5.3 with background contributions from the sample can subtracted out with an empty aluminum can measurement.

The six fold degenerate $J = 5/2$ multiplet can split into three doublets following Kramers theorem in $NaCeO_2$. The full details of the general CEF setup is explained above in the Introduction and Methods chapters, and the specific changes for $NaCeO_2$ are as follows: The minimal CEF Hamiltonian describing $NaCeO_2$ with Stevens parameters and operators is:

$$H_{CEF} = B_2^0\hat{O}_2^0 + B_4^0\hat{O}_4^0 + B_4^4\hat{O}_4^4 \tag{5.2}$$

Diagonalizing the CEF Hamiltonian returns the eigenenergies and eigevectors. The eigenvectors were used to determine g factor components and relative intensity ratios of the excited states with equations 1.25, 1.26, and 1.28. The refinement of CEF Stevens parameters was done with the procedure presented in the Methods chapter. Three point charge models calculated with equation 1.24 are displayed in Table 5.1 with the final CEF fits of $NaCeO_2$.

5.3 Results

5.3.1 Crystalline electric field

The inelastic neutron scattering data of $NaCeO_2$ are shown in Figures 5.2 and 5.3. The $E_i = 150$ meV data were used to analyze the $J = 5/2$ ground state multiplet crystalline electric field (CEF) of $NaCeO_2$. There are two excitations $E_1 = 117.8$ meV and $E_2 = 124.8$ meV from the ground state Kramers doublet in the data. Integrated energy cuts through the data in Figure 5.2 reveals that these two excitations are resolution limited and sharp. The first excited state at E_1 is extremely well separated from the ground state Kramers doublet, generating a $J_{eff} = 1/2$ ground state Kramers doublet. Fits to the data along with point charge models of $NaCeO_2$ are shown in Table 5.1. To initialize the fitting, a powder averaged g_{avg} from Curie-Weiss fits was utilized. Additionally, as discussed later, the refined magnetic moment of 0.57 μ_B was used as an additional constraint while fitting the CEF manifold. Overall, the CEF fit of $NaCeO_2$ reveals a mixed m_j Kramers doublet ground state with 5/2 and 3/2 terms and an anisotropic g factor of $g_{//} = 1.41$ and $g_{\perp} = 1.00$.

5.3.2 Bulk magnetic properties

The magnetic susceptibility and isothermal magnetization data collected for $NaCeO_2$ are shown in Figure 5.4. The susceptibility data was modeled with the Curie-Weiss relationship between 50 K to 200 K. Extracted parameters are $\mu_{eff} = 0.994\mu_B = \sqrt{8C}$ and $\theta_{CW} = -7.69$ K. A small background of $\chi_0 = 0.0022$ emu mol^{-1} was used to make the inverse susceptibility linear in this regime. There is a peak in the susceptibility at 3.4 K that has a corresponding inflection at $d(\chi T)/dT$ at 3.3 K. Below this peak, the zero field cooled (ZFC) and field cooled (FC) data sets diverge, indicating the onset of long

range magnetic ordering. This system is minorly frustrated, as θ_{CW} is twice as large as the ordering transition.

Below T_N, isothermal magnetization does not saturate up to $\mu_0 H = 14$ T. Instead, the maximal moment reaches 0.2 μ_B at 35% of what would be expected for $J_{eff} = 1/2$ Ce moments from elastic neutron powder diffraction fits in the following subsection.

Additionally, specific heat measurements were collected and are shown in Figure 5.5 in external magnetic fields of $\mu_0 H = 0$, 3, 5, and 9 T. There is a sharp ordering transition at $T_N = 3.18$ K where the Ce moments antiferromagnetically order. In an applied magneti field, the sharp transition slightly softens and shifts to lower temperatures. This occurs as Ce moments begin to polarize in the external field that is randomly oriented relative to the powder sample. This transition does not directly correspond to the transition observed in magnetic susceptibility, but it is close to the inflection in $d(\chi T)/dT$ where they should match up [195]. Since the magnetic susceptibility samples were smaller masses, any minor impurity from slight air exposure would alter this data more. Therefore, we set T_N from the specific heat data.

5.3.3 $I4_1/amd$ structure

High quality structural data of $NaCeO_2$ was not previously reported. A few previous publications have synthesized $NaCeO_2$ [189–191], but here we present high resolution data analysis from POWGEN. The crystal structure of $NaCeO_2$ was analyzed with Rietveld refinements in $I4_1/amd$ in origin setting 2 as shown in Table 5.2. There was a small amount of Ce_2O_3 and Na impurities as discussed in the experimental methods section, but the main $NaCeO_2$ phase had full occupation of all of its atomic species. These impurities could have resulted from some minor surface oxidation or trace water that decomposed $NaCeO_2$ fully into its constituents. This is unlike $NaTiO_2$, as will be

discussed in Appendix A, that decomposes in multiple steps that first removes Na from the base Na_xTiO_2 crystal structure. In other words, no Na deficient phase of $NaCeO_2$ was detected as a result of this decomposition which would have disrupted the analysis of the chemical and magnetic structures of this material.

The $NaCeO_2$ refined crystal structure contains D_{2d} edge sharing CeO_6 octahedra. The Ce network forms a bipartite lattice as in $LiYbO_2$ in the previous chapter. The nearest neighbor Ce ions along J_1 reside at 3.65105 Åat 1.5 K. The J_2 next nearest neighbor Ce ions are 4.77860 Åat 1.5 K. The difference in J_1 and J_2 is over 1.1 Åin $NaCeO_2$, but as in $LiYbO_2$ previously discussed, the oxygen mediated superexchange along J_2 is enhanced while along J_1 is reduced. The bond angle of J_2 is 164° and that of J_1 is 98 °. The length of the superexchange Ce-O-Ce pathways are 4.834 Åand 4.827 Åfor J_1 and J_2, respectively. Thus, there is precedent for geometric frustration despite J_1 and J_2 naively appearing too significantly different in length.

In the structural analysis of $NaCeO_2$, we observe intensity at the (110) reflection. This reflection should be forbidden in the $I4_1/amd$ space group, but there is weak intensity at 10 K above the magnetic ordering transition in Figures 5.6 and 5.7. There could be a weak violation of the $I4_1/amd$ space group, another minor impurity unaccounted for in this analysis, or a portion of the $NaCeO_2$ had not thermalized to 10 K (second measurement) after warming from 1.5 K (first measurement). We disregard this peak for this analysis, as no other weak peaks appear in the data that would have allowed us to determine its origin.

5.3.4 *A*-type magnetic structure

Elastic neutron powder diffraction data at 1.5 K for $NaCeO_2$ were analyzed in Figure 5.6. This is below the transition $T_N = 3.18$ K in specific heat data where $NaCeO_2$ develops

long range order. There are new magnetic Bragg reflections at $Q = (110)$ and (202) that can be indexed to a commensurate ordering wave vector of $k = (0, 0, 0)$. This wave vector also suggests that intensity should arise at $Q = (002)$, but since we do not observe intensity here, the magnetic moments must reside parallel to this direction. Therefore, the structure contains moments parallel to the c axis. The full structure is an A type antiferromagnet shown in Figure 5.1 and is generated by the irreducible representation Γ_7 in the $I4_1/amd$ space group. The magnetic space group is $I4'_1/a'm'd$. This magnetic structure has also been previously reported for other $I4_1/amd$ space group materials such as $YbVO_4$ [196] and $KRuO_4$ [177]. Rietveld refinement of the $NaCeO_2$ data generated 0.57(2) μ_B Ce moments. Since the Ce moments are $J_{eff} = 1/2$, this corresponds to a $g_{avg} = 1.14$, which is extremely close to the magnetic susceptibility value of $g_{avg} = 1.15$ from Figure 5.4.

5.4 Discussion

The purpose of fully analyzing $NaCeO_2$ after we discovered it magnetically ordered was to determine if it resided within the $J_1 - J_2$ Heisenberg Hamiltonian model's phases from the $LiYbO_2$ chapter. $NaCeO_2$, like $LiYbO_2$, contains $J_{eff} = 1/2$ moments in a tetragonally elongated diamond lattice. The main difference in what determines the underlying magnetic structure should therefore be reliant on the Ln ion identity and the strength of J_1 and J_2. In $LiYbO_2$, spiral magnetic order developed below approximately 1 K with a doubly degenerate incommensurate ordering wave vector of $k = (0.384, \pm 0.384, 0)$. In $NaCeO_2$, we observed a commensurate $k = (0, 0, 0)$ antiferromagnetic state. Both of these materials, in the Heisenberg limit, should have their magnetic structures determined by $J_2/|J_1|$.

The model predicts that when $J_1 > 4J_2$ and $J_1 > 0$, a Néel antiferromagnetic state

should arise. This is the commensurate state we observed fo $NaCeO_2$, suggesting that J_1 is much stronger than J_2 in this material. One could argue that J_2 is nearly nonexistent in this material and J_1 is the overwhelmingly primary interaction. This would make $NaCeO_2$ completely unfrustrated and not require the $J_1 - J_2$ Heisenberg model. However, the Curie-Weiss analysis in Figure 5.4 revealed $\theta_{CW} = -7.69$ K which is higher in temperature than $T_N = 3.18$ K. One can construct the frustration parameter $f = \theta_{CW}/T_N \sim 2.41$ to generate an intuitive sense of the frustration in $NaCeO_2$. If the material is unfrustrated, f is exactly 1. The larger the value of f, the greater the magnetic frustration. Even though $f \sim 2.41$ does not suggest strong magnetic frustration, it does indicate there is a moderate amount of frustration in this material. Therefore, even though J_2 is weaker than J_1, it likely has a moderate frustrating effect on J_1, preventing long range order at $|\theta_{CW}|$ and placing $NaCeO_2$ well within the $J_1 - J_2$ Heisenberg model regime.

In addition, the magnetic exchange interactions in $NaCeO_2$ and $LiYbO_2$ should differ as a result of the Ln ion local characteristics. These Ln ion properties are not captured in the $J_1 - J - 2$ Heisenberg model and could originate from properties such as XXZ anisotropy. This would greatly alter the $J_1 - J_2$ Heisenberg Hamiltonian and its phase boundaries we previously presented for $LiYbO_2$ in the previous chapter. We expect that the full details of the magnetic ordering in $LiYbO_2$ and $NaCeO_2$ depend on these additional Ln ion terms, but the primary facts about the magnetic ordering in these materials is captured in the simpler Heisenberg limit. Future single crystal measurements of these materials could elucidate the finer details of their magnetic interactions.

With both $NaCeO_2$ and $LiYbO_2$, we have parameterized the spiral and antiferromagnetic structures from the $J_1 - J_2$ Heisenberg model when $J_1 > 0$. This model further predicted numerous other phases, such as those shown in Figure 4.14, that depend on the ratio of J_2/J_1. Since $NaCeO_2$ and $LiYbO_2$ belong to the larger $ALnX_2$ family of materials, there is precedent for finding these other phases by varying A, Ln, and X separately

to chemically tune J_1 and J_2. There are reports of the magnetic properties of some of the other $ALnX_2$ materials that crystallize in $I4_1/amd$ down to 2 K. These reports are so far limited to LiLnO$_2$ (Ln = Sc, Lu, Er) [4] and NaLnO$_2$ (Ln = Nd, Sm, Eu, Gd) [3]. Most of these show sharp specific heat transitions with antiferromagnetic Curie-Weiss temperatures. In $NaNdO_2$, there is a sharp specific heat anomaly with overall ferromagnetic interactions [3]. Future experiments could easily identify if $NaNdO_2$ develops the commensurate $k = (0, 0, 0)$ ferromagnetic structure predicted in the $J_1 - J_2$ Heisenberg model. Together with $NaCeO_2$ and $LiYbO_2$, these three materials might fully map out the $J_1 > 0$ phase space from Figure 4.14. Understanding how tuning the chemical species alters the magnetic ground state could then also be used to further fine tune the overall Hamiltonian to determine which materials would generate unusual and exciting magnetic phases.

5.5 Conclusions

$NaCeO_2$ crystallizes in the $I4_1/amd$ space group with $J_{eff} = 1/2$ Ce moments generating a bipartite tetragonally elongated diamond lattice. The ground state Kramers doublet is mixed m_j character and is well separated by over 117 meV from its first excited state. This material displays long range antiferromagnetic ordering below $T_N = 3.18$ K as determined by specific heat measurements. This transition coincides close to a sharp inflection in magnetic susceptibility data where Ce moments are antiferromagnetically coupled with $\theta_{CW} = -7.69$ K. Additionally, elastic neutron powder diffraction revealed two new magnetic Bragg peaks below T_N that can be modeled with a commensurate wave vector $k = (0, 0, 0)$ in an A-type magnetic structure where the 0.57(2) μ_B Ce moments align with the c axis. This structure resides in the $J_1 - J_2$ Heisenberg model presented for $LiYbO_2$ in the previous chapter when J_1 is significantly stronger than J_2.

Table 5.1: Point charge (PC) models and the CEF fit for $NaCeO_2$ obtained by minimizing observed parameters from $E_i = 150$ meV inelastic neutron scattering data and the powder-averaged g_{avg} factor from the magnetic structure. Three PC models represent three coordination shells from a central Ce ion of increasing size, where the first includes O^{2-} ions only, the second has O^{2-} and Na^{+} ions, and the third has O^{2-}, Na^{+}, and nearest neighbor Ce^{3+} ions.

	E_1	E_2	$\frac{I_2}{I_1}$	g_{avg}	χ^2	B_2^0	B_4^0	B_4^4
PC (2.5 Å)	86.2	122.7	0.763	1.46	8.61	-2.4869	0.2766	1.4544
PC (3.5 Å)	104.6	223.5	0.243	2.07	80.73	-10.2981	0.2645	1.5953
PC (3.7 Å)	53.7	179.3	0.744	1.45	58.78	7.4129	0.2943	1.5249
Fit	117.9	124.8	0.844	1.15	0.0003	0.9254	0.3701	1.3928
Observed	117.8	124.8	0.840	1.14				

Fit wave functions:

$|\omega_{0,\pm}\rangle = 0.949|\pm 3/2\rangle - 0.316|\mp 5/2\rangle$

$|\omega_{1,\pm}\rangle = 1|\pm 1/2\rangle$

$|\omega_{3,\pm}\rangle = 0.316|\mp 3/2\rangle + 0.949|\pm 5/2\rangle$

Table 5.2: Rietveld refinement of structural parameters at 1.5 K from POWGEN Frame 2 and Frame 3 elastic neutron scattering data. $NaCeO_2$ was analyzed in the $I4_1/amd$ space group with origin setting 2. Within experimental error, all ions refine to full occupation and no site mixing is present.

T		1.5 K				
$a = b$		4.77860(3) Å				
c		11.04277(11) Å				
Atom	Wyckoff	x	y	z	B_{iso} (Å^2)	Occupancy
Ce	4a	0	0	0	0.057(20)	0.992(5)
Na	4b	0	0	0.5	0.564(20)	1.000(4)
O	8e	0	0	0.21921(9)	0.284(11)	1.000(2)

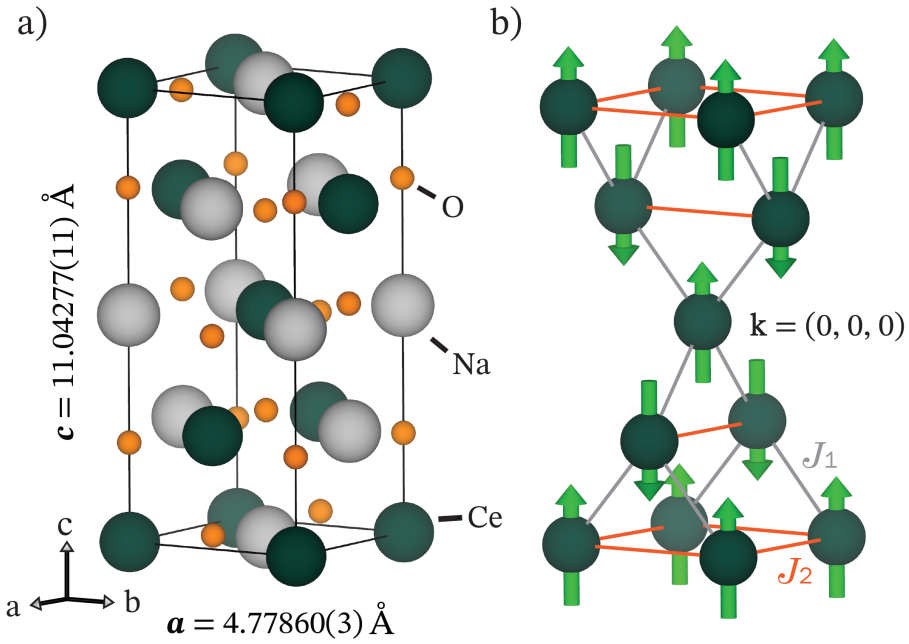

Figure 5.1: a) The crystal structure of $NaCeO_2$ refined in the $I4_1/amd$ space group setting 2 at 1.5 K from elastic neutron powder diffraction data. The Ce^{3+} ions sit in D_{2d} CeO_6 distorted octahedra with interspersed Na cations. This is the same bipartite lattice type as discussed for $LiYbO_2$ in the previous chapter. The paths of J_1 and J_2 are longer in $NaCeO_2$ at 3.65105 Åand 4.77860 Å, respectively. b) Below $T_N = 3.18$ K, $NaCeO_2$ develops long range antiferromagnetic order with wave vector $k = (0, 0, 0)$ and $0.57(2)\mu_B$ Ce moments parallel to the c axis.

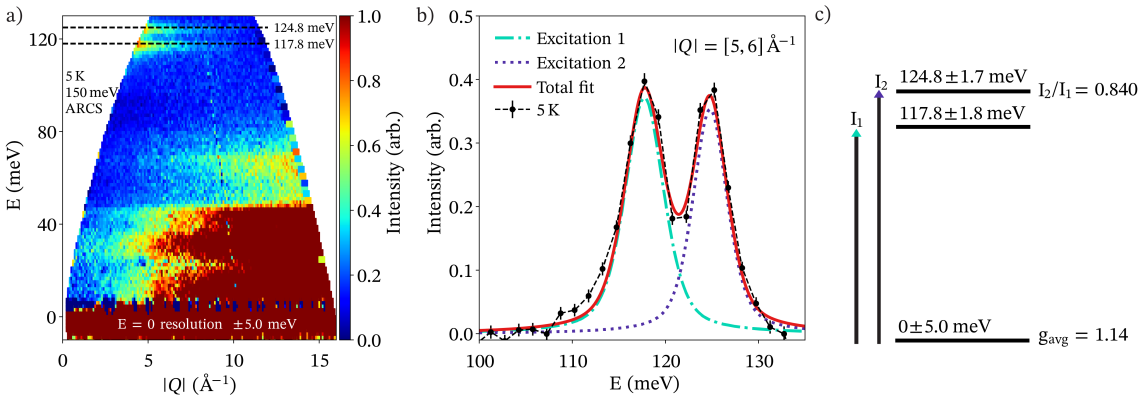

Figure 5.2: a) Inelastic neutron scattering data $S(Q, \hbar\omega)$ at 5 K collected on the ARCS spectrometer at ORNL with neutrons of $E_i = 300$ meV. The full width half maximum (FWHM) resolution at the elastic line is 5.0 meV. There are two resolution limited magnetic excitations out of the $J = 5/2$ Ce^{3+} ground state Kramers doublet at 117.8 meV and 124.8 meV as shown by the dashed black lines. b) The data in panel a) integrated from $|Q| = [5, 6]$ Å^{-1} with a linear background term subtracted. The two excitations were fit to psuedo Voigt peak shapes in dashed cyan and purple that add together (red) to fit the observed data. c) A pictorial representation of the $J = 5/2$ ground state manifold of $NaCeO_2$ shown with error bars as FWHM resolutions at each energy transfer, ground state g_{avg} factor, and integrated intensity ratio.

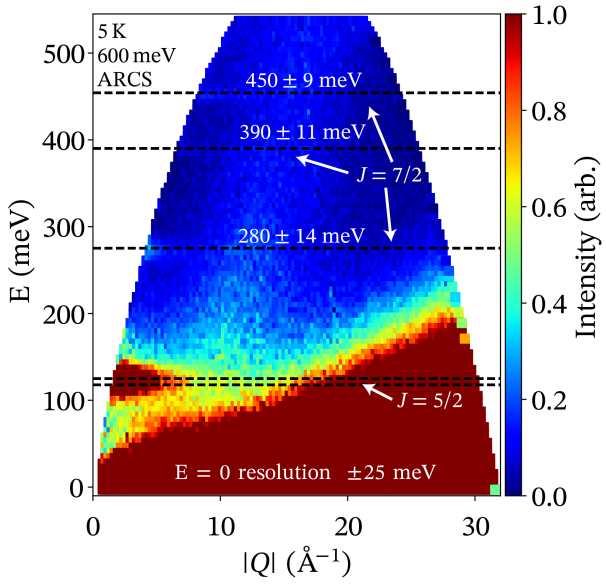

Figure 5.3: Inelastic neutron scattering data $S(Q, \hbar\omega)$ at 5 K collected on the ARCS spectrometer at ORNL with neutrons of $E_i = 600$ meV. The ground state multiplet $J = 5/2$ excitations are separated from the excited $J = 7/2$ multiplet by about 150 meV. There are three $J = 7/2$ excitations that can be identified in this data set near 280 meV, 390 meV, and 450 meV shown with full width half maximum (FWHM) instrumental resolution error bars. The final $J = 7/2$ doublet is out of resolution of this experiment, at a higher energy, or resides at the same energy as another doublet.

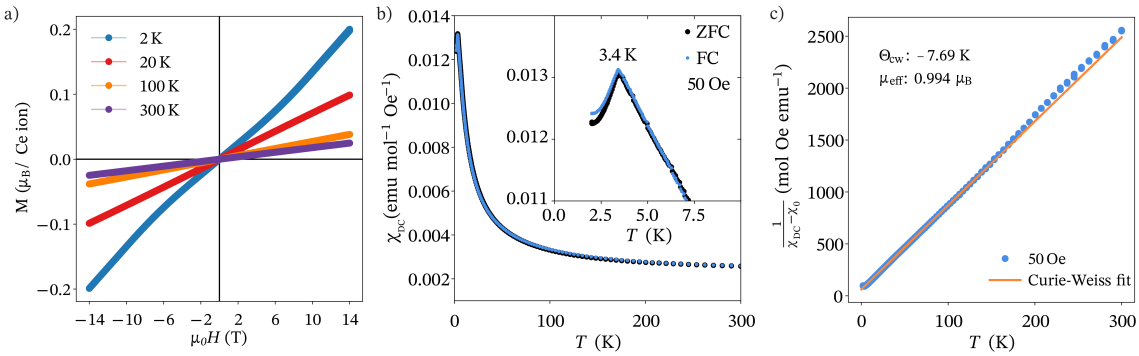

Figure 5.4: a) Isothermal magnetization curves collected at differing temperatures for $NaCeO_2$. The data do not show saturation behavior, but below $T_N = 3.18$ K, $NaCeO_2$ is antiferromagnetically ordered. The isothermal magnetization curve maximally reaches 0.2 μ_B / Ce ion at $\mu_0 H = 14$ T at 2 K. b) Magnetic susceptibility data under zero field cooled (ZFC) and field cooled (FC) states collected on a pristine $NaCeO_2$ sample. Inset: There is a peak in the data near 3.4 K indicating magnetic ordering onset. c) Curie-Weiss analysis from 50 K to 200 K reveals antiferromagnetically coupled Ce moments with $\theta_{CW} = -7.69$ K. The powder averaged $g_{avg} = 1.15$ is extracted from the effective magnetic moment μ_{eff} with $J_{eff} = 1/2$ Ce moments.

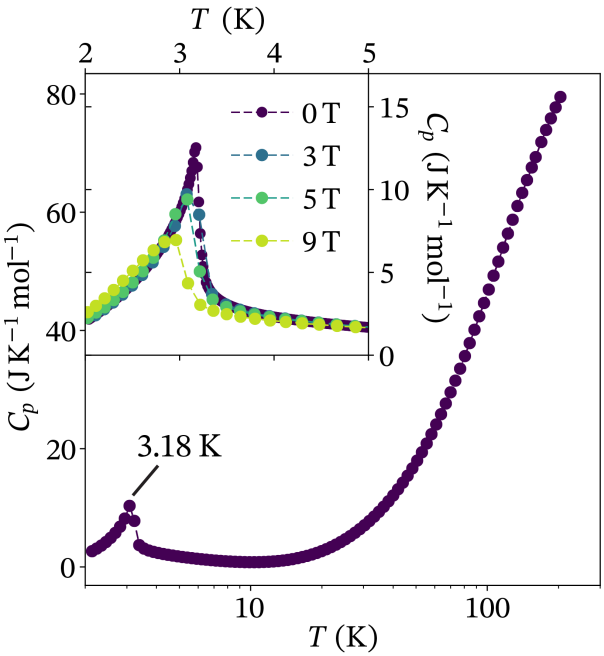

Figure 5.5: Specific heat data collected for $NaCeO_2$ between 2 K to 300 K. A sharp transition occurs at $T_N = 3.18$ K, indicating long range magnetic order. Inset: In an applied external magnetic field, the transition softens slightly and pushes to lower temperature but no new features arise.

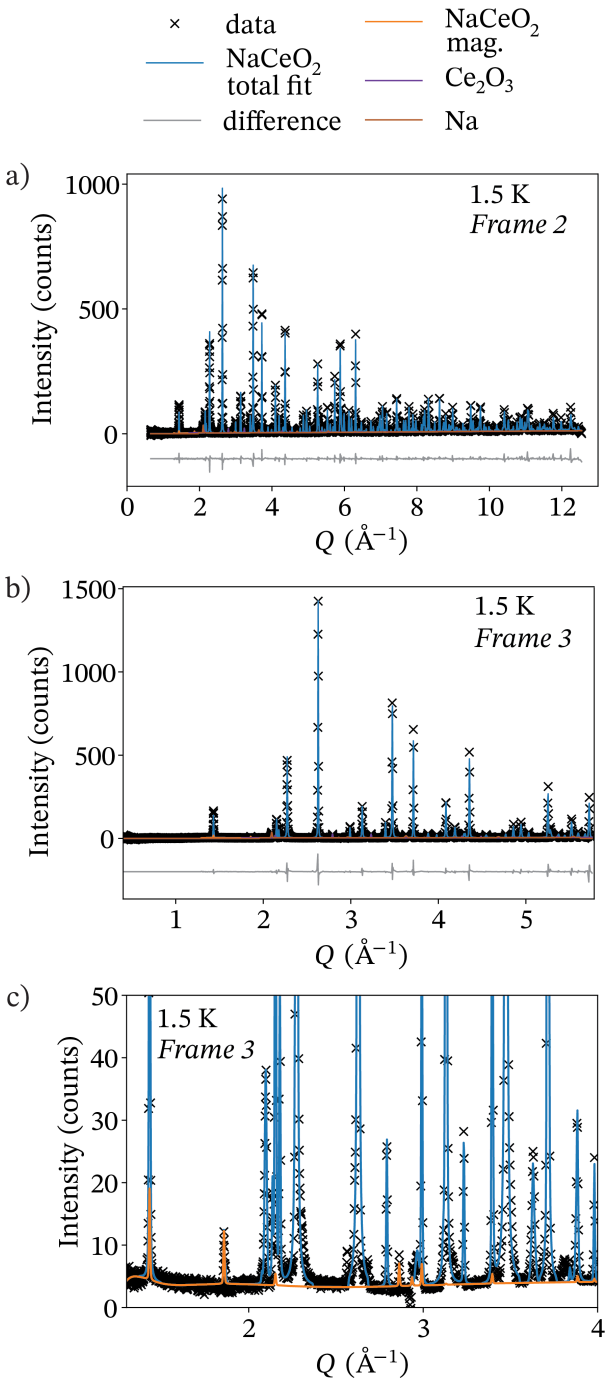

Figure 5.6: Elastic neutron powder diffraction collected on $NaCeO_2$ at POWGEN at 1.5 K in a) Frame 2 and b-c) Frame 3. Analysis of the crystal structure of $NaCeO_2$ was conducted by co-refining Frame 2 and Frame 3 together. The orange curve in c) highlights the magnetic structure fit to an *A*-type antiferromagnetic structure with 0.57(2) μ_B Ce moments.

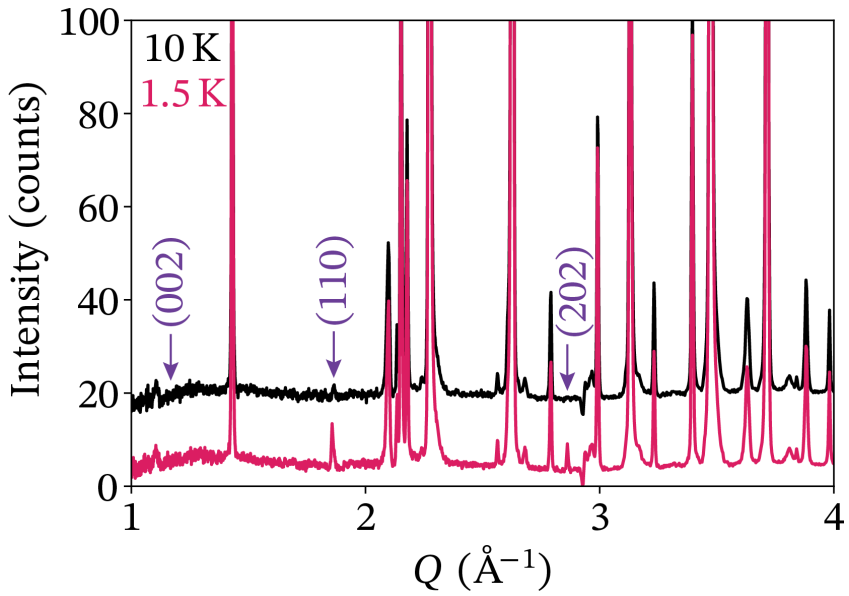

Figure 5.7: Elastic neutron powder diffraction collected on $NaCeO_2$ at POWGEN at 10 K in Frame 3 in black and at 1.5 K in Frame 3 in pink. The (110) reflection is forbidden by the $I4_1/amd$ space group, but there is weak intensity at this position above T_N at 10 K. The magnetic reflections below T_N at 1.5 K arise at (110) and (202). Indexing these peaks indicates a $k = (0, 0, 0)$ ordering wave vector that should also generate intensity at the (002) position. The only way to not generate any intensity at the (002) with this ordering wave vector is to have the Ce moments parallel to the c axis, as neutrons are only sensitive perpendicular to magnetization as discussed in the Introduction.

Chapter 6

Magnetic order in triangular lattice $KCeO_2$

6.1 Introduction

Magnetically frustrated materials are exciting platforms for revealing new magnetic and electronic phases of matter. The triangular lattice antiferromagnet is one of the most studied theoretically and experimentally lattices. Numerous exotic states such as the highly entangled quantum spin liquid ground state have been proposed to arise in the triangular lattice antiferromagnet [20–25], as detailed in the introduction . Strong antiferromagnetic nearest neighbor interactions can prevent conventional long range magnetic order when the underlying chemical lattice is robust, local anisotropies are favorable, and minimal further neighbor interactions are present. For instance, in the Heisenberg limit, the triangular lattice antiferromagnet orders with three sublattice 120° order [51–53]. In this case, strong quantum fluctuations from small spin 1/2 moments have been predicted to disrupt this state and instead induce a quantum spin liquid ground state. The exact form of the spin liquid ground state depends on the model, but two common examples

are the two dimensional Dirac quantum spin liquid [22, 79, 160, 161] or the resonating valence bond spin liquid [45–50]. In general, a small spin triangular lattice antiferromagnet with ideal equilateral geometry is a prime candidate for finding a new or theoretically proposed phase of matter.

However, despite the triangular lattice being a common structural motif in many materials, most materials have inherent issues that prevent them from realizing these exotic states. For instance, in the $NaYbO_2$ chapter, the two materials $YbMgGaO_4$ [48–50, 67–70, 73–77] and $NaYbO_2$ [14, 79–87] were initially compared as they both contain equilateral triangular lattices of YbO_6 octahedra. However, $YbMgGaO_4$ has intrinsic chemical disorder on the Mg and Ga sites, which some believe enhances quantum spin liquid chances while others believe it destroys it. They both display continuum spin excitations and thermodynamic properties indicative of quantum spin liquid ground states, but their origins vastly differ.

Overall, utilizing rare earth metals as the magnetic species in triangular lattice antiferromagnets is highly appealing. Specifically, within the $ALnX_2$ family of materials, there are many triangular lattice $R\bar{3}m$ materials that form. The characteristics of their magnetic ground states and single ion properties can then be chemically controlled by varying the Ln ion. Changing the magnetic ion will effect the moment size, local g factor anisotropy, and magnetic exchange strength and anisotropies. This has been previously seen in the $YbMgGaO_4$ family with $TmMgGaO_4$ [147–149]. In $TmMgGaO_4$, there is no evidence of a quantum spin liquid ground state, but rather there is multipolar three sublattice order that coincides with new magnetic Bragg reflections [147–149]. Understanding the origins of these changes is highly impactful, as it could help dictate which materials in the future would support a spin liquid or other exotic type of ground state.

This chapter overviews a chemical variation on $NaYbO_2$ presented in the last chapter. The material $KCeO_2$ adopts the $R\bar{3}m$ triangular lattice structure in the $ALnX_2$

materials family. Here, we will show that this material contains $J_{eff} = 1/2$ Ce moments with extreme g factor anisotropy resulting from a strong crystalline electric field environment around the D_{3d} Ce^{3+} ions. There is experimental evidence that $KCeO_2$ develops magnetic order in inelastic neutron scattering and thermodynamic probes, but we are unable to resolve magnetic Bragg reflections to fit this low moment system. One curious phenomenon arises in $KCeO_2$ that is also repeated in other $ACeX_2$ materials: an extra crystalline electric field excitation arises within the $J = 5/2$ ground state manifold. We show that this extra mode cannot be explained by any of the usual methods, and we will discuss the potential origin of this anomalous mode.

6.2 Experimental Methods

The synthesis and basic analysis methods for $KCeO_2$ are shown in Chapter 2. This section contains the specific instrumental setups and measurement conditions for this material.

6.2.1 Magnetic measurements

Magnetic properties of $KCeO_2$ were obtained on a Quantum Design MPMS3 with a 7 T magnet and a Quantum Design PPMS with a 14 T magnet and a vibrating sample magnetometer. Isothermal magnetization data were collected at 2, 10, 100, and 300 K on the 14 T PPMS. Magnetic susceptibility under zero field cooled and field cooled conditions were obtained on the MPMS3 with a moderate external magnetic field of $\mu_0 H = 5000$ Oe. The isothermal magnetization curves were linear in the entire temperature range collected up to $\mu_0 H = 14$ T, meaning that the approximation of $\chi = M/H$ is valid up to $\mu_0 H = 14$ T from 10 to 300 K. This is why the relatively large $\mu_0 H = 5000$ Oe field is justified for $KCeO_2$ in the MPMS3. Lower magnetic fields, such as the $\mu_0 H = 50$ Oe and $\mu_0 H =$

20 Oe used for $NaYbO_2$ and $LiYbO_2$ in this thesis, repeatedly observed ferromagnetic impurities in $KCeO_2$ with large and random offsets in magnetic susceptibility data. The origin of these impurities is from the synthesis method in stainless steel tubing and is discussed in the Methods chapter. Unlike $NaCeO_2$ and $NaTiO_2$, we were unable to find a pristine portion of $KCeO_2$ over numerous batches without a ferromagnetic impurity, so the sample that saturated the impurity at $\mu_0 H = 5000$ Oe was used for analysis. The ferromagnetic impurity is not detectable by x-ray diffraction and does not directly impart on the magnetic properties of $KCeO_2$. This extremely small impurity is only observable in magnetic susceptibility measurements.

Low temperature specific heat data was obtained on a PPMS with a dilution refrigerator insert from 80 mK to 300 K in external magnetic fields of $\mu_0 H = 0$, 9, and 14 T. The sample was pressed but not sintered for this measurement as sintering $KCeO_2$ destroys its crystallinity. A 1 mg chunk of $KCeO_2$ was broken from a pressed pellet and sent to Martin Mourigal to measure on his dilution refrigerator setup. The sample was loaded underneath grease on the heat capacity puck in a glove box to limit air exposure. Since the sample size was exceedingly small for this measurement, the dilution refrigerator specific heat data was scaled to high temperature 2 K to 300 K data collected in the normal heat capacity setup. Electron paramagnetic resonance (EPR) data was collected at 6.5 K on an EMXplus Bruker EPR spectrometer in the perpendicular operation mode. The data was modeled with the EasySpin package in MATLAB [151]. Since $KCeO_2$ is highly air sensitive, it was loaded into an EPR tube inside of an Ar filled glove box. The quartz tube was sealed with the torch near the top of the EPR tube. Heating and cooling the sealed tube to obtain the EPR measurements was done slowly as to not make the tube rupture. The final data used for $KCeO_2$ required only a few millimeters of powder inside of the tube.

6.2.2 Elastic neutron scattering

Elastic neutron powder diffraction data were collected on the high resolution BT-1 diffractometer at the National Institute of Standards and Technology (NIST) Center for Neutron Research (NCNR). The instrument was equipped with a ^{3}He cryostat that could get to 300 mK. Data were obtained with incident neutrons of wavelength 2.0774 Å using a Ge(311) monochromator. Structural analysis was performed with a Rietveld refinement in the GSAS/EXPGUI program [152, 153] and is shown in Figures 6.1 and 6.1 and in Table 6.1. No new magnetic Bragg reflections were observable in this data. There were small peaks close to the elastic line originating from the sample can and environment.

6.2.3 High energy inelastic neutron scattering

High energy inelastic neutron scattering (INS) data $S(Q, \hbar\omega)$ were collected at the wide Angular-Range Chopper Spectrometer (ARCS) at the Spallation Neutron Source (SNS) using 5g of $KCeO_2$ powder at 5 K and 300 K. The powder was placed in an aluminum can in a top loading cryostat. Two incident energies of $E_i = 300$ meV (Fermi 1, Fermi frequency 600 Hz) and 600 meV (Fermi 1, Fermi frequency 600 Hz) were used to analyze the crystalline electric field (CEF) transitions of $KCeO_2$ in the $J = 5/2$ ground state and $J = 7/2$ excited state. Contributions from the aluminum sample can were removed with empty can scans at both incident energies and temperatures. These data are shown in Figures 6.3, 6.5, and 6.4.

The six fold degenerate $J = 5/2$ multiplet can split into three doublets following Kramers theorem in $KCeO_2$. The general CEF setup procedure is explained above in the Introduction and Methods chapters. The specific changes for $KCeO_2$ are as follows: The minimal CEF Hamiltonian describing $KCeO_2$ with Stevens parameters and operators is:

$$H_{CEF} = B_2^0\hat{O}_2^0 + B_4^0\hat{O}_4^0 + B_4^3\hat{O}_4^3 \tag{6.1}$$

Diagonalizing the CEF Hamiltonian returns the eigenenergies and eigevectors. The eigenvectors were used to determine g factor components and relative intensity ratios of the excited states with equations 1.25, 1.26, and 1.28. The refinement of CEF Stevens parameters was done with the procedure presented in the Methods chapter. Three point charge models calculated with equation 1.24 are displayed in Table 5.1 with the final CEF fits of $KCeO_2$. In $KCeO_2$, an extra CEF mode arises. The choice of the $J = 5/2$ states was in the end finalized by comparing with recent quantum chemical calculations of this material in Ref. [15].

6.2.4 Low energy inelastic neutron scattering

Low-energy inelastic neutron scattering (INS) data $S(Q, \hbar\omega)$ were collected using 10 g of $KCeO_2$ powder at the Cold Neutron Chopper Spectrometer (CNCS) instrument at the Spallation Neutron Source (SNS), Oak Ridge National Laboratory (ORNL). The instrument was equipped with a 8 T magnet and a dilution insert capable of reaching 40 mK. Incident neutrons of $E_i = 3.32$ meV were used to search for low energy magnetic excitations. The magnet and instrument background were removed by subtracting empty copper can scans at 1.8 K. Further subtractions were done by taking out the high temperature lattice contributions at 12 K. Remnant vertical streaks in the data did occur in 12 K data subtraction as a result of thermal shifting and are visible in the 40 mK $-$ 12 K subtracted data sets. This is shown in Figure 6.8.

6.3 Results

6.3.1 $R\bar{3}m$ crystal structure

Elastic neutron powder diffraction collected at 300 mK on $KCeO_2$ are shown in Figure 6.2 The refined $R\bar{3}m$ structural parameters are displayed in Table 6.1 $KCeO_2$ has previously been synthesized and has structural properties reported near room temperature in Ref. [197]. The parameters from that study were used as initial starting points for the refinement of the neutron powder diffraction data. In our analysis, we did not observe any quantifiable chemical impurities, site mixing, or vacancies in the $KCeO_2$ phase within 1% of experimental resolution. There are additional small peaks near the elastic line, but they do not index to the main phase and are likely a result of the varying alloys in the sample can itself. No new magnetic Bragg peaks were observed down to 300 mK, and therefore no magnetic structure was determined. As will be discussed below, the ordering transition of $KCeO_2$ is close to 300 mK, and future experiments to lower temperature could be used to verify long range order with elastic neutron powder diffraction.

6.3.2 Bulk magnetic properties

The inverse magnetic susceptibility, isothermal magnetization, and electron paramagnetic resonance (EPR) data for $KCeO_2$ are shown in Figure 6.7. No splitting between zero field cooled and field cooled data were observed. Fits to inverse susceptibility to the Curie-Weiss law were conducted between 20 K to 200 K. However, the data is linear between 2 K to 300 K, and therefore any temperature regime taken over this data set returned similar Curie-Weiss parameters. The extracted parameters from the fit revealed antiferromagnetically coupled Ce moments with $\mu_{eff} = 1.22\mu_B = \sqrt{8C}$ and $\theta_{CW} = -7.7$ K. The calculated powder averaged Curie-Weiss $g_{avg} = 1.41$ assuming $J_{eff} = 1/2$ Ce

moments. The isothermal magnetization curves show linear behavior up to $\mu_0 H = 14$ T at 10, 100, and 300 K. The 2 K isothermal magnetization begins to curve slightly near $\mu_0 H = 5$ T. The expected maximal moment in $KCeO_2$ is 0.6 μ_B to 0.7 μ_B, and these isothermal magnetization curves are unable to saturate this system.

The EPR response of $KCeO_2$ is highly anisotropic. The data displays one sharp peak corresponding to $g_\perp = 2.0013$ with minimal broadening of the full width at half maximum (FWHM) of $\mu_0 H = 0.000307$ T. Normally, one peak in EPR indicates one overall symmetric g factor. However, the peak shape of this signal is not symmetric, meaning that $g_{//} \neq g_\perp$. Attempting to make the two equal overestimates the lower portion of the EPR curve. Therefore, $g_{//}$ must produce a peak at another location in the EPR spectrum. However, we did not observe any other peaks in this data set. The only way to account for this is by setting $g_{//} \sim 0$. It should be noted that the broad intensity near $\mu_0 H = 0$ mT is instrumental background. Calculating g_{avg} with equation 1.27 returns 1.6340, which is larger than the 1.41 value extracted from Curie-Weiss analysis. The EPR measurement is a more direct analysis of the g factor, so this value is what was used going forward in the crystalline electric field analysis.

Specific heat measurements of $KCeO_2$ collected from 80 mK to 300 K in external magnetic fields of $\mu_0 H = 0$, 9, and 14 T are shown in Figure 6.6. There are two distinct broad features in the specific heat data. The first arises near 3 K and it shifts to higher temperatures with increasing magnetic field. This likely indicates the onset of short range order in $KCeO_2$. The second is a slightly sharper feature near $T_N = 300$ mK. This peak indicates the onset of magnetic order. In an external magnetic field, the anomaly softens and shifts to lower temperatures due to Ce moments beginning to polarize under the field.

This second anomaly is not extremely sharp as is seen in the other materials measured in this thesis. This could be due to the fact that an extremely small sample size of 1

mg was required to measure on the dilution refrigerator setup. The sample was loaded and placed underneath grease in a glove box by Martin Mourigal who performed the measurement. However, since the sample is exceedingly small and the sample stage has to be kept in air for a significant period of time on the order of tens of minutes, small amounts of air could have gotten though the grease and begun to attack the outer layer of the $KCeO_2$ pressed piece. Regardless, the fact that we were able to obtain this measurement on such a highly air sensitive material is phenomenal and helps identify the ordering transition temperature in this material.

6.3.3 Crystalline electric field excitations

High energy inelastic neutron scattering data on $KCeO_2$ are shown in Figures 6.3, 6.5, and 6.4 Two incident energies of $E_i = 300$ meV and 600 meV were used. The crystalline electric field (CEF) of $KCeO_2$ is uncommonly large and on the same scale as $NaCeO_2$ in the previous chapter. The $J = 5/2$ ground state multiplet has its excitations at $E = 119$ meV and $E = 146$ meV. A third mode appears at $E = 171$ meV. All three of these excitations are limited by the instrumental resolution at their respective energy transfers. The $J = 5/2$ ground state should only have two CEF excitations as in $NaCeO_2$ in the previous chapter. The origin of the third mode will be discussed further down.

The higher energy $E_i = 600$ meV data collected for $KCeO_2$ were used to observe the $J = 7/2$ excited multiplet states. The $J = 7/2$ state can maximally split into four doublets, as previously discussed for $LiYbO_2$ and $NaYbO_2$. We observe three out of four doublet excitations at $E = 280$, 370, and 440 meV. The fourth doublet could be outside of the resolution of this experiment or close enough to one of the other doublets that they appear at the same energy with the instrumental resolution at $E_i = 600$ meV. Additionally, the final mode could be above 600 meV. The bottom of the $J = 7/2$

manifold at 280 meV is consistent with the expected spin orbit coupling strength of Ce^{3+}. No states originating primarily from the $J = 7/2$ manifold should appear significantly below 280 meV (i.e. the 171 meV mode cannot arise from the $J = 7/2$ manifold).

Analysis of the multiplets was conducted with energy cuts integrated in $|Q|$ in Figures 6.3 and 6.4. The $E_i = 300$ meV integrated intensities were used to model the CEF $J = 5/2$ multiplet structure, ignoring the 171 meV extra excitation. This extra excitation was ruled out by referencing a recent quantum chemical calculation approach to modeling the CEF in $KCeO_2$ [15]. This report used multireference configuration-interaction with spin orbit coupling (MRCI+SOC) to calculate the $J = 5/2$ and $J = 7/2$ multiplet structures. They determined the first two excitations should arise near $E = 121$ meV and $E = 143$ meV. The transition between $J = 5/2$ and $J = 7/2$ appears close to $E = 252$ meV. This further suggests that the 171 meV mode is anomalous and not originating directly from the CEF split J manifolds. Therefore, the CEF analysis presented herein excluded the 171 meV mode and its origin possibilities are discussed further on.

The CEF energy scheme with integrated intensity ratios and ground state Kramers doublet g factor components is shown in Figure 6.5. Fits to the CEF modes with these parameters is displayed in Table 6.2. The fit wave functions contains a mixed m_j 1/2 and 5/2 ground state. Calcuated g factor components are $g_{//} = 0.2825$ and $g_{\perp} = 2.0015$. While fitting this data, there was a trade off between forcing the fit to find $g_{//} \sim 0$ and getting the integrated intensities and energies close. The best compromise fit of the data ended up overestimating the integrated intensity of I_2/I_1 significantly. This possibly suggests that the leftover intensity is pushed into I_e of the extra excitation at 171 meV. Adding $I_e/I_1 + I_2/I_1 = 0.699$ which is close to the best fit presented in Table 6.2.

Also, we did attempt to model the data with the $J = 7/2$ as the ground state, as this would produce 3 excitations. However, there is no precedent for placing the $J = 7/2$ multiplet as the ground state. This would require inverting the sign of spin orbit coupling

or time. The way to model the system in this manner is to pretend that Ce^{3+} is replaced by Yb^{3+}. However, even in this case, there was never a fit that produced $g_{//} \sim 0$.

6.3.4 Low energy dynamics

Low energy inelastic neutron scattering spectra of $KCeO_2$ are shown in Figure 6.8. These data cover the field and temperature dependence of the low energy dynamics of the material at 40 mK and 12 K in external magnetic fields of $\mu_0 H = 0$ T and 8 T. These data are collected below the specific heat anomaly near 300 mK and are likely within the ordered regime of $KCeO_2$. Even though no Bragg reflections are observable, the magnetic spectral weight in these low energy spectra arise near $|Q| = 1.4$ Å. This is close to the magnetic zone centers along $(1/3, 1/3L = [0, 4])$, which would be expected for three sublattice magnetic order. The band width of excitations reaches approximately 1.5 meV in this data. The $\mu_0 H = 0$ T and 12 K data was used as an approximate background for the 40 mK data. At 12 K, $KCeO_2$ is in a paramagnetic state. The subtracted 40 mK − 12 K data reveal two spin wave branches. The first is gapless up to 1 meV with origin near $|Q| = 1.4$ Å. The second maximally reaches 1.5 meV but has spectral weight centered at 1.25 meV. This second branch has a smaller band width than the lower branch. When an external magnetic field of $\mu_0 H = 8$ T was applied, the low energy 40 mK fluctuations begin to suppress as Ce moments begin to polarize with the field. The low energy gapless modes of the first branch begin to quench at this field.

As a side note, the temperature of this experiment was determined by measuring the sample can temperature. It is difficult to reach thermal equilibrium at dilution refrigerator temperatures. The $KCeO_2$ sample was pressed, but as stated before in the methods section, it cannot be sintered. Therefore, we expect the actual temperature of $KCeO_2$ to be slightly higher than 40 mK, probably near 100 mK. It is definitely below the

300 mK transition from specific heat, otherwise spin wave excitations would not arise.

6.4 Discussion

Specific heat and low energy inelastic neutron scattering data suggest that $KCeO_2$ develops antiferromagnetic order below $T_N = 300$ mK. The correlations from magnetic susceptibility of $\theta_{CW} - 7.7$ K compared to the ordering transition also indicates strong geometrical frustration in this material. These observations of magnetic order are additionally consistent with recent reports on the sulfur-based $KCeS_2$ [198].

We were unable to determine the magnetic structure of $KCeO_2$ with elastic neutron scattering, but there are a couple of reasons why we did not detect new magnetic Bragg peaks. First, the elastic neutron scattering data was collected at 300 mK. This is right on top of the C_p anomaly. The BT-1 spectrometer was equipped with a ^{3}He insert, but it could only reach 300 mK. Going below 300 mK into the fully saturated ordered regime would help resolve any magnetic Bragg reflections.

Second, if we compare the ordered moment expected for $KCeO_2$ with the ordered moment observed in $NaCeO_2$ in the previous chapter, we can see that the magnetic moment in $KCeO_2$ should range somewhere between 0.5 μ_B to 0.8 μ_B. An ordered moment of 0.57 μ_B was visible in $NaCeO_2$ as the structure was commensurate and generated most of its new antiferromagnetic intensity at two new magnetic Bragg reflections. Additionally, the high flux of the time of flight POWGEN spectrometer helped resolve the new peaks. Simulating 120° order with ordering wave vector $k = (1/3, 1/3, 0)$ as the magnetic ground state for $KCeO_2$ is outside of the resolution of the BT-1 experiment when the Ce moments are 0.6 μ_B or smaller. The maximally expected moment for a fully ordered Ce moment would be 0.82 μ_B from $g_{avg} J_{eff} \mu_B = 0.82 \mu_B$ when $g_{avg} = 1.6340$ and $J_{eff} = 1/2$. As seen in $NaYbO_2$, the ordered moment is reduced by strong effective spin 1/2 moments,

and this could also happen here in $KCeO_2$.

The strongest indication that $KCeO_2$ develops three sublattice antiferromagnetic order is the low energy inelastic neutron scattering data in Figure 6.8. The sample in this measurement was placed in a dilution refrigerator that was capable of reaching 40 mK. The spin wave branches originate near the magnetic zone centers $(1/3, 1/3, L = [0, 4])$ and the K point of the material. This data was obtained on CNCS, which unfortunately trades off Q resolution for high neutron flux. Therefore, while we were able to see magnetic Bragg peaks in elastic cuts of the DCS data for $NaYbO_2$ in its chapter, this could not be done for $KCeO_2$. A future experiment on DCS for $KCeO_2$ or a lower temperature dilution refrigerator elastic powder diffraction measurement would greatly aid in determining the magnetic structure in this material.

However, the main conundrum surrounding $KCeO_2$ is not the magnetic structure in this material. Instead, the extra crystalline electric field (CEF) excitation at 171 meV is the most glaring piece of data out of place in this material. A Ce^{3+} ion has a $J = 5/2$ ground state manifold following Hund's rules explained in the Introduction and Methods chapters. In the local D_{3d} CEF environment, the six fold degenerate $J = 5/2$ manifold can maximally split into three doublets following Kramers theorem. The next excited $J = 7/2$ manifold begins at least 250 meV above the $J = 5/2$ manifold from the quantum chemical calculations [15]. Therefore, the 171 meV mode is well below the $J = 7/2$ manifold and cannot get its primary character from any of its m_j components.

The most comment explanations for an extra CEF mode in Ce^{3+} compounds is phonon coupling or vibronic bound states [112–115, 199–201], embedded hydrogen [31, 188, 198, 202–205], chemical impurities with multiple Ce environments [75, 115, 157, 198–201, 206], or any combination of these. The phonon and vibronic explanations are difficult to verify and require detailed understanding of the phonon branches and their symmetries relative to the symmetries of the CEF modes.

None of these conventional explanations, however, can come close to explaining the extra mode in $KCeO_2$, primarily because the 171 meV mode is (1) intense and (2) well above the phonon cutoff of $KCeO_2$. The Ce ground state wave function is commonly known to strongly couple to the chemical lattice [112–115, 199–201] which can split Kramers doublets without breaking time reversal symmetry. The CEF and phonon modes can bind to create a vibronic bound state, too. This has been observed in othe *Ln* materials like $CeAl_2$ [112, 113], $CeCuAl_3$ [114, 115], $LiYbF_4$ [199], and $YbPO_4$ [201]. Though, these materials have CEF modes that are well below the phonon cutoff of their respective lattices. Additionally, this type of phonon-CEF interaction usually generates two new modes symmetrically split around the origin of the CEF mode, which in total generates 3 states. If we assumed, for instance, that the 146 meV and 171 meV mode had such an origin, there should be intensity at their center near 158 meV where the original CEF mode would have arisen. If we assumed 146 meV was the center, then the 119 meV and 171 meV modes are not symmetrically split around it. Finally, if we compare the 119 meV and 146 meV modes to those calculated with the quantum chemical MRCI+SOC approach, they match up and only leave behind the 171 meV mode unaccounted for. These factors strongly suggest that a phonon or vibronic state cannot generate one mode well above the phonon cutoff in $KCeO_2$.

Hydrogen impurities in materials can generate single unexplained CEF modes [31, 188, 198, 202–205]. However, $KCeO_2$ is an incredibly air and moisture sensitive material. It degrades in under a minute when left in air, and air or moisture exposure is usually the most common reason why a material has a hydrogen CEF mode. In order to generate a strong 171 meV hydrogen mode, one would expect a massive amount of hydrogen near the same concentration per unit cell as the Ce ions would be required. This level of impurity would suggest that $KCeO_2$ has been exposed to anything but an Ar or He atmosphere for a significant amount of time, and in that case, it would have degraded

and absorbed water. Additionally, one would expect that random hydrogen inclusion would alter lattice parameters and local CEF environments randomly, which would incite significant broadening of the nominal Ce CEF modes at 119 meV and 146 meV or even more CEF peaks that would be unexplained. The peaks we observe in Figure 6.3 are instrument resolution limited.

In general, Ce^{3+} is unstable relative to Ce^{4+}. This valence impurity could arise if the material slightly oxidizes from minor air exposure. However, Ce^{4+} is non magnetic. It would not generate any CEF excitations. Therefore, this cannot account for the 171 meV mode either.

Another Ce environment in $KCeO_2$ could generate new CEF excitations. For instance, if there were two D_{3d} Ce^{3+} environments, one would expect two sets of three $J = 5/2$ doublets with two excitations from $E = 0$ meV each. This would generate four excitations, not three as observed in $KCeO_2$. Though, one could imagine that two of the excitations accidentally overlapped. On the other hand, if the second Ce environment was in a perfect cubic symmetry, then a quartet excitation rather than two doublet excitations would arise. This could generate exactly one new CEF excitation. However, there are two reasons why these Ce environments cannot account for the 171 meV mode. First, the 171 meV mode is on the same magnitude as the 119 meV and 146 meV modes. This suggests that the second environment should have a concentration in $KCeO_2$ similar to the first environment. This rampant type of impurity would have been easily discernible with our elastic neutron powder diffraction measurement in Figure 6.2. Only a single new environment would generate the required single unexplained 171 meV excitation. This, in turn, suggests it would be a periodic impurity, which, in turn, would generate new Bragg reflections or vastly alter the Bragg reflection intensities that are not part of the original structure. This is not observed in Figure 6.2. Second, the quantum chemical MRCI+SOC reference [15] did calculate the CEF modes of a local cubic CeO_6 in $KCeO_2$.

Even when the local octahedral symmetry was cubic, the CEF modes still generated doublets rather than a single quartet. This is due to the fact that the neighboring K^+ ions beyond the CeO_6 affect the CEF environment. The K^+ ions are situated in D_{3d} symmetry around the Ce ions, and therefore, they split the CEF maximally into a series of doublets. Overall, in order to generate one new magnetic CEF mode from a new Ce environment, a highly unlikely combination of coincidences would have to coincide: (1) the new environment does not change the crystal structure; (2) the new environment has at least one of its CEF excitations directly underneath one of the original Ce environment CEF modes; and (3) the concentration of the new environment has to match that of the original Ce environment.

Other materials have seen an extra CEF mode with D_{3d} Ce^{3+} magnetic ions. The aforementioned $KCeS_2$ [198] and $Ce_2Zr_2O_7$ [188, 204] are the most prominent examples in the literature with a single identifiable extra CEF mode. They reported a single extra CEF mode, but in both of these materials, the mode was disregarded as it was relatively weak in intensity relative to the main CEF modes. These modes were disregarded as weak impurities, hydrogen incorporation, or a vibronic state. The pyrochlore $Ce_2Sn_2O_7$ [31, 205] additionally shows extra CEF modes, but identifying if there is a single new mode or multiple new modes is difficult.

Perhaps the most intriguing study that is currently underway is the series of compounds $RbCeX_2$ from $X = [O, S, Se, Te, SeS, TeSe]$. Preliminary analysis of these materials shows that their D_{3d} Ce^{3+} ions have exactly one new CEF mode that is high in energy in the oxide and shifts with the overall CEF $J = 5/2$ states down in energy to the telluride. A chemical trend like this in the $R\bar{3}m$ structure from materials synthesized differently than $KCeO_2$ suggests this is an inherent property of Ce^{3+} in D_{3d}, at least in the $ALnX_2$ materials.

This extra 171 meV mode is not the only anomaly in the CEF fitting of $KCeO_2$.

The $g_{//}$ component measured by electron paramagnetic resonance (EPR) should be close to or exactly zero. This was similarly observed for $KCeS_2$ [198]. Ironically, there is a relatively straightforward way to make one of the g factor components zero in this Ce environment. In D_{3d} symmetry, Ce^{3+} can form a dipole-octupole ground state Kramers doublet [32, 207]. This special doublet is purely $m_j = 3/2$ and symmetrically enforces $g_{\perp} = 0$. However, this is the exact opposite of what is observed for $KCeO_2$ and $KCeS_2$. Furthermore, pushing the $m_j = 3/2$ states below $m_j = 1/2$ usually requires an extremely strong CEF environment like CeO_8 found in the Ce pyrochlores like $Ce_2Zr_2O_7$ [188, 204]. Our fit of the 119 meV and 146 meV excitations to the $J = 5/2$ manifold suggest that the ground state Kramers doublet contains no $m_j = 3/2$ character. This is, in part, enforced because we use the EPR analysis to constrain the CEF fitting procedure.

It will be intriguing to watch the development of understanding of the magnetic structures in the $ALnX_2$ materials adopting the triangular lattice $R\bar{3}m$ structure. In particular, why $NaYbO_2$ ($4f^{13}$, one hole) and $KCeO_2$ ($4f^1$, one electron) develop quantum disorder versus three sublattice order is a key question to understanding unconventional magnetism in triangular lattice materials. Both of these materials contain $J_{eff} = 1/2$ Ln^{3+} magnetic moments with strong antiferromagnetic θ_{CW} interactions. However, $NaYbO_2$ develops a continuum of excitations resembling a two dimensional Dirac spin liquid. The reason why $KCeO_2$ behaves significantly differently likely originates in its strong g factor component anisotropy and strange CEF manifold. Resolving the ordered ground state below $T_N = 300$ mK and understanding the 171 meV CEF mode will lead to a proper and more in depth future comparison of $NaYbO_2$ and $KCeO_2$.

6.5 Conclusions

$KCeO_2$ develops magnetic order below $T_N = 300$ mK as determined by specific heat measurements and low energy inelastic neutron scattering data. The low energy dynamics resemble spin waves that would appear in three sublattice antiferromagnetic order that originate close to the K point of $KCeO_2$. Elastic neutron scattering shows that $KCeO_2$ crystallizes in the ideal $R\bar{3}m$ equilateral triangular lattice structure devoid of significant chemical impurities or site mixing. The Ce moments reside in a strong crystalline electric field environment with D_{3d} symmetry that separates the $J_{eff} = 1/2$ Kramers doublet ground state by 118.8 meV to its first excited state and 146.2 meV to its secon excited state. High energy inelastic neutron scattering reveals that there is a third excitation at 170.5 meV that cannot be explained by conventional means. Investigating this extra mode and its origins could be fruitful for understanding why $KCeO_2$ develops magnetic order and why it exhibits extreme g factor anisotropy. In turn, studying $KCeO_2$ helps encompass the magnetic phenomena that appear in the $ALnX_2$ materials family.

Table 6.1: Rietveld refinement of structural parameters at 300 mK from elastic neutron scattering data on BT-1. Within error, all ions refine to full occupation and no site mixing is observed.

T		300 mK				
$a = b$		3.65861(8) Å				
c		18.58608(85) Å				
Atom	Wyckoff	x	y	z	U_{iso} (Å^2)	Occupancy
Ce	3a	0	0	0	0.84(11)	0.994(5)
K	3b	0	0	0.5	1.09(15)	0.992(7)
O	6c	0	0	0.26939(11)	0.97(8)	0.999(5)

Table 6.2: The fit and ground state CEF wave functions for $KCeO_2$ determined from minimizing parameters extracted from $E_i = 300$ meV INS data and EPR g factor components. The energy level scheme from Eldeeb et al. [15] calculated with multireference configuration-interaction and spin orbit coupling (MRCI+SOC) was used as a starting point for this analysis. The observed 170.5 meV excitation was excluded from this analysis.

	E_1	E_2	$\frac{I_2}{I_1}$	g_{avg}	$g_\perp$	$g_{//}$	χ^2
Fit	118.6	145.7	0.635	1.6424	2.0015	0.2825	0.557
Observed	118.8	146.2	0.257	1.6340	2.0013	~ 0	

B_2^0 B_4^0 B_4^3
3.80005 0.21181 -6.37770
Fit wave functions:
$|\omega_{0,\pm}\rangle = \mp 0.882|\pm 1/2\rangle + 0.471|\mp 5/2\rangle$
$|\omega_{1,\pm}\rangle = 1|\pm 3/2\rangle$
$|\omega_{3,\pm}\rangle = \mp 0.471|\mp 1/2\rangle + 0.882|\pm 5/2\rangle$

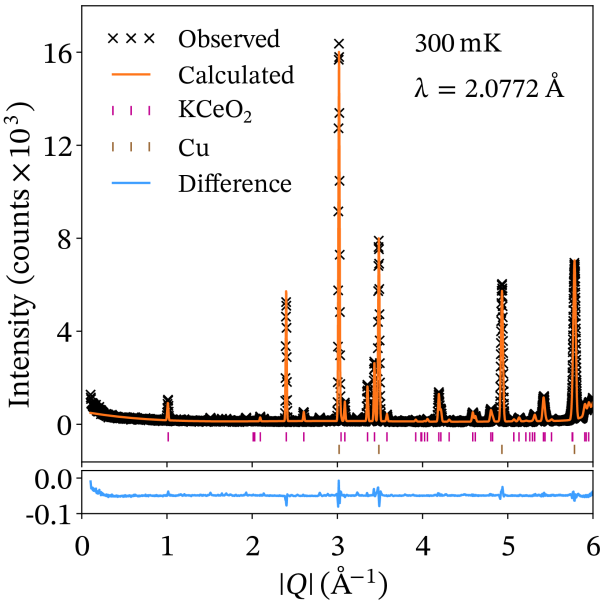

Figure 6.1: Rietveld refinement of elastic neutron powder diffraction of $KCeO_2$ from BT-1 at 300 mK. There are no new magnetic Bragg reflections at this temperature. Additionally, no strong structural peaks appear that could indicate multiple Ce environments.

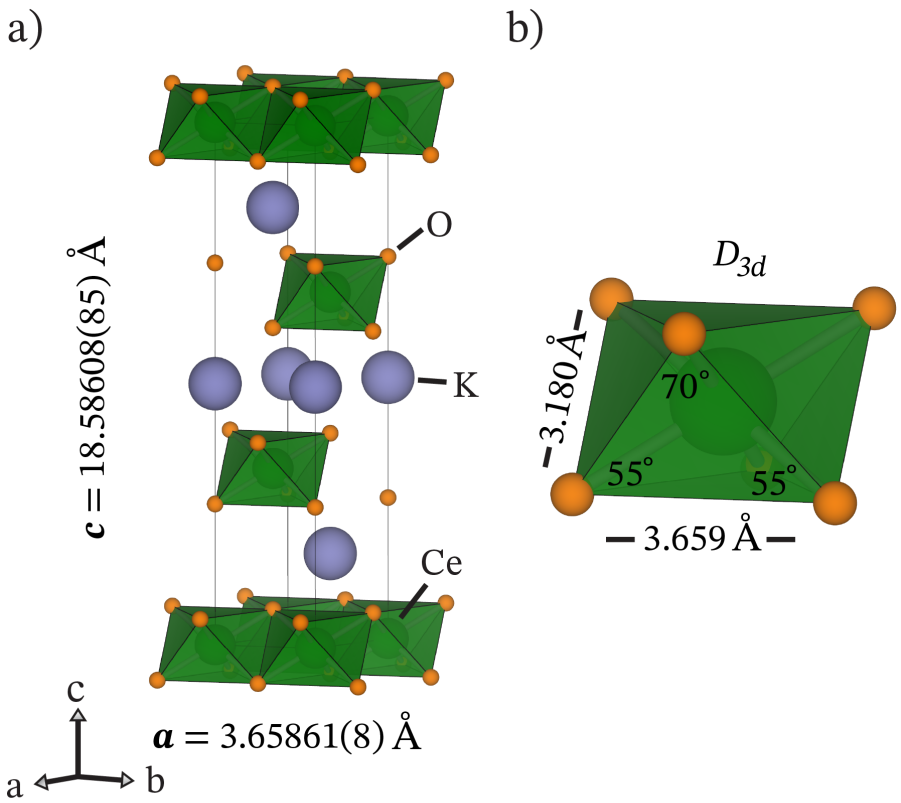

Figure 6.2: a) The $R\bar{3}m$ crystal structure of $KCeO_2$ with refined lattice parameters at 300 mK. The D_{3d} CeO_6 octahedral layers are separated by monolayers of K cations. b) The local D_{3d} environment of the Ce^{3+} ions. These CeO_6 octahedra are trigonally compressed along the crystallographic c axis.

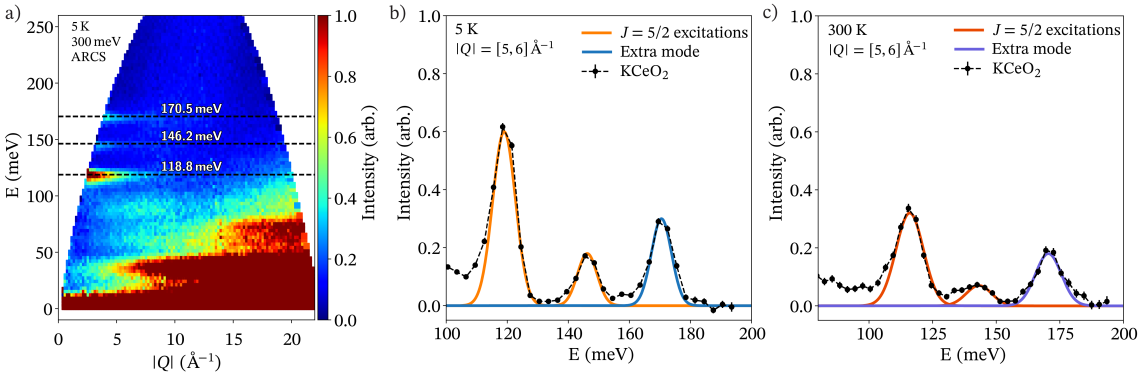

Figure 6.3: a) High energy inelastic neutron scattering (INS) $S(Q, \hbar\omega)$ data collected at 5 K and $E_i = 300$ meV at the ARCS spectrometer at ORNL. The full width at half maximum energy resolution of $E = 0$ meV is 12.8 meV. b) An energy cut through the data integrated from $|Q| = [5, 6]$ Å^{-1} reveals three instrumental resolution limited crystalline electric field modes. The first two lower energy modes are close to predictions for the $KCeO_2$ environment calculated with MRCI+SOC [15]. The third mode at 170.5 meV does not have a known origin. A linear background is subtracted from this energy cut. c) An energy cut through the data at 300 K under the same conditions as b) showing that all three modes remain at room temperature. These modes reside well below any strong perturbations from the excited $J = 7/2$ manifold.

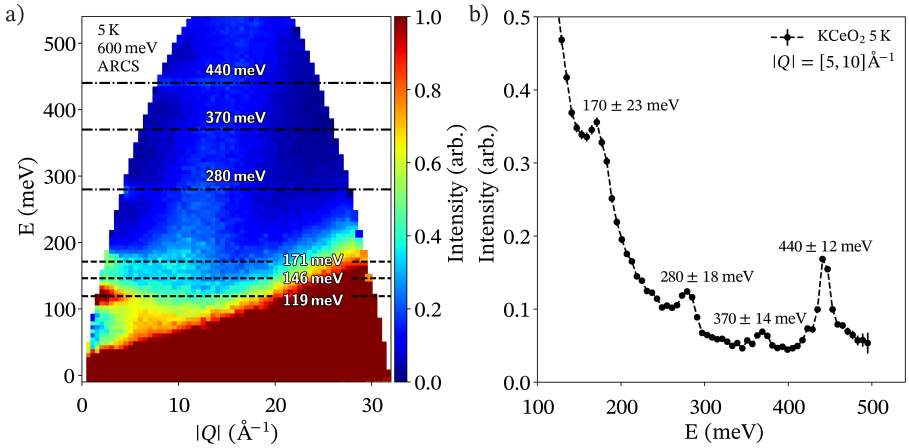

Figure 6.4: a) High energy inelastic neutron scattering (INS) $S(Q, \hbar\omega)$ data collected at 5 K and $E_i = 600$ meV at the ARCS spectrometer at ORNL. This data highlights the splitting of the $J = 5/2$ and $J = 7/2$ multiplet manifolds. The bottom three dashed lines are within the energy range of the $J = 5/2$ manifold. The top three are from the $J = 7/2$ manifold. The bottom of the $J = 7/2$ manifold begins at roughly 280 meV and no crystalline electric field excitations reside between 171 meV and 280 meV. b) An energy cut of the data integrated from $|Q| = [5, 10]$ Å^{-1} to highlight the observable excitations in this data set. Error bars represent the full width at half maximum (FWHM) energy resolution at each respective energy transfer for this instrumental configuration. Only three out of the four possible $J = 7/2$ Kramers doublets are observed at 280 meV, 370 meV, and 440 meV. The fourth doublet could be outside of experimental resolution or at a higher energy than measured.

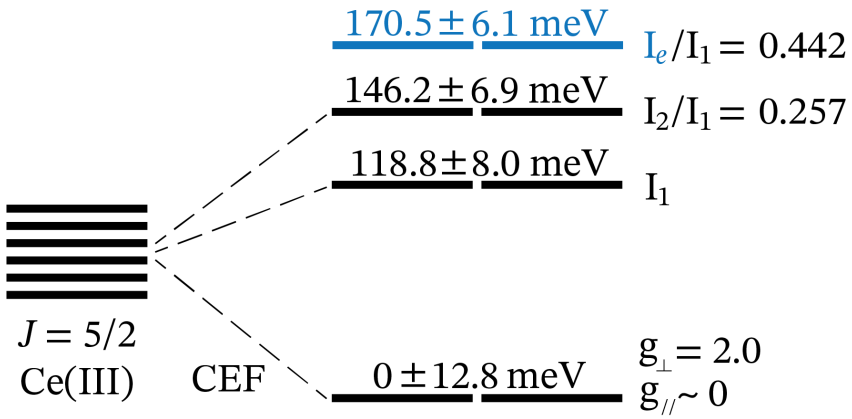

Figure 6.5: Schematic of the $J = 5/2$ ground state multiplet splitting in $KCeO_2$. The free ion Ce^{3+} has six fold degeneracy. This can be maximally split into a series of three doublets by a crystalline electric field (CEF) environment without breaking time reversal symmetry according to Kramers theorem. The observed CEF excitations and error bars corresponding to the full width at half maximum (FWHM) energy resolution at each respective energy transfer for $E_i = 300$ meV ARCS data is shown alongside the ground state Kramers doublet g factor components and excited state integrated intensity ratios.

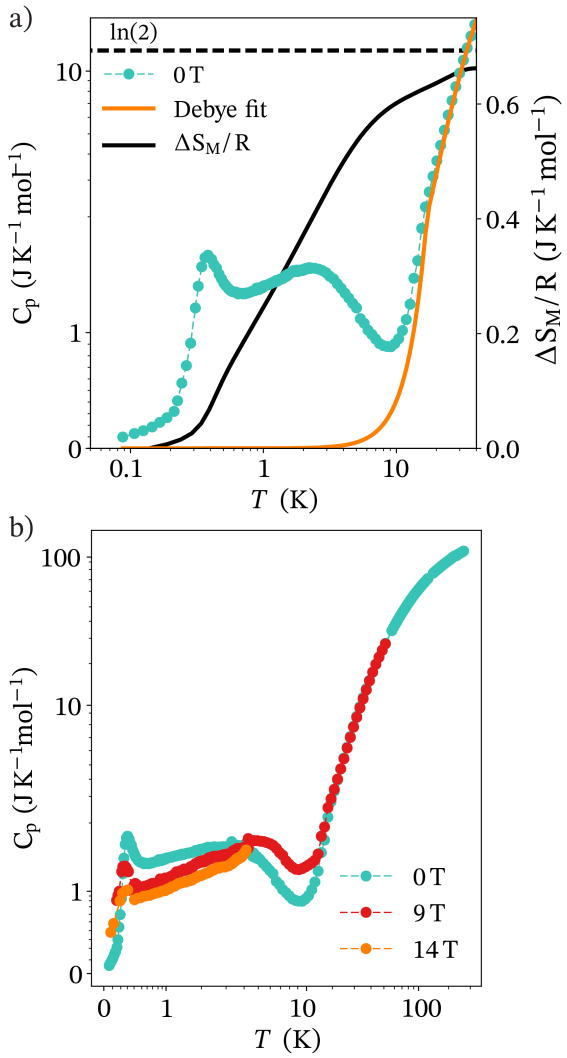

Figure 6.6: a) Zero field specific heat of $KCeO_2$ in cyan overplotted with the double Debye model of the lattice. The entropy integrated magnetic portion of the specific heat in black approaches $Rln(2)$ as expected for a $J_{eff} = 1/2$ system. Two features in the specific heat arise near 3 K and $T_N = 300$ mK where $KCeO_2$ magnetically orders. The high temperature feature indicates the onset of short range correlations. b) In fields of $\mu_0 H = 9$ T and 14 T, the high temperature feature shifts up in temperature while the lower temperature T_N feature shifts down as moments begin to polarize with the field, suppressing magnetic order.

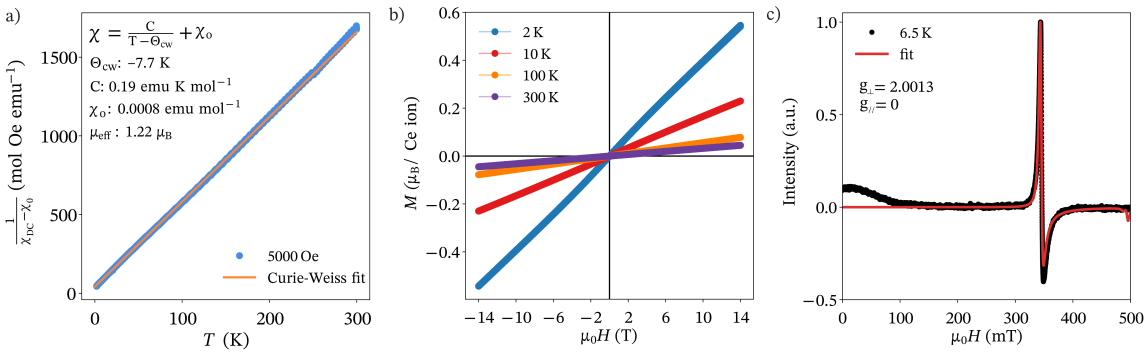

Figure 6.7: a) Inverse magnetic susceptibility of $KCeO_2$ fit to the Curie-Weiss law revealing antiferromagnetically coupled Ce moments of $\mu_{eff} = 1.22\mu_B$ and $\theta_{CW} = -7.7$ K. No antiferromagentic transitions are observed in this temperature range. b) Isothermal magnetization of $KCeO_2$ up to $\mu_0 H = 14$ T between 2 K to 300 K. The data above 2 K are linear while the 2 K data reveals slight curvature near $\mu_0 H = 6$ T. To saturate the magnetic moments, a higher external magnetic field is required. c) Electron paramagnetic resonance of $KCeO_2$ powder at 6.5 K. One sharp signal indicates one g factor component of $g_\perp \sim 2$ while $g_{//} \sim 0$ or is outside of the range of this measurement. The broad low field peak is instrumental background.

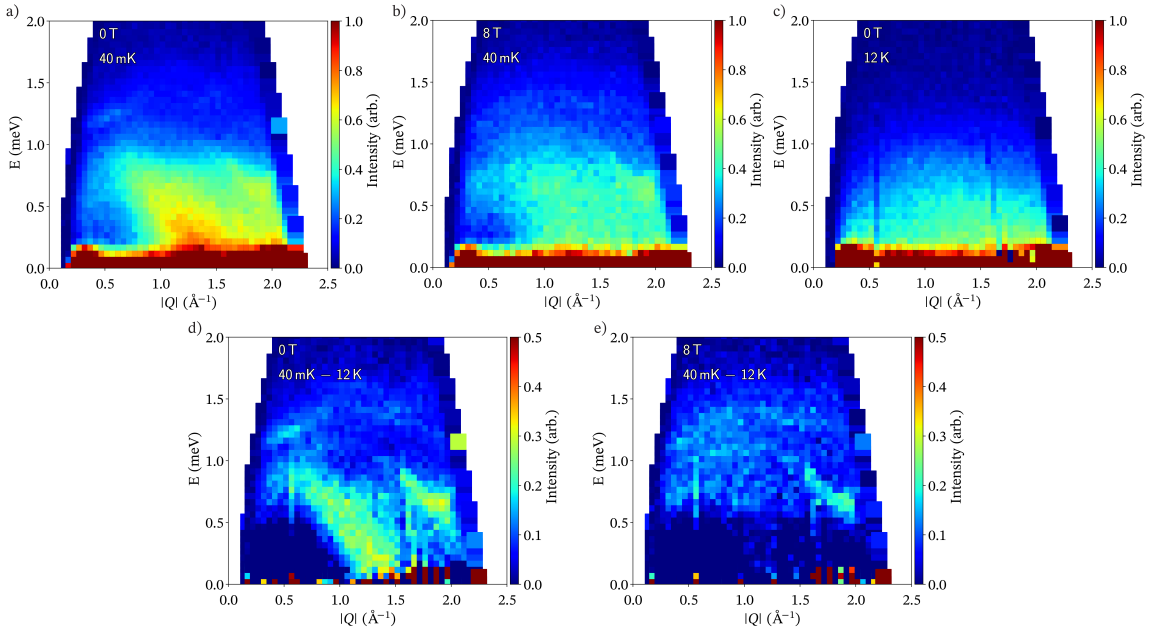

Figure 6.8: a-c) Inelastic neutron scattering (INS) $S(Q, \hbar\omega)$ data of $KCeO_2$ pressed powder on CNCS from ORNL. The data show two branches of spin waves originating near $|Q| = 1.4$ Å^{-1} and across $|Q|$ at $E = 1.25$ meV in zero field. The upper branch maximally reaches 1.5 meV while the lower branch extends to 1.0 meV. In increased external fields of $\mu_0 H = 8$ T the spin waves suppress as some Ce moments polarize. At 12 K, the remnant low energy fluctuations can be viewed as a paramagnetic background of this material. d-e) Subtracting c) from a) and b), respectively, shows that the zero field spin waves distinctly reveal the two branches. The lower branch in zero field is gapless but becomes gapped under $\mu_0 H = 8$ T as the Ce moments begin to polarize.

Appendix A

Magnetic susceptibility and neutron scattering investigation of $Na_{0.99}TiO_2$ and $Na_{0.85}TiO_2$

The purpose of this appendix is twofold. First, the magnetic properties and neutron scattering results on fully sodiated $Na_{0.99}TiO_2$ and sodium deficient $Na_{0.85}TiO_2$ will be discussed to show that the $S = 1/2$ material does not show magnetic order. Second, the magnetic susceptibility of a variety of $NaTiO_2$ measurements will be discussed. The purpose of this is a cautionary tale to those who measure magnetic properties of air sensitive materials synthesized inside of stainless steel, iron, or niobium tubing. The methods to identify impurities or sample degradation inside of the Quantum Design MPMS3 or PPMS will be shown.

A.1 Introduction

$NaTiO_2$ contains Ti^{3+} ions that are naively d^1 $S = 1/2$. This material was historically studied as the base candidate for a spin liquid as, at room temperature, it contains the same $R\bar{3}m$ equilateral triangular lattice as $NaYbO_2$. In fact, it was the first material suggested to fit the "resonating valence bond" idea proposed by Anderson [45]. The majority of the pristine magnetic properties of this material have been reported by Clarke [120], and this section of the thesis expands on the findings of Clarke. Other reports on $NaTiO_2$ previously had materials handling issues while measuring the magnetic properties of this system [26, 208, 209]. The material is extremely air and moisture sensitive and has to have strict air control at all times. The important features Clarke found when investigating $NaTiO_2$ are detailed in the following paragraphs.

$NaTiO_2$ is the α-$NaFeO_2$ $R\bar{3}m$ structure at room temperature. For reference, this is the same structure type shown for $NaYbO_2$ and $KCeO_2$ in this thesis. The $NaTiO_2$ lattice can exhibit site mixing of Na^+ (1.02 Å) and Ti^{3+} (0.67 Å) cations despite the large difference in size between the two. This occurs on the order of a couple of percent.

It should be noted that this phenomena was not observed in the Ce and Yb compounds in the main chapters of this thesis. This is likely due to the larger Ln ionic radii of Yb^{3+} (0.868 Å) and Ce^{3+} (1.01 Å) and more robust charge of the Ln ions relative to Ti.

Additionally, $NaTiO_2$ is a battery material as has been studied by numerous other groups [16, 210, 211]. Sodium can be removed from the lattice down to $Na_{0.5}TiO_2$. However, the material undergoes a monoclinic distortion to $C2/m$ after losing approximately 20% of its Na content. Near $Na_{0.7}TiO_2$, Ti ions move to the Na planes [211]. The $NaTiO_2$ lattice can also be stuffed with excess Na to form $Na_{1+}TiO_2$ phases. This results in multiple phases of $NaTiO_2$ polycrystalline powder. There is, however, a need to use a slight excess of Na when synthesizing $NaTiO_2$ to fully reduce TiO_2 with Na metal. A balance of Na excess is required to fully form $Na_{0.99}TiO_2$ without introducing multiple phases with differing lattice parameters.

In fact, the lattice parameters of Na_xTiO_2 are inherently linked to x. The most accurate and recent tracking of this phenomenon is shown by Wu [16]. Therefore, a laboratory x-ray diffraction measurement can determine the Na content of Na_xTiO_2. The closer x is to 1.0, the more sensitive the lattice parameters become. Above $x = 1.0$, there is a jump in cell volume and phase separation. An ideal $Na_{0.99}TiO_2$ sample has $a = b = 3.05$ Åand $c = 16.26$ Å. The c axis is the most sensitive lattice parameter to Na content.

Originally, Clarke reported that $Na_{0.99}TiO_2$ undergoes a monoclinic phase transition from high temperature $R\bar{3}m$ to low temperature $C2/m$ in a first order process between 210 to 260 K. They reported a sudden decrease in magnetic susceptibility in this temperature range, but the signal was highly sample dependent. The location and magnitude of the transition depended on the Na content of the sample. Later on, this thesis will show that the transition occurs at 250 to 265 K in $Na_{0.99}TiO_2$.

The monoclinic transition creates four short and two long Ti−Ti nearest neighbor bonds in the triangular planes of $Na_{0.99}TiO_2$. It was shown that $Na_{0.99}TiO_2$ does not show any strong magnetic behavior below this monoclinic transition. No indications of long range magnetic ordering were observed by Clarke despite the lattice naively containing $S = 1/2$ moments on a geometrically frustrated lattice. The downturn in magnetic susceptibility was therefore thought to be due to an orbital ordering transition, a spin quenching transition, or perhaps a dimer formation transition [56, 212, 213]. The nature of this transition is still not fully known, and this Appendix further expands on the indeterminably of the low temperature magnetism of $Na_{0.99}TiO_2$.

A.2 Magnetic susceptibility

Measuring the magnetic susceptibility of $NaTiO_2$ is an endeavor. The purpose of this section and its figures is mainly to show the issues that can arise when working with steel tubing as the synthesis container. $NaTiO_2$ is exceedingly air and moisture sensitive, more so than $NaCeO_2$ and $KCeO_2$ discussed in the above chapters. In a matter of seconds, $NaTiO_2$ will begin to degrade in air. It quickly loses Na content as Ti oxidizes

to form TiO_2 and Na_2O phases in the presence of oxygen and water. This means that even the usual methods of preparing samples for magnetic property measurements on the Quantum Design MPMS3 and PPMS are not sufficient for $NaTiO_2$.

Additionally, $NaTiO_2$ synthesis requires metal tubing. The tubing can induce small amounts of vapors or impurities from the tubing into the material. We found that, in general, using larger tubing with larger $NaTiO_2$ synthesis volumes created fewer impurity signals in $NaTiO_2$. This is likely due to a smaller surface to volume ratio of steel tubing wall to $NaTiO_2$ powder.

Since $NaTiO_2$ has these two issues (air stability and magnetic impurities), they often appeared in magnetic susceptibility measurements. Figure A.1 shows two different $NaTiO_2$ samples with vastly different magnetic susceptibilities. A large offset between zero field cooled (ZFC) and field cooled (FC) measurements are present in both m3 and m3t2. A random decrease in either ZFC or FC over time, such as that shown in m3 in Figure A.1, likely indicates the sample is degrading over the course of the measurement. Random decreases in susceptibility for $NaTiO_2$ occur when some of the Ti^{3+} moments oxidize to nonmagnetic Ti^{4+}. When ZFC and FC form a permanent offset as in m3t2, this is most likely caused by a ferromagnetic impurity within the sample that has a magnetic transition above the highest temperature measured. For instance, stainless steel could impart Fe_3O_4 into $NaTiO_2$.

A rough estimate of how much Fe_3O_4 is in these samples is shown in Figure A.2. This isothermal magnetization data is not what one would expect for an ideal antiferromagnet like $NaTiO_2$. An antiferromagnet should have a positive slope isothermal magnetization curve without the large jump near low field in this data. The data have been plotted versus the mass of Fe_3O_4 which has a large moment of roughly 80 emu/g. Assuming that the initial low field jump occurs from Fe_3O_4 and not $NaTiO_2$, only 0.00005g of Fe_3O_4 would be required. The samples used to measure magnetic properties of $NaTiO_2$ were on the order of roughly 10 mg to 20 mg. This means that only 0.25% to 0.5% Fe_3O_4 impurity by mass would be required to induce the ferromagnetic like behavior observed in $NaTiO_2$. This would not be observable in x-ray diffraction.

These data indicate that there is strong evidence for a ferromagnetic impurity in $NaTiO_2$ samples that randomly alters the magnetic susceptibility and isothermal magnetization curves of the material. To obtain measurements without the influence of the ferromagnetic impurities, ZFC and FC data were obtained above the saturation threshold of the ferromagnetic impurity as determined by isothermal magnetization.

Compounded with the extreme air sensitivity, the material was measured several times until a impurity free and non-degraded sample was obtained. The final method for keeping $NaTiO_2$ air free was to load the pressed pellet of $NaTiO_2$ into a 5mm Nuclear Magnetic Resonance (NMR) tube in a glove box. The top of the pellet was held in place at the bottom of the NMR tube with a gelatin cap. Afterwards, the NMR tube was flame sealed. If the sample degraded from a faulty seal, the material would have turned white over a couple of days. After ensuring the seal held for multiple days, the sample was measured.

The results of a clean $NaTiO_2$ measurement are shown in Figure A.3 There is one observable transition in both ZFC and FC measurements that overlap between 250 K to 265 K. This downturn corresponds to the start of the structural $R\bar{3}m$ to $C2/m$ phase transition discussed in the next section. There was a small amount of ferromagnetic impurity in this sample, but it was saturated out at $\mu_0 H = 10000$ Oe. Despite this transition occurring in $NaTiO_2$, no observable long range magnetic order appears in this material.

A.3 Neutron scattering

The magnetic properties of $NaTiO_2$ were investigate with elastic and inelastic neutron scattering. The elastic scattering data was obtained on HB2-A at Oak Ridge National Laboratory and the high energy inelastic data was measured at the Angle Resolved Chopper Spectrometer (ARCS) at Oak Ridge National Laboratory.

The purpose of measuring high energy inelastic neutron scattering data on $Na_{0.99}TiO_2$ was to determine if the material displayed a sharp magnetic feature resulting from its phase transition between 250 K to 265 K. A rough conversion of 10 K to 1 meV suggests that such a feature would reside around 25 meV to 30 meV. However, above and below the transition in $Na_{0.99}TiO_2$, no inelastic magnetic scattering was observed.

Elastic scattering measurements were conducted on $Na_{0.99}TiO_2$ and $Na_{0.85}TiO_2$ from $T = 10, 100, 250, 350$ K. These data are shown in Figures A.4 and A.5 with refined occupancies of the respective ions. The high temperature $R\bar{3}m$ and low temperature $C2/m$ phases help parameterize the Na content of these samples relative to their lattice parameters. The Na content in each measurement was within 2% error of the other measurements. At 350 K, the lattice parameters for $Na_{0.99}TiO_2$ were refined to $a = b = 3.050531(11)$ and $c = 16.26504(9)$. At 10 K, the $C2/m$ lattice parameters were refined to $a = 5.248929(8)$, $b = 3.032652(8)$, $c = 5.721498(9)$, and $\beta = 108.4570(1)$. Similarly, for $Na_{0.85}TiO_2$ the lattice parameters were refined to $a = b = 3.015002(10)$ and $c = 16.440529(12)$ at 350 K and $a = 5.207070(10)$, $b = 3.009735(12)$, $c = 5.740099(10)$, and $\beta = 107.7402(3)$ at 10 K.

At 250 K, the refinement of $Na_{0.99}TiO_2$ data was best represented by two structural phases. The data was fit with one phase as the 10 K $C2/m$ phase and the other as the 350 K $R\bar{3}m$ phase. The refinement indicated 52.65(0.77)% of $C2/m$ and 47.38(0.79)% $R\bar{3}m$. This refinement essentially indicates that the magnetic transition observed from 250 K to 265 K in magnetic susceptibility measurements discussed later on occurs over a larger temperature range for the structural transition. A fully detailed investigation of the multiphase structural transition has been reported by Clarke [120].

In both $Na_{0.99}TiO_2$ and $Na_{0.85}TiO_2$, no new magnetic Bragg reflections were observed upon cooling through the magnetic transition from 250 K to 265 K. There is one additional structural peak in $Na_{0.99}TiO_2$ near $2\theta = 29.5^\circ$ in Figure A.6. This is at the same location as a reported superlattice peak from Wu [16] that occurs only in the fully

sodiated $Na_{0.99}TiO_2$ material. However, this is not a magnetic peak, as it occurs above and below the magnetic transition.

It is surprising that no magnetic features appear even in the $Na_{0.85}TiO_2$ sample. If the material takes Ti^{3+} and forms dimers or orbitally orders, inducing a 15% deficiency of Na^+ should also correspond to a 15% deficiency in Ti^{3+}. In turn, this would leave some of the $S = 1/2$ Ti moments without a partner to pair with. If the Na deficiencies are localized, this might induce short range order of the unpaired Ti moments. However, a 15% reduction may not be enough to induce any short or long range magnetic features in the material. The lone Ti moments may have just remained paramagnetic above and below the transition temperature as they have no nearby free Ti moments to interact with.

A future experiment approaching the Ti^{3+} percolation threshold of the triangular lattice (50%) may be useful to determine if short range correlations can occur in this material from lone Ti moments. At 50% Na deficiency, this approaches the lower boundary of Na_xTiO_2 phase stability and would require a careful and controlled synthesis. If no magnetism appears in this phase either, the Ti moments may be quenched while going through the 250 K to 265 K magnetic phase transition.

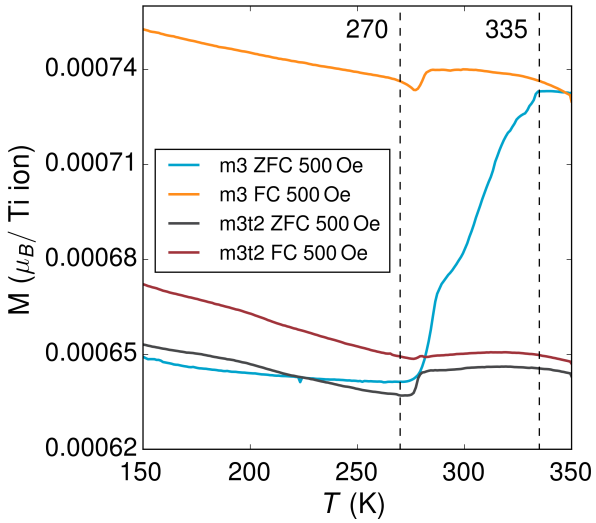

Figure A.1: Magnetic susceptibility of $NaTiO_2$ measured two times from the same sample batch. The first measurement is labeled m3 and the second is labeled m3t2. Despite both samples originating from the same synthesis batch, they show vastly different magnetic susceptibility behavior. The random decreases in zero field cooled (ZFC) and field cooled (FC) data sets in m3 indicate that the material is degrading over the course of the measurement. This sample went into the instrument fully black and returned partially white as some $NaTiO_2$ oxidized. The permanent offset between ZFC and FC in m3t2 indicated that a ferromagnetic impurity was inside of $NaTiO_2$ from the synthesis inside of stainless steel tubing. A higher magnetic field is needed to saturate out this impurity. Also, the two measurements are offset because of a small ferromagnetic impurity.

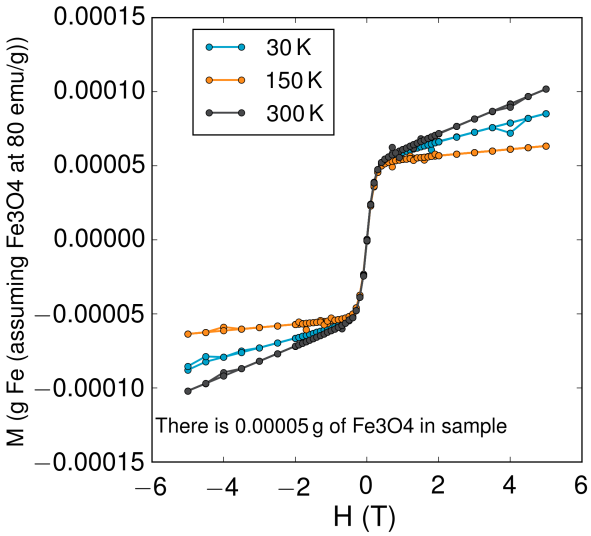

Figure A.2: Isothermal magnetization of $NaTiO_2$ plotted versus the magnetization of Fe_3O_4 assuming a moment of roughly 80 emu/g. Normally, only a linear curve would be expected for antiferromagnetic $NaTiO_2$ devoid of a ferromagnetic impurity. The sharp low field signal is likely due to a ferromagnetic impurity. This shows that only 0.00005g of Fe_3O_4 is needed to produce the sharp ferromagnetic like signal at low field in this sample.

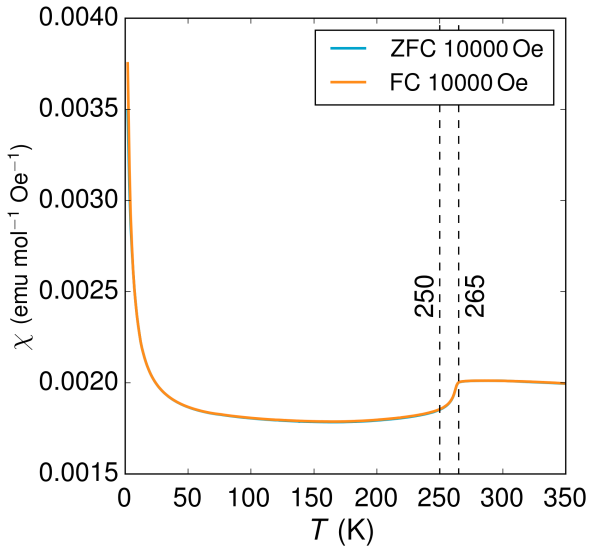

Figure A.3: Magnetic susceptibility of $NaTiO_2$ without sample degradation shows that zero field cooled (ZFC) and field cooled (FC) measurements overlap with a magnetic transition between 250 K to 265 K. The data were obtained by saturating a ferromagnetic impurity with a $\mu_0 H = 10000$ Oe field in the ZFC measurement. This means that the ZFC data was collected at $\mu_0 H = 10000$ Oe and the FC data was collected at $\mu_0 H = 20000$ Oe with a net $\mu_0 H = 10000$ Oe field difference.

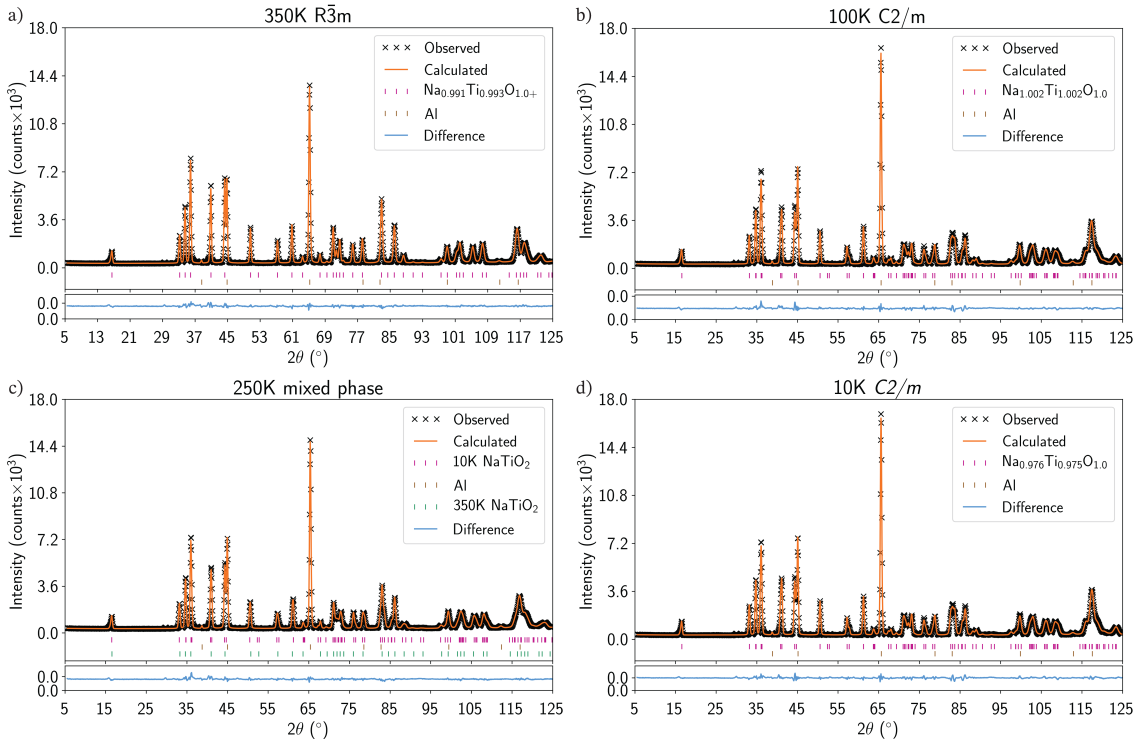

Figure A.4: a-d) Elastic neutron scattering collected on $Na_{0.99}TiO_2$ at 10, 100, 250, and 350 K from HB2-A at ORNL. The refined lattice parameters are in the main text. The sodium occupancies parameterize 97% to 99% Na occupation in this material. Despite undergoing a $R\bar{3}m$ to $C2/m$ phase transition, $Na_{0.99}TiO_2$ does not exhibit any magnetic Bragg reflections. The material would be expected to have small $S = 1/2$ moments, but no intensity from magnetic Ti moments is observed.

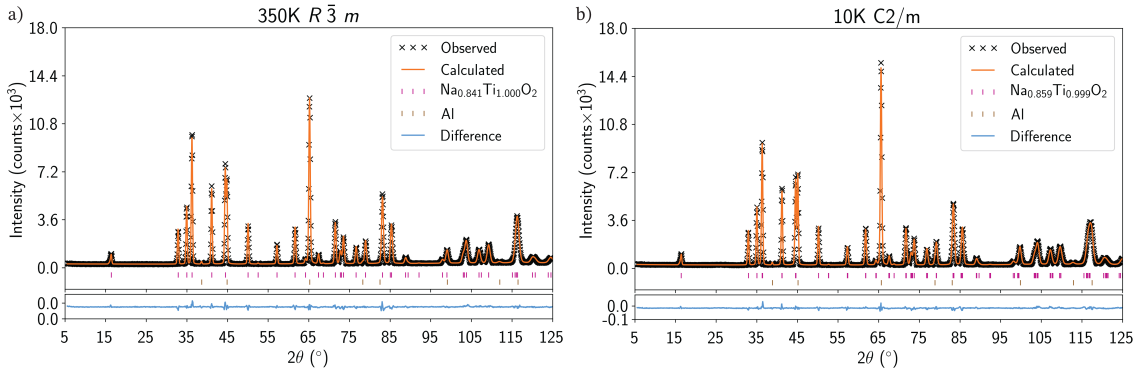

Figure A.5: a-b) Elastic neutron scattering collected on $Na_{0.85}TiO_2$ at 10, 100, 250, and 350 K from HB2-A at ORNL. The refined lattice parameters are shown in the main text. The sodium occupancies parameterize 84% to 85% Na occupation in this sample. As found in $Na_{0.99}TiO_2$, no magnetic Bragg reflections are seen below the phase transition in this sample.

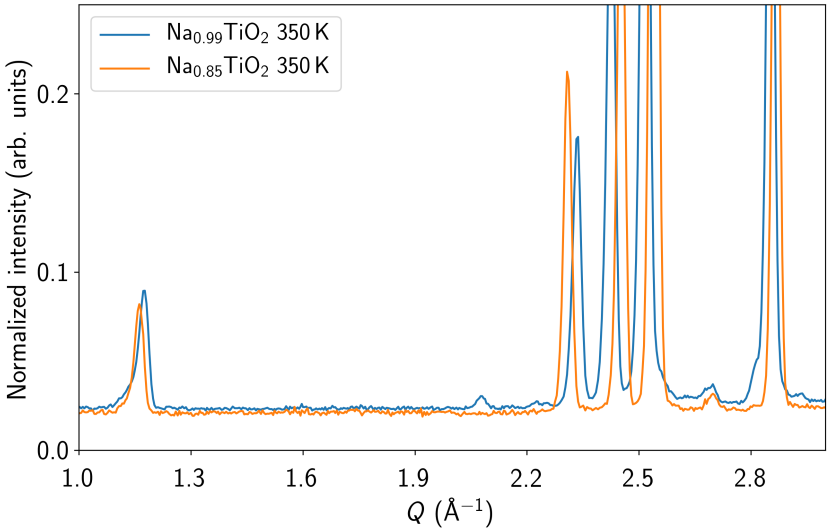

Figure A.6: Overplot of the 350 K elastic neutron scattering data collected on $Na_{0.99}TiO_2$ and $Na_{0.85}TiO_2$. The $Na_{0.99}TiO_2$ sample shows one extra peak near $Q = 2.1$ Å^{-1} ($2\theta = 29.5°$). This peak was similarly found in samples reported by Wu [16] and is a structural superlattice peak. This peak does not appear in the $Na_{0.85}TiO_2$ sample, but it is not a magnetic reflection.

Appendix B

Crystal growth techniques for $ALnX_2$ materials

This Appendix overviews the methods attempted for growing single crystals of $NaYbO_2$ and $LiYbO_2$. Primarily, the focus of crystal growth was on $NaYbO_2$, but some of the methods were also attempted for $LiYbO_2$ as will be discussed.

B.1 Floating zone

The floating zone method of crystal growth takes a pressed or sintered polycrystalline feed and seed rod of material, heats up a small counter-rotating section of the feed rod and seed rod (the 'floating' zone), and slowly pulls the melted zone through the entire feed rod. In theory, the molten floating zone should leave behind large single crystal facets after the polycrystalline material re-solidifies. It is beneficial since it does not require any contact with a container as the feed and seed rods are hung vertically without contact with any walls. However, preparing samples for this method can be difficult, as sintering long straight rods is a long process that can be extremely difficult if the material does not press well. Additionally, this method currently requires significant air exposure time while setting up, so mostly only air stable $LiYbO_2$ and $NaYbO_2$ were attempted. A few attempts with $NaTiO_2$ are also discussed. A full overview of this method will not be presented here and can be found in [214]. This section will overview the general attempts for $LiYbO_2$ and $NaYbO_2$ and the reasoning behind them.

B.1.1 Mirror furnace

The mirror furnace utilizes large curved mirrors to focus optical light onto a small section of the hanging polycrystalline rod to create the molten floating zone. The light passes through an optically transparent quartz inner chamber where the rod resides. If the material absorbs enough light to heat up and melt, does not decompose while doing so, and forms a stable melt, then it is likely a single crystal can be grown.

$NaYbO_2$

$NaYbO_2$ crystal growth was attempted in the mirror furnace multiple times. First, just a normal attempt with sintered $NaYbO_2$ was tried in an Ar environment. Up until the maximum power, the white material did not melt. There were fumes ablating off of the material during heating, but no melting occurred. In one attempt, the maximum power did, however, soften the wire holding the shielding around the quartz tube as light likely reflected off of the white powder, leading to the shielding descending during the growth attempt and melting to the quartz tube. After removing the rod from the furnace, the inner quartz chamber was coated in a fine white powder. $NaYbO_2$ and its reactants Yb_2O_3, and Na_2CO_3 are all white powders, so no observable change was immediately seen after removing the feed and seed rods from the furnace. The rods still appeared to be the same despite losing some mass to the quartz chamber walls. X-ray analysis of the feed rod at the tip where a molten zone was attempted revealed that some Yb_2O_3 had formed. This likely occured as a result of Na_2O or related Na species evaporation while heating $NaYbO_2$ in the chamber that likely coated the quartz walls. Increasing the pressure and changing the Ar environment to Ar/O_2 did not prevent the vaporization of the Na species from the material.

Another type of attempt was made by pressing differing ratios of $NaYbO_2$:Na_2CO_3 pellets and placing them on top of the seed rod prior to heating or incorporating excess Na_2CO_3 into the base rod. The idea is that the melt could be more stable in the presence of excess Na_2CO_3 that would travel with the molten zone through the feed rod. This is called the traveling solvent floating zone (TSFZ) method [214]. The melting point of Na_2CO_3 is 851 °C, which should be reachable in the mirror furnace. However, these attempts also just saw the vaporization of the feed rod. In one case with a 20:80 $NaYbO_2$:Na_2CO_3 pellet, the pellet did melt into the feed rod, but the feed rod and part of the pellet did not melt. The Na_2CO_3 that melted fell through the rod and an x-ray analysis found that the top of the rod was again primarily Yb_2O_3.

The main conclusion from these attempts for $NaYbO_2$ show that $NaYbO_2$ decomposes into Yb_2O_3 and Na species before melting, even with excess Na_2CO_3.

$NaTiO_2$

$NaTiO_2$ is a black, highly air sensitive material. However, it was capable of being sintered as a rod inside of a stainless steel tube. The setup for this material followed $NaMnO_2$ crystal growths in the mirror furnace [54]. The sintered rods were loaded quickly into the mirror furnace where the quartz chamber was filled with Ar gas. Unlike $NaYbO_2$, a molten zone at first appeared to be stabilized in $NaTiO_2$. There was evidence of a molten zone appearing at moderate power, but the feed and the seed rod processed around each other. This meant that while the outside was molten, the inside was still solid. The surface of the molten zone appeared metallic and shiny, and after turning off the power and removing the rod, the top of the rod was lighter in color. It is thought that $NaTiO_2$ was not the species melting, but rather Na melting out of $NaTiO_2$ to leave

behind Na_xTiO_2. The Na then oxidized when the rod was re-exposed to air.

B.1.2 Laser furnace

Both single crystal growths of $NaYbO_2$ and $LiYbO_2$ were attempted in the laser furnace setup in the Wilson lab. This furnace requires significantly longer air exposure to set up than the mirror furnace, so $NaTiO_2$ was not attempted. The high volatility of $NaYbO_2$ in the mirror furnace suggested we needed higher pressure and temperatures to melt the material without decomposing it. An initial melt test was conducted on $NaYbO_2$ with just a seed rod. Even under 50 atm, large volatility was observed and no melting. $LiYbO_2$ has significantly less volatility issues than $NaYbO_2$, and we therefore attempted to grow this material instead. Under 50 atm, the material appeared to begin to melt at 1100 °C, but the molten area quickly re-solidified even with increasing laser power. The material melted again close to the limit of the furnace near 2300 °C. However, that temperature is suspiciously close to the melting point of Yb_2O_3 at 2355 °C. The molten zone also did not travel when the rod was slowly pulled. In other words, only the section where the feed and seed rods met that had been heated for a significant amount of time would melt. After removing the rod from the furnace, there appeared to be a small clear section of single crystal, but grinding and x-ray diffraction showed that it was Yb_2O_3. The attempt left the inside of the chamber again coated in white powder, and due to safety uncertainties about Li/Na on the stainless steel wall, these growth attempts were stopped until a different chamber could be used.

B.2 Flux growth

The flux growth method generally takes reactants or products of a desired phase into a molten medium that allows for crystals to grow over a long period of time. This section goes over the methods attempted for $NaYbO_2$, as the floating zone technique appeared to be too high temperature for alkali species volatilization.

B.2.1 Salt fluxes

Common fluxes for oxide materials are based on salts. One way to search for a salt flux is to look for a salt with an atom in common with the desired crystal. For $NaYbO_2$, we attempted salt flux growths with NaCl, Na_2CO_3, and a mixture of the two. The fluxes were placed in capped alumina crucibles, sealed stainless steel tubes, or sealed in quartz ampules. They were then taken above their melting point, and slowly cooled through them. The charge of the fluxes was either $NaYbO_2$ or Yb_2O_3 plus Na_2CO_3 placed at either the top or the bottom of the flux. This section is brief, as no combination of flux, starting material, and temperature ever resulted in Yb incorporating into the flux. After every attempt, the charge always ended up at the bottom and unchanged.

B.2.2 Hydroxide melt

There have been numerous successful reports of lanthanide-based materials grown in the presence of strong molten bases[215–219]. This is the hydroxide flux growth technique that relies on oxo-acidity of the melt to mediate crystal growth. In general, lanthanide oxide materials are exceedingly stable and are unlikely to melt in common fluxes and often require the strong acid-base chemistry of a hydroxide melt to work. The concept of oxo-acidity relies on the auto-dissociation of hydroxide in its molten state (akin to water auto-dissociation) as [215]:

$$2\ OH^- \rightleftarrows H_2O\ (\text{acid}) + O^{2-}(\text{base}) \tag{B.1}$$

Here, the base is O^{2-} and the acid is actually H_2O. The neutral species in this case is OH^-. The lanthanide species can then be incorporated into this melt in either acidic or basic conditions. The dissociation constant depends on the alkali or alkaline cation counterpart of the original hydroxide, and larger charge density on the cation increases dissociation. Furthermore, the dissociation increases with increasing temperature. Overall, the tuning knobs for this type of flux growth are not only temperature, flux-to-charge ratio, and time, but also the effective pH of the melt. The pH can be controlled by adding small amounts of excess H_2O (acid) prior to heating. A great overview of this method is in Ref. [215].

For $NaYbO_2$, the hydroxide method was attempted in two types of crucibles. First, the easiest method is to place the hydroxide in alumina crucibles and cap them. This, however, is not generally successful as the hydroxide begins to eat away at the crucible over time and the hydroxide evaporates steadily above its melting point. These tests used $NaYbO_2$ or Yb_2O_3 as charges, but never saw crystals form.

Second, the same type of flux was sealed in Ag tubing. The bottom of the half inch diameter Ag tube was sealed in an arc melter, loaded with $NaYbO_2$ or Yb_2O_3 on ~ 0.1 g scale with 4 g NaOH, and then the top was folded over twice and crimped completely shut with a vise. The top could not be arc melted shut as the flux would melt prior to the metal melting. The tubes were placed in a furnace between 700 ° to 800 ° and heated for 1-2 days before slow cooling below the melting point of NaOH over a week. The tubes always had a small crust of NaOH coating the crimped Ag tube side when removing from the furnace.

The only way to effectively remove the flux for this method is with water. The flux was washed away with water with the aid of a sonicator. In some cases, we did end up finding small single crystals on the order of 100 μm in length. They appeared as white cubes as shown in Figures B.1, B.2 and B.3. Single crystal analysis of these crystals was attempted, but too few reflections arose to determine the structure. However, cubic facets do not usually coincide with an underlying $R\bar{3}m$ space group. The current best guess for the structure of these tiny cubes is they are highly disordered and may be related to the $Fm\bar{3}m$ disordered high temperature phase from the low temperature $R\bar{3}m$ space group discussed in the $ALnX_2$ crystal structure section of the introduction. Changing

temperature, dwell time, and charge concentration seemed to have no repeatable effect on growing these crystals. If the crystals grew, they were always the same small cubes shown in the Figures. Even repeating the same growth multiple times side by side in the same furnace did not always produce crystals. We expect this results from the imperfect pressed seals at the top of the Ag tube or the pH of the melt changing as a result of NaOH absorbing water prior to heating. Nevertheless, since the crystals that formed in this melt did not appear to be the right phase, this method was put to the side.

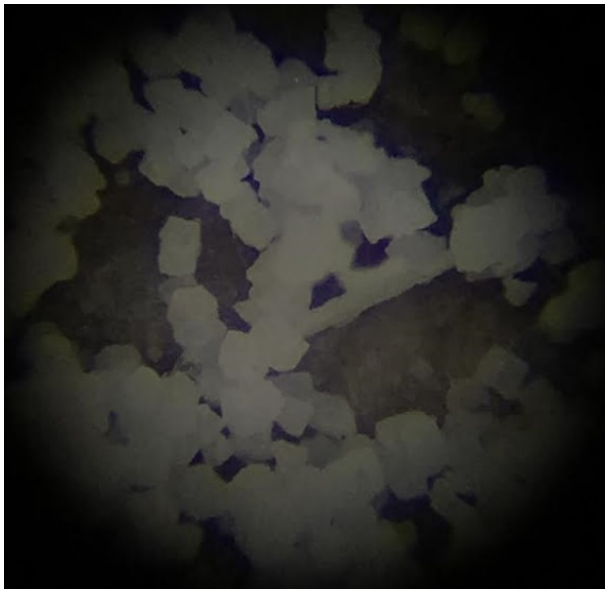

Figure B.1: Optical microscope picture of the white cubic crystals from Ag tube hydroxide melts attempting to grow $NaYbO_2$ crystals. These cubes are approximately 100 μm across.

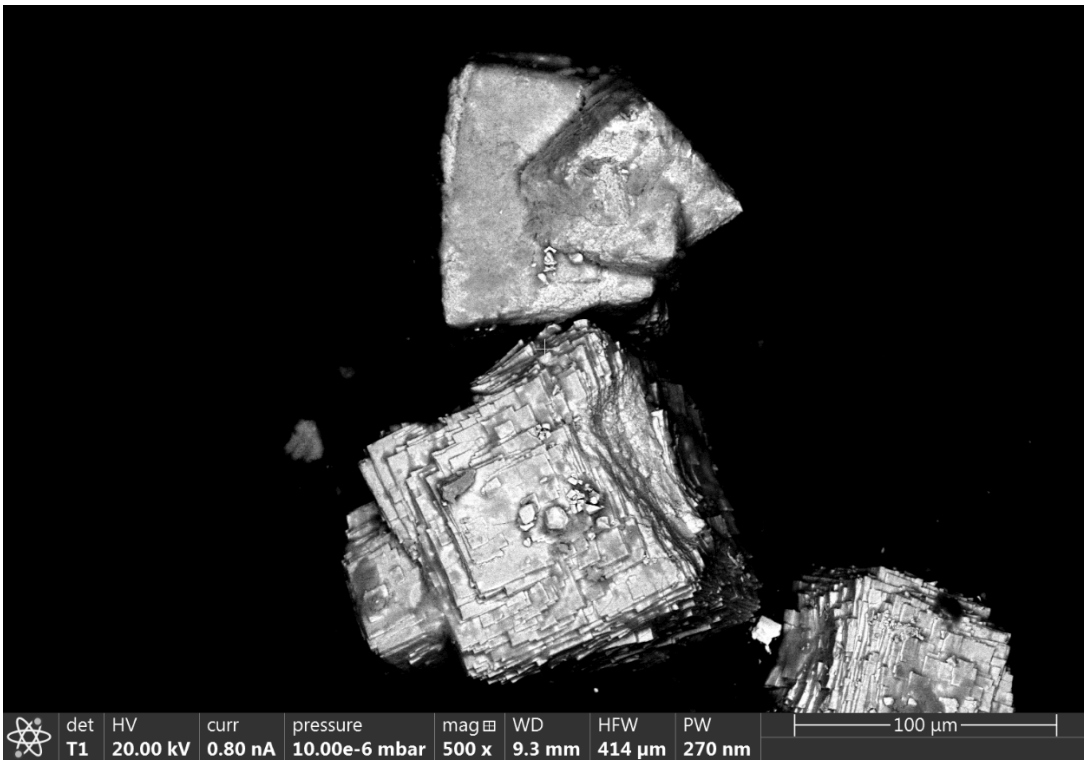

Figure B.2: Scanning electron microscope image of some of the crystals from the Ag tube hydroxide melt attempts for $NaYbO_2$. The facets of the crystals are square, which does not align with what would be expected for $R\bar{3}m$.

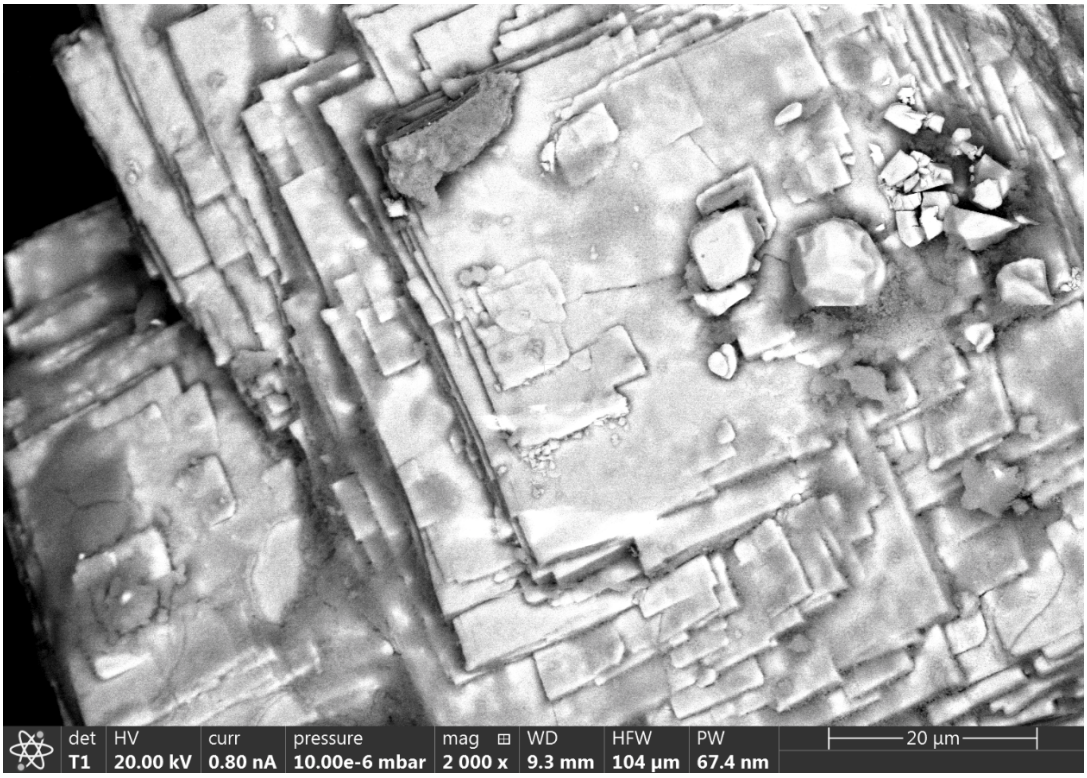

Figure B.3: Scanning electron microscope image close up from Figure B.2. This crystal appears lamellar and disordered. Single crystal x-ray was not able to identify enough peaks to determine the structure of these crystals.

Bibliography

[1] R. T. Shannon and C. T. Prewitt, Acta Crystallographica Section B: Structural Crystallography and Crystal Chemistry **25**, 925 (1969).

[2] R. D. Shannon, Acta Crystallographica Section A: Crystal Physics, Diffraction, Theoretical and General Crystallography **32**, 751 (1976).

[3] Y. Hashimoto, M. Wakeshima, and Y. Hinatsu, Journal of Solid State Chemistry **176**, 266 (2003).

[4] Y. Hashimoto, M. Wakeshima, K. Matsuhira, Y. Hinatsu, and Y. Ishii, Chemistry of Materials **14**, 3245 (2002).

[5] B. Dong, Y. Doi, and Y. Hinatsu, Journal of Alloys and Compounds **453**, 282 (2008).

[6] W. Bronger, W. Brüggemann, M. Von der Ahe, and D. Schmitz, Journal of Alloys and Compounds **200**, 205 (1993).

[7] W. Bronger, R. Elter, E. Maus, and T. Schmitt, Revue de chimie minérale **10**, 147 (1973).

[8] A. Verheijen, W. Van Enckevort, J. Bloem, and L. Giling, Le Journal de Physique Colloques **36**, 3 (1975).

[9] M. Tromme, Comptes Rendus des Seances de l'Academie des Sciences, Serie C: Sciences Chimiques **273**, 0567 (1971).

[10] T. Ohtani, H. Honjo, and H. Wada, Materials Research Bulletin **22**, 829 (1987).

[11] J. Fábry, L. Havlák, M. Dušek, P. Vaněk, J. Drahokoupil, and K. Jurek, Acta Crystallographica Section B: Structural Science, Crystal Engineering and Materials **70**, 360 (2014).

[12] J. Xing, L. D. Sanjeewa, J. Kim, G. R. Stewart, M.-H. Du, F. A. Reboredo, R. Custelcean, and A. S. Sefat, ACS Materials Letters **2**, 71 (2020).

[13] O. Arnold, J.-C. Bilheux, J. Borreguero, A. Buts, S. I. Campbell, L. Chapon, M. Doucet, N. Draper, R. F. Leal, M. Gigg, *et al.*, Nuclear Instruments and Methods in Physics Research Section A: Accelerators, Spectrometers, Detectors and Associated Equipment **764**, 156 (2014).

[14] L. Ding, P. Manuel, S. Bachus, F. Grußler, P. Gegenwart, J. Singleton, R. D. Johnson, H. C. Walker, D. T. Adroja, A. D. Hillier, and A. A. Tsirlin, Phys. Rev. B **100**, 144432 (2019).

[15] M. S. Eldeeb, T. Petersen, L. Hozoi, V. Yushankhai, and U. K. Rößler, Phys. Rev. Materials **4**, 124001 (2020).

[16] D. Wu, X. Li, B. Xu, N. Twu, L. Liu, and G. Ceder, Energy & Environmental Science **8**, 195 (2015).

[17] P. A. Lee, Reports on Progress in Physics **71**, 012501 (2007).

[18] M. Vojta, Advances in Physics **58**, 699 (2009).

[19] C. Proust and L. Taillefer, Annual Review of Condensed Matter Physics **10**, 409 (2019).

[20] P. A. Lee, Science **321**, 1306 (2008).

[21] L. Balents, Nature **464**, 199 (2010).

[22] L. Savary and L. Balents, Reports on Progress in Physics **80**, 016502 (2016).

[23] C. Broholm, R. Cava, S. Kivelson, D. Nocera, M. Norman, and T. Senthil, Science **367** (2020).

[24] W. Witczak-Krempa, G. Chen, Y. B. Kim, and L. Balents, Annu. Rev. Condens. Matter Phys. **5**, 57 (2014).

[25] Y. Zhou, K. Kanoda, and T.-K. Ng, Rev. Mod. Phys. **89**, 025003 (2017).

[26] A. Ramirez, Annual Review of Materials Science **24**, 453 (1994).

[27] J. G. Rau and M. J. Gingras, Annual Review of Condensed Matter Physics (2019).

[28] D. Bergman, J. Alicea, E. Gull, S. Trebst, and L. Balents, Nature Physics **3**, 487 (2007).

[29] S. Lee and L. Balents, Phys. Rev. B **78**, 144417 (2008).

[30] F. L. Buessen, M. Hering, J. Reuther, and S. Trebst, Phys. Rev. Letters **120**, 057201 (2018).

[31] R. Sibille, N. Gauthier, E. Lhotel, V. Porée, V. Pomjakushin, R. A. Ewings, T. G. Perring, J. Ollivier, A. Wildes, C. Ritter, *et al.*, Nature Physics **16**, 546 (2020).

[32] Y.-D. Li and G. Chen, Phys. Rev. B **95**, 041106 (2017).

[33] S. Sorella, Y. Otsuka, and S. Yunoki, Scientific Reports **2**, 1 (2012).

[34] S. Okumura, H. Kawamura, T. Okubo, and Y. Motome, Journal of the Physical Society of Japan **79**, 114705 (2010).

[35] A. Banerjee, J. Yan, J. Knolle, C. A. Bridges, M. B. Stone, M. D. Lumsden, D. G. Mandrus, D. A. Tennant, R. Moessner, and S. E. Nagler, Science **356**, 1055 (2017).

[36] S. Yan, D. A. Huse, and S. R. White, Science **332**, 1173 (2011).

[37] T.-H. Han, J. S. Helton, S. Chu, D. G. Nocera, J. A. Rodriguez-Rivera, C. Broholm, and Y. S. Lee, Nature **492**, 406 (2012).

[38] Y. Iqbal, F. Becca, S. Sorella, and D. Poilblanc, Phys. Rev. B **87**, 060405 (2013).

[39] P. Chandra and B. Doucot, Phys. Rev. B **38**, 9335 (1988).

[40] L. Wang and A. W. Sandvik, Phys. Rev. Lett. **121**, 107202 (2018).

[41] L. Wang, D. Poilblanc, Z.-C. Gu, X.-G. Wen, and F. Verstraete, Phys. Rev. Lett. **111**, 037202 (2013).

[42] J. Ferrer, Phys. Rev. B **47**, 8769 (1993).

[43] H.-C. Jiang, H. Yao, and L. Balents, Phys. Rev. B **86**, 024424 (2012).

[44] K. Uematsu and H. Kawamura, Phys. Rev. B **98**, 134427 (2018).

[45] P. W. Anderson, Science **235**, 1196 (1987).

[46] P. W. Anderson, Materials Research Bulletin **8**, 153 (1973).

[47] R. Moessner and S. L. Sondhi, Phys. Rev. Lett. **86**, 1881 (2001).

[48] Y. Li, D. Adroja, D. Voneshen, R. I. Bewley, Q. Zhang, A. A. Tsirlin, and P. Gegenwart, Nature Communications **8**, 1 (2017).

[49] I. Kimchi, A. Nahum, and T. Senthil, Phys. Rev. X **8**, 031028 (2018).

[50] Y. Li, D. Adroja, P. K. Biswas, P. J. Baker, Q. Zhang, J. Liu, A. A. Tsirlin, P. Gegenwart, and Q. Zhang, Phys. Rev. Lett. **117**, 097201 (2016).

[51] B. Bernu, C. Lhuillier, and L. Pierre, Phys. Rev. Lett. **69**, 2590 (1992).

[52] L. Capriotti, A. E. Trumper, and S. Sorella, Phys. Rev. Lett. **82**, 3899 (1999).

[53] T. Jolicoeur, E. Dagotto, E. Gagliano, and S. Bacci, Phys. Rev. B **42**, 4800 (1990).

[54] R. Dally, R. J. Clément, R. Chisnell, S. Taylor, M. Butala, V. Doan-Nguyen, M. Balasubramanian, J. W. Lynn, C. P. Grey, and S. D. Wilson, Journal of Crystal Growth **459**, 203 (2017).

[55] M. Giot, L. C. Chapon, J. Androulakis, M. A. Green, P. G. Radaelli, and A. Lappas, Phys. Rev. Lett. **99**, 247211 (2007).

[56] T. M. McQueen, P. W. Stephens, Q. Huang, T. Klimczuk, F. Ronning, and R. J. Cava, Phys. Rev. Lett. **101**, 166402 (2008).

[57] Z. W. Ouyang, N. M. Xia, S. S. Sheng, J. Chen, Z. C. Xia, G. H. Rao, and X. H. Zheng, Phys. Rev. B **83**, 094417 (2011).

[58] S. Y. Ezhov, V. Anisimov, H. Pen, D. Khomskii, and G. Sawatzky, EPL (Europhysics Letters) **44**, 491 (1998).

[59] J. Chamorro, L. Ge, J. Flynn, M. Subramanian, M. Mourigal, and T. McQueen, Phys. Rev. Materials **2**, 034404 (2018).

[60] S. Gao, O. Zaharko, V. Tsurkan, Y. Su, J. S. White, G. S. Tucker, B. Roessli, F. Bourdarot, R. Sibille, D. Chernyshov, *et al.*, Nature Physics **13**, 157 (2017).

[61] Y. Iqbal, T. Müller, H. O. Jeschke, R. Thomale, and J. Reuther, Phys. Rev. B **98**, 064427 (2018).

[62] A. Krimmel, M. Mücksch, V. Tsurkan, M. Koza, H. Mutka, C. Ritter, D. Sheptyakov, S. Horn, and A. Loidl, Phys. Rev. B **73**, 014413 (2006).

[63] R. Valdés Aguilar, A. B. Sushkov, Y. J. Choi, S.-W. Cheong, and H. D. Drew, Phys. Rev. B **77**, 092412 (2008).

[64] C. Kant, J. Deisenhofer, T. Rudolf, F. Mayr, F. Schrettle, A. Loidl, V. Gnezdilov, D. Wulferding, P. Lemmens, and V. Tsurkan, Phys. Rev. B **80**, 214417 (2009).

[65] S.-H. Lee, C. Broholm, T. H. Kim, W. Ratcliff, and S.-W. Cheong, Phys. Rev. Lett. **84**, 3718 (2000).

[66] A. B. Sushkov, O. Tchernyshyov, W. R. II, S. W. Cheong, and H. D. Drew, Phys. Rev. Lett. **94**, 137202 (2005).

[67] Y. Li, Advanced Quantum Technologies **2**, 1900089 (2019).

[68] Y. Li, S. Bachus, B. Liu, I. Radelytskyi, A. Bertin, A. Schneidewind, Y. Tokiwa, A. A. Tsirlin, and P. Gegenwart, Phys. Rev. Lett. **122**, 137201 (2019).

[69] X. Zhang, F. Mahmood, M. Daum, Z. Dun, J. A. M. Paddison, N. J. Laurita, T. Hong, H. Zhou, N. P. Armitage, and M. Mourigal, Phys. Rev. X **8**, 031001 (2018).

[70] Z. Zhu, P. A. Maksimov, S. R. White, and A. L. Chernyshev, Phys. Rev. Lett. **119**, 157201 (2017).

[71] Y.-D. Li, Y. Shen, Y. Li, J. Zhao, and G. Chen, Phys. Rev. B **97**, 125105 (2018).

[72] Y.-D. Li, X. Wang, and G. Chen, Phys. Rev. B **94**, 035107 (2016).

[73] Y. Li, G. Chen, W. Tong, L. Pi, J. Liu, Z. Yang, X. Wang, and Q. Zhang, Phys. Rev. Lett. **115**, 167203 (2015).

[74] Y. Li, H. Liao, Z. Zhang, S. Li, F. Jin, L. Ling, L. Zhang, Y. Zou, L. Pi, Z. Yang, *et al.*, Scientific Reports **5**, 1 (2015).

[75] Y. Li, D. Adroja, R. I. Bewley, D. Voneshen, A. A. Tsirlin, P. Gegenwart, and Q. Zhang, Phys. Rev. Lett. **118**, 107202 (2017).

[76] J. A. Paddison, M. Daum, Z. Dun, G. Ehlers, Y. Liu, M. B. Stone, H. Zhou, and M. Mourigal, Nature Physics **13**, 117 (2017).

[77] Y.-D. Shen, Yaoand Li, H. Wo, Y. Li, S. Shen, B. Pan, Q. Wang, H. C. Walker, P. Steffens, M. Boehm, Y. Hao, D. L. Quintero-Castro, L. W. Harriger, M. D. Frontzek, L. Hao, S. Meng, Q. Zhang, G. Chen, and J. Zhao, Nature **540**, 559 (2016).

[78] Y. Xu, J. Zhang, Y. S. Li, Y. J. Yu, X. C. Hong, Q. M. Zhang, and S. Y. Li, Phys. Rev. Letters **117**, 267202 (2016).

[79] M. M. Bordelon, E. Kenney, C. Liu, T. Hogan, L. Posthuma, M. Kavand, Y. Lyu, M. Sherwin, N. P. Butch, C. Brown, *et al.*, Nature Physics **15**, 1058 (2019).

[80] M. M. Bordelon, C. Liu, L. Posthuma, P. M. Sarte, N. P. Butch, D. M. Pajerowski, A. Banerjee, L. Balents, and S. D. Wilson, Phys. Rev. B **101**, 224427 (2020).

[81] K. M. Ranjith, D. Dmytriieva, S. Khim, J. Sichelschmidt, S. Luther, D. Ehlers, H. Yasuoka, J. Wosnitza, A. A. Tsirlin, H. Kühne, and M. Baenitz, Phys. Rev. B **99**, 180401 (2019).

[82] J. Guo, X. Zhao, S. Ohira-Kawamura, L. Ling, J. Wang, L. He, K. Nakajima, B. Li, and Z. Zhang, Phys. Rev. Materials **4**, 064410 (2020).

[83] M. Baenitz, P. Schlender, J. Sichelschmidt, Y. A. Onykiienko, Z. Zangeneh, K. M. Ranjith, R. Sarkar, L. Hozoi, H. C. Walker, J.-C. Orain, H. Yasuoka, J. van den Brink, H. H. Klauss, D. S. Inosov, and T. Doert, Phys. Rev. B **98**, 220409 (2018).

[84] W. Liu, Z. Zhang, J. Ji, Y. Liu, J. Li, X. Wang, H. Lei, G. Chen, and Q. Zhang, Chinese Physics Letters **35**, 117501 (2018).

[85] K. M. Ranjith, S. Luther, T. Reimann, B. Schmidt, P. Schlender, J. Sichelschmidt, H. Yasuoka, A. M. Strydom, Y. Skourski, J. Wosnitza, H. Kühne, T. Doert, and M. Baenitz, Phys. Rev. B **100**, 224417 (2019).

[86] R. Sarkar, P. Schlender, V. Grinenko, E. Haeussler, P. J. Baker, T. Doert, and H.-H. Klauss, Phys. Rev. B **100**, 241116 (2019).

[87] J. Sichelschmidt, P. Schlender, B. Schmidt, M. Baenitz, and T. Doert, Journal of Physics: Condensed Matter **31**, 205601 (2019).

[88] A. Kitaev, Annals of Physics **321**, 2 (2006).

[89] I. S. Hagemann, Q. Huang, X. P. A. Gao, A. P. Ramirez, and R. J. Cava, Phys. Rev. Lett. **86**, 894 (2001).

[90] J.-S. Bernier, M. J. Lawler, and Y. B. Kim, Phys. Rev. Letters **101**, 047201 (2008).

[91] L. Savary, E. Gull, S. Trebst, J. Alicea, D. Bergman, and L. Balents, Phys. Rev. B **84**, 064438 (2011).

[92] S. Bramwell and M. Harris, Journal of Physics: Condensed Matter **10**, L215 (1998).

[93] M. Harris and M. Zinkin, Modern Physics Letters B **10**, 417 (1996).

[94] M. Harris, S. Bramwell, P. Holdsworth, and J. Champion, Phys. Rev. Letters **81**, 4496 (1998).

[95] R. Moessner and J. T. Chalker, Phys. Rev. Letters **80**, 2929 (1998).

[96] B. Canals and C. Lacroix, Phys. Rev. Letters **80**, 2933 (1998).

[97] A. P. Ramirez, A. Hayashi, R. J. Cava, R. Siddharthan, and B. Shastry, Nature **399**, 333 (1999).

[98] S. T. Bramwell and M. J. Gingras, Science **294**, 1495 (2001).

[99] K. A. Ross, L. Savary, B. D. Gaulin, and L. Balents, Phys. Rev. X **1**, 021002 (2011).

[100] W.-J. Hu, S.-S. Gong, W. Zhu, and D. N. Sheng, Phys. Rev. B **92**, 140403 (2015).

[101] P. A. Maksimov, Z. Zhu, S. R. White, and A. L. Chernyshev, Phys. Rev. X **9**, 021017 (2019).

[102] Z. Zhu and S. R. White, Phys. Rev. B **92**, 041105 (2015).

[103] Y. Kamiya, L. Ge, T. Hong, Y. Qiu, D. Quintero-Castro, Z. Lu, H. Cao, M. Matsuda, E. Choi, C. Batista, *et al.*, Nature communications **9**, 1 (2018).

[104] G. Koutroulakis, T. Zhou, Y. Kamiya, J. D. Thompson, H. D. Zhou, C. D. Batista, and S. E. Brown, Phys. Rev. B **91**, 024410 (2015).

[105] J. Ma, Y. Kamiya, T. Hong, H. B. Cao, G. Ehlers, W. Tian, C. D. Batista, Z. L. Dun, H. D. Zhou, and M. Matsuda, Phys. Rev. Lett. **116**, 087201 (2016).

[106] Y. R. Wang, Phys. Rev. B **45**, 12608 (1992).

[107] M. Isoda, H. Nakano, and T. Sakai, Journal of the Physical Society of Japan **80**, 084704 (2011).

[108] N. Elstner and A. P. Young, Phys. Rev. B **50**, 6871 (1994).

[109] M. T. Hutchings, in *Solid state physics*, Vol. 16 (Elsevier, 1964) pp. 227–273.

[110] K. Stevens, Proceedings of the Physical Society. Section A **65**, 209 (1952).

[111] G. J. Nieuwenhuys, Phys. Rev. B **35**, 5260 (1987).

[112] P. Thalmeier and P. Fulde, Phys. Rev. Lett. **49**, 1588 (1982).

[113] P. Thalmeier, Journal of Physics C: Solid State Physics **17**, 4153 (1984).

[114] P. Čermák, A. Schneidewind, B. Liu, M. M. Koza, C. Franz, R. Schönmann, O. Sobolev, and C. Pfleiderer, Proceedings of the National Academy of Sciences **116**, 6695 (2019).

[115] D. T. Adroja, A. del Moral, C. de la Fuente, A. Fraile, E. A. Goremychkin, J. W. Taylor, A. D. Hillier, and F. Fernandez-Alonso, Phys. Rev. Lett. **108**, 216402 (2012).

[116] P. M. Sarte, A. M. Arévalo-López, M. Songvilay, D. Le, T. Guidi, V. García-Sakai, S. Mukhopadhyay, S. C. Capelli, W. D. Ratcliff, K. H. Hong, G. M. McNally, E. Pachoud, J. P. Attfield, and C. Stock, Phys. Rev. B **98**, 224410 (2018).

[117] J. R. Copley and T. J. Udovic, Journal of research of the National Institute of Standards and Technology **98**, 71 (1993).

[118] D. S. Sivia, *Elementary scattering theory: for X-ray and neutron users* (Oxford University Press, 2011).

[119] V. F. Sears, Neutron news **3**, 26 (1992).

[120] S. Clarke, A. Fowkes, A. Harrison, R. Ibberson, and M. Rosseinsky, Chemistry of Materials **10**, 372 (1998).

[121] M. M. Bordelon, C. Liu, L. Posthuma, E. Kenney, M. J. Graf, N. P. Butch, A. Banerjee, S. Calder, L. Balents, and S. D. Wilson, Phys. Rev. B **103**, 014420 (2021).

[122] M. M. Bordelon, J. D. Bocarsly, L. Posthuma, A. Banerjee, Q. Zhang, and S. D. Wilson, Phys. Rev. B **103**, 024430 (2021).

[123] K. Takada, H. Sakurai, E. Takayama-Muromachi, F. Izumi, R. A. Dilanian, and T. Sasaki, Nature **422**, 53 (2003).

[124] R. Jin, B. C. Sales, P. Khalifah, and D. Mandrus, Phys. Rev. Lett. **91**, 217001 (2003).

[125] J. Rodríguez-Carvajal, Physica B **192**, 55 (1993).

[126] A. Wills, Physica B: Condensed Matter **276**, 680 (2000).

[127] G. Jackeli and D. A. Ivanov, Phys. Rev. B **76**, 132407 (2007).

[128] S. Furukawa and G. Misguich, Phys. Rev. B **75**, 214407 (2007).

[129] A. Ralko, M. Ferrero, F. Becca, D. Ivanov, and F. Mila, Phys. Rev. B **71**, 224109 (2005).

[130] L. O. Manuel and H. A. Ceccatto, Phys. Rev. B **60**, 9489 (1999).

[131] Y. Iqbal, W.-J. Hu, R. Thomale, D. Poilblanc, and F. Becca, Phys. Rev. B **93**, 144411 (2016).

[132] G. Misguich, C. Lhuillier, B. Bernu, and C. Waldtmann, Phys. Rev. B **60**, 1064 (1999).

[133] R. V. Mishmash, J. R. Garrison, S. Bieri, and C. Xu, Phys. Rev. Lett. **111**, 157203 (2013).

[134] A. Wietek and A. M. Läuchli, Phys. Rev. B **95**, 035141 (2017).

[135] Y. Shirata, H. Tanaka, A. Matsuo, and K. Kindo, Phys. Rev. Lett. **108**, 057205 (2012).

[136] T. Ono, H. Tanaka, H. Aruga Katori, F. Ishikawa, H. Mitamura, and T. Goto, Phys. Rev. B **67**, 104431 (2003).

[137] N. A. Fortune, S. T. Hannahs, Y. Yoshida, T. E. Sherline, T. Ono, H. Tanaka, and Y. Takano, Phys. Rev. Lett. **102**, 257201 (2009).

[138] Y. Li, J. Fu, Z. Wu, and Q. Zhang, Chemical Physics Letters **570**, 37 (2013).

[139] Y. Li, B. Pan, S. Li, W. Tong, L. Ling, Z. Yang, J. Wang, Z. Chen, Z. Wu, and Q. Zhang, New Journal of Physics **16**, 093011 (2014).

[140] S.-H. Lee, H. Kikuchi, Y. Qiu, B. Lake, Q. Huang, K. Habicht, and K. Kiefer, Nature materials **6**, 853 (2007).

[141] C. M. Pasco, B. A. Trump, T. T. Tran, Z. A. Kelly, C. Hoffmann, I. Heinmaa, R. Stern, and T. M. McQueen, Phys. Rev. Materials **2**, 044406 (2018).

[142] K. Riedl, R. Valentí, and S. M. Winter, Nature communications **10**, 1 (2019).

[143] A. Zorko, S. Nellutla, J. van Tol, L. C. Brunel, F. Bert, F. Duc, J.-C. Trombe, M. A. de Vries, A. Harrison, and P. Mendels, Phys. Rev. Lett. **101**, 026405 (2008).

[144] L. Messio, S. Bieri, C. Lhuillier, and B. Bernu, Phys. Rev. Lett. **118**, 267201 (2017).

[145] K. Y. Povarov, A. I. Smirnov, O. A. Starykh, S. V. Petrov, and A. Y. Shapiro, Phys. Rev. Lett. **107**, 037204 (2011).

[146] S. A. Zvyagin, D. Kamenskyi, M. Ozerov, J. Wosnitza, M. Ikeda, T. Fujita, M. Hagiwara, A. I. Smirnov, T. A. Soldatov, A. Y. Shapiro, J. Krzystek, R. Hu, H. Ryu, C. Petrovic, and M. E. Zhitomirsky, Phys. Rev. Lett. **112**, 077206 (2014).

[147] F. A. Cevallos, K. Stolze, T. Kong, and R. Cava, Materials Research Bulletin **105**, 154 (2018).

[148] Y. Li, S. Bachus, H. Deng, W. Schmidt, H. Thoma, V. Hutanu, Y. Tokiwa, A. A. Tsirlin, and P. Gegenwart, Phys. Rev. X **10**, 011007 (2020).

[149] Y. Shen, C. Liu, Y. Qin, S. Shen, Y.-D. Li, R. Bewley, A. Schneidewind, G. Chen, and J. Zhao, Nature Communications **10**, 4530 (2019).

[150] D. Yamamoto, G. Marmorini, and I. Danshita, Phys. Rev. Lett. **112**, 127203 (2014).

[151] S. Stoll and A. Schweiger, Journal of Magnetic Resonance **178**, 42 (2006).

[152] A. Larson and R. Von Dreele, Los Alamos National Laboratory: Santa Fe, NM, USA , 86 (2004).

[153] B. H. Toby, Journal of Applied Crystallography **34**, 210 (2001).

[154] I. Sumarlin, J. Lynn, T. Chattopadhyay, S. Barilo, and D. Zhigunov, Physica C: Superconductivity **219**, 195 (1994).

[155] D. Yamamoto, G. Marmorini, and I. Danshita, Phys. Rev. Lett. **114**, 027201 (2015).

[156] M. Mourigal, W. Fuhrman, A. Chernyshev, and M. Zhitomirsky, Phys. Rev. B **88**, 094407 (2013).

[157] J. Gaudet, D. D. Maharaj, G. Sala, E. Kermarrec, K. A. Ross, H. A. Dabkowska, A. I. Kolesnikov, G. E. Granroth, and B. D. Gaulin, Phys. Rev. B **92**, 134420 (2015).

[158] P. Fulde and M. Loewenhaupt, Advances in Physics **34**, 589 (1985).

[159] F. Ferrari and F. Becca, Phys. Rev. X **9**, 031026 (2019).

[160] S. Hu, W. Zhu, S. Eggert, and Y.-C. He, Phys. Rev. Lett. **123**, 207203 (2019).

[161] J. Iaconis, C. Liu, G. B. Halász, and L. Balents, SciPost Phys **4** (2018).

[162] E. Rastelli and A. Tassi, Journal of Physics C: Solid State Physics **19**, L423 (1986).

[163] L. Chen, D.-W. Qu, H. Li, B.-B. Chen, S.-S. Gong, J. von Delft, A. Weichselbaum, and W. Li, Phys. Rev. B **99**, 140404 (2019).

[164] O. A. Starykh, Reports on Progress in Physics **78**, 052502 (2015).

[165] S. Gao, F. Xiao, K. Kamazawa, K. Ikeuchi, D. Biner, K. W. Krämer, C. Rüegg, and T.-h. Arima, Phys. Rev. B **102**, 024424 (2020).

[166] K. Tomiyasu, H. Suzuki, M. Toki, S. Itoh, M. Matsuura, N. Aso, and K. Yamada, Phys. Rev. Letters **101**, 177401 (2008).

[167] X. Bai, J. Paddison, E. Kapit, S. Koohpayeh, J.-J. Wen, S. Dutton, A. Savici, A. Kolesnikov, G. Granroth, C. Broholm, *et al.*, Phys. Rev. Letters **122**, 097201 (2019).

[168] L. Ge, J. Flynn, J. A. Paddison, M. B. Stone, S. Calder, M. Subramanian, A. Ramirez, and M. Mourigal, Phys. Rev. B **96**, 064413 (2017).

[169] O. Zaharko, N. B. Christensen, A. Cervellino, V. Tsurkan, A. Maljuk, U. Stuhr, C. Niedermayer, F. Yokaichiya, D. Argyriou, M. Boehm, *et al.*, Phys. Rev. B **84**, 094403 (2011).

[170] B. Roy, A. Pandey, Q. Zhang, T. Heitmann, D. Vaknin, D. C. Johnston, and Y. Furukawa, Phys. Rev. B **88**, 174415 (2013).

[171] G. J. MacDougall, D. Gout, J. L. Zarestky, G. Ehlers, A. Podlesnyak, M. A. McGuire, D. Mandrus, and S. E. Nagler, Proceedings of the National Academy of Sciences **108**, 15693 (2011).

[172] G. Chen, Phys. Rev. B **96**, 020412 (2017).

[173] M. E. Zhitomirsky, Phys. Rev. B **54**, 353 (1996).

[174] L.-J. Chang, D. Huang, W. Li, S.-W. Cheong, W. Ratcliff, and J. Lynn, Journal of Physics: Condensed matter **21**, 456008 (2009).

[175] G. Lawes, B. Melot, K. Page, C. Ederer, M. Hayward, T. Proffen, and R. Seshadri, Phys. Rev. B **74**, 024413 (2006).

[176] X. Chen, Z. Yang, Y. Xie, Z. Huang, L. Ling, S. Zhang, L. Pi, Y. Sun, and Y. Zhang, Journal of Applied Physics **113**, 17E129 (2013).

[177] C. A. Marjerrison, C. Mauws, A. Z. Sharma, C. R. Wiebe, S. Derakhshan, C. Boyer, B. D. Gaulin, and J. E. Greedan, Inorganic Chemistry **55**, 12897 (2016).

[178] Y.-J. Song, K.-H. Ahn, K.-W. Lee, and W. E. Pickett, Phys. Rev. B **90**, 245117 (2014).

[179] S. Injac, A. K. Yuen, M. Avdeev, F. Orlandi, and B. J. Kennedy, Physical Chemistry Chemical Physics **21**, 7261 (2019).

[180] L. Bellier-Castella, M. J. Gingras, P. C. Holdsworth, and R. Moessner, Canadian Journal of Physics **79**, 1365 (2001).

[181] V. Anand, A. Bera, J. Xu, T. Herrmannsdörfer, C. Ritter, and B. Lake, Phys. Rev. B **92**, 184418 (2015).

[182] E. Lhotel, S. Petit, S. Guitteny, O. Florea, M. C. Hatnean, C. Colin, E. Ressouche, M. Lees, and G. Balakrishnan, Phys. Rev. Letters **115**, 197202 (2015).

[183] H. Takatsu, S. Onoda, S. Kittaka, A. Kasahara, Y. Kono, T. Sakakibara, Y. Kato, B. Fåk, J. Ollivier, J. W. Lynn, *et al.*, Phys. Rev. Letters **116**, 217201 (2016).

[184] K. Tomiyasu, K. Matsuhira, K. Iwasa, M. Watahiki, S. Takagi, M. Wakeshima, Y. Hinatsu, M. Yokoyama, K. Ohoyama, and K. Yamada, Journal of the Physical Society of Japan **81**, 034709 (2012).

[185] O. Benton, Phys. Rev. B **94**, 104430 (2016).

[186] S. Petit, E. Lhotel, B. Canals, M. C. Hatnean, J. Ollivier, H. Mutka, E. Ressouche, A. Wildes, M. Lees, and G. Balakrishnan, Nature Physics **12**, 746 (2016).

[187] C. Mauws, A. Hallas, G. Sala, A. A. Aczel, P. Sarte, J. Gaudet, D. Ziat, J. Quilliam, J. Lussier, M. Bieringer, *et al.*, Phys. Rev. B **98**, 100401 (2018).

[188] J. Gaudet, E. M. Smith, J. Dudemaine, J. Beare, C. R. C. Buhariwalla, N. P. Butch, M. B. Stone, A. I. Kolesnikov, G. Xu, D. R. Yahne, K. A. Ross, C. A. Marjerrison, J. D. Garrett, G. M. Luke, A. D. Bianchi, and B. D. Gaulin, Phys. Rev. Lett. **122**, 187201 (2019).

[189] M. Mignanelli, P. Potter, and M. Barker, Journal of Nuclear Materials **97**, 213 (1981).

[190] M. G. Barker, S. A. Frankham, and P. G. Gadd, Journal of Inorganic and Nuclear Chemistry **43**, 2815 (1981).

[191] M. G. Barker, S. A. Frankham, and P. G. Gadd, Journal of Nuclear Materials **218**, 256 (1995).

[192] A. A. Coelho, Journal of Applied Crystallography **51**, 210 (2018).

[193] H. T. Stokes, D. M. Hatch, and B. J. Campbell, iso.buy.edu , 1 (2019).

[194] H. T. Stokes, D. M. Hatch, B. J. Campbell, and D. E. Tanner, Journal of Applied Crystallography **39**, 607 (2006).

[195] M. E. Fisher, Philosophical Magazine **7**, 1731 (1962).

[196] P. Radhakrishna, J. Hammann, and P. Pari, Journal of Magnetism and Magnetic Materials **23**, 254 (1981).

[197] R. Clos, M. Devalette, C. Fouassier, and P. Hagenmuller, Materials Research Bulletin **5**, 179 (1970).

[198] G. Bastien, B. Rubrecht, E. Haeussler, P. Schlender, Z. Zangeneh, S. Avdoshenko, R. Sarkar, A. Alfonsov, S. Luther, Y. A. Onykiienko, *et al.*, SciPost Phys. **9** (2020).

[199] P. Babkevich, A. Finco, M. Jeong, B. Dalla Piazza, I. Kovacevic, G. Klughertz, K. W. Krämer, C. Kraemer, D. T. Adroja, E. Goremychkin, T. Unruh, T. Strässle, A. Di Lieto, J. Jensen, and H. M. Rønnow, Phys. Rev. B **92**, 144422 (2015).

[200] A. Ellens, H. Andres, M. L. H. ter Heerdt, R. T. Wegh, A. Meijerink, and G. Blasse, Phys. Rev. B **55**, 180 (1997).

[201] C.-K. Loong, M. Loewenhaupt, J. C. Nipko, M. Braden, and L. A. Boatner, Phys. Rev. B **60**, R12549 (1999).

[202] J. Rush, J. Rowe, and A. Maeland, Journal of Physics F: Metal Physics **10**, L283 (1980).

[203] S. Wirth, R. Skomski, and J. M. D. Coey, Phys. Rev. B **55**, 5700 (1997).

[204] B. Gao, T. Chen, D. W. Tam, C.-L. Huang, K. Sasmal, D. T. Adroja, F. Ye, H. Cao, G. Sala, M. B. Stone, *et al.*, Nature Physics **15**, 1052 (2019).

[205] R. Sibille, E. Lhotel, V. Pomjakushin, C. Baines, T. Fennell, and M. Kenzelmann, Phys. Rev. Lett. **115**, 097202 (2015).

[206] J. Gaudet, A. M. Hallas, A. I. Kolesnikov, and B. D. Gaulin, Phys. Rev. B **97**, 024415 (2018).

[207] Y.-D. Li, X. Wang, and G. Chen, Phys. Rev. B **94**, 201114 (2016).

[208] K. Hirakawa, H. Kadowaki, and K. Ubukoshi, Journal of the Physical Society of Japan **54**, 3526 (1985).

[209] K. Takeda, K. Miyake, K. Takeda, and K. Hirakawa, Journal of the Physical Society of Japan **61**, 2156 (1992).

[210] Y. Wang, X. Yu, S. Xu, J. Bai, R. Xiao, Y.-S. Hu, H. Li, X.-Q. Yang, L. Chen, and X. Huang, Nature communications **4**, 1 (2013).

[211] A. Maazaz, C. Delmas, and P. Hagenmuller, Journal of Inclusion Phenomena **1**, 45 (1983).

[212] M. Dhariwal, L. Pisani, and T. Maitra, Journal of Physics: Condensed Matter **26**, 205501 (2014).

[213] G. Jackeli and D. A. Ivanov, Phys. Rev. B **76**, 132407 (2007).

[214] J. L. Schmehr and S. D. Wilson, Annual Review of Materials Research **47**, 153 (2017).

[215] S. J. Mugavero III, W. R. Gemmill, I. P. Roof, and H.-C. zur Loye, Journal of Solid State Chemistry **182**, 1950 (2009).

[216] H. Zhu, D. Jin, L. Zhu, H. Yang, K. Yao, and Z. Xi, Journal of Alloys and Compounds **464**, 508 (2008).

[217] P. L. Smallwood, M. D. Smith, and H.-C. zur Loye, Journal of Crystal Growth **216**, 299 (2000).

[218] X. Tang, J. He, K. Aaron, E. Abbott, J. K. Kolis, and T. M. Tritt, Journal of Crystal Growth **310**, 665 (2008).

[219] J. R. Cantwell, I. P. Roof, M. D. Smith, and H.-C. zur Loye, Solid State Sciences **13**, 1006 (2011).